

INFORMATION TO USERS

This manuscript has been reproduced from the microfilm master. UMI films the text directly from the original or copy submitted. Thus, some thesis and dissertation copies are in typewriter face, while others may be from any type of computer printer.

The quality of this reproduction is dependent upon the quality of the copy submitted. Broken or indistinct print, colored or poor quality illustrations and photographs, print bleedthrough, substandard margins, and improper alignment can adversely affect reproduction.

In the unlikely event that the author did not send UMI a complete manuscript and there are missing pages, these will be noted. Also, if unauthorized copyright material had to be removed, a note will indicate the deletion.

Oversize materials (e.g., maps, drawings, charts) are reproduced by sectioning the original, beginning at the upper left-hand corner and continuing from left to right in equal sections with small overlaps. Each original is also photographed in one exposure and is included in reduced form at the back of the book.

Photographs included in the original manuscript have been reproduced xerographically in this copy. Higher quality 6" x 9" black and white photographic prints are available for any photographs or illustrations appearing in this copy for an additional charge. Contact UMI directly to order.

UMI

**A Bell & Howell Information Company
300 North Zeeb Road, Ann Arbor MI 48106-1346 USA
313/761-4700 800/521-0600**

**NONLINEAR STOCHASTIC MODELS FOR OCEAN
WAVE LOADS AND RESPONSES OF OFFSHORE
STRUCTURES AND VESSELS**

**A DISSERTATION
SUBMITTED TO THE DEPARTMENT OF CIVIL ENGINEERING
AND THE COMMITTEE ON GRADUATE STUDIES
OF STANFORD UNIVERSITY
IN PARTIAL FULFILLMENT OF THE REQUIREMENTS
FOR THE DEGREE OF
DOCTOR OF PHILOSOPHY**

**By
Alok K. Jha
January 1997**

UMI Number: 9723375

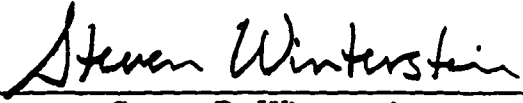
UMI Microform 9723375
Copyright 1997, by UMI Company. All rights reserved.

**This microform edition is protected against unauthorized
copying under Title 17, United States Code.**

UMI
300 North Zeeb Road
Ann Arbor, MI 48103

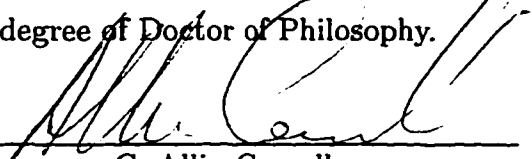
© Copyright 1997 by Alok K. Jha
All Rights Reserved

I certify that I have read this dissertation and that in my opinion it is fully adequate, in scope and quality, as a dissertation for the degree of Doctor of Philosophy.



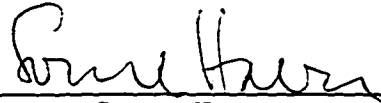
Steven R. Winterstein
(Principal Adviser)

I certify that I have read this dissertation and that in my opinion it is fully adequate, in scope and quality, as a dissertation for the degree of Doctor of Philosophy.



C. Allin Cornell
(Co-adviser)

I certify that I have read this dissertation and that in my opinion it is fully adequate, in scope and quality, as a dissertation for the degree of Doctor of Philosophy.



Sverre Haver

I certify that I have read this dissertation and that in my opinion it is fully adequate, in scope and quality, as a dissertation for the degree of Doctor of Philosophy.



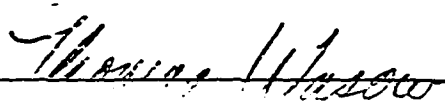
Helmut Krawinkler

I certify that I have read this dissertation and that in my opinion it is fully adequate, in scope and quality, as a dissertation for the degree of Doctor of Philosophy.



Tom Marthinsen

Approved for the University Committee on Graduate Studies:



Thomas Wasson

Abstract

Second-order nonlinear models have been increasingly used in recent years to model the behavior of offshore structures. We apply such models to study the properties of random ocean waves. We also study the global responses of a spar floating platform by modeling the incident wave forces as a second-order phenomenon. To reduce the intense computational expense involved in a time-domain analysis of such models, we develop efficient methods and demonstrate it for estimating the fatigue damage in offshore structures. A fatigue reliability analysis accounting for uncertainties in the wave environment, in the resulting response and in the material properties is then demonstrated for a ship structure.

Traditional linear models of wave loads on offshore structures tend to be inaccurate in the response predictions. Second-order nonlinear models although computationally more expensive provide an opportunity to better predict these loads. These nonlinear models are based on a perturbation expansion of the linear form of the associated problem.

In modeling the random ocean waves as a second-order phenomenon, we developed convenient analytic formulae to predict the nonlinearities as function of the wave climate and of the water depth at the site of interest. We compare the model predictions to measured waves in wave tanks and in oceans; and find the predictions to match the field data more than the wave tank data.

We model the tested spar floating platform as a linear rigid-body with 6 degrees of freedom. The incident wave loads are modeled as a second-order phenomenon. Of interest is the global response of the spar, which here is the total horizontal displacement near the spar deck. Although the apparent transient response and the

few measured response cycles pose difficulties in calibrating the model, we find the model to offer reasonable predictions when compared to the measured results in wave tanks.

We then show an efficient method to estimate fatigue damage which is especially beneficial when the nonlinear analysis is computationally expensive. We demonstrate this method for a ship structure where a two-dimensional strip theory is used to find the nonlinear wave loads by integrating the water pressures to the exact instantaneous wetted surface. In this method, fatigue damage estimated from a carefully selected set of sinusoidal waves from stochastic theory seems to well approximate the damage estimate from a full time domain ship analysis in random waves.

Finally, we also show a fatigue reliability example for a ship structure where the probability of failure is found by integrating the uncertainties at all three levels: the wave climate, the structural response given the wave climate and the material properties. Here an efficient method is shown to select the associated design parameters in order to achieve a preselected reliability level.

Acknowledgments

I wish to thank Dr. Steven R. Winterstein for advising me through my doctoral studies and for providing me the necessary guidance and training to successfully finish my studies at Stanford University. The skills I have acquired here will always help me in the years to come. I am very pleased to thank my co-adviser, Professor C. Allin Cornell for his participation in this research and for all his insightful discussions.

I would like to thank Dr. Sverre Haver and Dr. Tom Marthinsen for providing me with the field and wave tank data on wave measurements. Their active participation in improving the quality of my thesis is very much appreciated. I also want to thank Professor Helmut Krawinkler for serving on my reading committee.

The financial support of the Reliability of Marine Structures (RMS) program and its industry sponsors is gratefully acknowledged. I am also pleased to acknowledge the additional support provided by the Office of Naval Research (Grant Nos. N00014-95-1-0366 and N00014-96-1-0641). I thank Offshore Technology Research Center for providing me with the wave tank data on the spar platform and also wish to thank Det Norske Veritas for allowing access to the ship analysis program.

I will always remember the support, friendship and encouragement of all my friends at RMS, Satyendra Kumar, Nilesh Shome, Cliff Lange, Rune Torhaug, Todd Ude, Doug Schmucker, Paolo Bazzurro, Lance Manual, Knut Ronold, Jorge Carballo, Ron De Jong, and Tina Kashef.

I thank my mother, my father and my family for their encouragement and their confidence in me. I thank my wife Reeta for her love and care that gave me strength in all my endeavors.

Finally, I thank God Almighty.

Contents

Abstract	iv
Acknowledgments	vi
1 Introduction	1
2 Nonlinear Random Ocean Waves	4
2.1 Introduction	4
2.2 Wave Model	5
2.3 Comparison of α_3 and α_4 : Data vs. Prediction Models	11
2.4 Comparison of Distributions of Wave Elevation, Crest Height and Wave Height	16
2.4.1 Summary of Measured Wave Data Sets	16
2.4.2 Summary of Simulated Wave Data	23
2.4.3 Comparison of Wave Elevation Distributions	24
2.4.4 Comparison of Crest Height Distributions	35
2.4.5 Comparison of Wave Height Distributions	42
2.5 Comparison of Local Wave Statistics	47
2.6 Conclusions	52
2.7 Identification of First-order Waves	52
3 Spar Floating Platform	55
3.1 Introduction	55
3.2 Spar Model for Slow-drift Response	57

3.2.1	Experimental Data	57
3.2.2	Structural Model	65
3.2.3	Hydrodynamic Model Forms	68
3.2.4	Input Wave Histories for Models	72
3.2.5	Calibrated Damping Values	73
3.2.6	Estimation of Initial Conditions	75
3.3	Results	77
3.3.1	Wave-frequency (first-order) Response	77
3.3.2	Surge (DOF1) and Pitch (DOF5) Component Responses	81
3.3.3	Total Predicted Horizontal Displacement	93
3.4	Conclusion	99
4	Nonlinear Ship Loads	101
4.1	Introduction	101
4.2	Ship Model	102
4.3	Stochastic Fatigue Analysis	103
4.3.1	Existing Approaches to Fatigue Analysis	106
4.4	Ship Response Analysis Methods	109
4.4.1	Comparison of Ship Response from Linear and Nonlinear Analyses	110
4.5	Proposed NTF Approach	115
4.5.1	NTF Modeling Issues	117
4.5.2	Selection of Waves from Stochastic Theory	119
4.5.3	Selection of Side Wave Parameters	123
4.6	Predicted NTF Fatigue Damage vs. Data	125
4.6.1	Modeling Duration Correction Effects	135
4.6.2	Modeling Scatter Effects in Ship Loads	136
4.6.3	Inclusion of Bias Correction in the Prediction Model	143
4.7	Conclusions	147
5	Ship Fatigue Reliability	151
5.1	Introduction	151
5.2	General Fatigue Formulation	151

5.2.1	Load Environment	153
5.2.2	Gross Response	154
5.2.3	Failure Measure	157
5.3	Results	159
5.3.1	Numerical Values for Random Variables in Fatigue Analysis .	159
5.3.2	Importance Factors of Physical Random Variables	161
5.4	Selection of Material Properties in Design to Achieve Desired Reliability	164
5.4.1	Forward FORM	164
5.4.2	Inverse FORM	166
5.5	Conclusions	167
6	Summary and Recommendations	171
6.1	Nonlinear Random Ocean Waves	171
6.2	Spar Floating Platform	173
6.3	Nonlinear Ship Loads	175
6.4	Ship Fatigue Reliability	177
	Bibliography	179
	A First-order Wave Identification	189
	B QTF-surface Spline Interpolation	195
B.1	Introduction	195
B.2	Interpolation Options	196
B.3	Verification Studies of FITQTF Interpolation	198

List of Tables

2.1	Summary information of the four wave data sets used in CDF comparisons of wave elevations, wave crests, and wave heights	21
2.2	Observed statistics of the three (zero-mean) measured wave data sets. Note that these statistics have been estimated from the total durations (see last column of Table 2.1) of the data sets.	21
2.3	Spectral parameters for the four wave data sets	21
2.4	Predicted moments from fitted JONSWAP spectral parameters and from measured spectrum that has been smoothed	22
2.5	Skewness and kurtosis predictions from a consistent second-order analysis vs. exact second-order analysis	22
2.6	Number of simulations and durations (in hours) of each for the four data sets	23
2.7	Means and standard deviations of moments of simulated second-order histories for the four data sets. The standard deviation of the moments reflects the predicted scatter in the durations specified.	25
3.1	Details of the spar configuration (in prototype scale)	58
3.2	Reference wave summary statistics for the OTRC wave tank tests used for slow-drift response analysis of the spar	61
3.3	Statistical moments of the measured horizontal displacements for the seastates. Note that the maximum and minimum values contain μ	63
3.4	Statistical moments of the filtered components (with zero mean) of measured horizontal displacements	64
3.5	Nomenclature for the four proposed model forms	72

3.6	Calibrated damping ratios (%), ξ , for the models in surge (DOF1) and pitch (DOF5) components	75
3.7	Estimated initial conditions in surge and pitch DOFs for the three seastates	76
4.1	Main Particulars of Ship presented in Fig. 4.1	103
4.2	Statistics of Ship Load History	113
5.1	Estimated mean and standard deviation of the regression parameters for bending moments (kN.m) given wave heights. The bending moments have been divided by 10^5	158
5.2	Numerical values of means and COVs of random variables and their distribution types used in fatigue formulation. These are common to all three stresses: sag, hog and range.	160
5.3	Calibrated factor δ for the three cases: sag, hog and range. Note that δ is a deterministic variable.	160
5.4	Values of associated random variables at "failure" point and their uncertainty contributions (for Service life of 20 years)	162
B.1	Description of error messages from FITQTF	197

List of Figures

2.1	Low, Mid, and High frequency components of measured wave history demonstrating presence of phase-locking and potential second-order effects	7
2.2	Skewness and kurtosis comparison for Snorre model test wave measurements and the second-order model	13
2.3	Skewness and kurtosis comparison for Ekofisk ocean wave measurements and the second-order model using fitted H_s , T_p and γ values from measurements	15
2.4	Definition for wave parameters used in the comparison studies	17
2.5	Normalized wave elevation PDF: Data vs. second-order simulations for Set 1 (Snorre wave tank data: Tests 504, 505, 505)	29
2.6	Normalized wave elevation PDF: Data vs. analytical models for Set 1 (Snorre wave tank data: Tests 504, 505, 505)	30
2.7	Normalized wave elevation PDF: Data vs. Hermite models. Elevation from simple Hermite model using predicted moments and cubic Hermite models using predicted and observed moments are shown. . .	31
2.8	Normalized wave elevation CDF: Data vs. second-order simulations and analytical models for Set 1 (Snorre wave tank data: Tests 504, 505, 505)	32
2.9	Normalized wave elevation CDF: Data vs. second-order simulations and analytical models for Set 2 (Snorre data set: Test 304)	33
2.10	Normalized wave elevation CDF: Data vs. second-order simulations and analytical models for Set 3 (Ekofisk data set)	34

2.11	Normalized crest height CDF: Data vs. second-order simulations and analytical models for Set 1 (Snorre wave tank data: Tests 504, 505, 505)	38
2.12	Normalized wave crest CDF: Data vs. Hermite models. Elevation from simple Hermite model using predicted moments and cubic Hermite models using predicted and observed moments are shown.	39
2.13	Normalized wave crest CDF: Data vs. second-order simulations and analytical models for Set 2 (Snorre data set: Test 304)	40
2.14	Normalized wave crest CDF: Data vs. second-order simulations and analytical models for Set 3 (Ekofisk data set)	41
2.15	Normalized wave height CDF: Data vs. Second-order simulations and analytical models for Set 1 (Snorre wave tank data: Tests 504, 505, 505)	44
2.16	Normalized wave height CDF: Data vs. Second-order simulations and analytical models for Set 2 (Snorre data set: Test 304)	45
2.17	Normalized wave height CDF: Data vs. Second-order simulations and analytical models for Set 3 (Ekofisk data set)	46
2.18	Definition for wave parameters used in the comparison studies	49
2.19	Crest height to wave height: Data vs. first- and second-order models	49
2.20	Crest Period T_C to wave period T_W : Data vs. first- and second-order models	50
2.21	Crest front period T_{CF} to crest period T_C : Data vs. first- and second-order models	50
2.22	Wave period T_W to crest height: Data vs. first- and second-order models	51
2.23	Maximum of crest front (T_{CF}) and crest back (T_{CB}) periods to crest height: Data vs. first- and second-order models (for application to "ringing")	51
2.24	Wave history in wave tank: observed vs. identified first- and second-order	54
2.25	Wave spectrum in wave tank: observed vs. identified first- and second-order	54
3.1	Elevation view of Spar platform	57
3.2	Degrees of freedom for spar	59

3.3	Spectrum of measured surge displacements at 54.8m elevation above MWL for GOM1 seastate	62
3.4	Total measured horizontal displacement and its filtered surge, pitch and wave-frequency components for GOM1 seastate	66
3.5	Reference (observed) wave vs. underlying first- and second-order waves	74
3.6	Comparison of the first-order (wave-frequency) response statistics: Standard deviation σ_1 (top left), maximum normalized by the standard deviation (top right) and absolute maximum displacements (bottom)	79
3.7	Comparison of predicted first-order response time histories to measurements across the three tests. Agreement is similar over all portions of the 1-hour tests, for clarity only the first 500 seconds of each test is shown here.	80
3.8	Comparison of statistical moments for surge and pitch components in the three seastates: Predictions from the four models vs. measurements. The moments include total mean, and standard deviations in surge and pitch frequency components (see titles in the figure).	86
3.9	Comparison of statistical moments for surge and pitch components in the three seastates: Predictions from the four models vs. measurements. The moments include maximum normalized by the standard deviation and the absolute (unnormalized) maximum displacements in each of surge and pitch frequency components (see titles in the figure).	87
3.10	Comparison of (zero-mean) response time histories in DOF1: prediction vs. measurement	88
3.11	Zero-mean pitch (DOF5) time histories for GOM1: prediction vs. measurement	89
3.12	Zero-mean pitch (DOF5) time histories for GOM2: prediction vs. measurement	90
3.13	Zero-mean pitch (DOF5) time histories for NS: prediction vs. measurement	91

3.14	Second-order (=surge+pitch components) predicted and measured response to indicate preservation of net input initial conditions found from observed histories	92
3.15	Comparison of standard deviation and maximum of combined response: prediction vs. measurement	95
3.16	Combined (total) surge response time history for GOM1: prediction vs. measurement	96
3.17	Combined (total) surge response time history for GOM2: prediction vs. measurement	97
3.18	Combined (total) surge response time history for NS: prediction vs. measurement	98
4.1	Model of monohull ship that will be analyzed using strip theory . . .	104
4.2	Sag and Hog Bending Condition of Ship in Waves	105
4.3	Linear Transfer Function for Mid-ship Bending Moment Response . .	111
4.4	Partial wave and response histories at mid-ship	112
4.5	Comparison of fatigue damage from linear and nonlinear analysis for sag, hog and range bending moments	115
4.6	Damage density from a linear analysis vs. long-term seastate parameters. The damage rate shown has been normalized by the largest value.	118
4.7	Comparison of simulated wave heights to Forristall and to Rayleigh distributions	121
4.8	Simulated wave period vs. modified Longuet-Higgins wave period . .	122
4.9	Relation of side wave height to middle wave height	124
4.10	Construction of Wave Triplet for NTF Load Prediction	125
4.11	Wave heights and periods for the 30 waves used in the NTF model . .	127
4.12	Damage prediction from response to selected sinusoidal waves. The single-wave cycle responses are used in this prediction.	128
4.13	Damage prediction from response to selected sinusoidal waves. The steady-state responses to each of the regular sinusoidal waves are used in the prediction.	130

4.14	Damage prediction from response to selected waves with side waves. 30 wave triplets have been used in the fatigue prediction.	131
4.15	Damage prediction from response to selected waves with side waves. 15 wave triplets have been used in the fatigue prediction.	132
4.16	Wave parameters of the 15 waves used for predicting ship response. The wave heights and wave periods have been obtained using quadrature points. (Note the largest wave period for the smallest wave height has not been shown in this plot, to facilitate direct comparison of these parameters to the ones in Fig. 4.11)	133
4.17	Demonstration of impact of duration correction on predicted fatigue damage for sag and hog bending moments	137
4.18	Coefficient of Variation (COV) of simulated ship loads (sag and hog) for H-T cells in Fig. 4.11	139
4.19	Coefficient of Variation (COV) of simulated ship loads (range) for H-T cells in Fig. 4.11	140
4.20	Demonstration of need for scatter estimate of response in H-T cells .	140
4.21	Demonstration of impact of inclusion of scatter effects in the predicted fatigue damage for sag and hog bending moments	142
4.22	Ratios of predicted to mean simulated (sag and hog) bending moments in H-T cells	144
4.23	Ratios of predicted to mean simulated (range) bending moments in H-T cells	145
4.24	Effects of including bias-correction in hog damage prediction	146
4.25	Linear, NTF, and Nonlinear Bending Moment Fatigue Damage for Range of S-N Exponents	148
4.26	Linear, NTF, and Nonlinear Bending Moment (Ranges) Fatigue Dam- age for Range of S-N Exponents	149
5.1	Nonlinear least squares regression analysis to fit sag, and hog bending moments to wave heights from 1 hour simulation of bending moments in seastate with $H_s = 5\text{m}$, and $T_p = 10\text{sec}$	156

5.2	Nonlinear least squares regression analysis to fit half-range bending moments to wave heights from 1 hour simulation of bending moments in seastate with $H_s = 5\text{m}$, and $T_p = 10\text{sec}$	157
5.3	Failure probabilities for a range of target lifetimes for the three stresses: sag, hog and range	163
5.4	Transformation of standard normal variables (U_1 and U_2) to physical variables ε_C and ε_{SCF} to find material contour	168
5.5	Material contour: Locus of points of ε_C and ε_{SCF} for which FORM method gives a reliability $\beta = 3.02$	169
5.6	Design choices of ε_C and ε_{SCF} for different S-N exponents b that result in desired reliability $\beta = 3.02$	170
B.1	Frequency grid points of the sparse and the finely meshed QTF values from SWIM	198
B.2	Direct statistics mean for interpolated QTFs from sparse QTF vs. exact mean from finely meshed QTF (from diffraction analysis)	201
B.3	Direct statistics standard deviation for interpolated QTFs from sparse QTF vs. exact mean from finely meshed QTF	201
B.4	1-hour predicted mean for interpolated QTFs from sparse QTF vs. exact mean from finely meshed QTF	202
B.5	1-hour predicted standard deviation for interpolated QTFs from sparse QTF vs. exact mean from finely meshed QTF	202

Chapter 1

Introduction

In designing offshore structures, the engineer faces the difficulties of modeling the structural behavior and using the developed model to proportion the structure so that it functions safely. This is generally true for any structure on-land or offshore. The difficulties are due to the random nature of the environment (wave loads for offshore structures, earthquake ground motions in earthquake engineering, for example). Given the environment, the response (for example, deck or top-story horizontal displacement) of a structure is not deterministic either. This adds to the complexity in estimating the reliability or safety of a structure during its service life.

Approaches to resolve these difficulties include performing model tests to understand the structural behavior in different climate conditions. This is generally very expensive and so an alternative is to formulate numerical (possibly theoretical) models for the different parameters associated in the problem, i.e., the wave loads and the resulting response of the structure. If the model predictions compare well with experiments or observed data, they (the model) can then be used as a design tool to check the structure safety against different failure modes (e.g., fatigue failure, or

ultimate load failure). The models for the waves and response given the waves may then be integrated to predict reliability estimates for a chosen design. Such integration, for rare failure events, can be efficiently performed using first- or second-order reliability methods (e.g., [36]).

In this dissertation, we focus on wave loads and the behavior of offshore structures (here, a spar and a ship) to these. We will first use existing theoretical models for the wave surface and systematically compare model predictions to measured waves in oceans and to in wave tanks. This study is detailed in Chapter 2.

Incident wave loads and the resulting responses are demonstrated for a Spar floating platform and a ship. The details of the Spar study are presented in Chapter 3, while the ship study is presented in Chapter 4. The Spar platform is a new concept in the offshore industry and only one such platform has been built so far. This platform is a large vertical cylinder with a center well, held down to the sea floor by mooring lines. The cylinder provides buoyancy to keep the spar afloat and can also be used to store oil. We model the spar as a rigid 6-DOF body and given the complex hydrodynamical loads, predict the spar response. Similar model forms have been applied before for other platform types, for example, the tension-leg platform (TLP) [59]. For the spar model, we calibrate the damping characteristics using wave tank tests conducted on this spar. Finally, we compare the model predictions to the wave tank measurements in order to check the accuracy of the model. Given a successful comparison, the model can then be used in designing the spar.

For ship structures, efforts are being made to better predict the ship response in waves by including increasingly complex hydrodynamical models in the analysis [5, 31, 44]. Such models are predicted to be more accurate than the more traditional linear response analyses of ships. The computational expense, however, seems to

be very large compared to a linear analysis. In this study, we propose use of a “nonlinear transfer function” model, to predict the ship response across different climate conditions. In applying this model to a fatigue analysis, for example, the available ship analysis program is used to find the ship stresses (response) for a carefully selected set of waves from stochastic theory. These stresses in conjunction with the probabilities of “seeing” the waves, can be used to predict fatigue damage in the ship element. Similar models have been applied before for extreme ship-response analysis [69] and fatigue damage in side-shells of ships [15].

Finally, in Chapter 5, we present an integrated analysis of structural response to assess the design reliability in a given service life. We demonstrate this application by studying the fatigue reliability of ship structural elements. Here uncertainty is considered in: (1) the wave climate, (2) the ship response given the wave climate, and (3) the material properties of the ship element. A FORM analysis is then used to find the reliability achieved given all the associated parameters.

Chapter 2

Nonlinear Random Ocean Waves: Prediction and Comparison with Data

2.1 Introduction

Nonlinear hydrodynamic effects are of growing interest for ocean structures and vessels. Here we study such effects in one of the most fundamental nonlinearities in ocean engineering: the wave elevation $\eta(t)$ at a fixed spatial location.

It is common practice to model $\eta(t)$ using linear wave theory, which results in a Gaussian model of $\eta(t)$. This ignores the marked asymmetry in the waves: wave crests that systematically exceed the neighboring troughs. Such an asymmetry increases with decreasing water depth. This asymmetry has several practical implications, for example: (1) asymmetric waves are more likely to strike decks on offshore platforms, particularly older Gulf-of-Mexico structures designed with fairly low decks; and (2)

unusually large dynamic structural responses have been found in high, steep waves that may not follow linear wave theory.

Second-order random wave models are not new; indeed, they have been a research topic for more than 30 years (e.g., [3, 17, 20, 21, 29, 33, 51, 54, 55, 70]) and remain so today (e.g., [19, 39, 63, 71]). However, they have not entered common offshore engineering practice, which applies either random linear (Gaussian) waves, or regular waves that fail to preserve $S_\eta(\omega)$, the wave power spectrum. Several drawbacks to second-order random waves may be suggested: (1) they may be inaccurate, for example due to their neglect of higher-order effects; and (2) convenient statistical analysis methods for second-order models are often lacking. We seek to consider both concerns here — the first through comparison of theory with various wave tank and ocean wave measurements. The second issue is addressed by fitting new analytical results for wave moments, and studying the accuracy of using these to construct simple Hermite models of extreme crests.

2.2 Wave Model

Second-order Volterra models [50] have come under increasing use for modeling nonlinear random processes in offshore engineering (e.g. [53, 64, 73]). $\eta(t)$ is accordingly modeled as the sum of a linear (Gaussian) process $\eta_1(t)$ plus a second-order correction $\eta_2(t)$ from the nonlinear hydrodynamic problem associated with waves.

$$\eta(t) = \eta_1(t) + \eta_2(t) \tag{2.1}$$

Before presenting the details of the model, we show the low, mid, and high frequency components of a measured wave tank history in Fig. 2.1 to demonstrate the

presence of potential second-order effects in waves. This history is from wave measurements taken during the Snorre Tension-Leg Platform (TLP) model tests [37]. The waves have been measured without the structure in the tank. More details of these wave tank histories are presented in Sec. 2.3. The significant wave height H_s is 14.1m and the spectral peak period T_p is 13.75 seconds. For this example, we chose the mid-frequency component around the spectral peak of the measured history, from 0.025 Hz to 0.14 Hz. The upper bound of 0.14 Hz is chosen to be a little smaller than twice the peak spectral frequency where we expect to see the most dominant second-order wave contribution. The range below 0.025 Hz represents the low-frequency component and the range above 0.14 Hz represents the high-frequency range, in this example. Fig. 2.1 shows that while the low and high frequency components have small energies (standard deviations) as compared to the mid-frequency component, the three components seem to be phase-locked, a phenomenon which would not be seen in a linear process. This observation supports the modeling of the waves as at least a second-order process.

For the second-order $\eta(t)$ in Eqn. 2.1, the standard Fourier sum for the linear part $\eta_1(t)$ is

$$\eta_1(t) = \sum_{k=1}^N A_k \cos(\omega_k t + \theta_k) = \text{Re} \sum_{k=1}^N C_k \exp(i\omega_k t) \quad (2.2)$$

in which Re indicates the real part of a complex number, and $C_k = A_k \exp(i\theta_k)$ are the complex Fourier amplitudes, defined in terms of Rayleigh distributed amplitudes A_k , and uniformly distributed phases θ_k . The C_k 's are mutually independent of one another. The mean-square value of A_k is

$$E[A_k^2] = 2S_\eta(\omega_k)d\omega_k; \quad d\omega_k = \omega_k - \omega_{k-1} \quad (2.3)$$

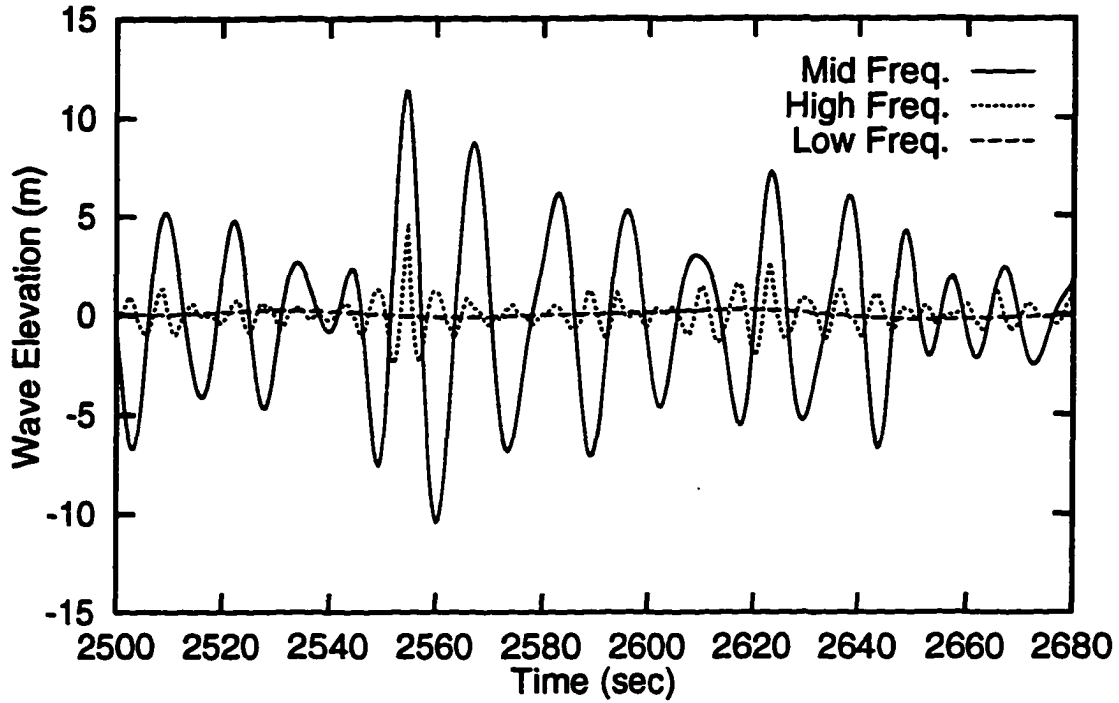


Figure 2.1: Low, Mid, and High frequency components of measured wave history demonstrating presence of phase-locking and potential second-order effects

Based on Volterra theory [50], second-order corrections are induced at the sums and differences of all wave frequencies contained in $\eta_1(t)$:

$$\eta_2(t) = \text{Re} \sum_{m=1}^N \sum_{n=1}^N C_m C_n \left[H_{mn}^+ e^{i(\omega_m + \omega_n)t} + H_{mn}^- e^{i(\omega_m - \omega_n)t} \right] \quad (2.4)$$

In general, the functions H_{mn}^+ and H_{mn}^- are known as quadratic transfer functions (QTFs), evaluated at the frequency pair (ω_m, ω_n) . Similar expressions arise in describing second-order diffraction loads of floating structures (see Chapter 3); in this case the QTFs are calculated numerically from nonlinear diffraction analysis (e.g.,

[64]).

In predicting motions of floating structures, in view of the relevant natural periods, interest commonly lies with either H_{mn}^+ (springing) or H_{mn}^- (slow-drift) but not both. For example, in the case of the spar floating structure shown in the next chapter, the slow-drift forces and hence the difference-frequency components generally govern the global motions of the spar. In contrast, in the nonlinear wave problem both sum and difference frequency effects play a potentially significant role. Fortunately, unlike QTF values for wave loads on floating structures, which must be found numerically from diffraction analysis, closed-form expressions are available for both the sum- and difference-frequency QTFs for second-order waves (e.g., [29, 39]). Including the effect of a finite water depth d , for example, the sum-frequency QTF can be written as

$$H_{mn}^+ = \frac{\frac{gk_mk_n}{\omega_m\omega_n} - \frac{1}{2g}(\omega_m^2 + \omega_n^2 + \omega_m\omega_n) + \frac{g}{2} \frac{\omega_mk_n^2 + \omega_mk_n^2}{\omega_m\omega_n(\omega_m + \omega_n)}}{1 - g \frac{k_m + k_n}{(\omega_m + \omega_n)^2} \tanh(k_m + k_n)d} - \frac{gk_mk_n}{2\omega_m\omega_n} + \frac{1}{2g}(\omega_m^2 + \omega_n^2 + \omega_m\omega_n) \quad (2.5)$$

in which the wave numbers k_n are related to the frequencies ω_n by the linear dispersion relation $\omega_n^2 = gk_n \tanh(k_n d)$. The corresponding difference-frequency transfer function, H_{mn}^- , is found by replacing ω_n by $-\omega_n$ and k_n by $-k_n$.

Because $\eta(t)$ is non-Gaussian, interest focuses on its skewness α_3 and kurtosis α_4 . In terms of the significant wave height $H_s = 4\sigma_\eta$, and peak spectral period T_p , these are predicted by a second-order wave model to be of the form:

$$\alpha_3 \sigma_\eta^3 = \overline{(\eta_1 + \eta_2)^3} = m_{31}(T_p)H_s^4 + m_{33}(T_p)H_s^6 \quad (2.6)$$

$$(\alpha_4 - 3)\sigma_\eta^4 = \overline{(\eta_1 + \eta_2)^4} = m_{42}(T_p)H_s^6 + m_{44}(T_p)H_s^8 \quad (2.7)$$

The $m_{ij}(T_p)$ are “response moment influence coefficients,” the contribution to response moment (cumulant) i due to terms of order $O(\eta_1^j)$. In general these coefficients are conveniently calculated from Kac-Siebert analysis (Eqns. 12–15, [60, 73]). We assume here the spectrum of $\eta_1(t)$ is of the form $H_s^2 T_p f(\omega T_p)$, so that $\eta_1(t)$ scales in amplitude with H_s and in time with T_p . Such is the form, for example, of a JONSWAP spectrum.

It is useful to define the unitless wave steepness $S_p = H_s/L_p$, in which the characteristic wave length $L_p = gT_p^2/2\pi$ uses the linear dispersion relation. Note that S_p is far less than unity and a second-order perturbation is performed by retaining terms only up to S_p^2 . For deep-water waves the coefficients $m_{ij}(T_p)$ are proportional to L_p^{-j} , and they remain nearly so for finite depths as well. Retaining the leading terms in S_p from Eqns. 2.6–2.7:

$$\alpha_3 = k_3 S_p ; \quad \alpha_4 - 3 = k_4 \alpha_3^2 \quad (2.8)$$

In particular, for a JONSWAP wave spectrum with peakedness factor γ , we have fit the following k_3 and k_4 expressions to results for a wide range of depths [71]:

$$k_3 = \frac{\alpha_3}{S_p} = 5.45\gamma^{-0.084} + \left\{ \exp \left[7.41 (d/L_p)^{1.22} \right] - 1 \right\}^{-1} \quad (2.9)$$

$$k_4 = \frac{\alpha_4 - 3}{\alpha_3^2} = 1.41\gamma^{-0.02} \quad (2.10)$$

The second term in this result for α_3 reflects the effect of a finite water depth d : in shallower waters the skewness α_3 grows, as the waves begin to “feel” the bottom. When comparing model predictions to data we will investigate the magnitudes of the omitted (second) terms in Eqns. 2.6, and 2.7.

Note also that while the skewness is predicted to vary linearly with steepness, the

kurtosis is predicted from Eqn. 2.8 to vary quadratically with the steepness S_p . Since the steepness is far less than unity (squared steepness even smaller), this suggests that nonlinear effects will be most strongly displayed by the skewness, and hence by the wave crests rather than the total peak-to-trough wave heights. This second-order model may less accurately predict kurtosis, however, as higher-order omitted effects may be of the same order of magnitude.

In the following sections, we compare predictions from the second-order random wave model to both wave tank data and ocean wave measurements. The comparisons are at the following three levels:

- **Section 2.3: Moments of wave time histories, skewness α_3 and kurtosis α_4 or coefficient of excess $\alpha_4 - 3$.** We will first compare the predicted moments across a broad range of seastates in both the wave tank and the measured ocean data.
- **Section 2.4: Cumulative Distribution Functions (CDF) of wave elevations, wave crests and wave heights.** These comparisons will demonstrate whether or not the second-order model is able to predict the CDFs, over and above predicting the third and fourth moments of the waves.
- **Section 2.5: Local Wave Parameters.** This study investigates the ability of the model to predict local properties of the wave profile; e.g., marginal mean and standard deviation of a wave crest given a wave height, of wave period given a wave height and similar marginal moments of other local wave properties.

2.3 Comparison of α_3 and α_4 : Data vs. Prediction Models

In this section, we shall compare the predicted and observed skewness and kurtosis from two different data sets; one from a wave tank and one from the ocean. The wave tank measurements reflect wave histories with target H_s of 4m to 18m in approximately 308m water depth [37, 38]. We consider 18 wave tank histories each about 2 hours long with a sampling frequency of approximately 0.42 seconds. When estimating moments from the wave tank histories we process hourly portions and as a result have moments from 36 hourly time histories. The ocean wave histories are laser measurements at Ekofisk in the Southern North Sea in approximately 70m water depth. These measurements are for durations of about 18 minutes (2048 samples at time steps of 0.5 seconds) collected every 3 hours during the year 1984. From the annual data set, we select seastates with H_s above 4.5m and with skewness values between -0.05 and 0.4 from the Ekofisk data set. The H_s and skewness cutoffs are introduced to seek to filter out any “noisy” measurements. This resulted in selection of 132 time histories (each of about 18 minutes duration).

Figure 2.2 shows comparisons of predicted skewness and kurtosis with the corresponding sample moments obtained from wave tank histories. Hourly segments of wave tank histories are processed to obtain estimates of skewness and kurtosis, and the predicted skewness and kurtosis are based on Eqns. 2.9 and 2.10. A linear regression (with zero intercept) of observed skewness vs steepness yields an estimated slope of 4.97 ± 0.12 (mean \pm std. error), close to the predicted slope k_3 of 4.93 in Eqn. 2.9 for $\gamma = 3.3$. Note that the target γ values for most of the wave tank tests were 3.3. The

effect of the depth-dependent ($d \approx 308\text{m}$) term in Eqn. 2.9 will cause only a slight increase in the prediction and is neglected here. The seastate-to-seastate scatter σ_{α_3} in the observed skewness values is also consistent; the observed σ_{α_3} is found reasonably well-predicted by that from the simulated hourly segments of second-order seastates (using WAVEMAKER [23]). The simulation is based on a fitted JONSWAP spectrum for each of the hourly measurements. The simulated skewness values show a $\sigma_{\alpha_3} = 0.023$, which is smaller than the observed $\sigma_{\alpha_3} = 0.033$ for the hourly segments of the measurements. The observed seastate-to-seastate kurtosis scatter σ_{α_4} in the hourly measurements is 0.11. In Fig. 2.2b, the mean regression slope of 4.96 ± 0.33 for observed k_4 is about 4 times the predicted k_4 regardless of γ . This lends some support to the view that the second-order model predicts the kurtosis value less accurately due to omitted higher-order effects [63].

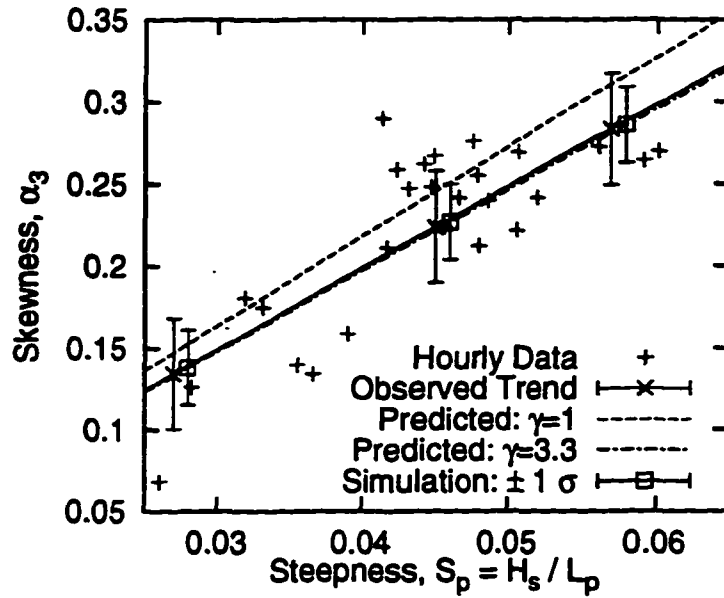
Figure 2.3 similarly compares predicted α_3 and α_4 values to Ekofisk data. For the predicted skewness and kurtosis values, we fit the JONSWAP spectrum parameters to each of observed time histories. $H_s = 4\sigma_\eta$ where σ_η is standard deviation of an observed history. T_p and γ are found from the measured T_z and T_1 , the mean zero-crossing period and the central period, respectively, as shown below. T_z and T_1 are found from measured spectral moments $\lambda_n = \int f^n S(f) df$ as

$$T_z = \sqrt{\lambda_0/\lambda_2}; \quad T_1 = \lambda_0/\lambda_1 \quad (2.11)$$

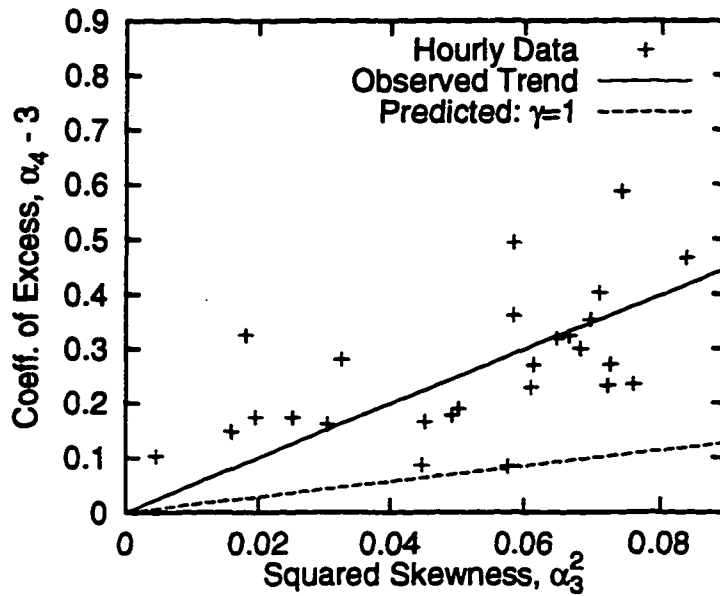
For a JONSWAP spectrum, we have fit these periods and γ for a broad range of bandwidths δ ,

$$\delta = \sqrt{1 - \frac{\lambda_1^2}{\lambda_0\lambda_2}} = \sqrt{1 - \left(\frac{T_z}{T_1}\right)^2} \quad (2.12)$$

A quadratic regression form resulted in the following expressions, for a JONSWAP



(a) Skewness comparison



(b) Kurtosis comparison

Figure 2.2: Skewness and kurtosis comparison for Snorre model test wave measurements and the second-order model

spectrum:

$$\gamma = 458\delta^2 - 423\delta + 96 \quad (2.13)$$

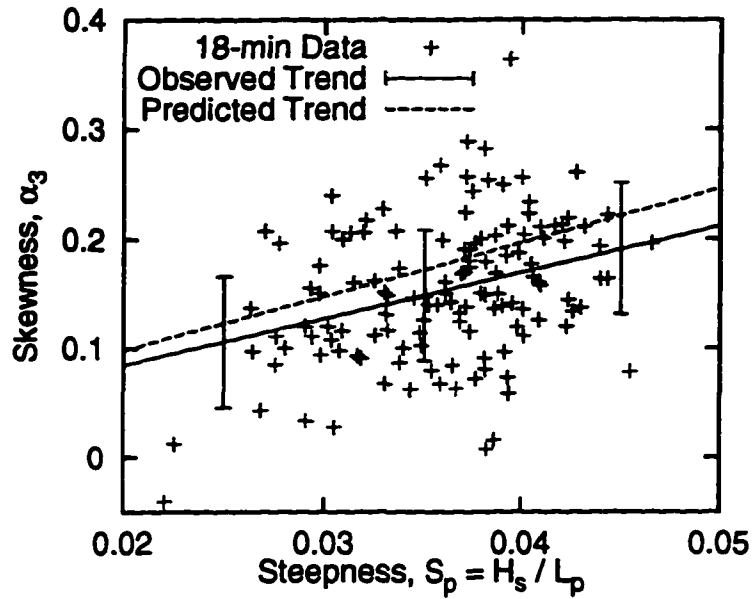
$$T_z/T_p = -0.0023\gamma^2 + 0.0372\gamma + 0.68 \quad (2.14)$$

$$T_1/T_p = -0.0024\gamma^2 + 0.0353\gamma + 0.743 \quad (2.15)$$

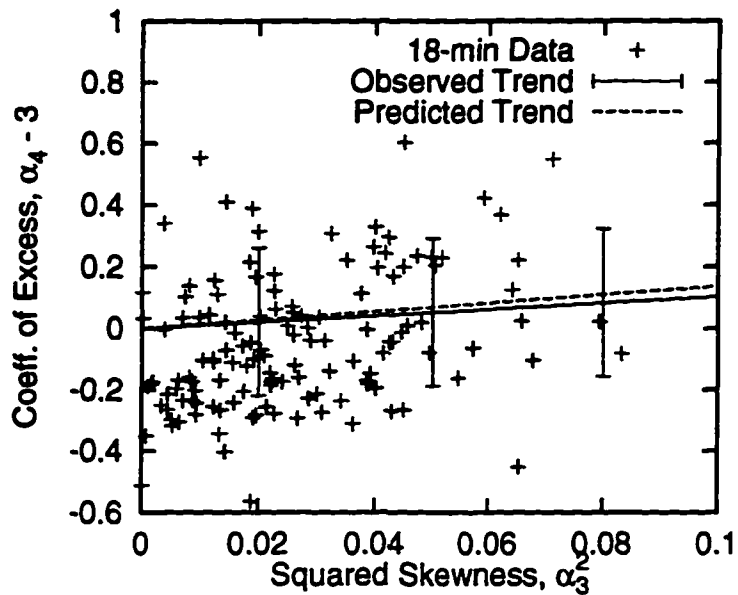
Using the fitted γ (Eqn. 2.13), H_s , T_p (from Eqn. 2.14), we predict skewness and kurtosis using Eqns. 2.9 and 2.10.

For the Ekofisk data set, the slope of the observed trend on α_3 is 4.24 ± 0.14 , while the above prediction scheme indicates a larger skewness trend of 4.92. Note the increase in observed scatter ($\sigma_{\alpha_3} = 0.06$) in skewness compared to the wave tank data. This is due to the noisy estimate of skewness from the 18-minute samples compared to the hourly samples in the wave tank case. The observed trend for kurtosis ($k_4 = 1.03 \pm 0.61$) is also quite accurately predicted by the second-order model (predicted $k_4 = 1.37$), contrary to what we saw for the wave tank data. Again, the kurtosis scatter σ_{α_4} has increased to 0.24 when compared to the hourly estimates for the wave tank data.

The question is: why should the second-order model better match field data than the wave tank data when comparing kurtosis estimates? Recall that the wave tank data represents long-crested waves, while the field data probably represents short-crested sea conditions. The short-crestedness may likely cause a reduction in the nonlinearity in the waves at a point, due to the net effect of waves coming from different directions. In any case, it may seem that the second-order model generally underpredicts nonlinear effects, as seen in comparisons with the wave tank tests. The model prediction, on the other hand, seems better for Ekofisk data set; this may, however, be due to the effect of short-crestedness that leads to reduced nonlinear



(a) Skewness comparison



(b) Kurtosis comparison

Figure 2.3: Skewness and kurtosis comparison for Ekofisk ocean wave measurements and the second-order model using fitted H_s , T_p and γ values from measurements

effects in the measurements.

Owing to the underpredicted kurtosis for wave tank data, it may be anticipated that the second-order model will most likely underpredict the “tails” (extremes) of the distributions for wave elevations, crest heights, and wave heights. On the other hand, for the Ekofisk data set where skewness and kurtosis are well predicted we may hope to find good agreement in predictions and measurements for the wave elevations, wave crests and wave heights. This is studied in detail in the next section.

2.4 Comparison of Distributions of Wave Elevation, Crest Height and Wave Height

In this section, we compare the observed distributions of the wave elevation, crest heights, and wave heights to second-order simulations (using WAVEMAKER [23]). Comparisons of data to analytical or empirical distributions are also presented. A summary of the measured wave data sets follows. Figure 2.4 gives a schematic picture of the definitions of the wave parameters. Crest height is defined as the elevation above mean water level to the highest point between two adjacent mean level upcrossings. Wave height is the elevation difference from the highest to the lowest point between two adjacent mean-upcrossings. The other wave parameters will be discussed in Section 2.5.

2.4.1 Summary of Measured Wave Data Sets

We will compare model predictions to measurements across multiple data sets in order to study the generality of any conclusions made. We focus here on four wave data sets: (1) three 2-hour measurements representing the same seastate from the

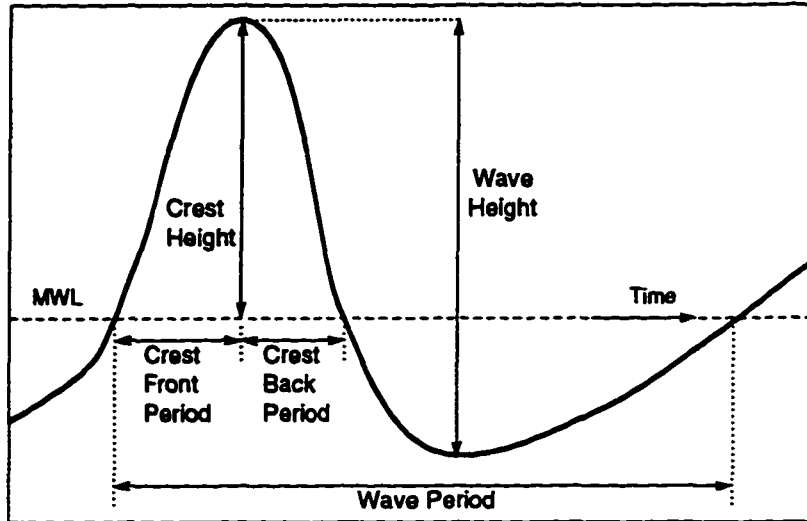


Figure 2.4: Definition for wave parameters used in the comparison studies

Snorre wave tank tests, (2) one 2-hour measurement again from the Snorre wave tank tests, but now representing another seastate, (3) fourteen 18-minute Ekofisk wave measurements representing similar climate conditions. The first data set is chosen because it reflects 6 hours of wave measurement for a severe sea (see Table 2.3). The second data set represents a less severe sea with a different steepness S_p . Out of the year-long Ekofisk measurement, we select time histories that have close H_s and T_p values and, generally, reflect a large S_p value. We present a summary of the three data sets in Table 2.1.

Recall that the first two data sets are wave measurements in the wave tank taken in the absence of any structure. The waves in the wave tank are intended to be long-crested or unidirectional waves. The third data set is for ocean surface measurements taken by a down-looking radar. Since this a field measurement, we may not expect the waves to be long-crested. The model predictions that follow use only long-crested waves, because no short-crested information is available. The observed wave statistics

for these data sets are summarized in Table 2.2. Here, μ is the mean, σ is the standard deviation, and “Min.” and “Max.” are the minimum and maximum elevations in the wave histories for the total durations given in Table 2.1.

Of the three sets, the first data set shows the largest nonlinear effects: largest skewness, kurtosis and maximum/ σ values. The last column $\sqrt{2\ln N}$ is an estimate of the most probable Gaussian maximum (or —minimum—) value (normalized by σ) in N cycles. We define the cycle count as $N = T_{\text{dur}}/T_z$ (see Tables 2.1 and 2.3), where T_z is the mean zero-crossing period. In the first data set, note that the normalized maximum (max./ σ) is about 22% larger than the Gaussian extreme, while the normalized minimum value is about 13% smaller than the Gaussian minimum value. This is a manifestation of the nonlinearity (or skewness effect) that makes the crest (maximum) larger and troughs (minimum) smaller. Such nonlinear effects are also seen in the other two data sets, although to a lesser extent. The Ekofisk set, as noted earlier, shows the least nonlinear effects. The seastate steepness S_p also provides a measure of the nonlinearity to be anticipated in the histories, so we will next find the H_s and T_p parameters in order to find S_p .

In order to use the analytic formulations of predicted α_3 and α_4 we fit JONSWAP spectrum parameters (the significant wave height H_s , spectral peak period T_p , and the peakedness factor γ) to the measured spectrum for each of the data sets. In fitting the JONSWAP spectrum to measurements we choose $H_s = 4\sigma$ and we tune T_p and γ so as to best fit the measured spectrum around the peak. The measured spectrum for each data set is found by averaging the spectrum across the different observations in each data set. For example, for the first data set, we average the spectrum of the three tests (504, 505 and 506) to find the final spectrum for this data set. For the second data set, we directly use the measured spectrum, while for the Ekofisk data,

we average across the 14 measured spectra to find the resulting spectrum used in fitting a JONSWAP spectrum.

Table 2.3 shows the target (nominal) and observed JONSWAP spectrum parameters in the wave tank tests. The observed H_s value for Set 1 seems to be different from the nominal H_s values (by about 5%), while observed T_p and γ for Set 1 and 2 seem to agree with the nominal values. For the ocean wave measurements, of course, we do not have any nominal values. A summary of the calculated mean zero-crossing period T_z and the central period T_1 from the measured spectral moments (Eqn. 2.11) is also shown in Table 2.3.

Table 2.4 gives the seastate steepness (based on the fitted H_s and T_p values) along with the predicted moments from Eqns. 2.9 and 2.10. We see excellent agreement in the skewness values for the wave tank data sets, however, as also pointed out earlier on average we underpredict the kurtosis values. Note also that that skewness is overpredicted by about 30% for the Ekofisk data set, when using the fitted skewness form in Eqn. 2.9. This leads to the question of whether accounting for the right spectral shape rather than using the fitted JONSWAP parameters would improve this prediction at all.

To understand the impact of spectral shape on the predicted α_3 and α_4 estimates, we use a smoothed spectrum for each data set and predict the moments using the leading terms in Eqn. 2.6 and 2.7. The averaged spectrum that was used to fit equivalent JONSWAP spectra, contains thousands of frequency components and so a Kac-Seigert analysis that involves an eigenvalue analysis of the frequency components becomes prohibitive. We smooth the averaged spectrum across frequency components, so that the resultant spectrum contains only 256 frequencies. Although this smoothing might lead to some loss in the frequency resolution, we show that the predicted moments will

largely be insensitive to this smoothing. The last two columns (labeled “Smoothed Spectrum”) in Table 2.4 are the predicted moments using only the leading terms. A difference in these moments and those from the fitted JONSWAP reflects the impact of spectral shape on the predictions. The kurtosis estimates seem virtually the same across all three sets. For skewness, Set 1 shows about 8% reductions, while Set 3 shows about 5% reduction when using the measured spectrum.

We investigate next the magnitude of the omitted terms shown in the above moment comparisons for the three data sets. We refer to the second-order prediction as “consistent” when considering only the leading terms in Eqn. 2.6 and 2.7. The predictions where we included all the terms in Eqn. 2.6 and 2.7, is what we refer to as “exact” second-order predictions. Such predictions will describe, for example, the ensemble moments of simulated wave histories from a second-order analysis. These histories will contain nonlinearities up to second-order reflected by both the terms in Eqns. 2.6 and 2.7. Table 2.5 compares the moments from a consistent to an exact second-order analysis for the three sets, using the smoothed spectrum in either case. Note that the exact α_3 prediction is smaller than the consistent second-order estimate. This is because the higher-order term in Eqn. 2.6 gives a negative contribution to skewness [39]. The exact analysis gives on average a 10% reduction in skewness from a consistent second-order analysis. The kurtosis values appear to be almost the same in the two analyses, indicating insignificant contributions from the higher-order terms in Eqn. 2.7.

To compare the CDFs of the wave elevations, crest heights, and wave heights we simulate the first- and second-order wave time histories using WAVEMAKER [23]. The details of the resulting simulations are outlined in the following section.

Table 2.1: Summary information of the four wave data sets used in CDF comparisons of wave elevations, wave crests, and wave heights

Set	Description	Water Depth (m)	Sampling Frequency (sec)	Duration T_{dur} (hours)
1	Snorre wave tank data: Tests 504, 505 and 506	308	0.424264	5.79
2	Snorre wave tank data: Test 304	308	0.424264	1.93
3	Ekofisk data set (Year 1984)	70	0.5	3.98

Table 2.2: Observed statistics of the three (zero-mean) measured wave data sets. Note that these statistics have been estimated from the total durations (see last column of Table 2.1) of the data sets.

Set	σ (m)	α_3	α_4	Min. (m)	Max. (m)	Min./ σ	Max./ σ	$\sqrt{2\ln N}$
1	3.358	0.230	3.263	-11.33	15.90	-3.374	4.735	3.881
2	1.762	0.154	3.141	-6.047	7.944	-3.432	4.509	3.633
3	1.285	0.113	3.012	-5.280	5.490	-4.109	4.272	3.883

Table 2.3: Spectral parameters for the four wave data sets

Set	Nominal Spectrum			Fitted JONSWAP			Calculated	
	H_s (m)	T_p (s)	γ	H_s (m)	T_p (s)	γ	T_z (s)	T_1 (s)
1	14.1	13.75	3.3	13.4	13.75	3.3	11.16	12.
2	7.0	12.0	3.3	7.048	12.0	3.3	9.45	10.05
3	*	*	*	5.14	9.8	3.3	7.62	8.21

Table 2.4: Predicted moments from fitted JONSWAP spectral parameters and from measured spectrum that has been smoothed

	Steepness	Observed		Fitted JONSWAP		Smoothed Spectrum	
Set	S_p	α_3	α_4	α_3	α_4	α_3	α_4
1	0.0454	0.230	3.263	0.224	3.07	0.207	3.06
2	0.0314	0.154	3.141	0.155	3.03	0.153	3.03
3	0.0343	0.113	3.012	0.170	3.04	0.162	3.04

Table 2.5: Skewness and kurtosis predictions from a consistent second-order analysis vs. exact second-order analysis

	Steepness	Consistent 2nd Ord.		Exact 2nd Ord.	
Set	S_p	α_3	α_4	α_3	α_4
1	0.0454	0.207	3.06	0.181	3.07
2	0.0314	0.153	3.03	0.141	3.04
3	0.0343	0.162	3.04	0.143	3.04

Table 2.6: Number of simulations and durations (in hours) of each for the four data sets

Set	No. of Simulations	Duration of 1 simulation	Total duration (hours)
1	20	1.93	38.6
2	10	1.93	19.3
3	50	0.28	14.2

2.4.2 Summary of Simulated Wave Data

The simulations of the first- and second-order histories for the four data sets are based on the measured spectrum of each. The time resolution and the duration of each simulated history are chosen to be the same as those for a single measured history. For example, for the first data set, each simulated history has a duration of 1.93 hours with a time resolution $dt=0.424264$ seconds; similarly, for Set 3 each simulated history contains 2048 points with $dt=0.5$ seconds. A summary of the number of simulations (N_{sim}) and total durations ($N_{sim} \times$ duration of 1 history) of the simulated histories is given in Table 2.6. The number of simulations is generally chosen so that the total simulated durations are longer than the total observed ones. The longer simulations are more likely to “fill in” the tails of the distributions and thereby offer a more robust comparison in the tails.

In order to compare predicted moments to observed results from similar durations, we combine the simulated histories to replicate the total durations in the observed results. For example, in Set 1 we combine (concatenate) 3 histories into 1 and as result have 6 simulated histories each of duration 5.79 hours. Similarly, for Set 3 we combine 14 histories into 1 and as a result have 3 histories each of duration 3.98 hours. For Set 2, we do not need any concatenation since the observed history is itself

1.93 hours long. Of particular interest here, is the scatter in the maximum elevation of simulated histories of different durations.

Table 2.7 summarizes the means and standard deviations of the simulated time histories. These means and standard deviations have been found for moments from the combined histories in each data set. For example, for Set 1 we estimate the moments for the 6 simulated histories each of duration 5.79 hours and then estimate the mean and standard deviations from these 6 values for each moment. Similarly, for Set 3 we find the mean and standard deviations of the moment from 3 simulated histories each of duration 3.98 hours. As Table 2.7 reports, the second-order σ 's are very close to the observed σ 's in Table 2.2 indicating that the second-order corrections contribute insignificantly to the standard deviation of the process.

As noted earlier, the simulated α_3 and α_4 values agree with the predicted moments from an exact second-order analysis in Table 2.5. The largest difference in case of Set 2 is about 9% and this is within the simulated scatter (0.1289 ± 0.0226). These simulated moments, when compared to the observed moments in Table 2.2, appear to be close. The largest discrepancy in α_3 and α_4 is seen in Set 1. We will investigate the impact of these differences between predicted and observed moments on the distributions of elevations, crests, and wave heights in the next section.

2.4.3 Comparison of Wave Elevation Distributions

We first study the comparisons of normalized wave elevation for data set 1, shown in Figure 2.5. The probability density function (PDF) of observed data is shown with $\pm 1 \sigma$ bands on it. This scatter or sigma band of the probability density is estimated as [47]:

$$\text{scatter, } \sigma = \frac{1}{d\eta} \sqrt{\frac{p(1-p)}{N}} \quad (2.16)$$

Table 2.7: Means and standard deviations of moments of simulated second-order histories for the four data sets. The standard deviation of the moments reflects the predicted scatter in the durations specified.

Set	Duration		σ (m)	α_3	α_4	Min. (m)	Max. (m)
1	5.79	Mean	3.3830	0.1815	3.0393	-12.7550	15.0283
		Sigma	0.0411	0.0140	0.0760	0.8195	1.1667
2	1.93	Mean	1.7612	0.1289	2.9855	-6.0894	7.1302
		Sigma	0.0874	0.0226	0.1093	0.8442	0.9656
3	3.98	Mean	1.3060	0.1397	3.0923	-4.9153	6.4073
		Sigma	0.0285	0.0132	0.1412	0.1843	0.5593

where $d\eta$ is the bin-width used, N is the total number of samples in the observation, and p is the estimated probability of being the bin. Note that $1/d\eta$ is included to reflect a probability density scatter. The PDF of the second-order simulation agrees with observed results at almost all probability levels. Note the slight underprediction of elevations around $\pm 3\sigma$ levels. Such a comparison of the PDF plots offers independent comparisons across different elevation levels. The distinctly positively skewed nature of the observed PDF compared to standard Normal PDF $\phi(u)$ in Fig 2.6 shows the non-Gaussianity of the observed elevations. This figure also compares analytical models for elevation distribution to data. Although, the Charlier series (see, e.g., [33]) using predicted moments (see Table 2.4) seems to agree here with the observed PDF over the range plotted, the demerits of this series approximation include (e.g., [70]): (1) for extreme elevations the PDF may become negative, and (2) it may show multimodal characteristics not inherent in observations. For example, in Fig. 2.6, the Charlier series shown on log scale could not be plotted below about $-3.5\sigma_\eta$ because the Charlier PDF is negative below this elevation value.

The Hermite model [72] is a cubic transformation of standard Gaussian process based on the first four predicted moments. We present a simplified form of the Hermite

model applicable over a wide probability range for waves. This simplification results because the predicted kurtosis levels for the waves do not significantly affect the transformations, as a result we only need up to the quadratic term in the Hermite transform. At a given fractile, the standard normal variable u can be transformed to a non-Gaussian wave elevation level x in the simplified Hermite model as

$$x = g(u) = \bar{\eta} + \kappa\sigma_{\eta} \left[u + \frac{\alpha_3}{6}(u^2 - 1) \right] ; \quad \kappa = 1/\sqrt{1 + \alpha_3^2/18} \quad (2.17)$$

in which $\bar{\eta}$ is the mean wave elevation. We will compare the predictions of this simplified model to the full cubic-transformation result, which is given as:

$$x = g(u) = \bar{\eta} + \kappa\sigma_{\eta} \left[u + c_3(u^2 - 1) + c_4(u^3 - 2u) \right] ; \quad \kappa = 1/\sqrt{1 + 2c_3^2 + 6c_4^2} \quad (2.18)$$

Optimal values of c_3 and c_4 are found in order to minimize lack-of-fit errors in α_3 and α_4 [72]. Fig. 2.7 compares the Hermite predictions to data, where the three Hermite predictions include:

- simplified model (Eqn. 2.17) with *predicted* moments (labeled “Sim.Herm. w/ Pred.Mom.”). Note that this prediction is labeled “Hermite” in Fig. 2.6.
- cubic Hermite (Eqn. 2.18) with *predicted* moments (labeled “Cub.Herm. w/ Pred.Mom.”)
- cubic Hermite (Eqn. 2.18) with *observed* moments (labeled “Cub.Herm. w/ Pred.Mom.”)

This figure reports virtually no difference in the simple and cubic Hermite predictions using the predicted moments. The cubic Hermite model using observed moments (from Table 2.2) improves the prediction, especially around -3.5σ . Larger extremes

have been shown in this figure, to emphasize the elevation difference likely to be seen when using observed or predicted moments in the Hermite predictions. The cubic Hermite model with observed moments appears to best match data; however, this model uses *observed* moments and requires that data be available to find the observed moments. A simplification would be to empirically relate these observed moments to the seastate parameters and use these in the cubic Hermite model. We propose that the simple Hermite model with *predicted* moments from second-order theory offers a convenient alternative to predict a broad range of wave elevations.

Before we look at comparisons of the crest heights (the peaks of the elevation process), we will look again at the wave elevations on a different scale — the CDF or rather the exceedance probability $1 - \text{CDF}$. As seen in Fig. 2.8a, the exceedance probability permits comparisons of the cumulative effects of the process. The second-order simulation appears to agree, within the observed scatter, with the observed CDF out to $2\sigma_\eta$. We note a slight underprediction of the observed wave elevation, for example, of about $0.15\sigma_\eta$ at 0.001 exceedance probability. This slight underprediction may have been anticipated in view of the underprediction of the observed kurtosis by the model. A Gaussian model underpredicts the observed wave elevations (see Fig. 2.8b), for example, by about 20% at 0.0001 exceedance probability and the (simplified) Hermite model (Eqn. 2.17) improves the agreement and offers a similar comparison as the second-order simulated result. There appears to be a discrepancy of about 7% (well within the observed scatter shown by error-bars) at the same 0.0001 fractile. As noted earlier, using the observed instead of the predicted moments in the cubic Hermite transformation improves the agreement even in the large extremes. Both the Hermite models: cubic and simple, however, seem to be within the error-bars of the observed CDF and are considered equally good predictors. Note that in

the all the figures to follow, the predictions from the simplified Hermite model using the predicted skewness (from Eqn. 2.9) are labeled as “Hermite”.

For the second data set, we similarly find the second-order wave elevations to generally agree with the observed results (see Fig. 2.9). The underprediction of observed elevations in the tails seems to be within the observed scatter in the elevations. The Gaussian model systematically underpredicts the elevations (a discrepancy of about 20% at 0.0001 fractile), while the Hermite model improves the agreement (i.e., the discrepancy is now within observed scatter).

Finally, for the third (Ekofisk) data set, the second-order simulation and the Hermite model appear to yield excellent agreement with observed wave elevations (see Fig. 2.10). The Gaussian underprediction also seems to be less severe as compared to the previous two data sets. Recall that this a field measurement where short-crestedness may cause a reduction in the nonlinear wave effects, so the second-order model, which underpredicts the long-crested waves, seems to better agree with the field data. Further investigations, however, have not been done to verify this hypothesis.

Based on the wave elevation comparisons, we may anticipate the second-order model to best predict the Ekofisk crests, and possibly to slightly underpredict the wave tank crests. We will investigate this in the next section.

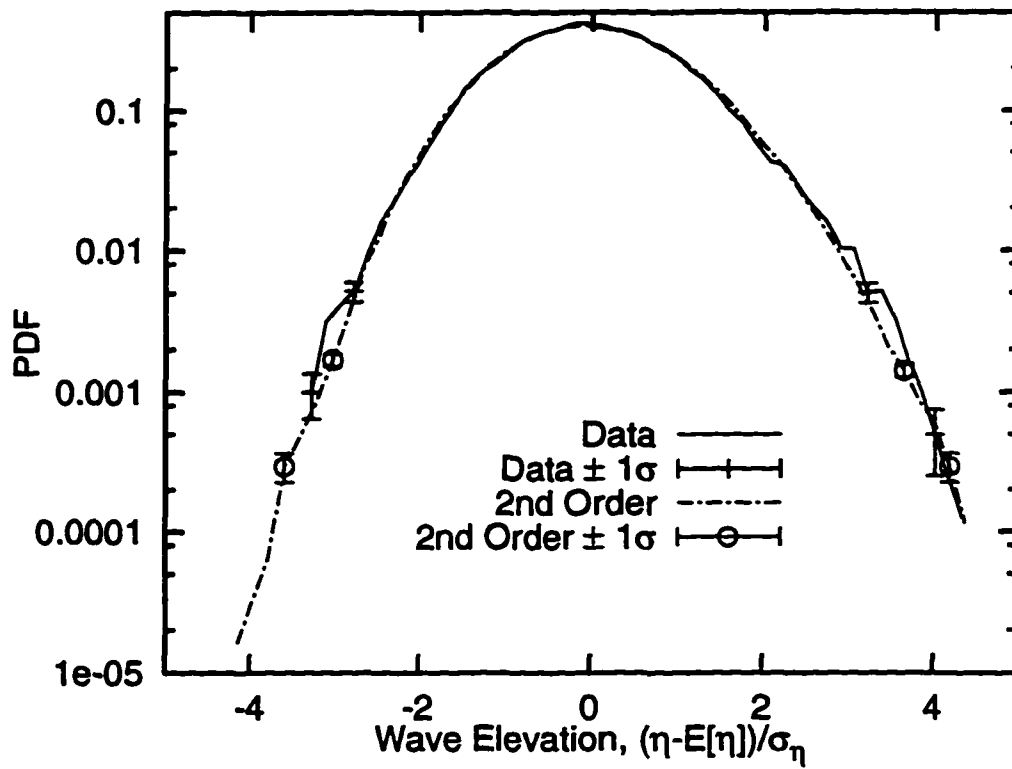


Figure 2.5: Normalized wave elevation PDF: Data vs. second-order simulations for Set 1 (Snorre wave tank data: Tests 504, 505, 505)

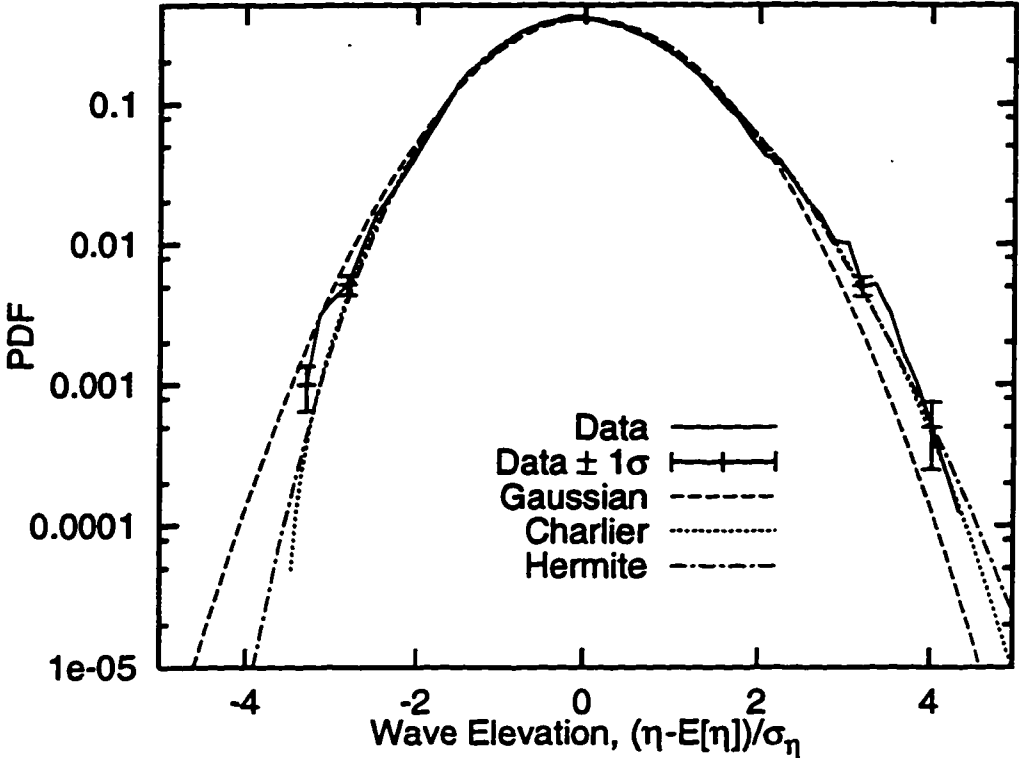


Figure 2.6: Normalized wave elevation PDF: Data vs. analytical models for Set 1 (Snorre wave tank data: Tests 504, 505, 505)

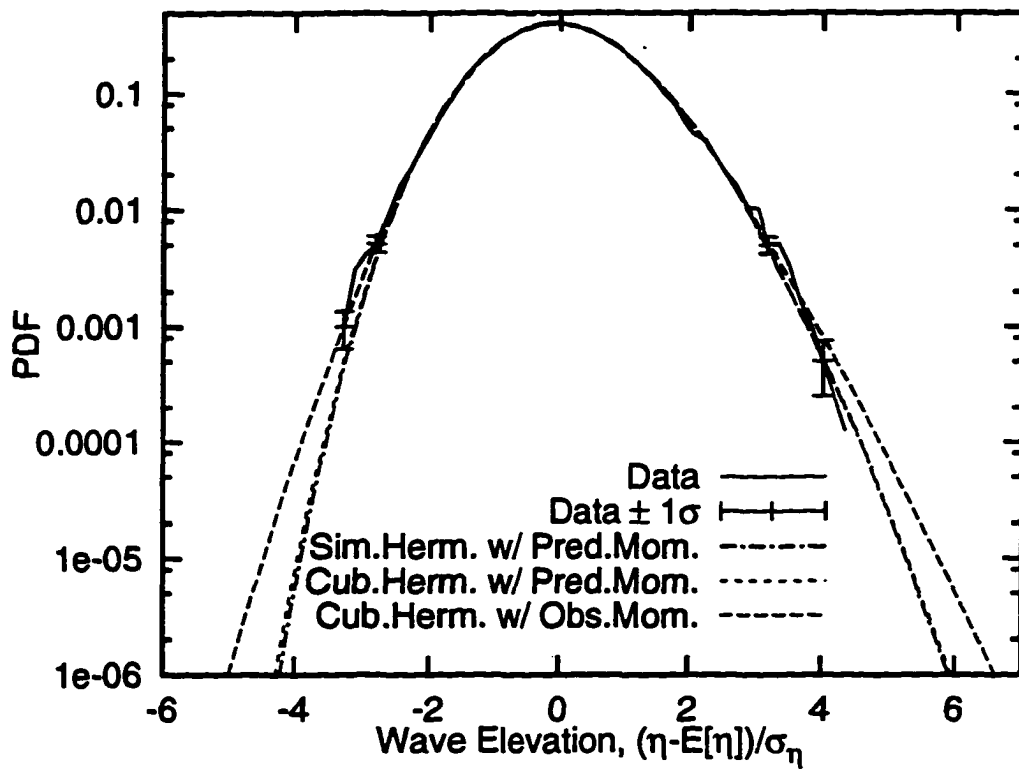
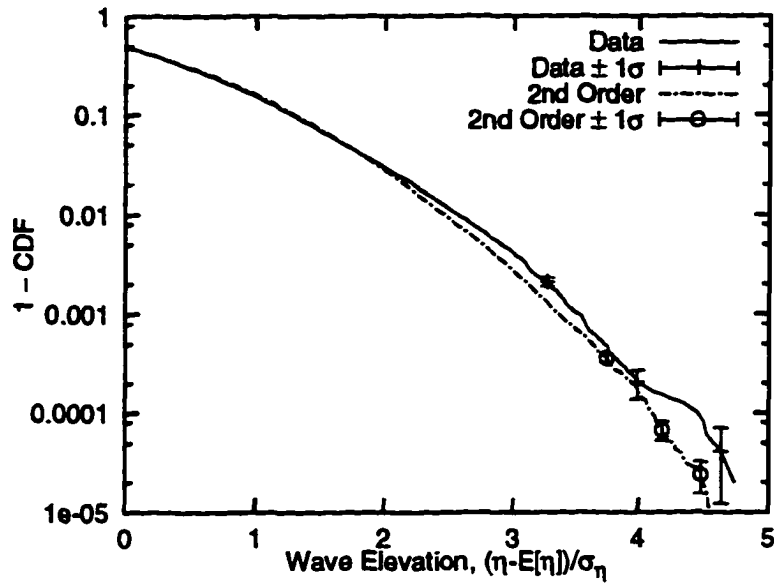
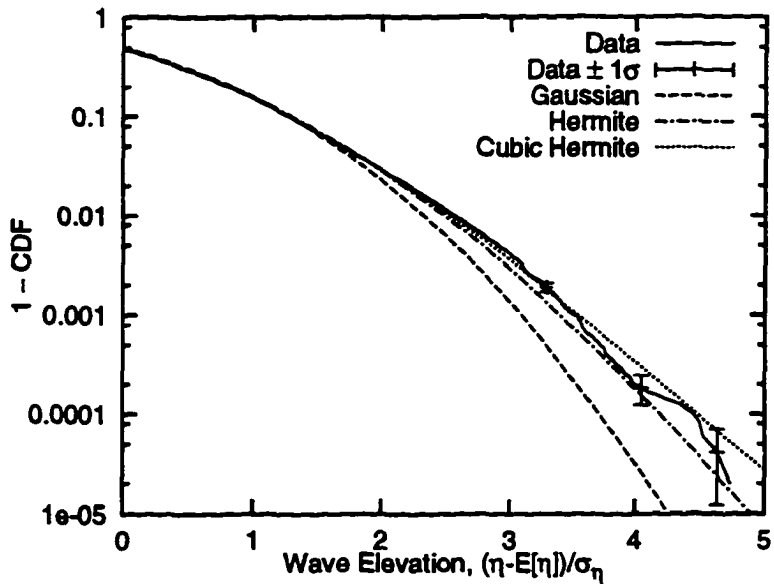


Figure 2.7: Normalized wave elevation PDF: Data vs. Hermite models. Elevation from simple Hermite model using predicted moments and cubic Hermite models using predicted and observed moments are shown.

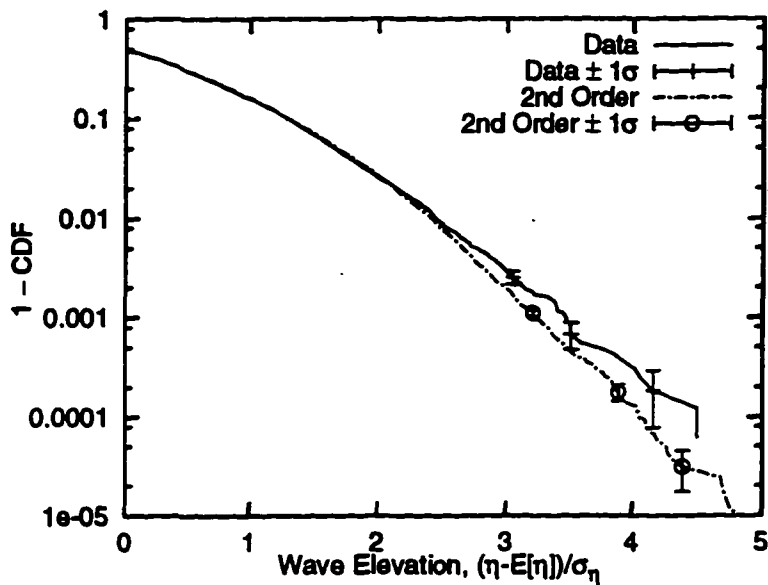


(a) Data vs. Second-order simulation

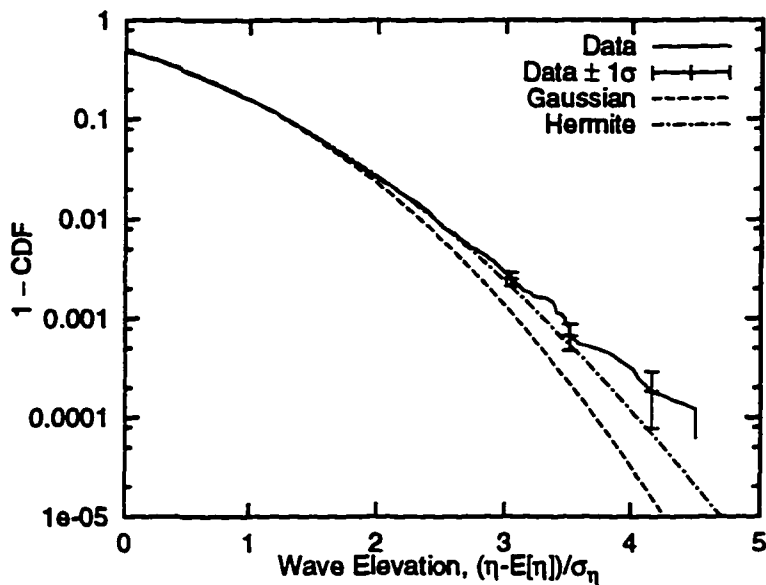


(b) Data vs. Analytical models

Figure 2.8: Normalized wave elevation CDF: Data vs. second-order simulations and analytical models for Set 1 (Snorre wave tank data: Tests 504, 505, 505)

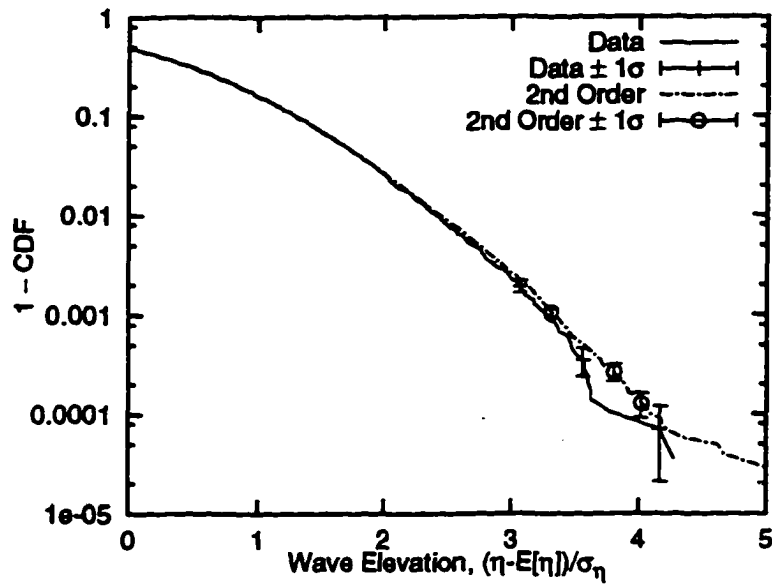


(a) Data vs. Second-order simulation

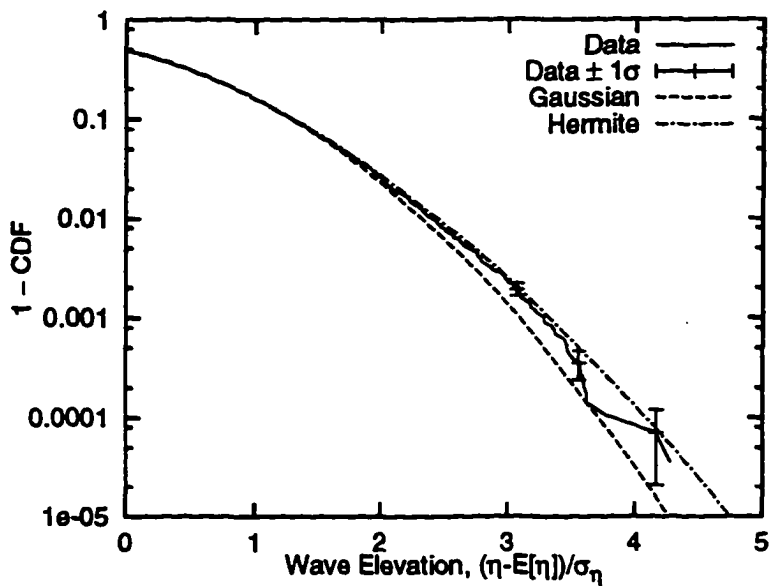


(b) Data vs. Analytical models

Figure 2.9: Normalized wave elevation CDF: Data vs. second-order simulations and analytical models for Set 2 (Snorre data set: Test 304)



(a) Data vs. Second-order simulation



(b) Data vs. Analytical models

Figure 2.10: Normalized wave elevation CDF: Data vs. second-order simulations and analytical models for Set 3 (Ekofisk data set)

2.4.4 Comparison of Crest Height Distributions

The crest height comparison shown in Fig 2.11a for Set 1, shows that while the second-order model accurately predicts the small crests, it appears to underpredict the large observed crests. For example, at 0.001 fractile we find the model underpredicts crests by about 10%. The underprediction in crests heights seems more severe than the wave elevation prediction (see Fig. 2.8). An hypothesis is that the underprediction may be due to higher-order effects. This seems supported at least in the wave elevation case, where the agreement improves when including the observed moments in a cubic Hermite transformation.

Fig 2.11b, which compares the analytical models to data, shows that the Rayleigh crest model given as $\text{Prob}[\text{Crest} > c] = \exp(-0.5(c/\sigma_\eta)^2)$ from linear (Gaussian) wave theory, underpredicts the crests at almost all probability levels of interest (discrepancy of about 25% at the 0.001 fractile). The depth-dependent Haring et al [16] crest height distribution empirically fitted to observed ocean crest data, offers only a slight improvement (discrepancy of about 20% at the 0.001 fractile) over the Rayleigh model. The Haring distribution has been calibrated for a range of water depths less than 200 meters. A similar form was also proposed by Jahns and Wheeler [22]; in this case the wave data comprised of shallow water storm wave records obtained in the Gulf of Mexico. The Haring et al exceedance distribution function is given as

$$\text{Prob}[\text{Crest} > c] = \exp[-0.5(c/\sigma_\eta)^2] \{1 - 4.37(c/d)(0.57 - c/d)\} \quad (2.19)$$

Finally, the Hermite model (a transformation of the Rayleigh crests using Eqn. 2.17) offers a closer fit to observed crests than the Haring distribution. The discrepancy (underprediction) now is about 13% at the same 0.001 fractile level.

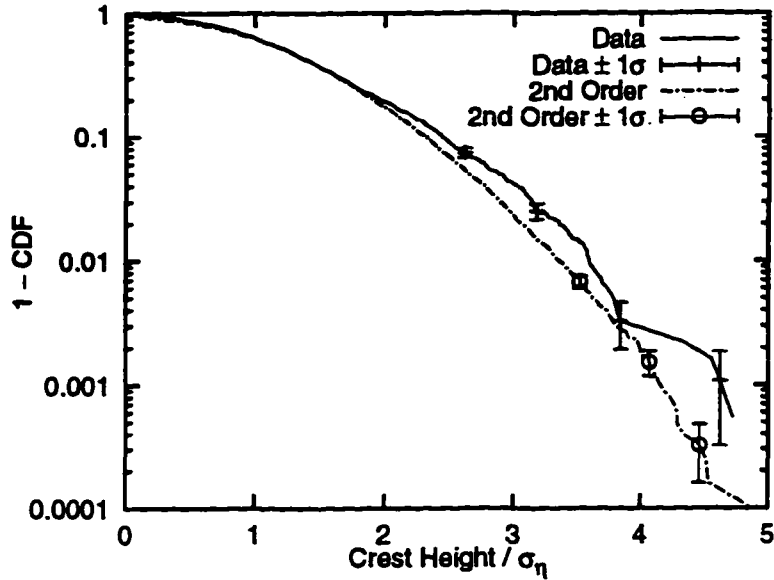
Fig. 2.12 shows similar results as in Fig. 2.7 where we had investigated the impact of kurtosis on the predicted elevations. We first look at the impact of omitting the predicted kurtosis in the crest prediction. Using analytic predicted skewness and kurtosis (see Table 2.4 for actual values) in the cubic Hermite instead of just skewness in the simple Hermite prediction hardly changes the predicted levels; “Cub.Herm. w/ Pred.Mom.” vs. “Sim.Herm. w/ Pred.Mom” are virtually the same in Fig. 2.12. Using the observed moments (see Table 2.2) in the cubic Hermite improves the agreement with observed crests; however, we still see some underprediction in the crest levels around 2 to 3 σ_η . This indicates that even including the correct kurtosis in the cubic Hermite prediction model may not yield perfect crest predictions, implying that other contributing effects may not be predicted exactly. An hypothesis is that, while the Hermite model (using observed moments) predicts the elevations quite accurately, it may still not be modeling the slopes or the velocities of the wave surface and thereby is unable to correctly predict the crests heights. Another hypothesis is that these long-duration wave measurements may be nonstationary. A way of investigating this (not done in this study) may be to divide the measurements into smaller segments and then compare model predictions with observed results from these small segments, where presumably the wave conditions could be assumed to be stationary.

The second data set, again, shows (see Fig. 2.13) similar crest comparisons as in the first set. The second-order simulation offers good agreement for the small crests and underpredicts the large crests (discrepancy of about 12% at 0.01 fractile). Of the analytical models, the Rayleigh distribution underpredicts the observed crests more severely (discrepancy of about 17% at 0.01 fractile). The Haring et al distribution offers only a slight improvement over the Rayleigh crests, while the Hermite model offers slightly better agreement to observed results (discrepancy of 7% at 0.01 fractile).

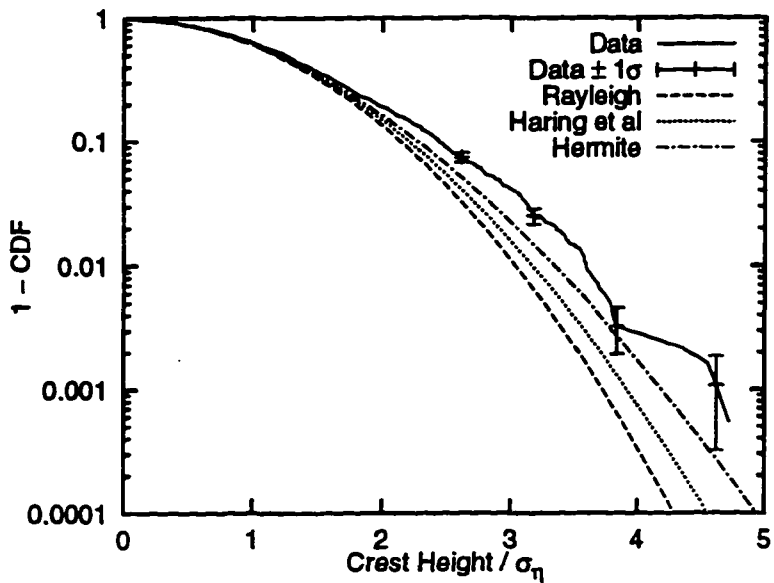
As anticipated for the Ekofisk data set, the second-order model agrees well with the observed crests (see Fig. 2.14). While the Rayleigh model underpredicts the crests, now both the Hermite and the Haring et al. models seem to be agree with the observed crests at all probability levels.

In summary, given that the wave tank data and the field measurements are accurate, we may conclude that while skewness is well-predicted in both types of measurements, the wave tank kurtosis is large than that predicted from a second-order model and the field wave kurtosis can be well-predicted by the second-order model. On the other hand, a hypothesis could be that the wave tank data is in “error” due to its limited ability to generate intended waves. This may be due to scaling issues in the wave tank tests or due to nonstationarity effects in the long measurements. One could on the other hand argue that the field tests may be in error due to measurement noise from the water spray or a direct comparison of field data to the model predictions may be inconsistent due to the presence of short-crested effects in the field data which we are not able to include in the second-order model predictions for lack of information on the directional spread. Recall a third source of error in the field data may be the pooling of the 18-minute histories across different measurements during the year. Further studies along these lines may help explain the differences in the measured results and the model predictions.

We will next look at the model and observed wave heights; we expect any discrepancies to be less severe than seen for the crest comparisons. This expectation is due to the wave elevation being skewness rather than kurtosis-driven; because skewness effects both crests and troughs in compensating ways the wave heights tend, therefore, to show less nonlinear effects than the wave crests alone.



(a) Data vs. Second-order simulation



(b) Data vs. Analytical models

Figure 2.11: Normalized crest height CDF: Data vs. second-order simulations and analytical models for Set 1 (Snorre wave tank data: Tests 504, 505, 505)

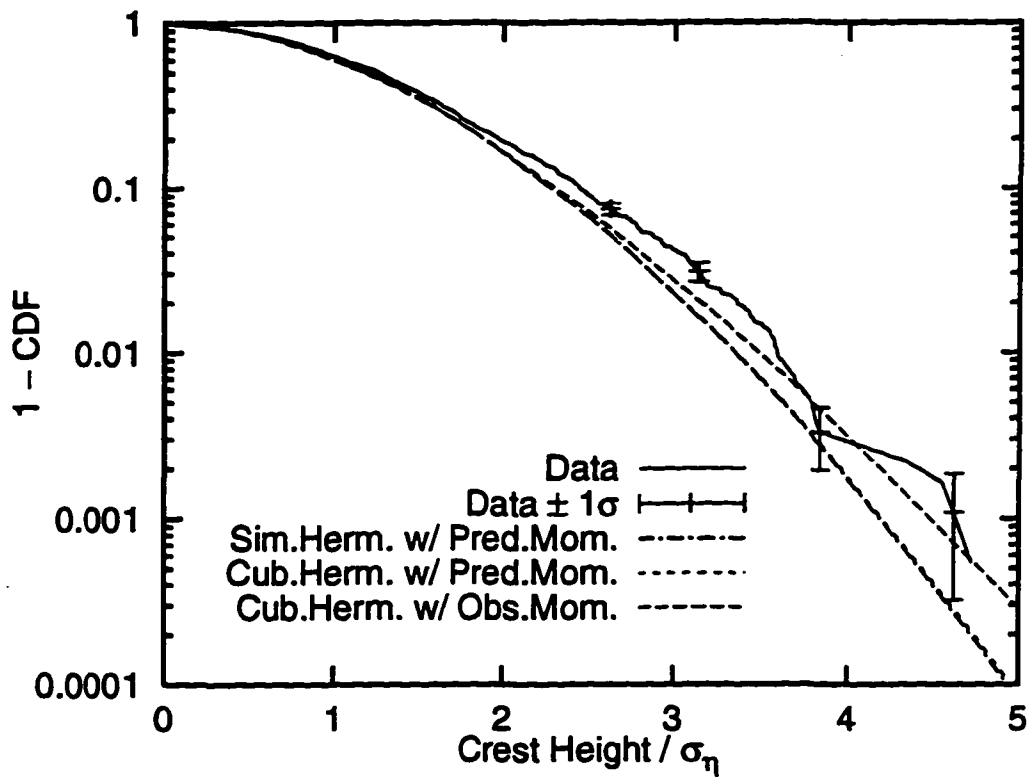
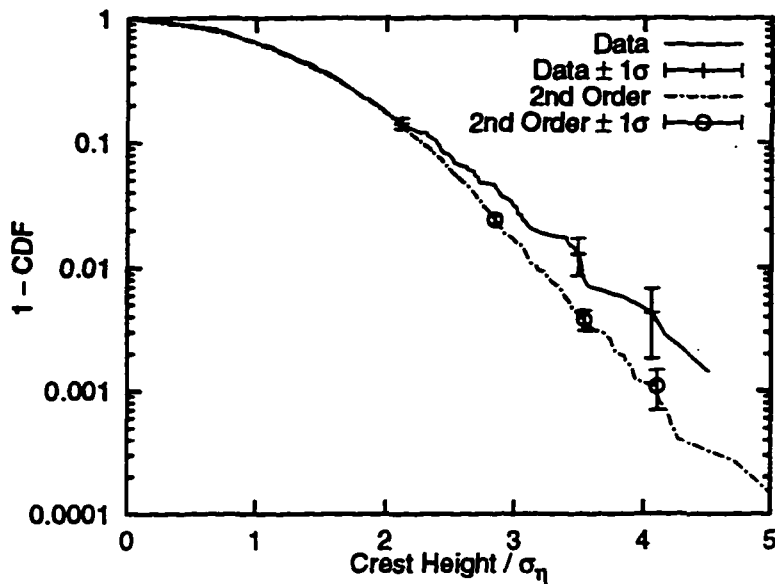
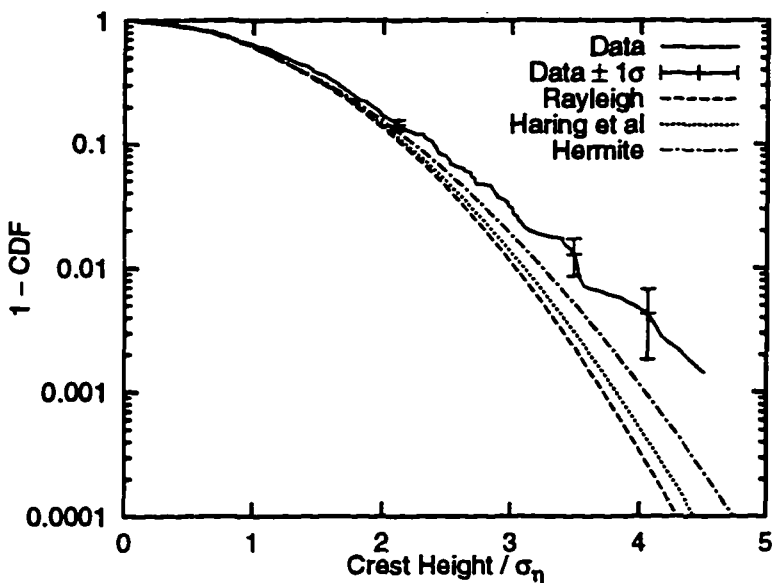


Figure 2.12: Normalized wave crest CDF: Data vs. Hermite models. Elevation from simple Hermite model using predicted moments and cubic Hermite models using predicted and observed moments are shown.

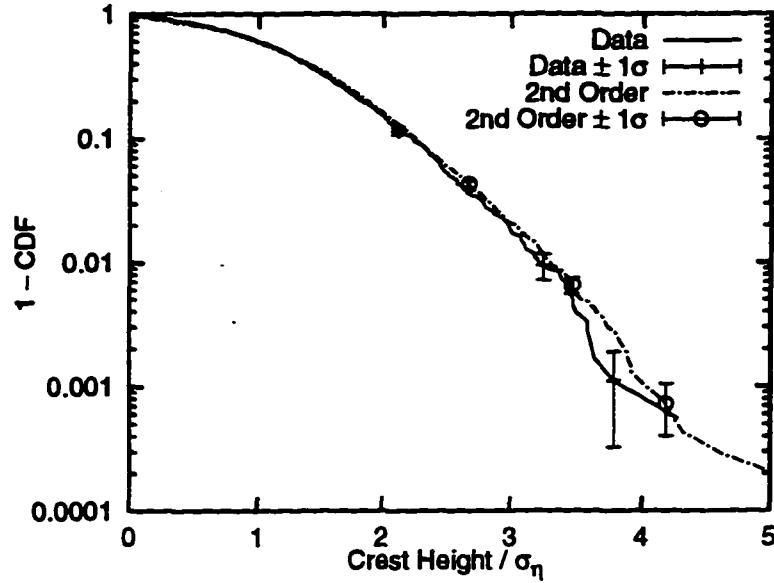


(a) Data vs. Second-order simulation

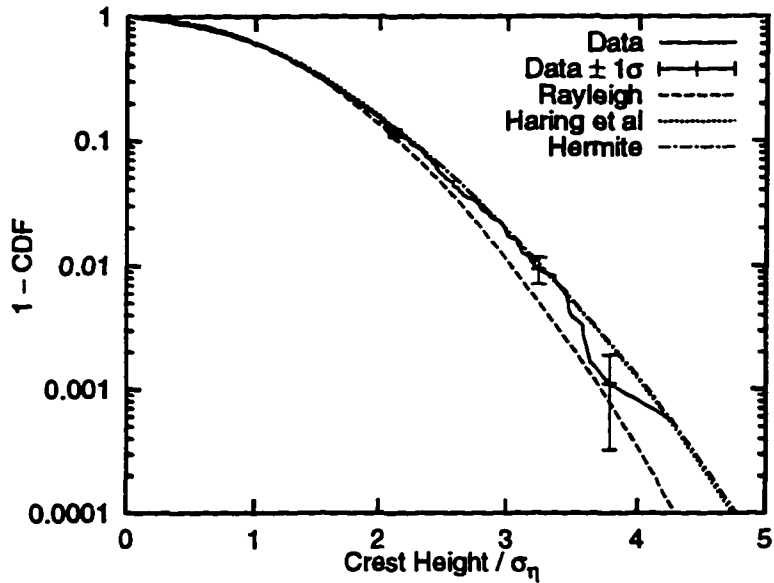


(b) Data vs. Analytical models

Figure 2.13: Normalized wave crest CDF: Data vs. second-order simulations and analytical models for Set 2 (Snorre data set: Test 304)



(a) Data vs. Second-order simulation



(b) Data vs. Analytical models

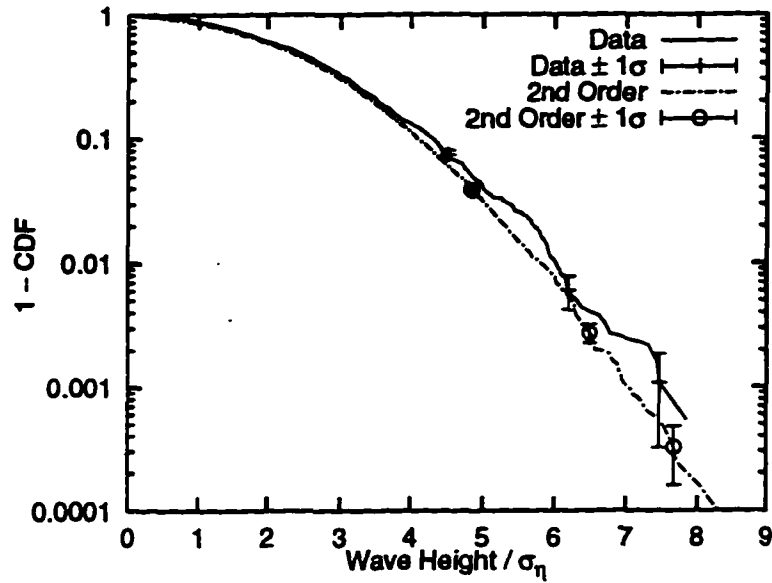
Figure 2.14: Normalized wave crest CDF: Data vs. second-order simulations and analytical models for Set 3 (Ekofisk data set)

2.4.5 Comparison of Wave Height Distributions

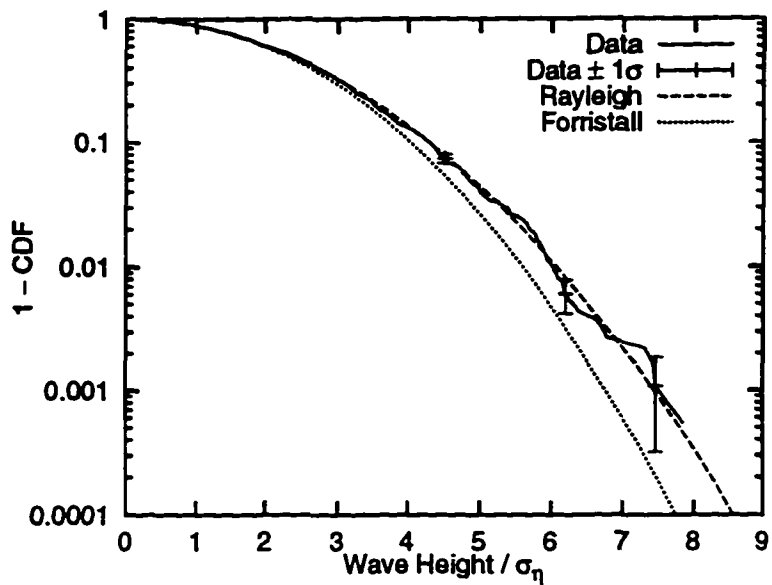
Figure 2.15 compares model and observed wave heights for the first data set. The second-order model offers a closer agreement (within observed scatter) to observed wave heights than the corresponding crest height comparison. For example, at the same 0.001 exceedance probability, the second-order model now underpredicts the observed wave height only by about 6%. Recall the crest height underprediction at this fractile was 10%. Of the analytical models, the Rayleigh model, typically used for wave heights, is given as $\text{Prob}[\text{Height} > h] = \exp[-(h/\sigma_\eta)^2/8]$, while the Forristall distribution [12], an empirical fit to observed ocean wave heights, is given as $\text{Prob}[\text{Height} > h] = \exp[-(h/\sigma_\eta)^{2.126}/8.42]$. The Rayleigh model seems to best fit the observed wave heights, while the Forristall distribution underpredicts the wave heights for this wave tank data. The simplified Hermite wave height prediction, which can now be a transformation of the Rayleigh crests and troughs to make heights, is not shown on the plot. The Hermite model finds the heights by transforming a Rayleigh crest and a Rayleigh trough at a desired fractile using Eqn. 2.17. The transformed crest and trough are added to result in the predicted height at this fractile. Note that in the simplified Hermite transformation the skewness shifts the crest and the trough in the same way so that the wave height remains identical to the Rayleigh height (= Rayleigh crest plus Rayleigh trough). A cubic Hermite transformation that includes the kurtosis effect increases the crest heights and the trough depths depending on the kurtosis magnitude. For kurtosis larger 3, this may only lead to larger wave heights than the Rayleigh distribution. Since the predicted kurtosis values are small, using these in the Hermite model may not significantly affect the wave height results. We choose, therefore, to not show the Hermite wave height model in the comparisons.

A comparison of the wave heights (Fig 2.16) for the second data set offers similar

conclusions as the first data set. The second-order simulation offers good agreement for the small heights and slightly underpredicts the large heights. Of the analytical models, the Rayleigh distribution agrees well with observed wave heights. Finally, the second-order model and observed wave heights agree well for the Ekofisk data set (see Fig. 2.17). Now, however, the Rayleigh model slightly overpredicts the observed heights, and the Forristall distribution agrees well with the Ekofisk heights.

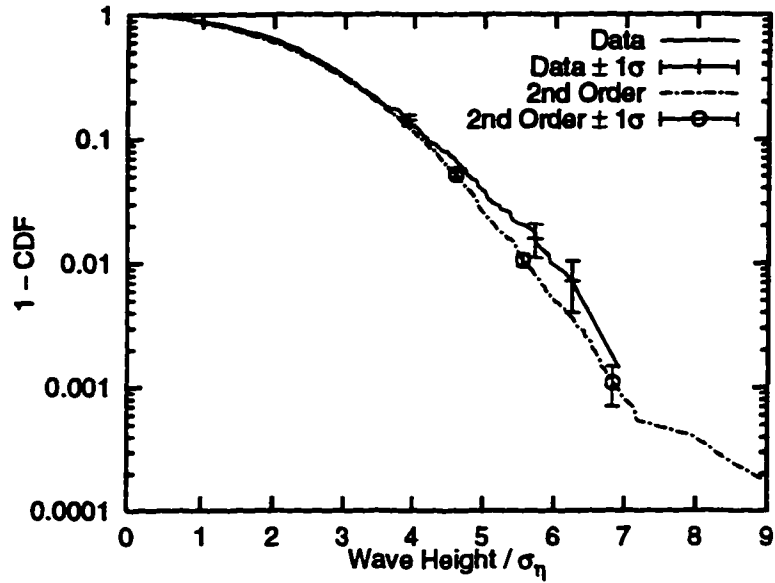


(a) Data vs. Second-order simulation

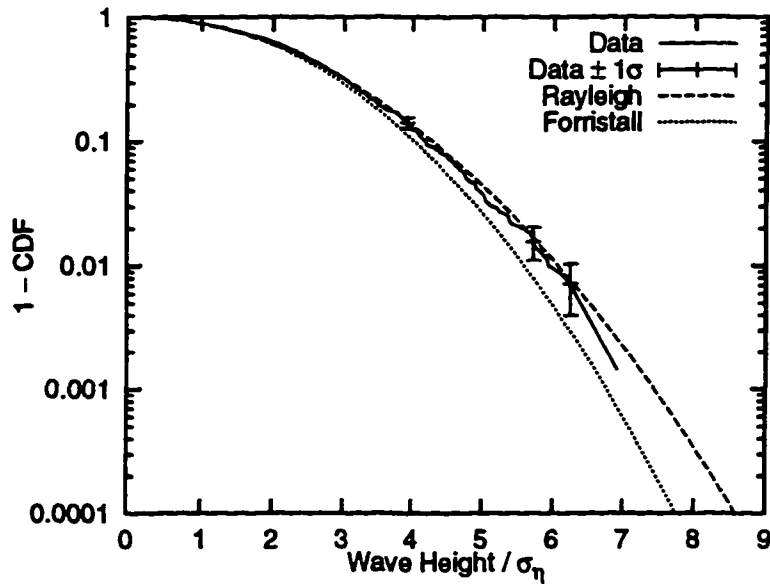


(b) Data vs. Analytical models

Figure 2.15: Normalized wave height CDF: Data vs. Second-order simulations and analytical models for Set 1 (Snorre wave tank data: Tests 504, 505, 505)

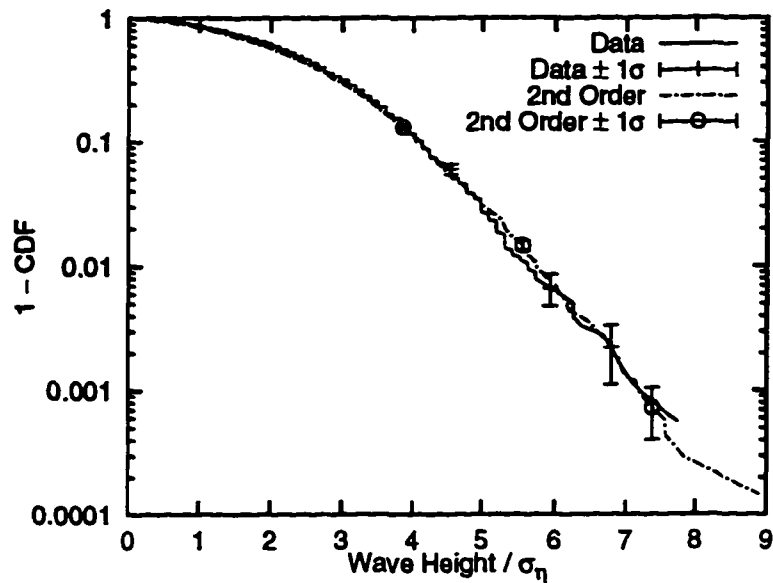


(a) Data vs. Second-order simulation

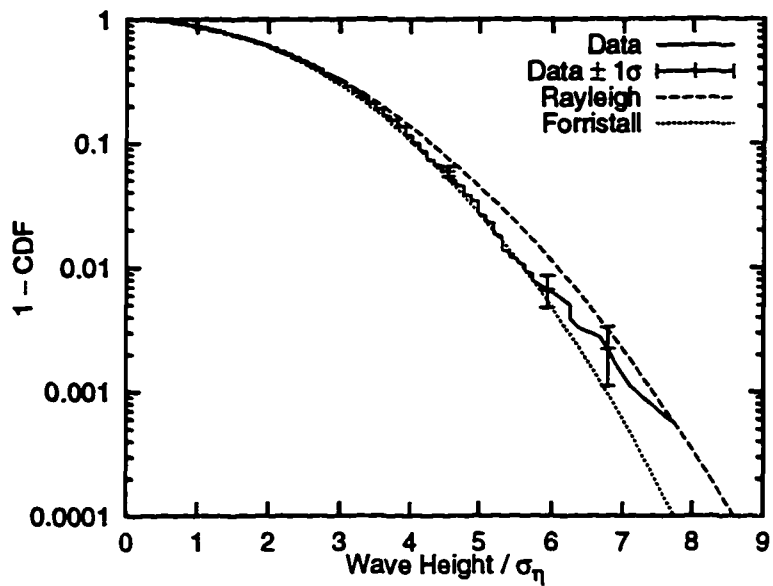


(b) Data vs. Analytical models

Figure 2.16: Normalized wave height CDF: Data vs. Second-order simulations and analytical models for Set 2 (Snorre data set: Test 304)



(a) Data vs. Second-order simulation



(b) Data vs. Analytical models

Figure 2.17: Normalized wave height CDF: Data vs. Second-order simulations and analytical models for Set 3 (Ekofisk data set)

2.5 Comparison of Local Wave Statistics

In this section we compare conditional distributions of local wave parameters. Figure 2.18 defines the local wave parameters to be studied in this section. Crest front period T_{CF} is the period from a mean-upcrossing to the time of occurrence of the highest point in a crest. Crest back period T_{CB} is similarly defined as the period between the highest point in a crest to the following mean-downcrossing. Crest period T_C is the sum of T_{CF} and T_{CB} and is the period between a mean-upcrossing and the following mean-downcrossing in the wave. The wave period T_W , finally, is the period between the two mean-upcrossings in a wave.

We will compare the conditional distribution of the local wave parameters from the second-order model to data. We will demonstrate these comparisons with the first wave data set that represents the Snorre wave tank measurements. We will first look at the conditional distribution of a wave's crest height given its wave height. Figure 2.19 shows the conditional mean and standard deviation of the wave crest given a wave height for the first- and second-order simulated histories and measured data. The Gaussian (first-order) simulation, of course, shows that the crest heights are on average half the corresponding wave heights. The data shows systematically larger crests conditionally, given the corresponding wave height. The second-order model is found to predict this conditional vertical asymmetry quite accurately. Note that even though the model slightly underpredicts the marginal distributions of the crests and of the wave heights, the conditional crest mean and standard deviation seem accurately predicted.

We next consider the horizontal asymmetry in the waves. Figures 2.20 and 2.21 compare T_C to T_W , and T_{CF} to T_C , respectively. As may be expected, the first-order and second-order simulations do not indicate presence of any horizontal asymmetry.

As seen in the figures, T_C is approximately half of T_W . Similarly, T_{CF} is approximately half of T_C . No horizontal asymmetry can be found in the observed data either, indicating that the first- and second-order simulations are statistically equivalent to the observations as regards horizontal asymmetry.

Figure 2.22 shows the conditional distributions of wave periods given crest heights for data, first- and second-order simulations. This figure shows the conditional median along with 16- and 84-percentile spread of wave periods given crest heights. All results show the same trend of increasing wave periods for small to moderate crest heights, and constant wave periods for large crest heights. The asymptotic wave period is close to the central period obtained from the first moment of the wave spectrum (in this case the central period is about 12 seconds, Table 2.3). Figure 2.23 shows a similar comparison of conditional distribution of maximum of T_{CF} and T_{CB} in a wave vs. the crest height of the wave. This is again shown as the conditional median with 16- and 84-percentile scatter of $\text{Max.}(T_{CF}, T_{CB})$ given crest heights. Such statistics are of interest, for example, in identifying the large high-frequency resonant (“ringing”) responses that may be observed in offshore structures. Again, all results show the same trend of increasing periods for small crests and a gradual asymptote period for large crest heights, with the second-order model offering a slightly better agreement to data. The asymptotic maximum of the crest front and back period for large crest heights is about 25% of the central wave period.

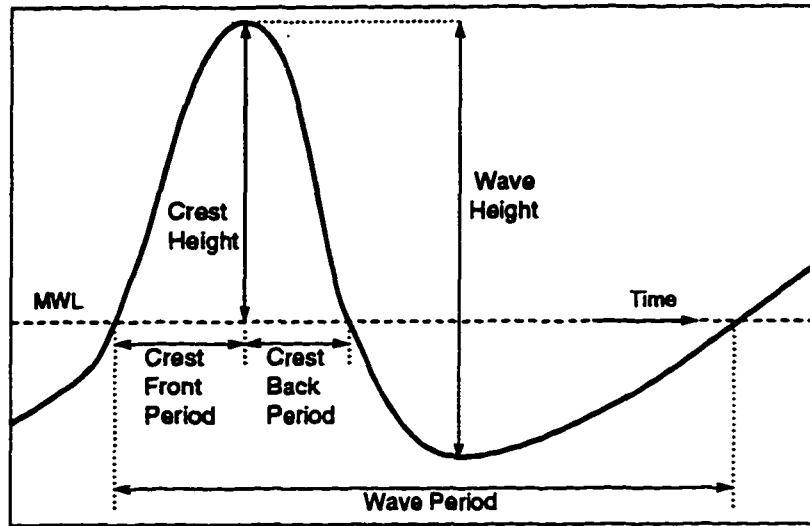


Figure 2.18: Definition for wave parameters used in the comparison studies

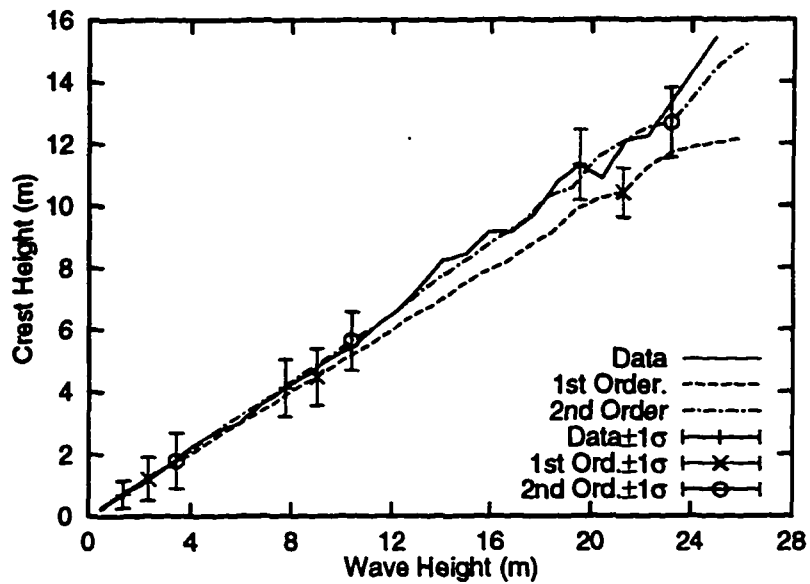


Figure 2.19: Crest height to wave height: Data vs. first- and second-order models

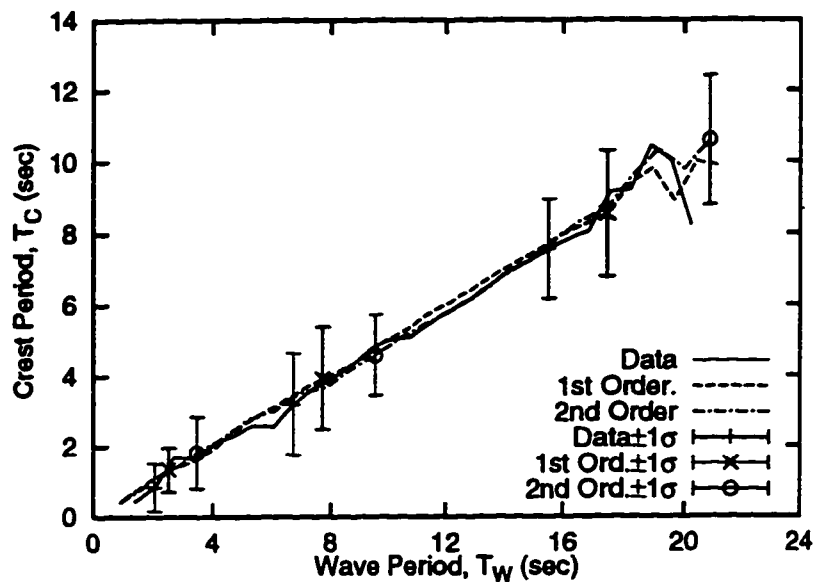


Figure 2.20: Crest Period T_C to wave period T_W : Data vs. first- and second-order models

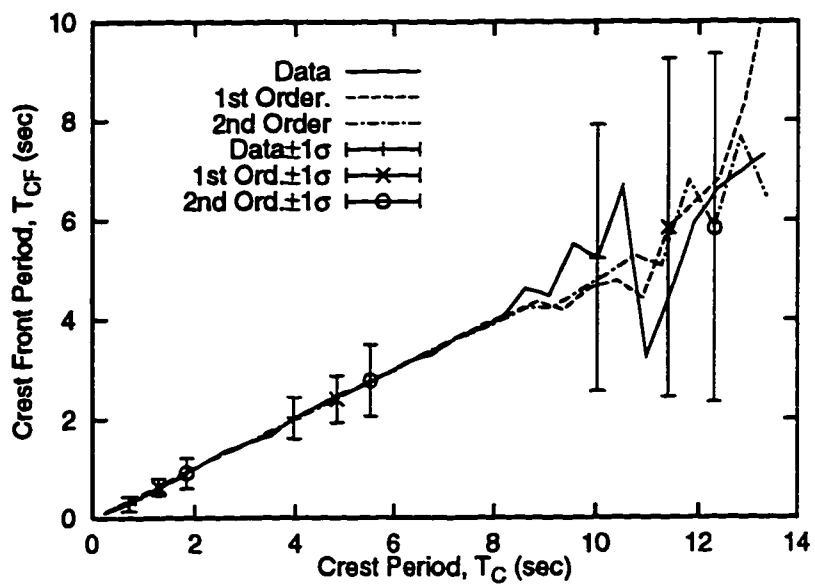


Figure 2.21: Crest front period T_{CF} to crest period T_C : Data vs. first- and second-order models

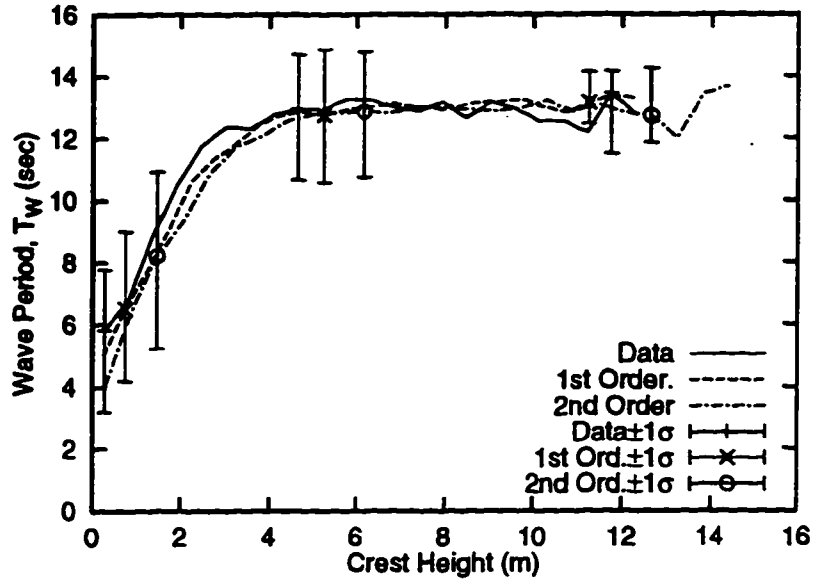


Figure 2.22: Wave period T_W to crest height: Data vs. first- and second-order models

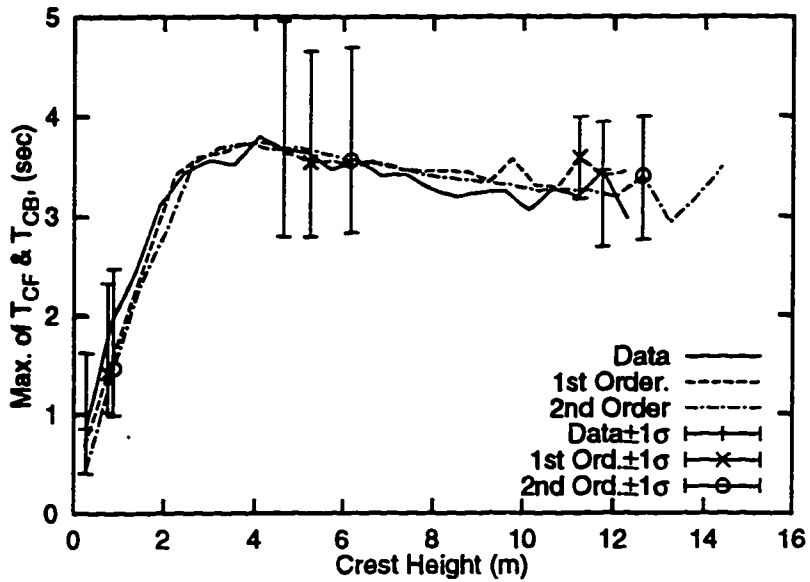


Figure 2.23: Maximum of crest front (T_{CF}) and crest back (T_{CB}) periods to crest height: Data vs. first- and second-order models (for application to "ringing")

2.6 Conclusions

- The second-order wave model adequately reflects the nonlinearity of observed waves in finite water depths, and has the ability to include arbitrary frequency content in the waves. This model provides a better alternative to regular wave models or the linear Gaussian wave models.
- Convenient analytic formulae for skewness and kurtosis from the second-order model are given by Eqn.s 2.9 and 2.10.
- The second-order model (WAVEMAKER) provides a convenient tool to simulate various wave statistics of interest. Alternatively, the Hermite model coupled with analytically predicted moments (Eqn.s 2.9 and 2.10) could be used to yield various wave statistics.
- Comparison of the model predictions to field data appeared to be better than the wave tank test comparisons. Some differences in the characteristics of the wave tank and field data were pointed.

2.7 Identification of First-order Waves

In ocean engineering practice it is common to assume the waves to be Gaussian when estimating forces on large volume structures and any nonlinearity in the waves is embedded in the structural response analysis (e.g., [64]). It has been shown in this chapter that observed time histories generally contain nonlinearities, it is thus imperative to remove any second-order effects in the incident waves so that these effects are not double-counted in the resulting response estimation. Recent studies ([59]) have demonstrated the impact of double-counting such second-order effects on

various structural response characteristics. We demonstrate this issue further in the next chapter on the spar floating platform.

The methodology to identify the underlying first-order waves is to seek the implied first-order wave history which, when run through the second-order wave predictor, yields an incident wave that agrees with the target observed history at each time point. This identification is performed using a Newton-Raphson scheme to achieve simultaneous convergence at each complex Fourier component. If the observed history has N components, we iteratively solve N simultaneous nonlinear equations to identify the first-order components. Refer to Appendix A for more details.

As an example we will identify the underlying first-order wave component for the Snorre wave tank history (Test 504) that reflects a water depth of about 308m. Figure 2.24 shows a portion where the maximum crest height occurs in the measured wave tank history. The figure also shows the identified first-order and the corresponding second-order wave histories. Note how the second-order wave component affects the first-order peaks, amplifying the crests and moderating the troughs. Figure 2.25 shows the wave spectra for the measured history along with the first-order and the second-order spectra. Note that the second-order energy is significantly smaller (even at twice the peak spectral frequencies) than the first-order energy; it is the phase locking of the first- and the second- component (Fig. 2.24) leads to larger crests and flatter troughs.

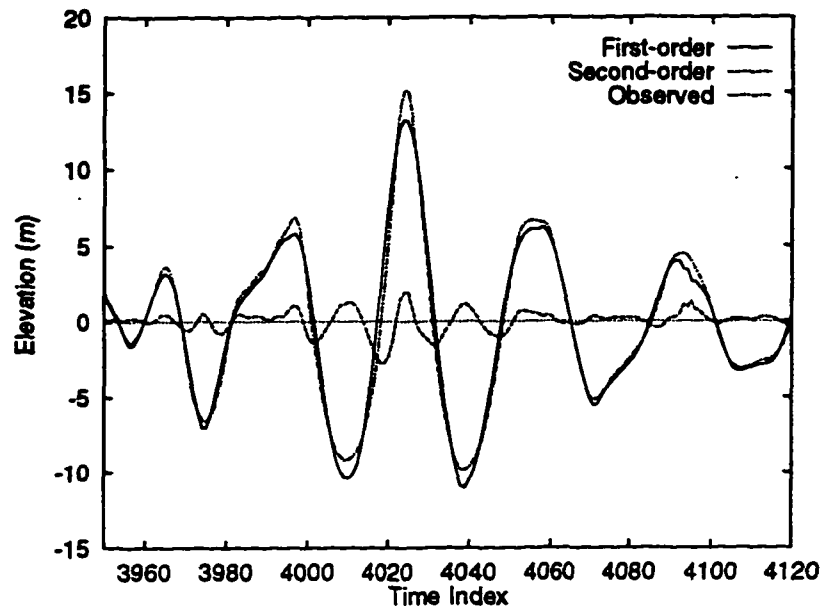


Figure 2.24: Wave history in wave tank: observed vs. identified first- and second-order

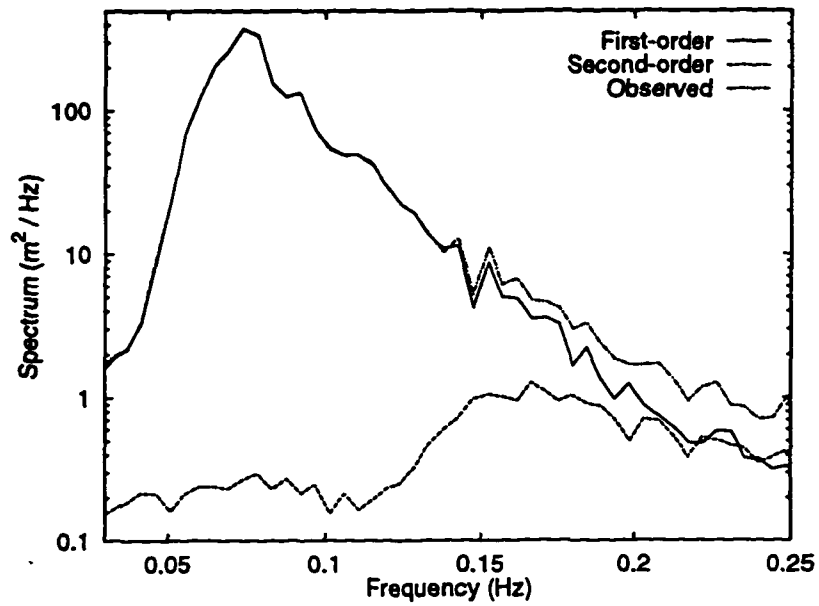


Figure 2.25: Wave spectrum in wave tank: observed vs. identified first- and second-order

Chapter 3

Spar Floating Platform: Numerical Analysis and Comparison with Data

3.1 Introduction

In this study, we will investigate the global response behavior of a large-volume floating structure (here, a spar platform) and compare model predictions to measurements in wave tank tests on this structure. Given good agreement to data, the model can then be used as a tool in designing various structural components of the spar.

Large-volume floating structures are being increasingly used for deep-water drilling and production of oil and natural gas. Examples of such structures include tension-leg platforms (TLP), semi-submersibles and spar floating platforms. For a TLP the deck is placed on a hull made up of three to five columns, with the columns extending into the water and connected to each other by pontoons. The floating hull is held

down to the sea bottom by vertical mooring lines in tension. A semi-submersible is a similar structure, but it is held down by slack mooring lines. On the other hand, a spar floating platform is a large vertical cylinder, held down to the sea floor by slack or taut mooring lines. The cylinder provides buoyancy to keep the spar afloat and can also be used to store oil. The spar considered here has a center well that encloses the production risers. This provides for additional protection and easier maintenance of the production risers.

The mooring lines are typically designed so that the resonance periods of these large-volume structures are outside the dominant wave energy periods. For example, resonance periods in the horizontal direction of the spar can be of the order of 5 minutes, far above the wave periods that may be around 5 to 15 seconds. In this study, we will analyze these long-period responses in the wave direction, often referred to as slow-drift responses, for a spar platform and compare model predictions to wave tank measurements. Similar models have been applied before to TLPs [59] and will be extended here for the spar platform. The large slow-drift motions seem to be critical in various design aspects of the spar and the model can, generally, be extended to analyze other motions of the spar as well.

The spar platform is a relatively new concept (compared to TLPs, for example) and the few studies done before [41, 42, 49, 66] do not seem to systematically compare model predictions to wave tank data in random seas. In this study, we strive to apply different hydrodynamic models and systematically compare time domain predictions (using measured waves) to the measured response time histories in random seas. The response here refers to the horizontal displacement measured near the spar deck in irregular random waves.

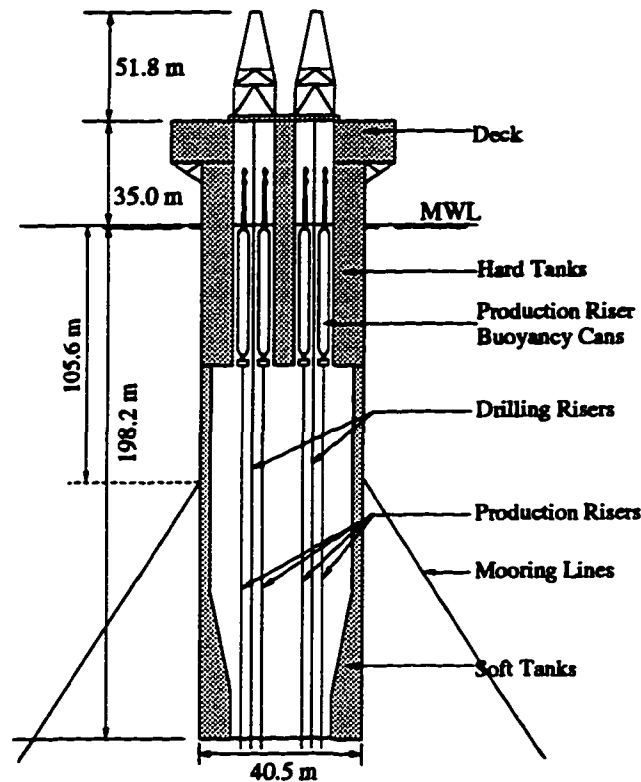


Figure 3.1: Elevation view of Spar platform

3.2 Spar Model for Slow-drift Response

3.2.1 Experimental Data

The floating structure chosen for this study, shown in Fig. 3.1, is a catenary-moored spar buoy, intended for deep-water production and storage. The important properties required in modeling the spar are summarized in Table 3.1. A 1:55 model scale of the spar was tested in the OTRC wave tank [46] under various wave conditions. We will look here at the random sea simulations of waves and resulting displacements in the horizontal along-wave direction. To investigate these motions, we will need to

Table 3.1: Details of the spar configuration (in prototype scale)

Description	Notation	Value
Diameter	D	40.5 m
Draft from Mean Water Level (MWL)	H	198.2 m
Mass with entrapped water	m	2.59×10^8 kg
MWL to Center of Gravity	Z_{CG}	105.8 m
MWL to Center of Buoyancy	Z_{CB}	99.1 m
MWL to mooring connection	Z_f	105.6 m
Radius of gyration wrt MWL	K_r	122.8 m
Mooring stiffness in horizontal direction	k	191 kN/m
Measurement gauge location above MWL	Z_m	54.8 m
Water Depth	d	922 m

look at surge and heave displacements, pitch rotations and airgap measurements (see Fig. 3.2) in the wave tank. If the MWL is the origin, surge is defined to be horizontal displacement along the wave direction at the MWL. Pitch rotation is the rotation of the spar measured at the MWL in the plane of wave direction. Finally, heave is the vertical motion of the spar.

In the wave tank, the spar was tested for the following wave conditions:

- 12 different regular waves
- 14 different combinations of bi-chromatic waves
- 4 different random wave seastates
- various tests for combinations of random waves, currents and variable winds

The random wave measurements are for durations of one hour each with a sampling frequency of 0.37 seconds, and simulate the following storms:

- operational and installation seastates, both long-crested and short-crested

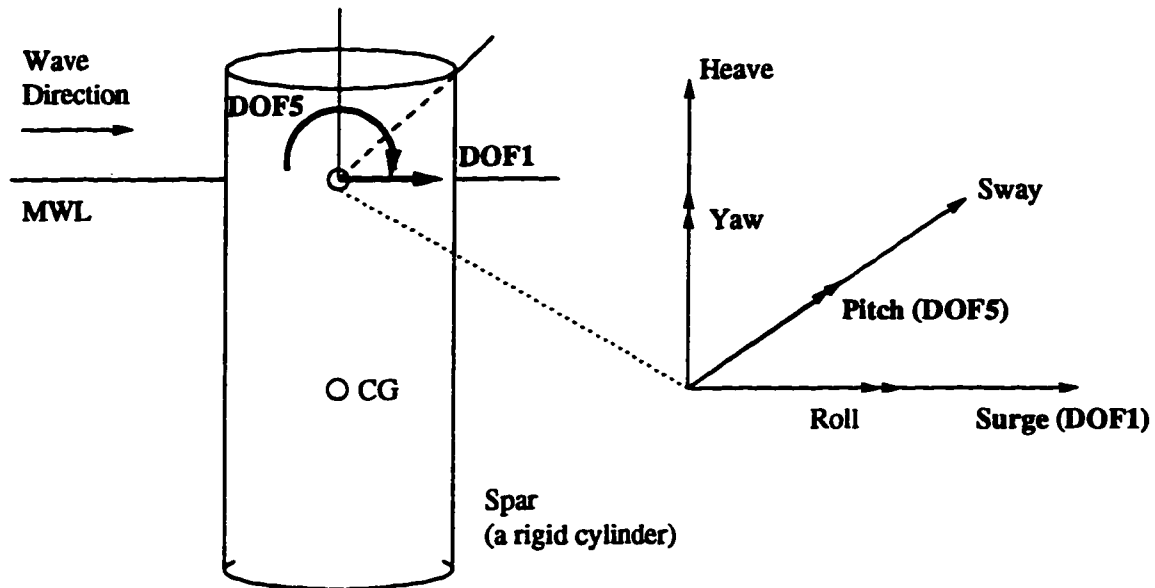


Figure 3.2: Degrees of freedom for spar

- a 10-year Gulf of Mexico storm
- a 100-year Gulf of Mexico storm
- a North Sea storm
- a West Africa storm

Of these, we focus on the two most severe storms: (1) the 100-year Gulf of Mexico, and (2) the North Sea storm. The experiments include two different hourly realizations of the same Gulf of Mexico storm and one hourly realization of the North Sea storm. The remaining smaller storms are not considered in this study. A summary of the wave tank measurements in the two storm is:

- two realizations (1 hour each) of a seastate described by a JONSWAP spectrum with significant wave height $H_s = 13.1\text{m}$, $T_p = 14\text{s}$, and a peakedness factor $\gamma =$

2.0. These seastates are intended to represent roughly 100-year H_s conditions in Gulf of Mexico sites and we will refer to these tests as GOM1 and GOM2

- one realization (of 1 hour) reflecting a second seastate characterized by $H_s = 14m$, $T_p = 16.3s$, and $\gamma = 2.0$. This seastate roughly represents 100-year H_s conditions in the North Sea and we will refer to this test as NS.

In these experimental tests, the surge and heave responses are recorded by a video camera tracking a light source placed 54.8 meters above MWL along the cylinder vertical axis. The pitch rotations were recorded by an inclinometer mounted on the deck of the model. The airgap measurements were recorded by a probe attached to the spar deck facing the waves, while another probe measuring the wave surface was placed 125 meters (prototype scale) away from the spar, in a direction perpendicular to the propagating waves. This probe placed away from the spar is intended to measure the undisturbed waves, or what is typically referred to as the “reference” waves. The airgap probe measures the “disturbed” waves, which refers to the waves in the presence of a structure.

A summary of the reference wave statistics, as found from the measurements, is reported in Table 3.2. The observed H_s is defined to be four times the wave σ_η , while the observed T_p has been found from an averaged spectrum from the measured wave histories. $T_z = \sqrt{\lambda_0/\lambda_2}$ is found from second (λ_2) and zeroth (λ_0) moments of wave spectrum $S(f)$ with no smoothing, where $\lambda_n = \int f^n S(f) df$. Note the presence of nonlinearities in the waves ($\alpha_3 > 0$ and $\alpha_4 > 3$), and the differences in the target (nominal) and observed H_s values.

In the response measurement we focus here on the surge displacement of the spar. These slow-drift responses in the surge direction are usually large and can govern the design of many structural elements, for example the mooring lines, of the

Table 3.2: Reference wave summary statistics for the OTRC wave tank tests used for slow-drift response analysis of the spar

Test	GOM1	GOM2	NS
Npts	9702	9702	9702
Nominal H_s (m)	13.1	13.1	14
Nominal T_p (m)	14	14	16.3
Observed H_s (m)	14.15	13.98	14.78
Observed T_p (sec)	14.1	14.1	16.1
Calculated T_z (sec)	10.83	10.74	12.0
Mean, μ (m)	.063	.076	-.040
Sigma, σ_η (m)	3.537	3.495	3.699
Skewness, α_3	0.307	0.309	0.173
Kurtosis, α_4	3.057	3.242	3.277
Minimum (m)	-9.054	-9.711	-11.12
Maximum (m)	12.74	16.21	17.52

spar. The heave response for a spar platform is comparatively small and will not be investigated in this study. We anticipate no significant roll, sway or yaw motions to occur in unidirectional seas for this axi-symmetric structure and will not study these motions either. For the spar considered here, the horizontal displacement is measured at an elevation of 54.8 m above the MWL. Since this measurement point is away from the center of rotation, the horizontal displacement will be contributed by the surge displacement and the pitch rotation (about the center of rotation). Note that the center of rotation is close to the center of gravity of the spar. If we define the rigid-body degrees of freedom (DOF) at the MWL (see Fig. 3.2), then a unit radian pitch rotation will cause a 46 meter ($= 54.8 \times \sin(1)$) displacement in the horizontal direction at the measurement point. We will refer to surge-induced displacement as “DOF1 displacement”, and the pitch-induced displacement at the measurement point as “DOF5 displacement”.

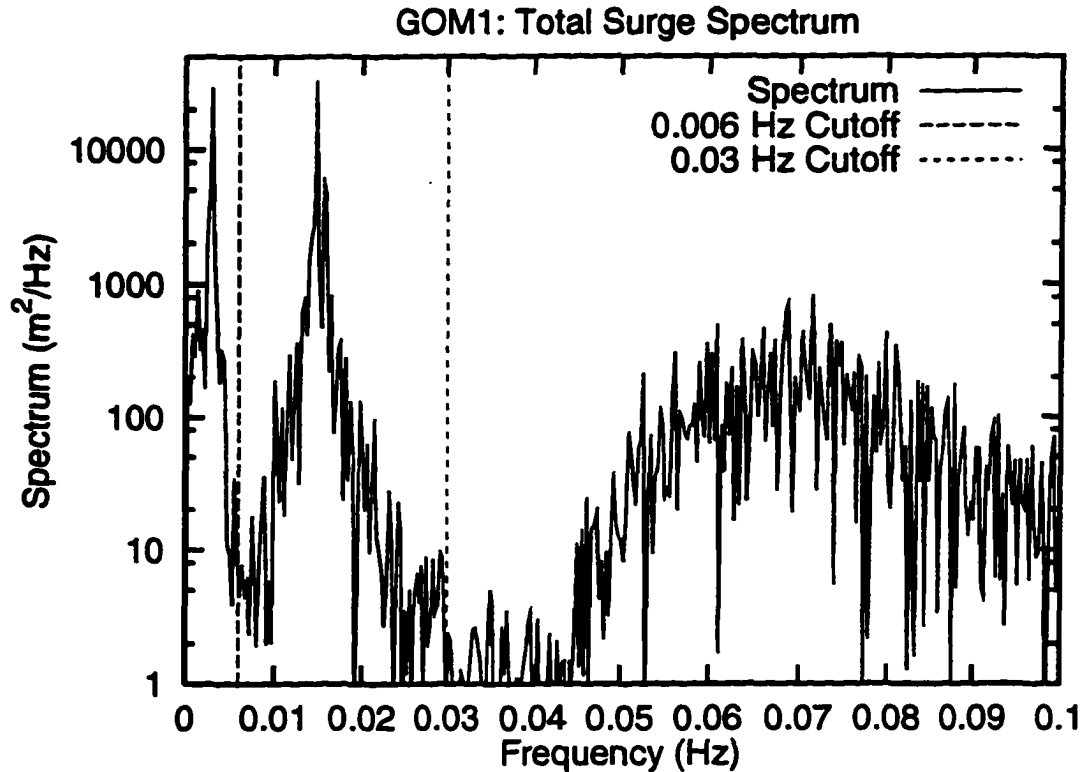


Figure 3.3: Spectrum of measured surge displacements at 54.8m elevation above MWL for GOM1 seastate

To understand these surge- and pitch-induced displacements, we will look at one of the measured horizontal displacements. Figure 3.3 shows the power spectrum of the measured horizontal displacements for GOM1. This spectrum shows three prominent peaks which in sequence left to right are: the surge-induced, the pitch-induced and the wave-frequency components. Note how small the wave-frequency contribution (around $f=0.07$ seconds $\approx 1/T_p$) is compared to the other two components. The surge and pitch components appear to contribute more to the total horizontal displacement.

The peaks in the spectrum indicate natural periods in surge (DOF1) and pitch

Table 3.3: Statistical moments of the measured horizontal displacements for the seastates. Note that the maximum and minimum values contain μ .

Seastate	μ (m)	σ (m)	α_3	α_4	Min.(m)	Max.(m)
GOM1	4.942	5.788	0.078	2.677	-12.32	22.76
GOM2	5.130	6.176	0.052	2.965	-14.95	25.99
NS	3.396	7.949	0.144	3.163	-21.87	29.35

(DOF5) to be about 330 and 70 seconds, respectively. Independent free decay tests of this spar also indicate the natural periods in surge and pitch to be about 330 and 67 seconds [46]. To study the three components separately, we introduce frequency cutoffs at 0.006 Hz and 0.03 Hz to filter the contributions from the three components. The frequency range below 0.006 Hz indicates the surge component, and the range above 0.03 Hz indicates the wave-frequency component. Finally, the pitch-component range is assumed to be between 0.006 Hz and 0.03 Hz.

Table 3.3 summarizes the statistical moments of the horizontal displacement histories, and the moments of its filtered components is presented in Table 3.4. A comparison of standard deviations σ of filtered components in the three measurements, confirms that compared to the wave-frequency component, the low-frequency or slow-drift components (DOF1 and DOF5) dominate the total horizontal displacement. Thus a force model capturing only the wave-frequency components is likely to severely underpredict the horizontal displacements. Such a force model is usually referred to as a linear or a first-order model. For example, in Fig. 3.3 a linear force model would attempt to predict only the wave-frequency component, and it would fail to predict the DOF1 and DOF5 components. Another force model that, instead, attempts to predict the force components away from the wave-frequency region is often referred to as a second-order model. In general, a second-order model includes

Table 3.4: Statistical moments of the filtered components (with zero mean) of measured horizontal displacements

Component	σ (m)	α_3	α_4	Min.(m)	Max.(m)
GOM1					
Wave-frequency	2.473	-0.023	2.697	-7.882	7.158
Surge component	3.375	0.091	2.196	-6.378	7.229
Pitch component	3.997	-0.005	2.177	-9.733	9.520
Surge+Pitch Comp.	5.233	0.044	2.443	-8.466	18.52
GOM2					
Wave-frequency	2.508	-0.032	2.843	-7.933	7.604
Surge component	3.937	0.185	2.959	-8.818	10.24
Pitch component	4.040	-0.002	2.357	-9.516	9.854
Surge+Pitch Comp.	5.643	0.026	2.968	-11.94	20.77
NS					
Wave-frequency	3.159	0.028	3.006	-10.36	11.32
Surge component	4.373	-0.113	2.051	-8.938	7.897
Pitch component	5.906	-0.077	2.625	-18.57	15.38
Surge+Pitch Comp.	7.356	0.048	3.094	-17.05	26.12

forces that are at the sums and differences of the wave frequencies. In modeling the high-frequency heave response of a TLP, for example, interest focuses on the sum-frequency component, while in this study where the slow-drift response is of interest, a difference-frequency model would be more appropriate. Recall that in modeling the wave elevations in Chapter 2, we needed both the sum- and difference-components.

We will next look at the component time histories in Fig. 3.4. The vertical axis label in each plot indicates the component being displayed. For the total horizontal displacement (shown in the topmost plot in Fig. 3.4), note the distinct transition in response characteristics around 1500 seconds. The displacement prior to 1500 seconds seems to be due to dominant pitch motions, while after 1500 seconds the surge-induced (low) frequency response seems more dominant. This is also evident

in the time history components shown, where the surge amplitudes are larger in the second half hour than in the first. Such a transition shows the difficulty in modeling a seemingly non-stationary behavior of the spar. The very limited number of surge response cycles seen in the hourly measurement additionally contribute to the difficulty in calibrating a model to this data. In this study, we investigate four such model forms that attempt to capture the nonlinear forces and the resulting responses of the spar. The model predictions will be compared to the wave tank measurements. Note that in these models, while the forces can be nonlinear, the structure is still assumed to respond linearly to the incident forces.

3.2.2 Structural Model

As mentioned earlier, the surge displacement, measured at an elevation of 54.8 m above the MWL, is contributed by the surge and pitch DOFs defined at the MWL. In order to capture this dual-contribution to the total horizontal displacement, we model the spar as a rigid cylinder with two DOFs (surge and pitch) defined at the MWL, see Fig. 3.2. To define the DOFs we choose the MWL as the origin because the first- and second-order waves forces have been defined with the MWL as the origin. Note that the spar is modeled as a rigid body, and the surge and pitch DOFs or modes refer to the rigid body motions of the spar close to the surge and pitch resonance frequencies.

From geometry considerations, we find that the structural mass matrix M_{str} , from

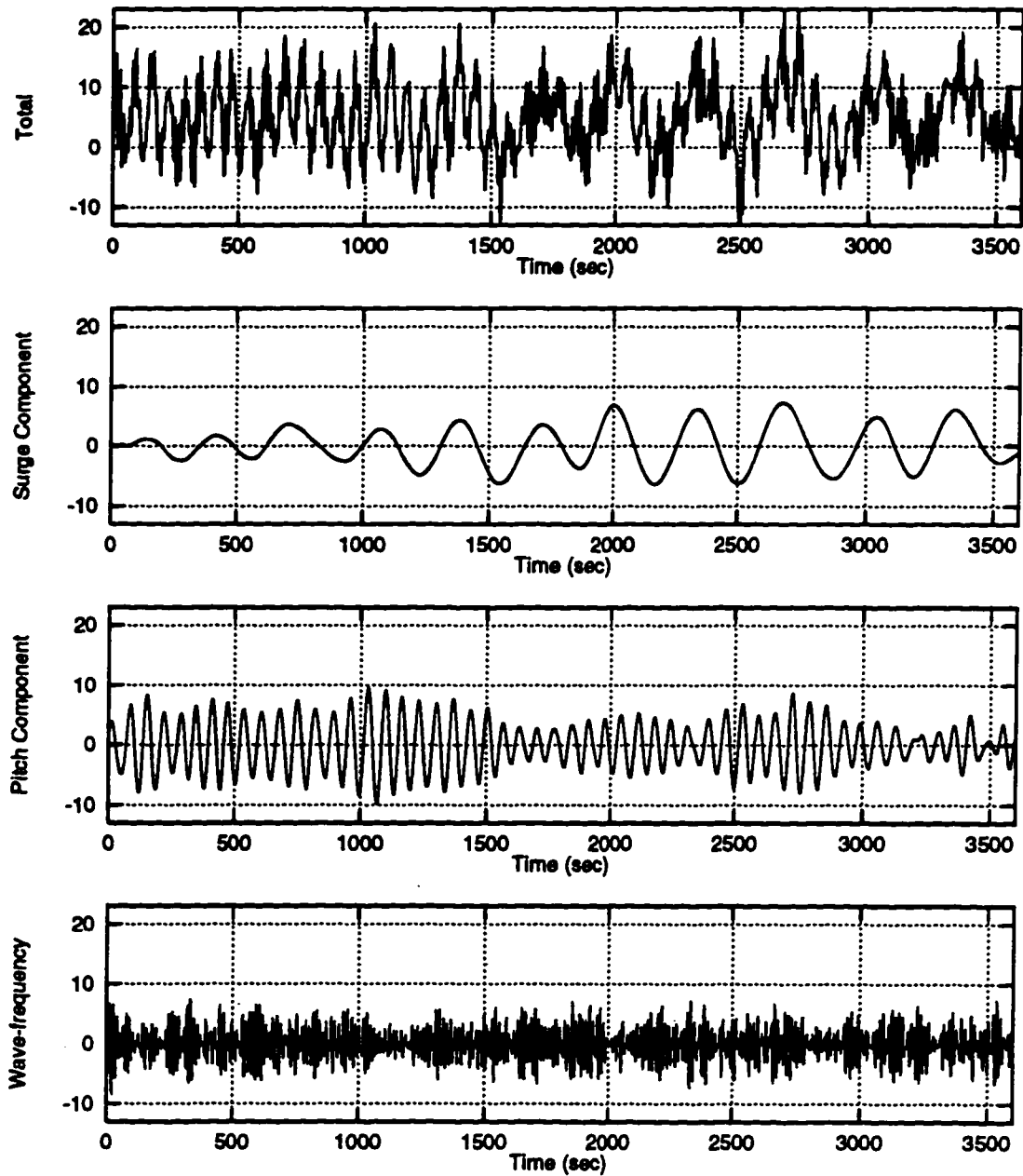


Figure 3.4: Total measured horizontal displacement and its filtered surge, pitch and wave-frequency components for GOM1 seastate

properties summarized in Table 3.1, for the 2-DOF model is

$$M_{\text{str}} = \begin{bmatrix} m_{11} & m_{15} \\ m_{51} & m_{55} \end{bmatrix} = \begin{bmatrix} m & -mZ_{CG} \\ -mZ_{CG} & I(=mK_r^2) \end{bmatrix} \quad (3.1)$$

$$= \begin{bmatrix} 2.59 \times 10^8 \text{kg} & -2.74 \times 10^{10} \text{kg.m} \\ -2.74 \times 10^{10} \text{kg.m} & 3.91 \times 10^{12} \text{kg.m}^2 \end{bmatrix}$$

The added mass matrix M_{add} , reflecting the effects of waves radiated by the oscillating spar, is assumed to be constant for the low-frequency modes, and is found from diffraction analysis [25] to be

$$M_{\text{add}} = \begin{bmatrix} 2.71 \times 10^8 \text{kg} & -2.60 \times 10^{10} \text{kg.m} \\ -2.60 \times 10^{10} \text{kg.m} & 3.20 \times 10^{12} \text{kg.m}^2 \end{bmatrix} \quad (3.2)$$

Note that M_{add} is of the same order of magnitude as M_{str} for this large-diameter structure. The stiffness matrix, again from geometry considerations, is found to be

$$K = \begin{bmatrix} k & -kZ_f \\ -kZ_f & kZ_f^2 + k_h \end{bmatrix} \quad (3.3)$$

where k_h is the hydrostatic stiffness encountered by the spar when rotated in the pitch direction, and is given for small rotations as [42]

$$k_h = \pi R^2 H \rho g (Z_{CG} - Z_{CB}) - \frac{\pi}{4} \rho g R^4 \quad (3.4)$$

where ρ is the water density, g is the acceleration due to gravity and $R = D/2$ is the

spar radius. On substituting these, we find

$$K = \begin{bmatrix} 1.91 \times 10^5 \text{N/m} & -2.02 \times 10^7 \text{N} \\ -2.02 \times 10^7 \text{N} & 1.6 \times 10^{10} \text{N.m} \end{bmatrix} \quad (3.5)$$

An eigenvalue analysis of the 2-DOF spar is solved for the shapes Φ and squared frequencies Λ using

$$K\Phi = M\Phi\Lambda \quad (3.6)$$

in which $M = M_{\text{str}} + M_{\text{add}}$ and Λ is a diagonal matrix of the squared frequencies and results in the natural surge and pitch periods of 331 seconds and 69.9, respectively. This is very close to the natural periods observed for the GOM1 seastate (see Fig. 3.3) and also close to the natural periods found from the free decay tests. This confirms the modeling of the mass and stiffness properties. The eigenmodes, scaled to unit values in the DOFS,

$$\Phi = \begin{bmatrix} 1 & 100.6 \\ 6.8 \times 10^{-5} & 1 \end{bmatrix} \quad (3.7)$$

indicate the first mode of the cylinder to be surge dominated, while second mode shows a 100.6 meter horizontal displacement for every unit radian rotation in pitch. Note that this system shows strong “geometric-coupling” induced by the distance from measurement point to the center of rotation.

3.2.3 Hydrodynamic Model Forms

The base case model considered here for the spar is a linear, 2-DOF (DOF1 and DOF5) rigid cylinder with incident wave forces estimated from diffraction analysis of the structure [25]. The diffraction analysis for any structure is commonly done

by applying sinusoidal waves of different frequencies ω_k chosen from the wave power spectrum. Irregular waves can be written as $\eta(t) = \text{Re} \sum C_k \exp(i\omega_k t)$ where C_k are complex Fourier amplitudes. The first-order forces $f_1(t)$ are then found at these incident wave frequencies as

$$f_1(t) = \text{Re} \sum C_k H_1(\omega_k) \exp(i\omega_k t) \quad (3.8)$$

where H_1 is the first-order transfer function, while the second-order forces are found as the forces at pairs of wave frequencies as

$$f_2(t) = \text{Re} \sum \sum C_m C_n H_2^-(\omega_m, \omega_n) \exp[i(\omega_m - \omega_n)t] \quad (3.9)$$

where H_2^- is referred to as the difference-frequency transfer function.

Note that in finding these transfer functions through second-order diffraction analysis, the spar was allowed to float freely [25, 26]. A linear diffraction analysis was used to estimate the frequency-dependent added mass and damping for the spar. Note that the second-order diffraction analysis is computationally intensive and limited to a few wave frequency pairs (here 8×8 frequency grid ranging from 0.2 to 1.18 rad/sec.). We adopt a surface spline fitting scheme FITQTF [24] to interpolate the sparse QTF to a fine mesh for use in predictions using TFPOP [58]. See Appendix B for some studies on the sensitivity of the predicted results to different interpolation schemes.

What remains to be modeled are the damping ratios, ξ_1 and ξ_5 , of the system in the two DOFs that can be used to construct the damping matrix C of the system as

$$\Phi^T M^{-1} C \Phi = \begin{bmatrix} 2\xi_1\omega_1 & 0 \\ 0 & 2\xi_5\omega_5 \end{bmatrix} \quad (3.10)$$

where ω_1 and ω_5 are the resonance periods in surge and pitch DOFs.

The damping ratios ξ_1 and ξ_5 for the 2-DOF system are calibrated using measured data. An approach for such a calibration could be to tune ξ_1 and ξ_5 such that the predicted σ matches measured σ in each mode. This approach, however, may mask potential errors in the force levels. For example, if the force levels from diffraction analysis are overestimated, then the system will end up being tuned to an overly large ξ values to compensate the large forces. Alternatively, we can tune ξ 's from the measured spectral bandwidth δ [9] in each DOF. Other methods include half-power bandwidth, or random decrement method [62]. In this study, we will use the spectral moments λ_n to estimate the bandwidths δ .

$$\delta = \sqrt{1 - \lambda_1^2 / (\lambda_0 \lambda_2)}; \quad \lambda_n = \int f^n S(f) df \quad (3.11)$$

where $S(f)$ is the measured spectrum. Note that δ_1 the bandwidth of the surge component is found from $S(f)$ for $f \leq 0.006$ Hz. Similarly, pitch component bandwidth δ_5 is from the spectral moments for $0.006\text{Hz} < f < 0.03\text{Hz}$. We resort to an iterative identification of the damping ratios, so that the predicted response bandwidth matches the measured bandwidth simultaneously in both DOFs.

We may additionally recognize wave-drift damping [11, 59] as another damping mechanism in the system. This damping is due to the spar (slow) drifting in the waves. The resulting force is proportional to the spar velocity and to the wave amplitude-squared [11]. A consequence of this extra damping force is that it “clips” the peaks of the surge response, and as such is a “beneficial” nonlinearity that we will include in our second model. Wave-drift damping, similar to nonlinear force, is a second-order effect and is to be defined across pairs of wave frequencies (as in the QTF definition). In this study, the diagonal values for wave-drift damping definition were found using

SWIM [40] and the off-diagonal terms estimated using Newmann's approximation [45]. The effect of this approximation should be small for this slow-drift problem, as the interesting frequency pairs lie very close to the diagonal.

As will be demonstrated in the comparisons to follow, we see that both of these models appear to underestimate the value of the most basic indicator of nonlinearity: the net mean applied force and hence the observed mean horizontal displacement. This mean underprediction may be due to the absence of viscous forces in the models. An asymmetry in the viscous forces, due to the effect of integrating to the time-varying surface, causes a net mean offset of the structure in the wave direction. A third model is thus considered that additionally includes viscous force effects. The viscous forces are found as Morison's drag force integrated from the spar bottom (keel) to the free surface. The drag force is based on absolute fluid velocity with an assumed coefficient of drag $C_D = 0.6$ to reflect large viscous effects in a wave tank. A Wheeler stretching [67] of the water particle kinematics is used above the mean water level.

It may be argued that the disturbed waves, instead of the reference waves (as used in the third model) better represent the wave surface close to the cylinder and as a result will capture the viscous forces effects more appropriately. Recall that the disturbed waves have been measured in the wave tank by a wave probe attached to the deck of the spar. Inclusion of viscous forces from disturbed waves leads to the formulation of a fourth model. We will compare predictions from these four models in the following sections. Reference will be made to the models by names as given in Table 3.5.

Table 3.5: Nomenclature for the four proposed model forms

	Description	Model
1	Base-case model with diffraction forces	DF
2	Model with diffraction forces and wave-drift damping	DF/WDD
3	Model with diffraction forces, wave-drift damping and viscous forces from reference (undisturbed) waves	DF/WDD/VF(u)
4	Model with diffraction forces, wave-drift damping and viscous forces from disturbed waves	DF/WDD/VF(d)

3.2.4 Input Wave Histories for Models

To consistently use the LTFs and QTFs from the diffraction analysis, which assumes the input waves to be Gaussian, we seek to infer consistent first-order wave components from the measured reference waves. We will apply these first-order waves to estimate the diffraction forces on the spar. We use WAVEMAKER [23] to identify the first-order components of the reference waves for each of the three seas: GOM1, GOM2, and NS. The methodology to identify the underlying first-order waves is to seek the implied first-order wave history that, when run through the second-order wave predictor, yields an incident wave that agrees with the target observed history at each time point. This identification is performed using a Newton-Raphson scheme to achieve simultaneous convergence at each complex Fourier component. Details of this identification scheme can be found in Appendix A. Figure 3.5a shows a comparison of the reference wave spectrum for GOM1 seastate being studied here and the identified underlying first-order wave spectrum. Note that, as observed in Chapter 2, the spectral density of the second-order component is significantly smaller (even at twice the peak spectral frequencies) than that of the first-order component, however,

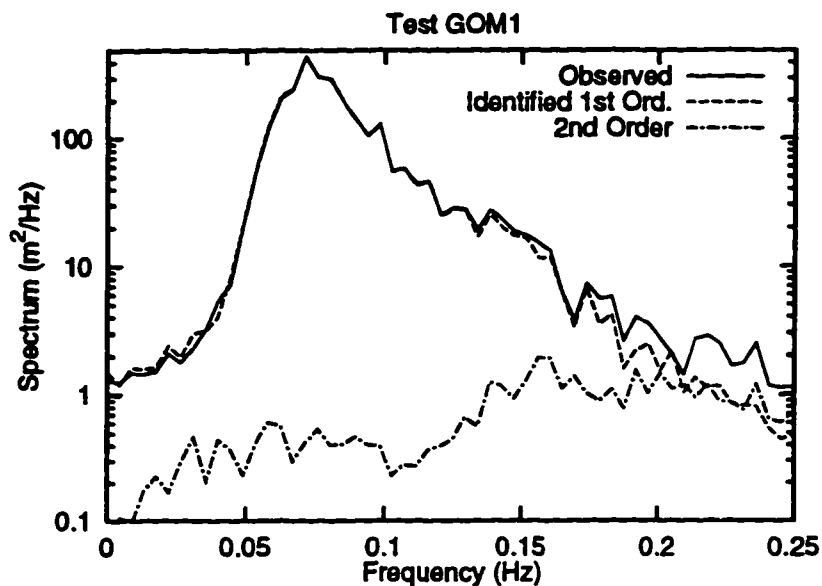
phase locking of the first- and the second-order component (see Fig. 3.5b) leads to larger crests and flatter troughs.

In the DF/WDD/VF(u) model, while diffraction forces are still based on the underlying first-order waves, viscous forces are based on the observed reference waves. In the DF/WDD/VF(d) model, viscous forces are based on the disturbed waves as measured by the airgap probe attached to the spar. Note that the airgap probe, measuring the free surface elevation above the still water level, includes the heave (vertical) motions of the spar. We compensate the airgap measurements for these heave motions to get the time-varying free surface. This inferred wave time history is referred to as disturbed waves.

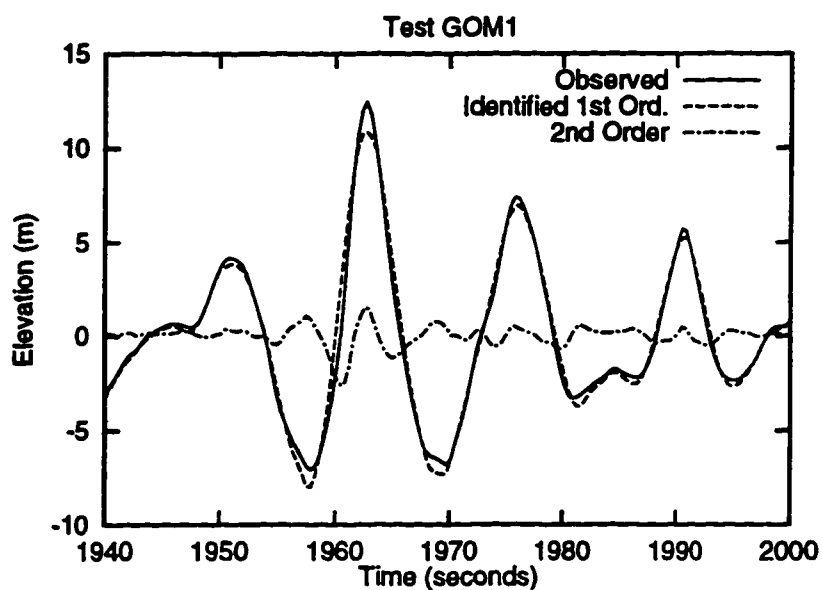
3.2.5 Calibrated Damping Values

As proposed, we iteratively identify the damping ratios ξ_1 and ξ_5 in surge and pitch DOFs, so that the predicted spectral bandwidths in each frequency component simultaneously match measured results. Since GOM1 and GOM2 are two realizations of the same seastate, we find common damping ratios across the seastates for each mode. We do this by tuning ξ_1 and ξ_5 so the bandwidths δ_1 and δ_5 of the predicted spectrum that has been averaged across the two seastates, match simultaneously the bandwidths of the observed spectrum which also has been similarly averaged across the two seastates. Table 3.6 summarizes the calibrated ξ 's for the four models.

Note that if we sought to estimate damping ratios by matching the rms of the response we would expect the damping ratios from the DF/WDD models to be smaller than those of the DF models. We would similarly expect the damping ratios from the VF models to be larger than the WDD model. This is not guaranteed since we are matching the spectral shape (bandwidth); it is comforting, however, to still



(a) Wave Spectrum



(b) Wave History near maximum crest over one hour test

Figure 3.5: Reference (observed) wave vs. underlying first- and second-order waves

Table 3.6: Calibrated damping ratios (%), ξ , for the models in surge (DOF1) and pitch (DOF5) components

Model	GOM1 & 2		NS	
	Surge	Pitch	Surge	Pitch
DF	4.5	1.6	1.7	.001
DF/WDD	3.3	0.6	.001	.001
DF/WDD/VF(u)	4.0	0.5	2.5	.001
DF/WDD/VF(d)	6.5	.001	0.1	.001

see this comparison in the damping ratios. For the NS case, we find that even with $\xi_5 \approx 0$ we are still not able to match the observed bandwidth exactly and the observed bandwidth is still narrower than predicted. This may be due to limited pitch data in the 1-hour measurements or there may be some effects that the model is not able to predict in the pitch motions. This may be the cause for inability of the model to match the noisy bandwidth estimates.

3.2.6 Estimation of Initial Conditions

Finally, we observe the need to include measured initial conditions in our prediction results. Note that a 1-hour measurement includes only about 10 ($\approx 3600/331$) response cycles in DOF1. Note also the time variation of the relative contributions of the surge and pitch components in the different parts of the time history in Fig. 3.4. In the experiments, the measurements were recorded after about 15 minutes (prototype scale) when the wave tank conditions were deemed to have achieved steady-state conditions and hence the spar is not initially at rest. In order to include transient effects and to model these few cycles appropriately, we include measured initial conditions in the predictions. If, instead, the structure were assumed in the prediction to be start from at-rest conditions, these incorrect initial conditions would corrupt

Table 3.7: Estimated initial conditions in surge and pitch DOFs for the three seastates

Sea	Surge DOF		Pitch DOF	
	Displ. (m)	Vel. (m/s)	Displ. (rad.)	Vel. (rad/s)
GOM1	6.09	0.0135	0.188	0.00152
GOM2	4.46	-0.00951	-0.0362	-0.000694
NS	-9.22	-0.0706	-0.254	-0.00171

the predictions, more so in DOF1 response (where we see only a few cycles) than in DOF5 (where we see about $50 \approx 3600/69.9$ cycles).

In order to estimate the initial conditions in the surge and pitch DOFs in each seastate, we need to use the measured horizontal displacements and the measured pitch rotations. The measured horizontal displacement is filtered to obtain the zero-mean surge and zero-mean pitch components. The mean offset is directly found from the measured history prior to imposing any filters. This mean contains the mean offset due to both surge and pitch components. A separate measurement of the pitch rotations is used to find the mean pitch rotation which then is converted to a mean offset due to pitch rotation. Given this pitch mean, we subtract it off from the total horizontal mean offset to get the mean offset due to surge. We add the mean surge and mean pitch offsets back into the filtered zero-mean surge and pitch histories. The initial displacement and velocity in surge DOF is then found from the first two time points of this mean-corrected surge history. Similarly, we find the initial displacement and velocity for the pitch DOF from the first two time points of the mean-corrected pitch history. Table 3.7 gives these estimated initial conditions at the MWL for the three seastates. Note how different they are from at rest initial conditions (zero displacements and zero velocities).

Note that the first-order response is estimated separately and does not depend on

the second-order response calculation. So we, instead, efficiently predict the first-order response in the frequency domain. No initial conditions are forced on the first-order response calculation. Initial conditions will only affect the first few cycles, and will have little impact of the time histories that have hundreds of cycles.

3.3 Results

To investigate the model accuracy, we will compare predicted response moments of the three frequency components: wave-frequency, surge (DOF1) component, and pitch (DOF5) component. This will give an insight into model behavior at the component level. We then will look at the combined (total) surge response to see how well the pieces fit together to yield the combined predictions, i.e., the total predicted horizontal displacement.

3.3.1 Wave-frequency (first-order) Response

Figure 3.6 compares the statistics of the predicted to observed first-order response. These statistics include standard deviation σ_1 , the maximum response normalized by σ_1 , and the absolute maximum response. The first-order response, being primarily inertia dominated, is almost the same for all the four models. The viscous effects are accounted for in the second-order response estimation. Stiffness and damping terms contribute little to the first-order response because the natural periods are far away from the wave-frequency range (see Fig. 3.3). We see reasonable agreement of measured and predicted σ_1 , suggesting that the mass properties, and the LTFs have been modeled adequately. The normalized maximum first-order displacements from predictions also agree with observations. Note the slight overprediction for the GOM

seastates in σ_1 and the normalized maximum displacements. These overpredictions combine to cause an overprediction of the absolute maximum values for the GOM seastates, as seen in Fig. 3.6. The NS first-order prediction seems to agree with observations for all three statistics.

Figure 3.7 shows time histories of the first-order response and shows good agreement in the amplitudes and phases of measurements and predictions. Note the change in the y-axis captions, when viewing Fig. 3.7. Here the first 500 seconds have been shown for convenience; the rest shows similar comparison. An agreement in the time histories confirms the LTF formulation from diffraction analysis and also confirms the identification of the first-order input wave components from the measured undisturbed waves. Since all the four models predict almost the same first-order response, only one predicted history is shown each of the seastates.

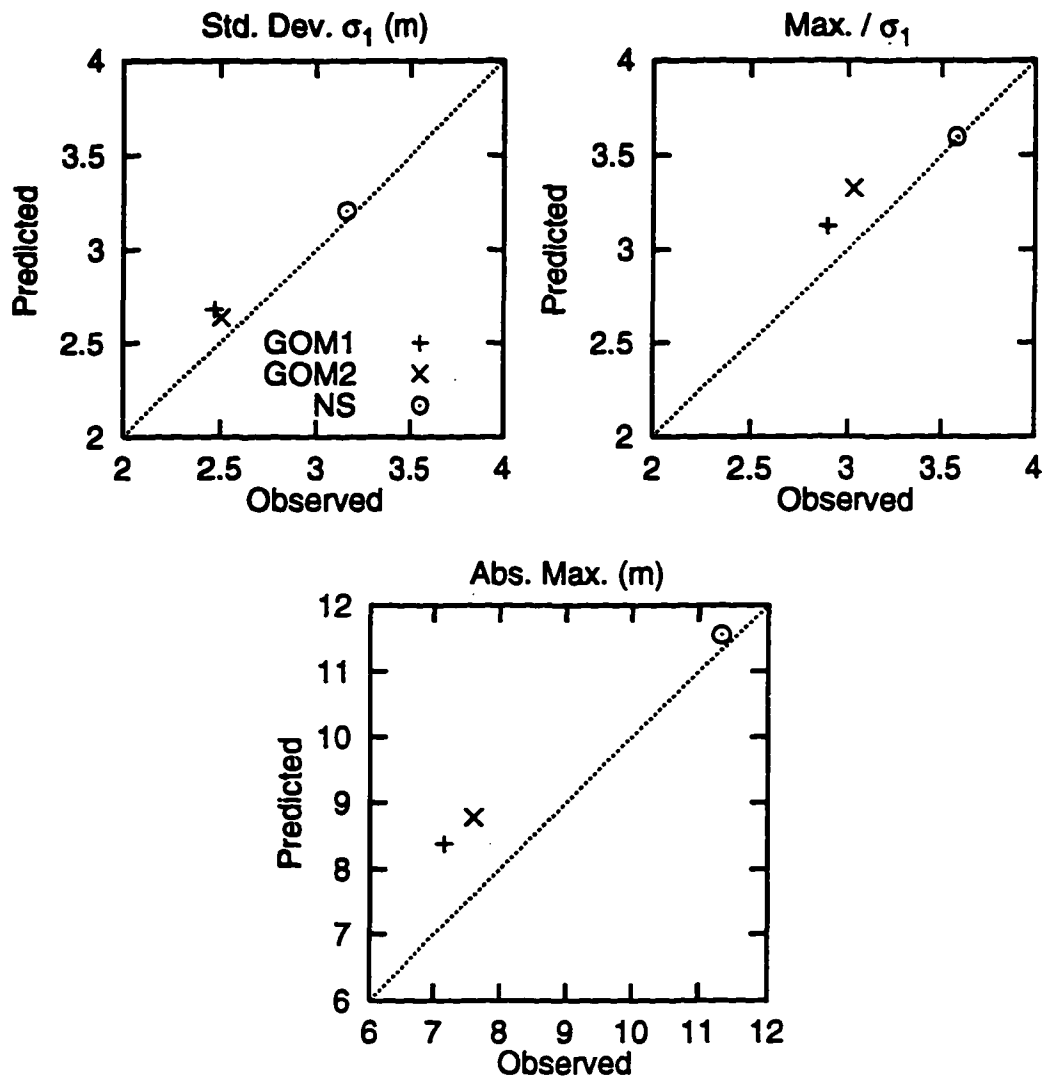


Figure 3.6: Comparison of the first-order (wave-frequency) response statistics: Standard deviation σ_1 (top left), maximum normalized by the standard deviation (top right) and absolute maximum displacements (bottom)

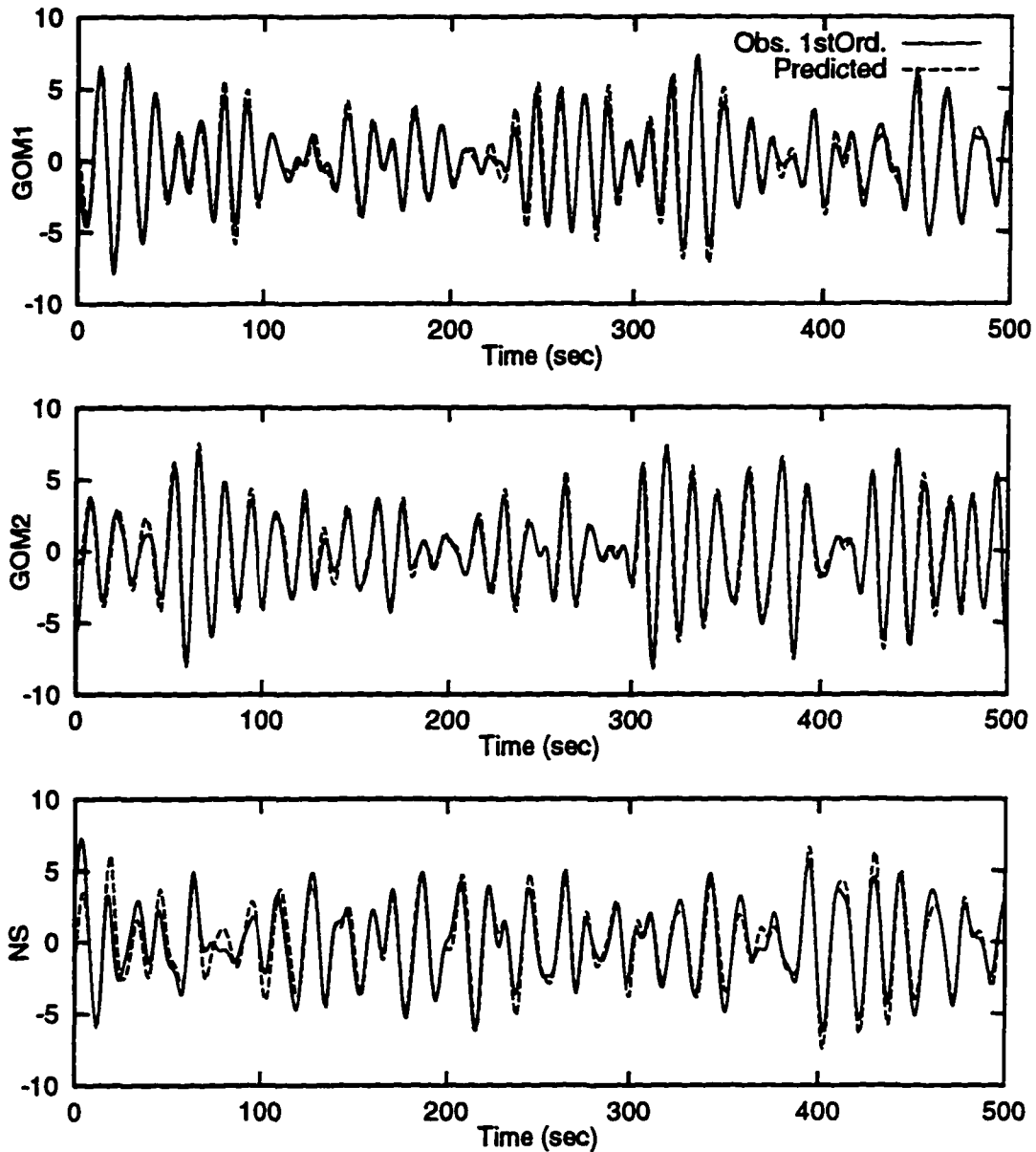


Figure 3.7: Comparison of predicted first-order response time histories to measurements across the three tests. Agreement is similar over all portions of the 1-hour tests, for clarity only the first 500 seconds of each test is shown here.

3.3.2 Surge (DOF1) and Pitch (DOF5) Component Responses

Figure 3.8 compares the predicted statistical moments to the corresponding observed values. For each moment, the observed value for each seastate appears on the X-axis, and the predicted values are shown on the Y-axis. Note that we use three symbols on the X-axis to indicate the observed values in the three seastates. See Tables 3.3 and 3.4 for numerical values of these moments. For each symbol on the X-axis, we have four model predictions each shown using a different symbol. Consequently, in one plot we should see four symbols aligned vertically, for every symbol on the X-axis, indicating four model predictions for every observed value. Each of the model predictions is shown using the same symbol across the three tests, in order to gauge the model predictions across tests. Perfect prediction is shown as a 45 degree dotted line on each plot.

As noted previously, we find here that the DF and DF/WDD models underestimate the total mean offset in surge (see Fig. 3.8). However, as also was anticipated, inclusion of viscous forces considerably improves the agreement in the predicted mean offsets. Use of disturbed waves in the VF(d) models yields, in all three tests, a slightly larger mean offset than the VF(u) model. Note that in the plot the observed mean offsets for each of the three seastates (see Table 3.3) have been marked on the X-axis (observed axis) by three different symbols. A difference in the observed values for GOM1 and GOM2 indicates the level of observed scatter to be expected when comparing model predictions to measurements.

In Fig. 3.8, a comparison of σ_{DOF1} and σ_{DOF5} , the standard deviations in the surge and pitch frequency components, shows that on average the DF model underpredicts the rms of the response. The largest DF underprediction in σ_{DOF1} , which in the case of the NS, is about 40% of the observed value. This is also the case for GOM2.

σ_{DOF5} seems only slightly underpredicted by the DF model for GOM1 and GOM2; however, σ_{DOF5} appears to be overpredicted by the DF model for the NS case. This may be due to the noisy estimate of the pitch damping ratio ξ_5 . Recall that in the NS seastate, ξ_5 is close to zero, but still the predicted spectral bandwidth was broader than observation.

In general, the underprediction in the standard deviations becomes slightly more severe on inclusion of wave-drift damping (DF/WDD model). Inclusion of viscous forces from either the disturbed or the reference waves leads to better agreement in the σ 's. From the plots, it may be argued that the VF(d) models gives better agreement in σ 's than the VF(u) model when compared across the three seastates. Note how close the VF(d) prediction is in all the three tests for both σ_{DOF1} and σ_{DOF5} , except for σ_{DOF1} in GOM2. This discrepancy for GOM2 still appears to be within the observed scatter in the rms response (difference in the rms value for GOM1 and GOM2).

Instead of comparing the predicted skewness and kurtosis values, we will directly look at the maximum response in each frequency component. We will first look at maximum displacement normalized by the rms response for each component. Note that the filtered components have zero mean in all comparisons to follow. A normalized maximum comparison will give a sense of the tail prediction by the models independent of the rms comparisons. Finally, we will look at the absolute values of hourly maximum displacements. In Fig. 3.9, the top figures compare the normalized maximum values for the two frequency components. In both the components, all predictions, in general, show good agreement with observations for GOM1 and GOM2. In the NS case, however, surge (normalized) maximum seems to be overpredicted by almost 35% for all models. We will investigate this issue when comparing

the response time histories of the surge component. Results for the absolute maximum displacements for each component can be anticipated from comparisons of the standard deviations and the normalized maximum displacements. For the maximum surge, we may anticipate that the maximum value comparisons will be similar to the rms comparison, since the normalized maximum value is well predicted in this case. The bottom-left plot in Fig. 3.9 confirms this. As may also be anticipated, the maximum response comparison in the NS case shows a large scatter in across model predictions. The underpredicted rms seems to compensate the overpredicted normalized maximum displacement in the VF(u) model so that it is closest to the observed maximum response in the NS case, while other models either underpredicted or overpredict severely the observed NS maximum surge displacement.

The bottom-right plot in Fig. 3.9, shows similar results for pitch frequency component. Here, we find the VF(d) model to yield the closest agreement to observation. The other prediction models, also yield good agreement (largest discrepancy of 12%) for the GOM seas, while they underpredict the maximum pitch response in the NS case by about 30%.

Figure 3.10 compares the measured and predicted time histories filtered to include only the DOF1 frequency range. The filtered DOF1 results for all three tests (see the Y-axis caption) along with the corresponding predictions from the DF and the DF/WDD/VF(d) models. Note how few surge (DOF1) cycles are observed in the 1-hour duration, and consequently, as noted earlier, the potential difficulty in using these few cycles to tune the prediction models. Reasonably good agreement is seen between the measured and predicted time histories for all three tests, except in the case of the VF(d) model for NS. Note how close the predicted surge is in the GOM1 case over almost the entire duration. For GOM2 the observed surge shows a general

decay in amplitude until about 1500 seconds following which we see large surge cycles. This general trend seems to be shown by both the prediction models as well. For the NS, however, the DF model prediction seems to underpredict the surge response at almost all time points and the VF(d) model seems to give better agreement with observed results. In the last two cycles, however, the VF(d) model appears to overpredict the surge amplitudes. Note that the predicted surge from either models is in phase with the observed surge, more so in the VF(d) case than in the DF case.

A comparison of the pitch (DOF5) time histories from measurement, the DF model and the DF/WDD/VF(d) model is shown in Figs. 3.11, 3.12, and 3.13. We will first focus on the GOM1 pitch histories in Fig. 3.11, where for convenience, the first half hour is shown on the top plot and the second half hour is shown in the bottom plot. A comparison of amplitudes and phases across the entire histories shows that the predicted pitch from both the models tends to generally follow the observed amplitudes, and occasionally disagrees in phase. For example, the DF model agrees with observed phase until about 1000 seconds and gradually goes out of phase around 1600 seconds and comes back in phase around 2000 seconds. The VF(d) prediction follows a similar in-out phase agreement, however, the disagreement seems less severe than the DF model. See, for example around 3000 seconds, while the DF model is completely out of phase, the VF(d) is still in phase with observation. Also, notice around 500 seconds, the VF(d) agrees with observed amplitudes much better than the DF model.

Similar, observations can also be made for the GOM2 and NS tests. It, generally, appears that the VF(d) predicted amplitudes and phases agree with observed results better than the DF model.

Recall that we incorporate measured initial conditions for each of surge and pitch

components, when predicting response. The input initial conditions for each DOF at the mean water level result in a net initial condition at the measurement point (54.8 m above the MWL). We show in Fig. 3.14, that indeed the prediction model preserves the net input initial conditions. Here we show the initial portions of the net horizontal displacement due to the surge and pitch components from observation and from prediction models: DF and DF/WDD/VF(d). Recall that the first-order or wave-frequency component is found from frequency domain analysis with no input initial conditions. Fig. 3.14 shows that we identically reproduce the net initial conditions in all the three tests and in the two prediction models. This is also true for the other two predictions not shown in this figure.

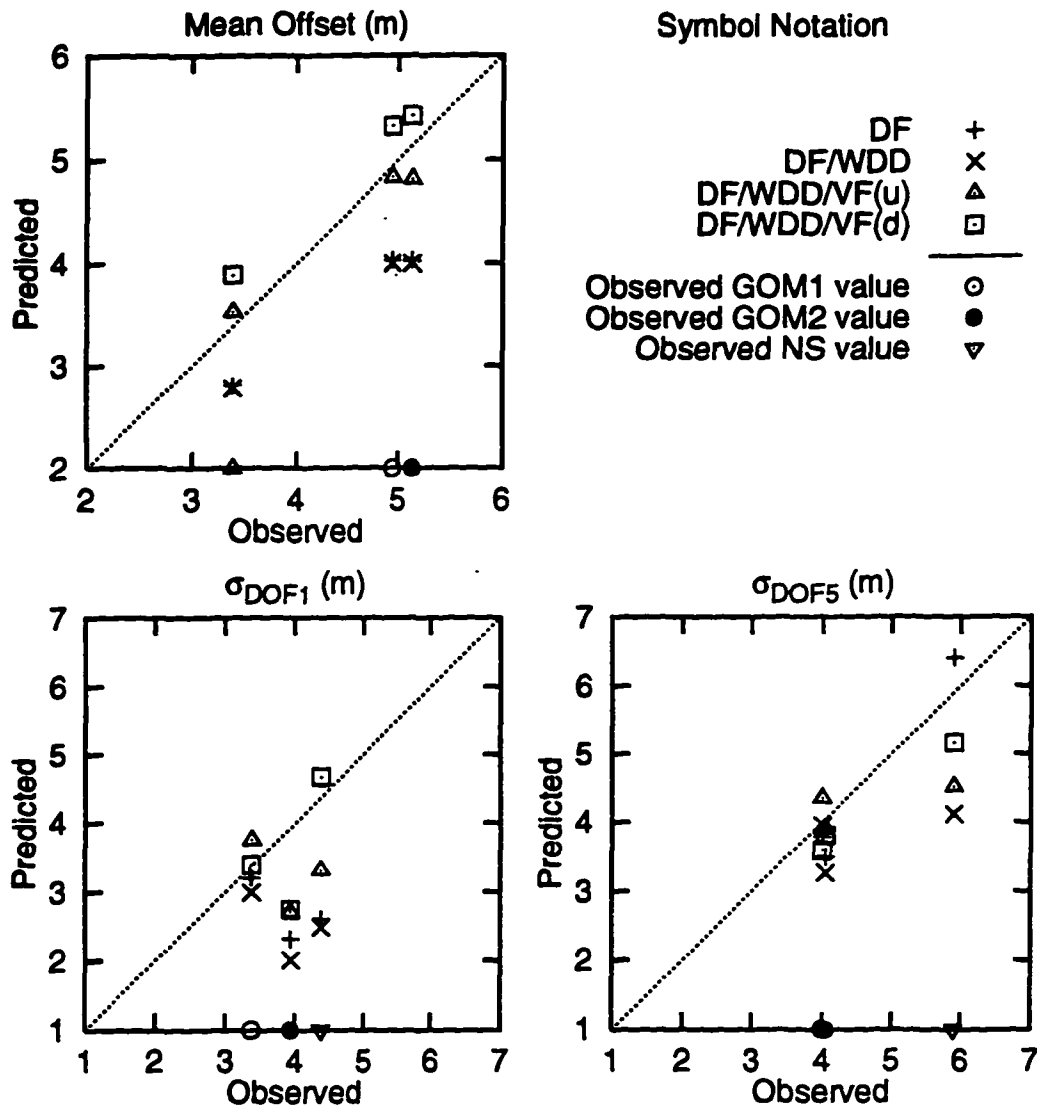


Figure 3.8: Comparison of statistical moments for surge and pitch components in the three seastates: Predictions from the four models vs. measurements. The moments include total mean, and standard deviations in surge and pitch frequency components (see titles in the figure).

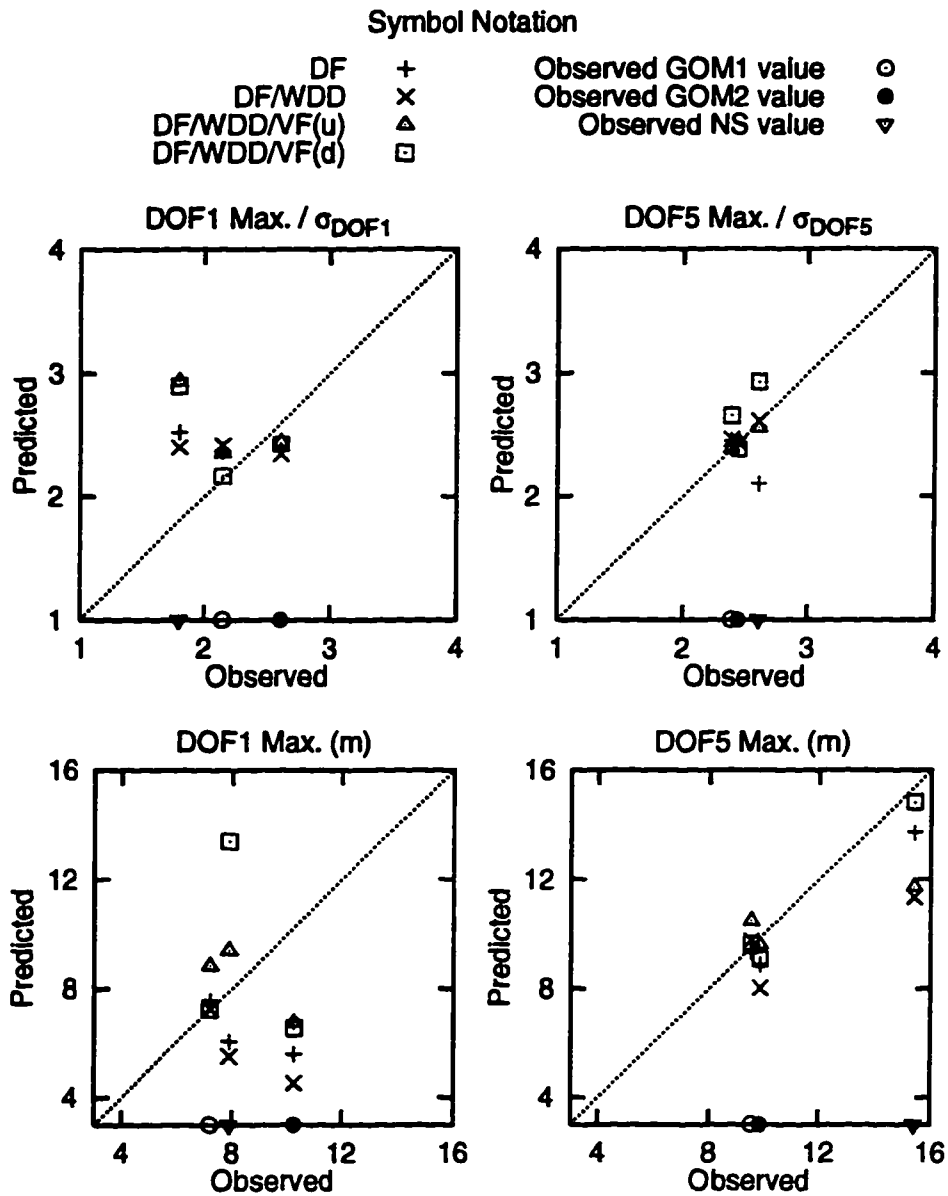


Figure 3.9: Comparison of statistical moments for surge and pitch components in the three seastates: Predictions from the four models vs. measurements. The moments include maximum normalized by the standard deviation and the absolute (unnormalized) maximum displacements in each of surge and pitch frequency components (see titles in the figure).

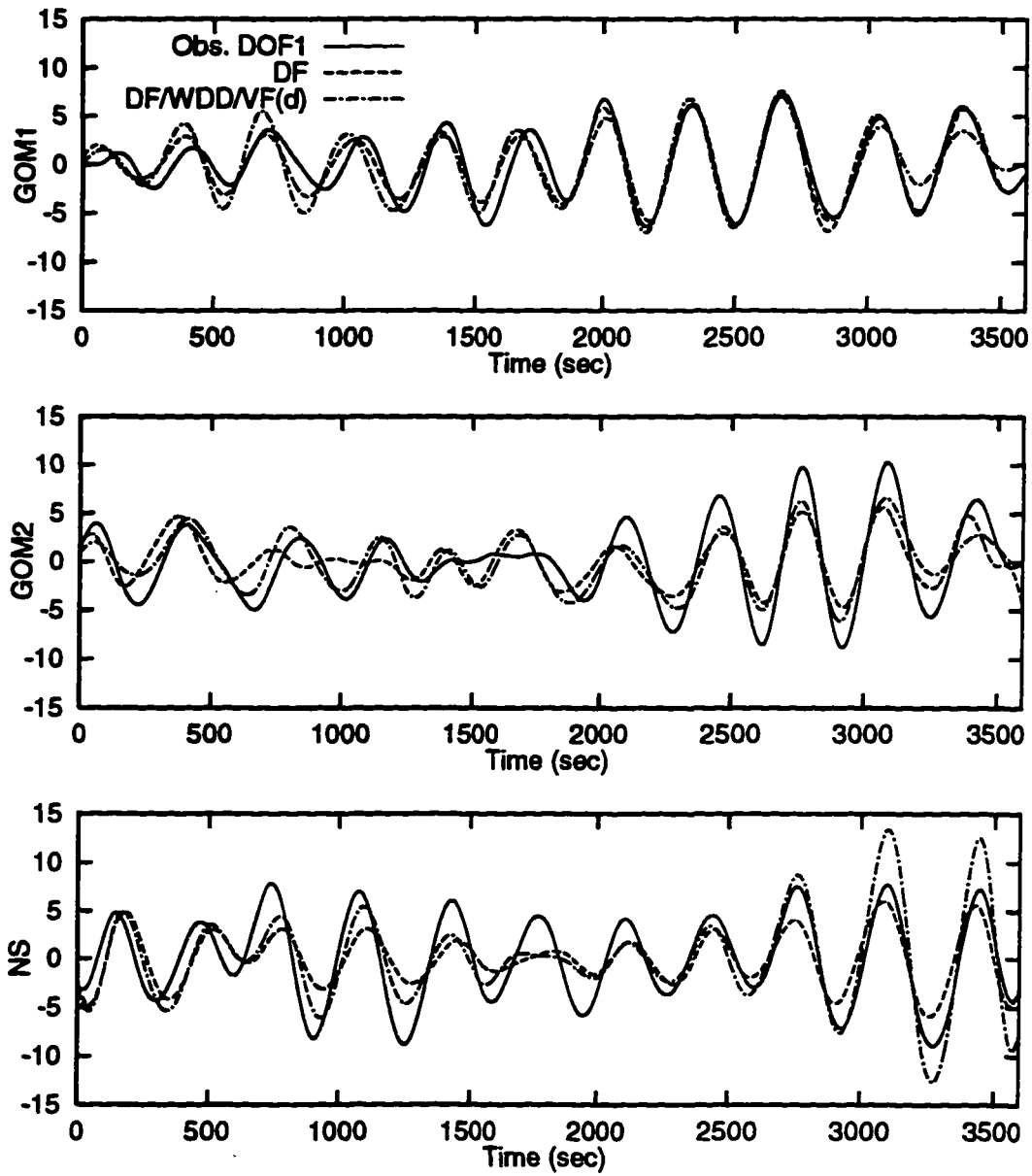


Figure 3.10: Comparison of (zero-mean) response time histories in DOF1: prediction vs. measurement

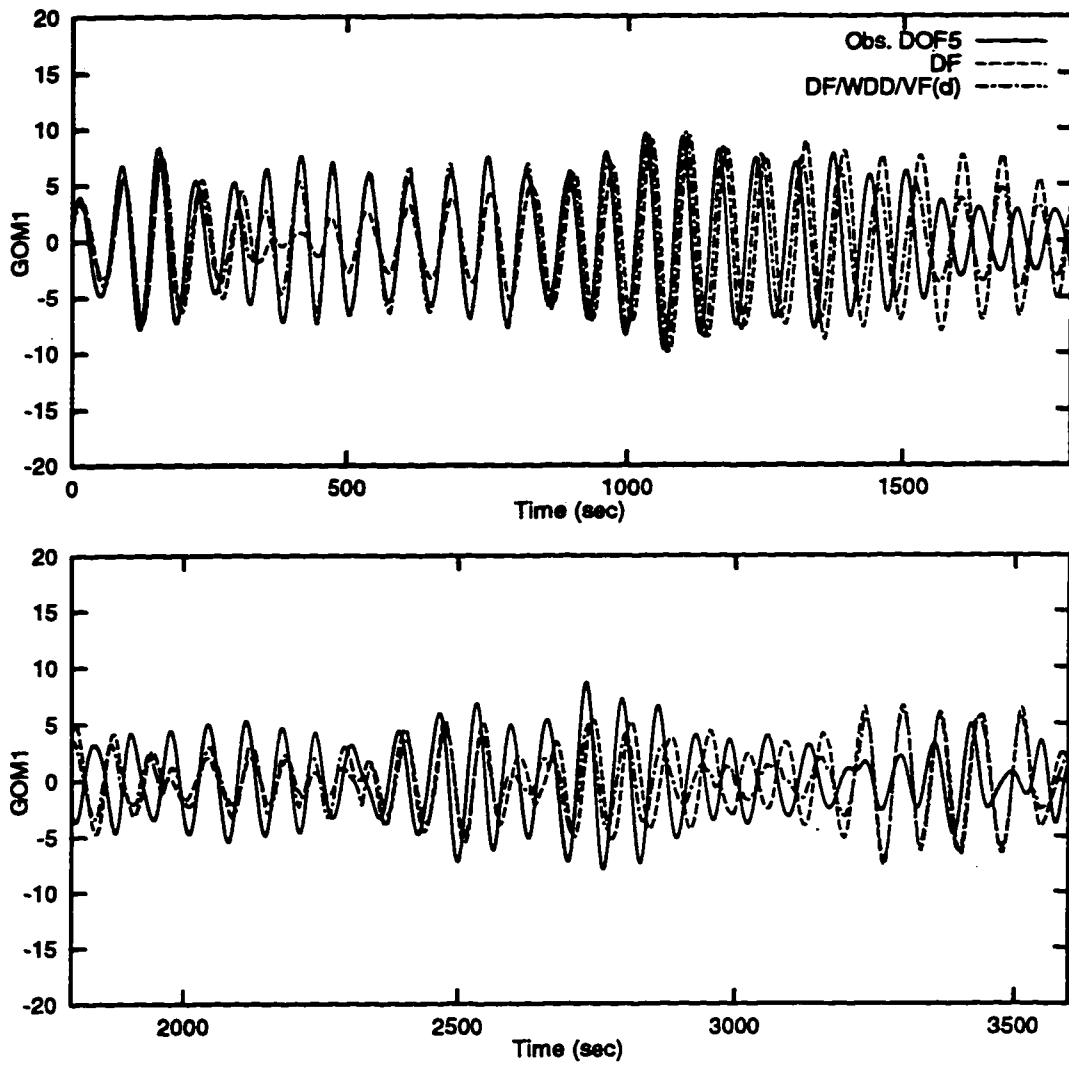


Figure 3.11: Zero-mean pitch (DOF5) time histories for GOM1: prediction vs. measurement

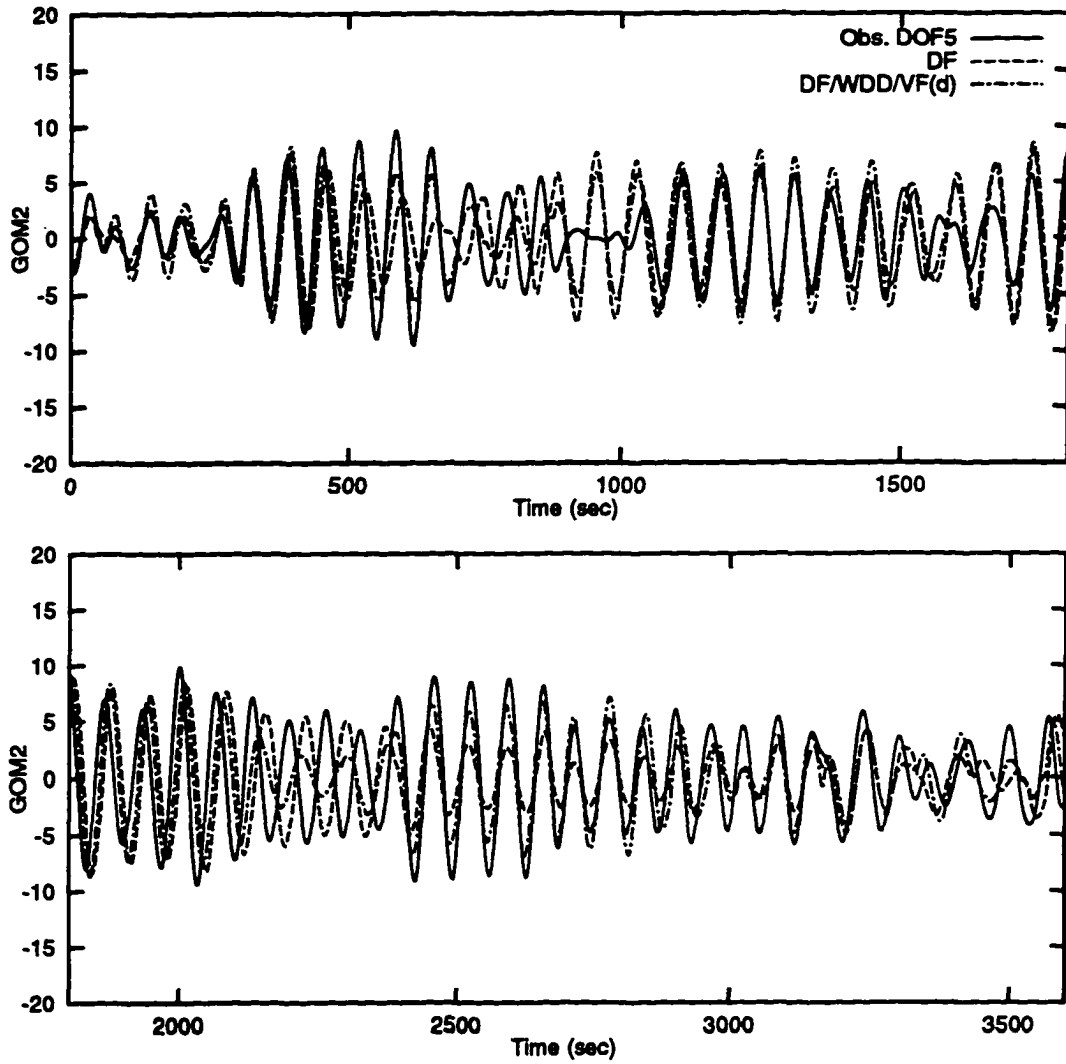


Figure 3.12: Zero-mean pitch (DOF5) time histories for GOM2: prediction vs. measurement

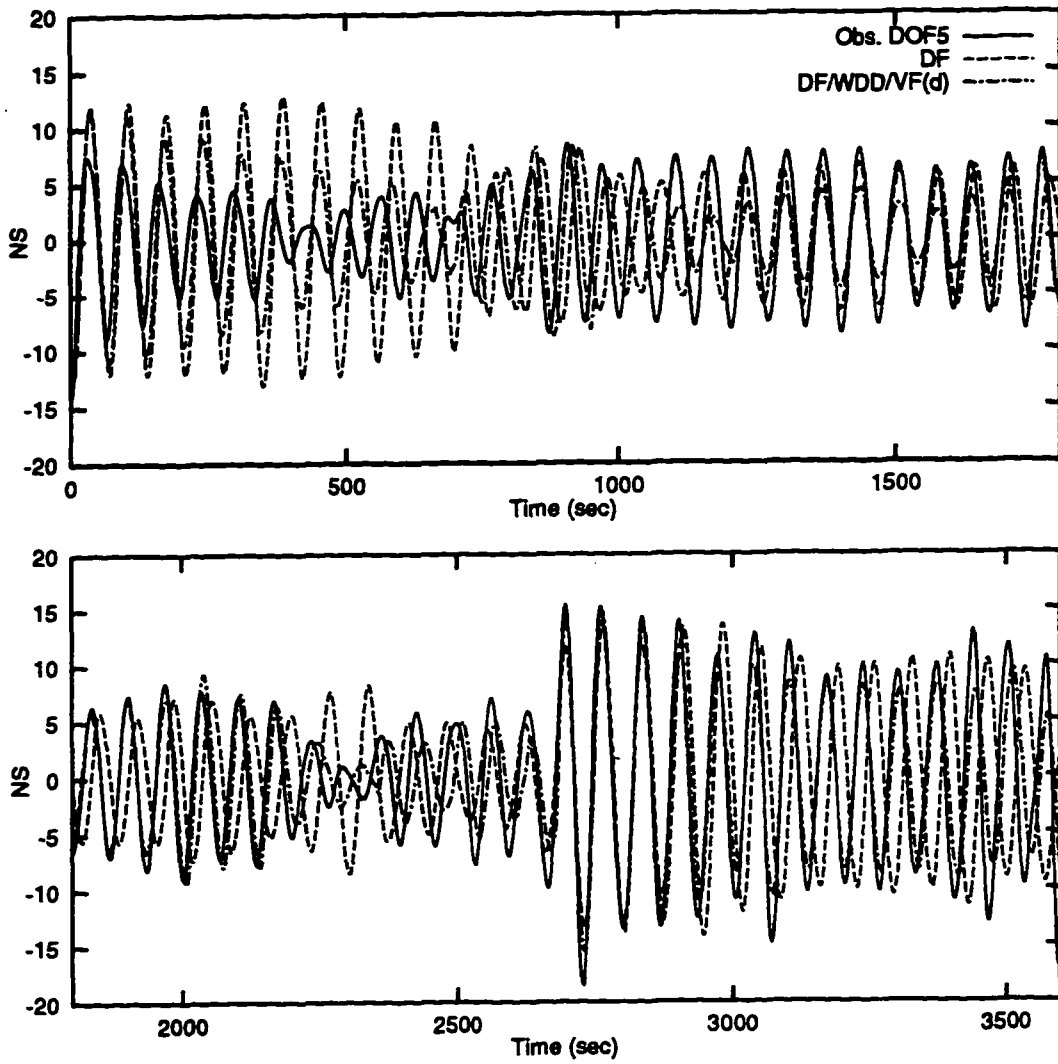


Figure 3.13: Zero-mean pitch (DOF5) time histories for NS: prediction vs. measurement

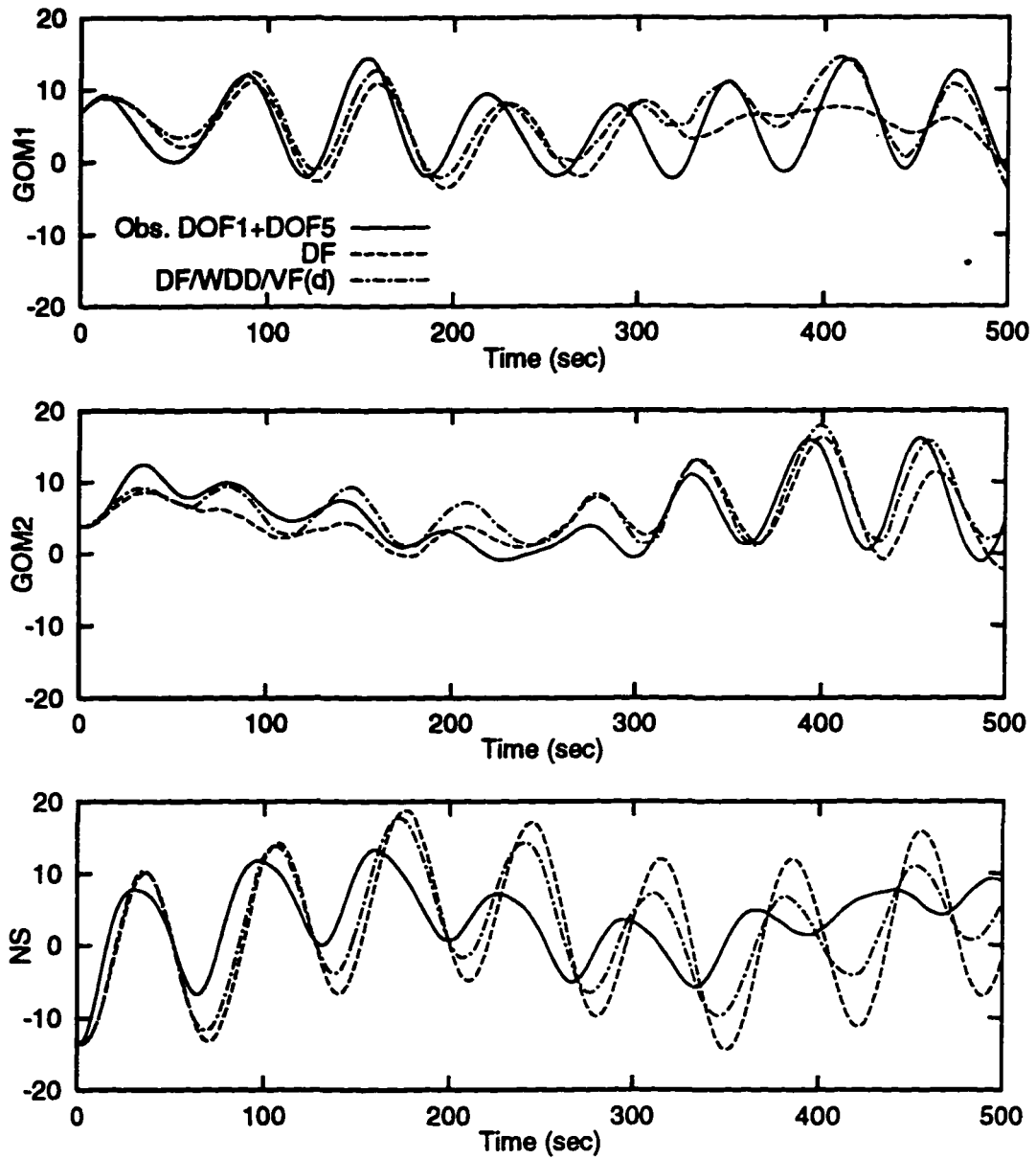


Figure 3.14: Second-order (=surge+pitch components) predicted and measured response to indicate preservation of net input initial conditions found from observed histories

3.3.3 Total Predicted Horizontal Displacement

Finally, we add all the predicted components together to get the total predicted horizontal displacement and compare to measurements. We add the three predicted components (wave-frequency, surge and pitch) time point by point to get a time history of the total horizontal displacement or what we may take as the total or combined response. Since the surge and pitch contributions to total surge response is significantly (as seen in Table 3.4) more than the first-order response, we may anticipate similar comparisons at the total response level as we did in each of surge and pitch component comparisons in Sec. 3.3.2. Note that the variance of the total response σ_t^2 is simply the sum of the variance of each of the three components ($=\sigma_{\text{DOF1}}^2 + \sigma_{\text{DOF5}}^2 + \sigma_1^2$). Fig. 3.15 compares predicted and observed σ_t , where the VF(d) model appears to give the closest prediction of all, with a slight disagreement (underprediction of about 12%) on the GOM2 case where it still seems within the observed scatter in GOM1 and GOM2. The normalized maximum displacement (bottom-left figure in Fig. 3.15) shows a similar result as seen for the surge component case (in Fig. 3.9). This is because the other two contributing components (pitch, and wave-frequency) generally show good agreement in the normalized maximum displacement comparisons (see Figs. 3.6 and 3.9). Finally, the bottom-right plot in Fig. 3.15 reports the maximum horizontal displacement of the total response. We find that the DF/WDD model predicts smaller maximum response levels than the DF model, and inclusion of viscous effects makes the agreement better.

A qualitative comparison of the predicted and measured combined time histories is shown in Figs. 3.16, 3.17, and 3.18 for the three seastates, respectively. We will first look at the GOM1 test in Fig. 3.16. As noted previously (in Fig. 3.4), the measured displacement shows a transition in the response around 1500 seconds (from visual

inspection). The prediction models also show a similar transition: the DF and VF(u) models around 1800 seconds, and the VF(d) also around 1500 seconds. Also around 500 seconds, the general nature of the prediction differs among the three models. Here again, the VF(d) model seems to better compare with the measurements. Similarly, for the GOM2 test in Fig. 3.17, the predicted amplitudes and phases generally follow the measured results in the top plot. The prediction models appear to have different frequency-component contribution around 2500 seconds, and of these the VF(d) model seems to be closest to measurements. Finally, for the NS case in Fig. 3.18, the prediction models predict similar displacements after about 2500 seconds. From about 1000 to 2500 seconds, we find absence of the low-cycle or surge frequency components when compared to the measured result. This was also seen in Fig. 3.10 where the predicted surge component is very small compared to the observed component. For the VF(u) model, it seems that in the same time range (100 to 2500 seconds) even the pitch component is underpredicted, and the total predicted displacement is predominantly first-order.

The prediction models, in general, seem to predict the GOM1 and GOM2 test results better than in the NS case. Recall the difficulty in calibrating pitch damping ratios for the NS case (that turned out to be almost zero).

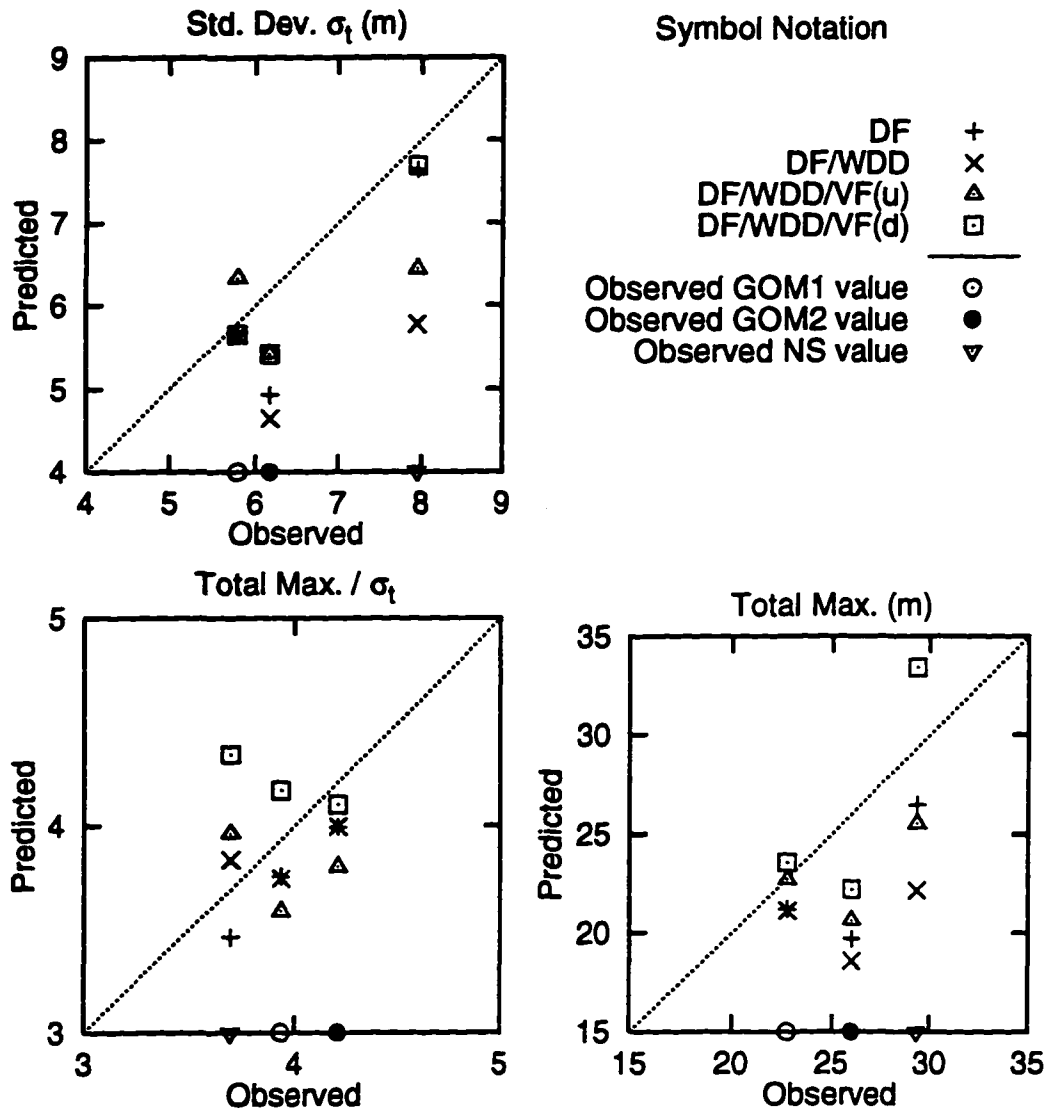


Figure 3.15: Comparison of standard deviation and maximum of combined response: prediction vs. measurement

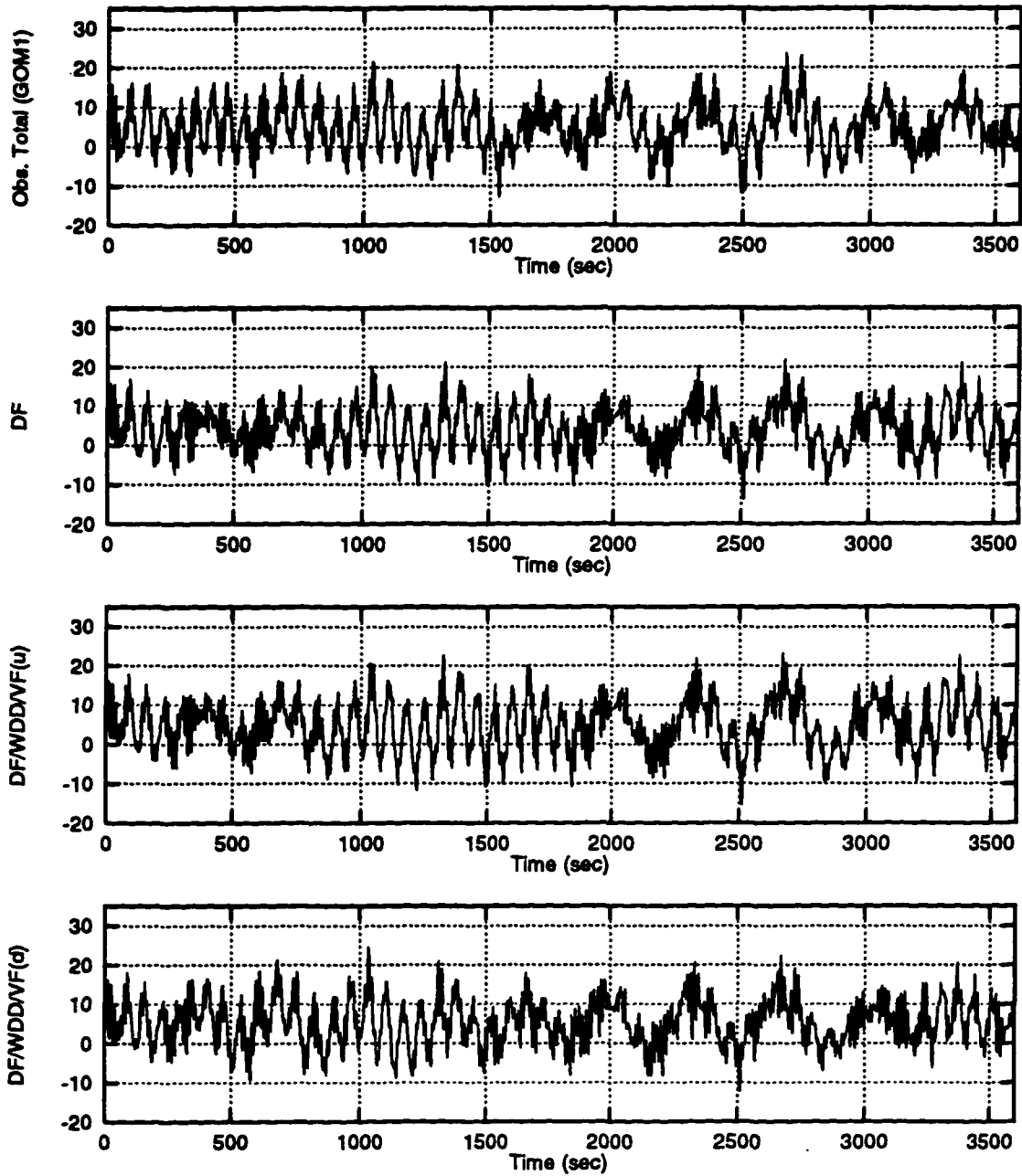


Figure 3.16: Combined (total) surge response time history for GOM1: prediction vs. measurement

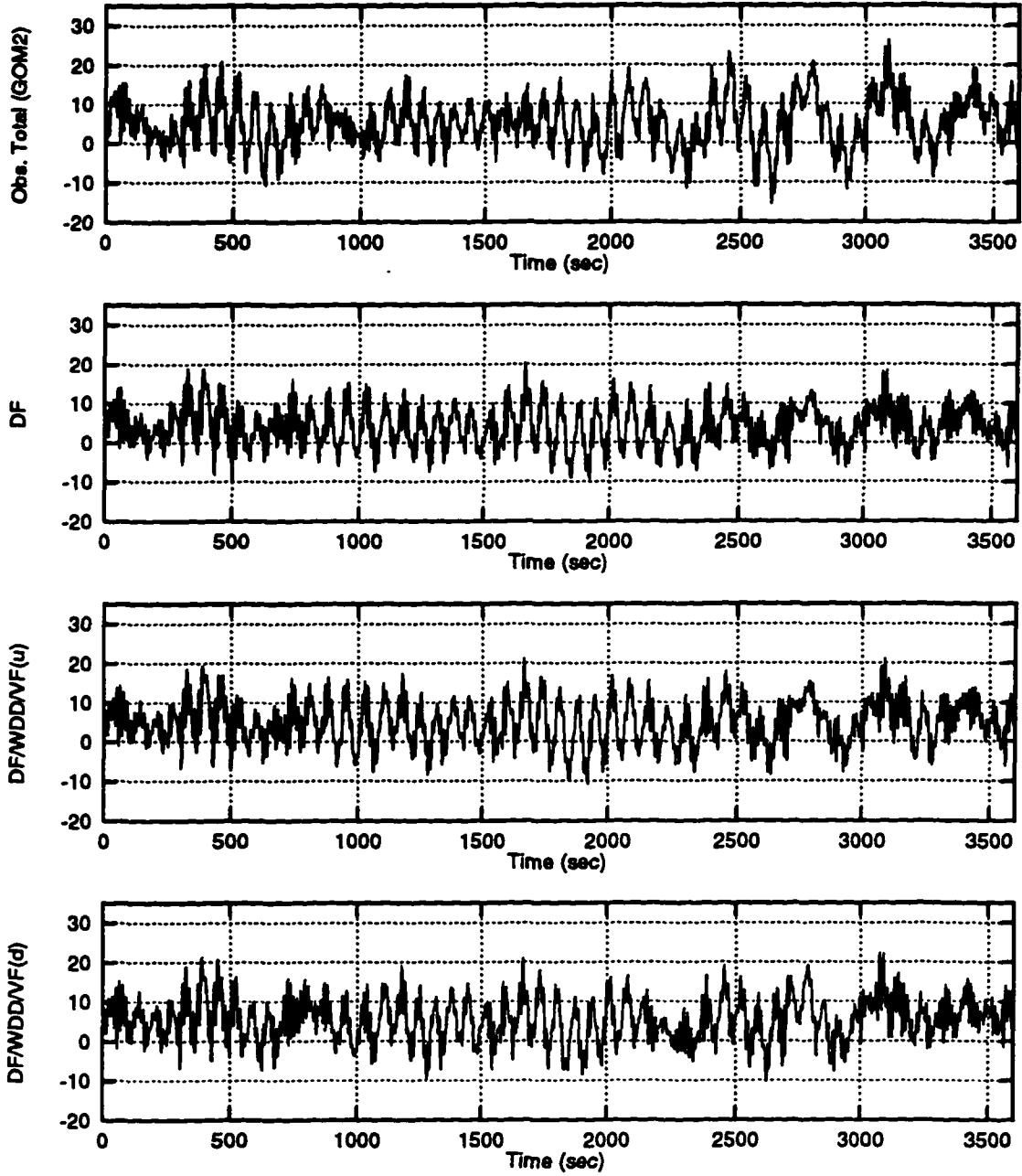


Figure 3.17: Combined (total) surge response time history for GOM2: prediction vs. measurement

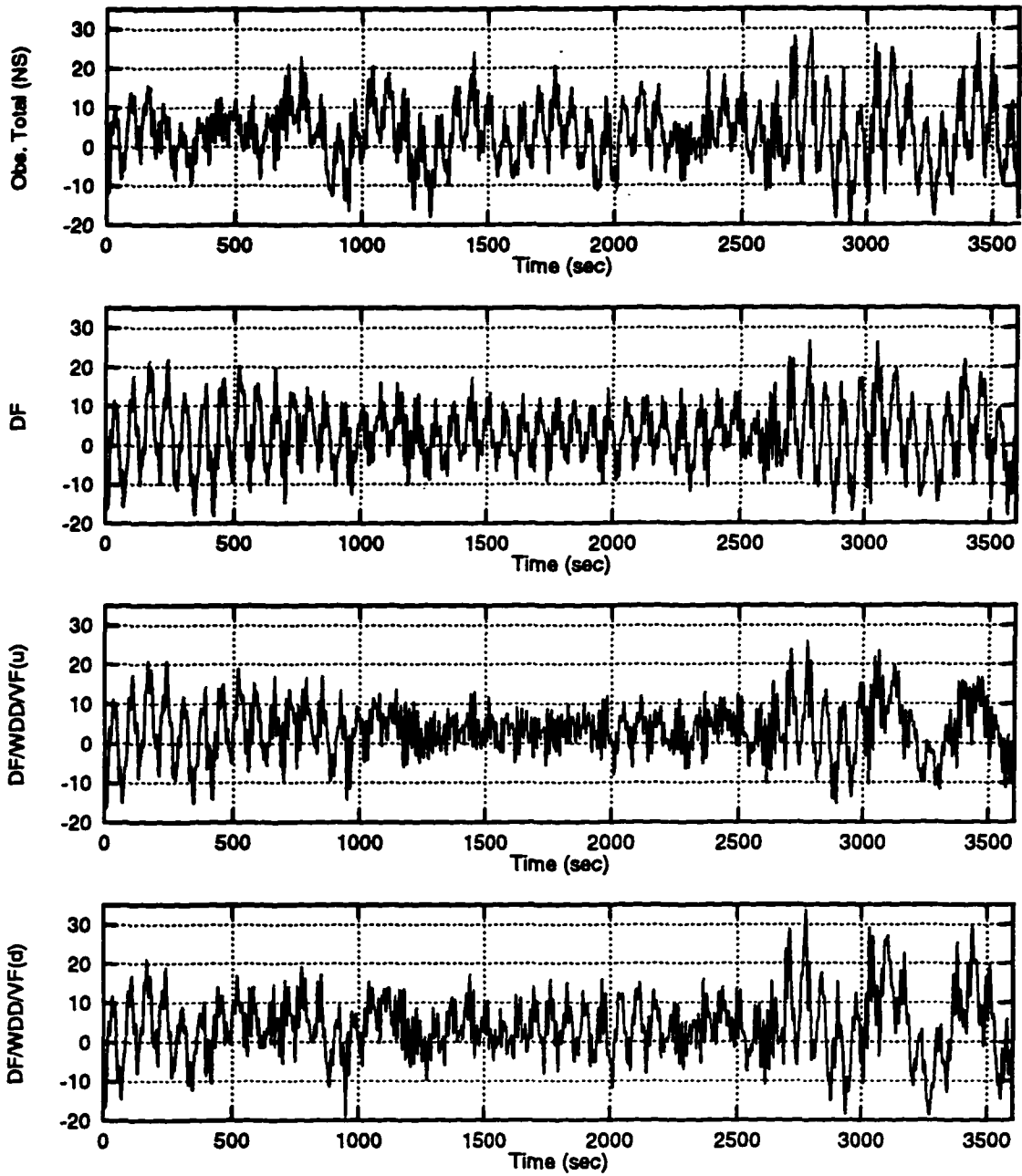


Figure 3.18: Combined (total) surge response time history for NS: prediction vs. measurement

3.4 Conclusion

In order to predict the global response of a spar platform, we used different hydrodynamic force models and applied it to a linear rigid-body model of the spar. Such models have been applied earlier to other large-volume floating structures. Existing studies on the spar, however, do not appear to systematically compare model predictions in the case of random sea measurements.

Geometry considerations led to the development of the rigid-body structural model and the incident forces were modeled as second-order diffraction forces. We incrementally added other hydrodynamic effects, for example: the wave drift damping, and viscous forces on the spar (from disturbed or undisturbed waves) in order to better match model predictions to data. For the damping characteristics (over and above the added/diffraction damping and wave drift damping) of the spar, we calibrated the damping ratios in each of the two contributing modes (surge and pitch) so that the predicted spectral bandwidth matched observed results.

The limited number of response cycles (in surge) and the apparent “mode-swapping” in the measured horizontal displacements posed practical difficulties in calibrating the prediction models to the measured results. We applied measured initial conditions in an effort to better predict such transient characteristics.

The prediction models generally appear to give good agreement with the measured results. The comparisons were based on the moments (mean, standard deviation and maximum displacement) of the predicted and measured time histories, as well as on direct comparison of the time histories itself. Such comparisons were made for the total displacement histories and its filtered components (surge, pitch, and wave-frequency) across the three random sea measurements (reflecting severe storm conditions) in the wave tank.

We surveyed four prediction models: (1) nonlinear diffraction forces only, (2) diffraction force plus wave drift damping effect, (3) model 2 plus additional viscous forces due to undisturbed waves, and (4) model 2 plus viscous forces from disturbed waves. The diffraction force model seemed to underpredict the observed mean offset, inclusion of viscous effects then better predicted the mean offset. The four models generally give good agreement with observed results and even appear to predict the apparent mode-swapping seen in the observations.

Chapter 4

Nonlinear Ship Loads: Stochastic Models for Fatigue Analysis

4.1 Introduction

Fatigue cracking in ship details can lead to much expensive repair and should be considered in design of structural elements. A ship is typically designed to have a service life of about 20 years, during which it undergoes millions of load cycles that may result in fatigue cracks. In general, the fatigue hot spots can be at the ship bottom, the side shell, or in the main deck. A Swedish study conducted on 85 ships (see [43]) for damage due to cracks, deformations, and corrosion suggested that about 70% of the damage was due to fatigue.

Existing recommendations (see [1, 8]) for fatigue analysis and design (outlined in the following sections) either tend to be limited in accuracy of load analysis and hence fatigue damage, or are prohibitive in terms of computational resources. The study here suggests an approach that efficiently uses state-of-the-art nonlinear ship analysis

tools to accurately predict fatigue damage without the heavy computational burden. This method also finds application in fatigue analysis of side shells [15] and in extreme ship-response analysis [69].

4.2 Ship Model

The fatigue reliability studies presented here are demonstrated for ships and in general should be applicable to any offshore structure that responds primarily in a quasi-static manner to the wave loads. We focus here on a monohull ship with flared cross-sections. A body plan and a strip model of this ship are shown in Figure 4.1 and the main particulars of the ship are given in Table 4.1. The cross-section of the ship changes along the length of the ship with flared cross-sections at the ends of ship and box cross-sections towards mid-ship (see Fig. 4.1b). The ship-equipment mass and the ship dead-weight cause nonuniform mass distribution along the ship. A ship moving in the waves is subjected to many kinds of loads: vertical and horizontal bending moments, torsional moments, side shell intermittent water pressures, etc. In this study we consider only the mid-ship vertical bending moments (or equivalent mid-ship bending stresses) as loads on the ship (see Fig. 4.2). The sagging condition causes tensile stresses in the ship bottom, while the hogging condition may extend fatigue cracks in the ship deck. Lateral side shell or torsional loads are not considered in this study; however, the methodology developed here should be equally applicable for these loads as well.

The ship is assumed to be rigid and respond to the wave loads in heave and pitch degrees of freedom. We use a strip theory analysis program NV1418 [6, 13] to perform a time domain estimation of the ship loads. This program is limited to

Table 4.1: Main Particulars of Ship presented in Fig. 4.1

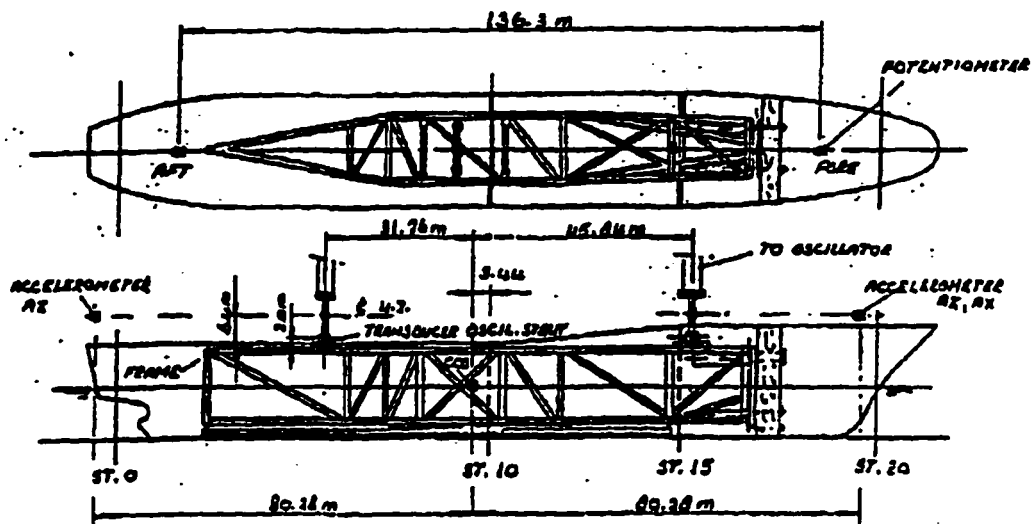
Specification	Value
Length between perpendiculars	166m
Beam	24.65m
Draught	8.85m
Weight	2×10^5 kN
Waterplane Area	2.84×10^3 sq.m

head seas loads. While no slamming or water on deck are considered, we integrate the water pressures to the exact wetted surface to find the rigid body forces on the ship and the resulting mid-ship bending moments. The pressure integration to the instantaneous wetted surface, and the flared hull cross-section, contribute primarily to the nonlinearity in the ship loads. The sag bending moments are typically larger than the hog bending moments, for example. A linear analysis, on the other hand, is based on the assumptions of small ship oscillations and, consequently, the bending moments do not show any nonlinearity (see Sec. 4.4.1).

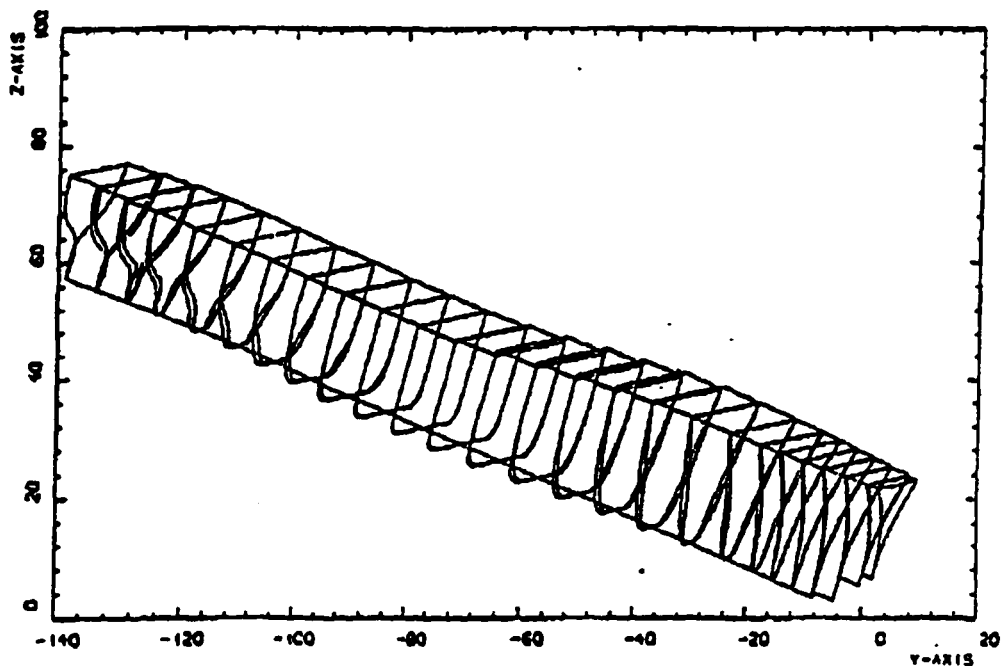
4.3 Stochastic Fatigue Analysis

A general approach to fatigue analyses in reliability-based fatigue design, is to use available fatigue test data [52]. Typically, in fatigue tests a specimen undergoes constant amplitude S cyclic loading and the number of cycles N to “fail” is recorded. A linear fit to $\log S$ vs. $\log N$, called an S - N curve, provides the following relation:

$$N = CS^{-b} \quad (4.1)$$



(a) Body Plan



(b) Strip Model

Figure 4.1: Model of monohull ship that will be analyzed using strip theory

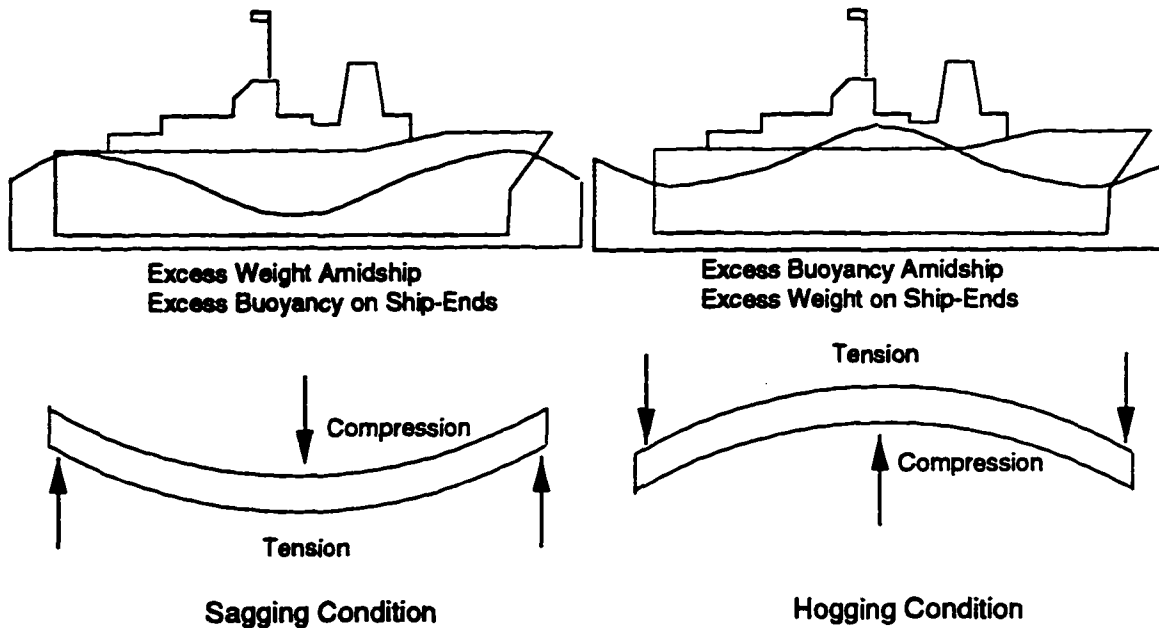


Figure 4.2: Sag and Hog Bending Condition of Ship in Waves

where C and b are the intercept and the slope of the fitted curve. This relation gives the mean number of stress loading cycles N with amplitude S that a fatigue specimen can tolerate before failing [14]. The material factor C , in general, shows a large scatter (coefficient of variation on the order of 50 to 60%). Typical values of the exponent b for steel material may be 3–6, and may be as high as 7–10 for composite materials. Values of S – N parameters for offshore structure materials and their uncertainties can be found in various literature, including API [2] and SSC reports [43] among others.

For real structures, however, the loading is random in nature and we need to relate the random stress amplitudes to the number of cycles to fail. The Palmgren-Miner linear cumulative damage hypothesis [14] may be used to apply the S – N relation to estimate the fatigue damage from a random stress history. Linearity of this hypothesis lies in the absence of any sequence effects of the random stresses. The hypothesis

estimates the mean damage due to a single stress cycle with amplitude s to be $1/N_s$, where $N_s = Cs^{-b}$ is the mean number of cycles to fail at stress amplitude s . Thus, according to this hypothesis, the mean damage \bar{D} in N cycles from a random stress history, whose stress amplitudes have probability density function $f_S(s)$, is

$$\bar{D} = \int_0^{\infty} \frac{N f_S(s)}{N_s} ds = \frac{N}{C} \int_0^{\infty} s^b f_S(s) ds = (N/C)E[S^b] \quad (4.2)$$

where $N = \nu T$ is the number of stress cycles in a given duration T due to a stress cycle rate ν . The mean value of the b -th power of S can be found once its distribution $f_S(s)$ is known. Note that $E[S^b]/C$ is the mean damage per cycle, and $\nu E[S^b]/C$ is then the mean damage rate (damage per unit time) which when multiplied by a duration T gives the mean damage \bar{D} in T . For high-cycle rate applications, variations about the mean damage per cycle will average out quickly, so that the actual damage in time T can be quite accurately approximated by the mean damage \bar{D} in time T . The following section outlines a few approaches typically used to identify $f_S(s)$.

4.3.1 Existing Approaches to Fatigue Analysis

This section briefly summarizes the existing approaches to model the distribution of the stress load cycles. According to existing guidelines for fatigue analysis (for example, [8]) we need to formulate the long-term stress distribution $f_S(s)$ for the structural component. Some ways to find it are:

1. Simplified analysis in conjunction with ship guidelines:

$f_S(s)$ can be modeled as a Weibull distribution:

$$P[S > s] = \exp[-(s/\beta)^\alpha] \quad (4.3)$$

where α and β are the shape and the scale parameters of the distribution. The b -th moment of a Weibull S is given as

$$E[S^b] = \beta^b \Gamma(1 + b/\alpha) \quad (4.4)$$

where $\Gamma(u) = \int_0^\infty t^{u-1} e^{-t} dt$ for $u > 0$ is the Gamma function.

Simple empirical rules (or more refined long-term analysis) may be used to find α . For example, Ref. [8] suggests $\alpha \approx 2.21 - 0.54 \log_{10}(L)$ for fatigue analysis of deck longitudinals, where L is the ship length in meters. The second parameter β is then found from an estimated stress value at a known fractile in the distribution. This stress is found by performing a detailed analysis due to an assumed wave cycle that is likely to result in stresses at the desired fractile. Although this method permits a quick and simple fatigue analysis scheme, drawbacks do exist. For example, β is tuned to a single stress analysis and may be sensitive to the choice of the stress return period. This can, of course, be resolved by tuning β to different stresses and studying the consequence on fatigue damage estimates. Another problem that still exists, however, is how do we select a wave (or the wave parameters: height H and period T) that should result in stresses with a desired return period? If the response given a wave with height H were deterministic, and if T varied deterministically with H , then the return period of the wave would exactly be the return period of the resulting stress. In general, the response given a wave is random (also T given H is

random) and hence the difficulty in identifying the wave.

2. Long-term stresses based on long-term climate conditions:

The long-term wave climate is divided into short-term climatic conditions called seastates. The duration of a seastate, typically 1–6 hours, reflects the time in which the waves can be assumed to be stationary. Parameters typically chosen to characterize a seastate are the significant wave height H_s , defined to be four times the wave elevation standard deviation σ_η , and the peak spectral period T_p . A ship response analysis in irregular waves (see Sec. 4.4) could then provide the stresses as a function of H_s and T_p . This leads to the long-term stress distribution

$$f_S(s) = \iint f_{S|H_s, T_p}(s|h_s, t_p) f_{H_s, T_p}(h_s, t_p) dh_s dt_p \quad (4.5)$$

where $f_{S|H_s, T_p}(s|h_s, t_p)$ is the conditional probability density function of stresses given H_s and T_p , and $f_{H_s, T_p}(h_s, t_p)$ characterizes the long-term joint probability density of the seastate parameters. Such joint distributions, characterized for many ship routes around the world, can be found in the literature, for example see Ref. [10]. Note the stress cycle rate $\nu(h_s, t_p)$ may also be a function of the seastate parameters h_s and t_p . In this case, one needs to consider a weighted form of $f_s(s)$ above; e.g.,

$$f_S(s) = \frac{\iint \nu(h_s, t_p) f_{S|H_s, T_p}(s|h_s, t_p) f_{H_s, T_p}(h_s, t_p) dh_s dt_p}{\iint \nu(h_s, t_p) f_{H_s, T_p}(h_s, t_p) dh_s dt_p} \quad (4.6)$$

Alternatively, with normalized damage (per cycle) given by S^b , long-term mean damage must consider not just $E[S^b|H_S, T_P]$ but more generally the mean damage $\nu(H_S, T_P)E[S^b|H_S, T_P]$ per unit time (as in section 4.5).

An alternative approach (see, for example, API [2]), would be to use the local

wave heights (wave height H in a single wave) to characterize the wave climate and relate the stresses directly as a function of the wave height H . $f_S(s)$ then based on a long-term distribution of the local wave heights $f_H(h)$ is

$$f_S(s) = \int f_{S|H}(s|h) f_H(h) dh \quad (4.7)$$

in which $f_{S|H}(s|h)$ is the probability density of stresses S given the local wave height H . This method does not explicitly assume dependence of stresses on the wave periods.

4.4 Ship Response Analysis Methods

This section discusses different methods to perform a ship response analysis to find the stresses given the climate conditions. These methods differ in the complexities of the hydrodynamical and mechanical models used to perform the analysis. For example, a linear analysis (see below) is based on small ship oscillations, while a 2-D strip theory, studied here, accounts for the ship position in the wave and integrates the water pressure to the exact wave surface. This approach can be extended to perform a 3-D analysis accounting for fluid-structure interaction effects.

- **Linear Ship Load Analysis:** A linear analysis is used to find the Linear Transfer Function (LTF) that relates waves to ship loads for a ship traveling at a given speed. In this study, a strip theory is used to estimate the linear loads by integrating the water pressures to the mean water level [65]. In a short-term seastate (typically of 1 to 6 hours duration), the ship load is assumed to be Rayleigh distributed with the load standard deviation σ (and stress cycle rate) found from the spectrum of linear loads. A weighted Rayleigh distribution across

all seastates accounting for different ship speeds, and the long-term distribution of the seastates, may then in turn be used to directly find $E[S^b]$, or to calibrate an equivalent Weibull model, which may then be used to find $E[S^b]$. Although still a linear analysis, this approach includes the frequency content in the load estimation and is computationally inexpensive.

- **Nonlinear Ship Load Analysis:** State-of-the-art 3-D nonlinear ship analysis tools like SWAN [27, 44], Lamp [30, 31], and USAERO [5], for example, can be used to estimate the global loads. In this study, we use a 2-D strip theory [6, 13], as described in Sec. 4.2, to estimate the loads on a ship, and then find the resulting fatigue damage. Such tools perform increasingly complex nonlinear analyses to gain accuracy in the load estimates; the computational burden increases in intensity, however. We need to use these expensive tools minimally to predict fatigue damage with the least computational burden.

In the following section, we demonstrate the need to perform a nonlinear load analysis, instead of a linear one, to estimate fatigue damage, and then propose a new approach to perform such a nonlinear damage estimate.

4.4.1 Comparison of Ship Response from Linear and Nonlinear Analyses

We compare the ship loads (mid-ship bending moments) from linear and nonlinear analyses in an irregular sea to emphasize the effects of nonlinearities in the loads. The example sea chosen here is described by a JONSWAP spectrum with significant wave height $H_s = 5\text{m}$, spectral peak period $T_p = 10\text{s}$, and peakedness factor $\gamma = 3.3$. The ship is assumed to be traveling at a speed of 10 knots ($\approx 5.144\text{ m/s}$) into a head

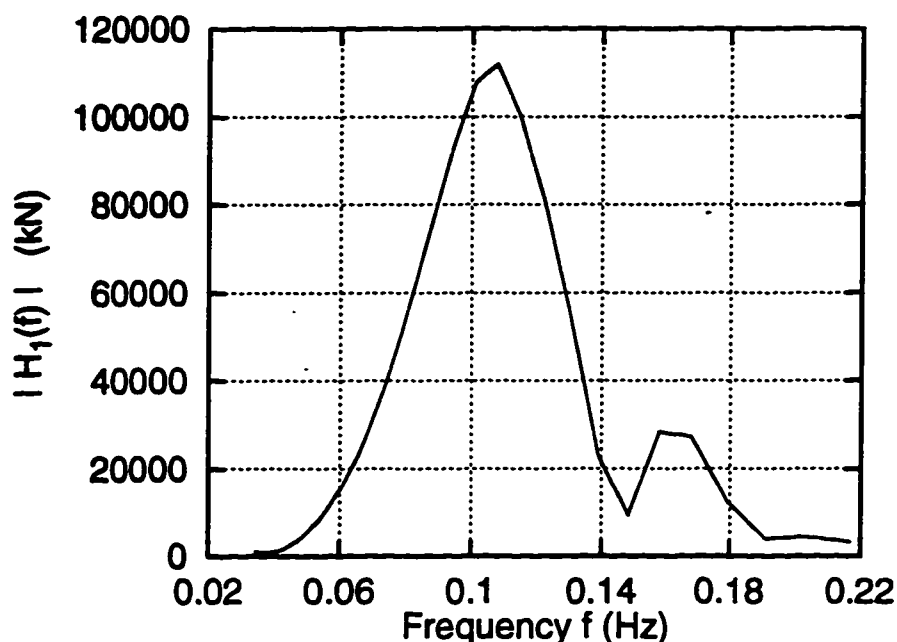
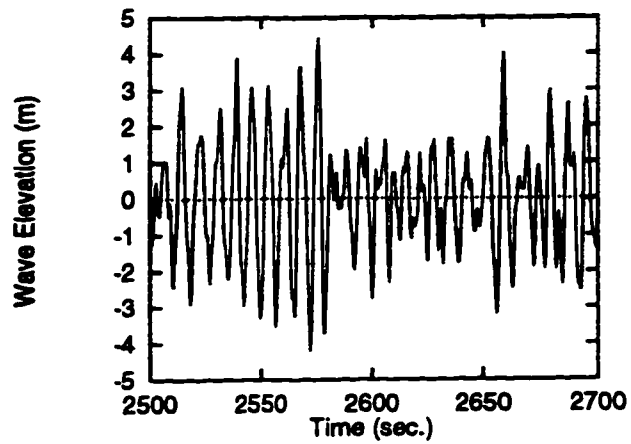


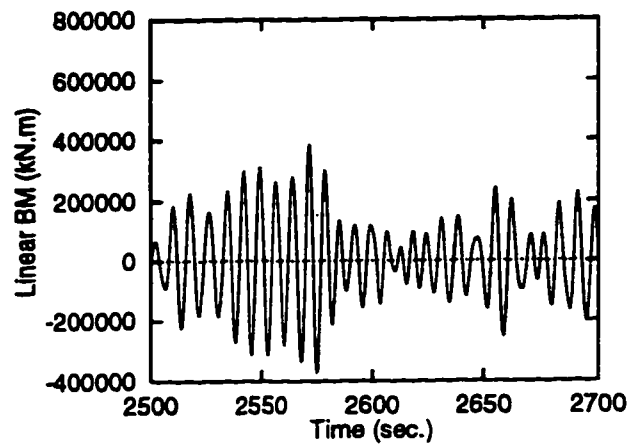
Figure 4.3: Linear Transfer Function for Mid-ship Bending Moment Response

sea. The linear bending moments are estimated from a linear transfer function (see Fig. 4.3) relating the wave elevation process $\eta(t)$ to the mid-ship bending moments. Note that the linear transfer function peaks at about $f = 0.1\text{Hz}$, or wavelength = 156 m (from linear dispersion relation). This is close to the ship length and so this chosen sea reflects a ship-length tuned sea. The nonlinear history is estimated from NV1418 using a 2-D strip theory [6, 13]. Partial mid-ship time histories of the Gaussian waves, the linear bending moments, and the nonlinear bending moments from an hourly analysis are shown in Figure 4.4.

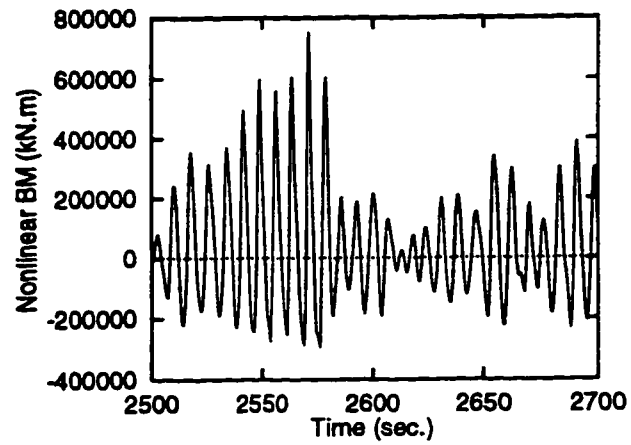
The sag bending moments (positive peaks) are typically larger than the neighboring hog bending moments (absolute value of negative peaks) in the nonlinear load history, while the bending moments are symmetrically distributed in the linear load history. Note that the range bending moment (=sag+hog) is also, on average, smaller



(a) Wave History



(b) Linear Response History



(c) Nonlinear Response History

Figure 4.4: Partial wave and response histories at mid-ship

Table 4.2: Statistics of Ship Load History

	Linear Analysis	Nonlinear Analysis
Mean μ	0	0.21×10^5 kN.m
Sigma σ	1.06×10^5 kN.m	1.36×10^5 kN.m
Skewness α_3	0	0.6
Kurtosis α_4	3.0	3.4

from the linear analysis. The history statistics of the two analyses are given in Table 4.2. The skewness of 0.6 in the nonlinear history provides a measure of the marked asymmetry between the sag and hog bending moments. Note also that standard deviation of the linear history is approximately 30% smaller than that of the nonlinear analysis. This may be due to the limitation of the small oscillation assumption in linear theory, which thereby ignores the increasing nonlinearity as the length of the waves approach the ship length (see Fig. 4.3). Owing to the smaller sag bending moments from linear theory and the resulting smaller ship keel (bottom) tensile stresses, the rate of crack growth will be considerably underpredicted by linear theory.

Fig. 4.5 compares the fatigue damage from the linear analysis to that from the nonlinear analysis. The linear fatigue damage D_L in duration T_d is (see Eqn. 4.2):

$$D_L = T_d \nu_0 E[S^b] \quad (4.8)$$

in which ν_0 is the stress cycle rate and $E[S^b]$ can be found from Eqn. 4.4, where for a Rayleigh stress (due to linear theory) distribution $\alpha = 2$ and $\beta = \sqrt{2}\sigma$. Note that in Eqn. 4.8, we have ignored the S - N coefficient C and the section-modulus in converting bending moments to stresses. These are treated as material constants and will cancel out when looking at ratios of damage estimates.

The fatigue damage D_{NL} is estimated from 20 hours of simulated nonlinear response in irregular waves in this seastate and is given as

$$D_{NL} = T_d \nu_0 E[S^b] = \sum_{i=1}^N S_i^b \quad (4.9)$$

in which N is the total number of stress cycles, and S_i , $i = 1 \dots N$ are the sag, hog or range stresses seen in 20 hours. In this study, we will refer to D_{NL} as the “exact” damage estimate and ask how close are the damage estimates from simpler prediction models. A comparison of linear to nonlinear fatigue damage shows that the sag-induced fatigue damage can be considerably underpredicted by the linear model. Linear hog damage is closer to the nonlinear hog damage, since the predicted hog bending moments from linear theory seem close to those from the nonlinear analysis (see Fig. 4.4). Recall that hog bending moments occur due to wave crests near mid-ship (see Fig. 4.2) where the cross-section is box-like, and so there, indeed, is potential for linear theory to correctly predict hog bending moments. As a net effect of sag and hog, the range fatigue damage is also underpredicted by the linear model, although, to a lesser extent than the sag underprediction.

As seen in Fig. 4.5, a nonlinear analysis of sag-induced fatigue for a flared ship can provide larger fatigue damage estimates than a linear analysis, particularly for large values of the fatigue exponent b . Such a nonlinear analysis is computationally intensive, however, and is thus an expensive solution to find accurate damage estimates. In this study, we look at an alternative method to estimate damage from nonlinear ship loads. This method is referred to here as a “Nonlinear Transfer Function” (NTF) model, as described in Section 4.5.

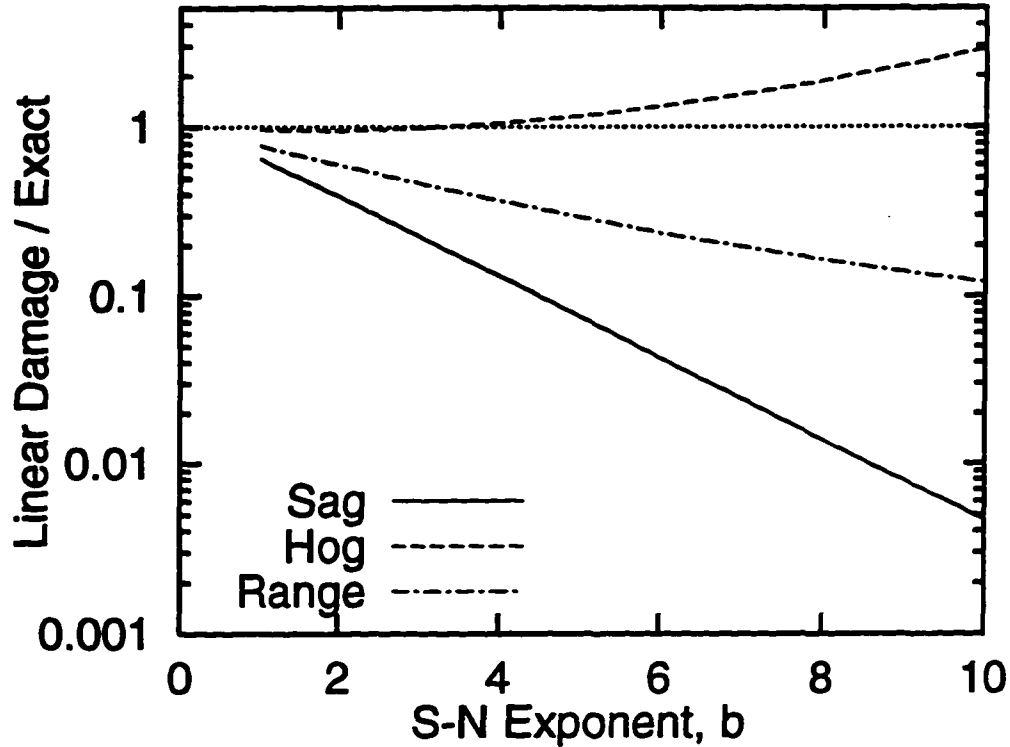


Figure 4.5: Comparison of fatigue damage from linear and nonlinear analysis for sag, hog and range bending moments

4.5 Proposed NTF Approach

In this study, we propose an NTF model to estimate ship loads and the resulting fatigue damage. In this model, we apply the expensive nonlinear analysis to find stresses for only a limited, carefully selected set of wave amplitudes and frequencies. As the force analysis may be rather complex, a minimal set of amplitude and frequency values is chosen. The results are then appropriately weighted to reflect the amplitude-frequency distribution of actual random waves. The numerical set of stress values for the selected waves represents what we call the “Nonlinear Transfer Function”.

The stresses from this limited set of waves, in combination with their associated probability weights, can be used to estimate the resulting fatigue damage estimate. This cheaply estimated fatigue damage is intended to approximate the relatively expensive, exhaustively simulated damage from a complete irregular nonlinear time domain analysis.

We will first confirm out theoretical distributions of the wave amplitudes and frequencies by comparing the results with simulated random waves. We then investigate the adequacy of such waves in successfully predicting the load statistics. This is done by comparing the regular wave results to a corresponding complete random wave analysis.

We test this model by comparing, in this example seastate ($H_s = 5\text{m}$, $T_p = 10\text{sec}$), the predicted damage to the exact damage from Eqn. 4.9. Linear theory predicts this seastate to be about the most damaging seastate for an $S-N$ exponent $b = 4$ (chosen to reflect steel materials), as explained below.

In linear theory, the ship load (stress) process X is assumed to be Gaussian and hence the sag (or hog) bending moments (or stresses S) are Rayleigh distributed. The mean damage rate $E[D_r|H_s, T_p]$ given H_s and T_p can then be written (from Eqn. 4.8) as

$$E[D_r|H_s, T_p] = E[\nu S^b|H_s, T_p] = \nu(H_s, T_p) (\sqrt{2}\sigma(H_s, T_p))^b \Gamma(1 + b/2) \quad (4.10)$$

where $\sigma(H_s, T_p)$ is the standard deviation and $\nu(H_s, T_p)$ is the cycle rate of process X , both of which are seastate-dependent. The total long-term damage D_{LT} is

$$D_{LT} = T_d \iint E[D_r|H_s, T_p] f_{H_s, T_p}(h_s, t_p) dh_s dt_p \quad (4.11)$$

in which the integrand $E[D_r|H_s, T_p] f_{H_s, T_p}(h_s, t_p)$ is the contribution to D_{LT} from each seastate (sometimes called the damage density) and is shown in Fig. 4.6 for a joint distribution model of H_s, T_p , representing Northern North Sea data as suggested in [18]. The damage density is largest in approximately $H_s = 5\text{m}$, $T_p = 10\text{sec.}$, and because large linear loads probably imply large nonlinear loads, as seen in Fig. 4.4, we choose this example seastate to study the accuracy of the NTF model. Note however the modeling errors may be greater in this seastate than in D_{LT} ; we use this seastate to most severely test the NTF model and not to suggest typical errors to be expected in estimates of D_{LT} , the long-term damage.

4.5.1 NTF Modeling Issues

As proposed, the idea of the NTF model is to find reliable estimates of fatigue damage from a limited set of wave runs rather than performing expensive nonlinear analyses across all the climate conditions. The key issues in the development of this model are:

- **Selection of waves from theory:** The selection of wave parameters (here the wave height and the wave period) and their associated probabilities of occurrence is based on stochastic theory. Each of the selected waves is stepped through the nonlinear time domain analysis to estimate the ship loads. The questions that arise here are: how accurately does this stochastic theory characterize the waves? And how many waves should we choose to robustly estimate fatigue damage? We will address the first issue in Section 4.5.2 in more detail. The second issue will be discussed by choosing different numbers of selected waves and then comparing the resulting fatigue damage estimates to simulated data.

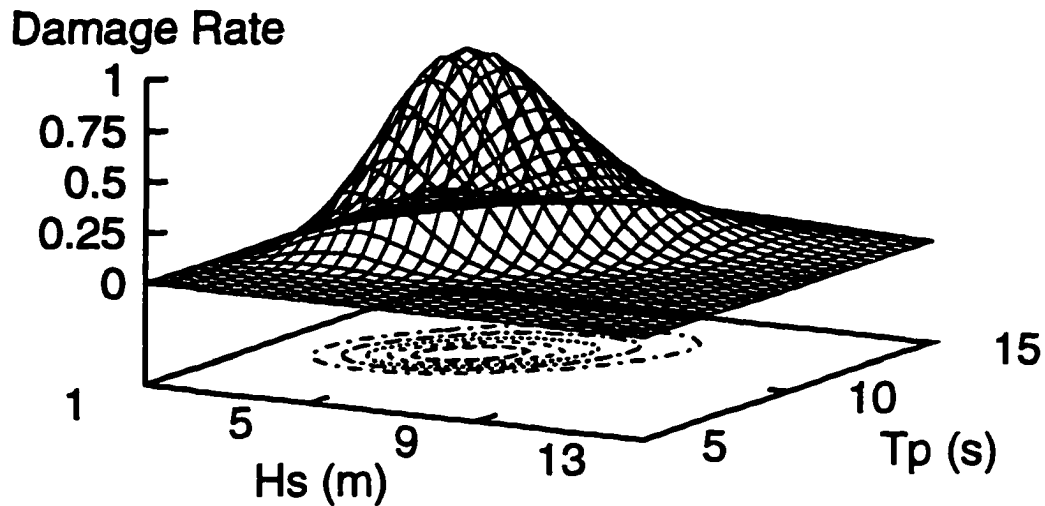


Figure 4.6: Damage density from a linear analysis vs. long-term seastate parameters. The damage rate shown has been normalized by the largest value.

- Inclusion of spatial wave effects:** In order to include the spatial wave effects, stepping the ship through just one wave cycle may not suffice in estimating the ship loads. This is because at any given time instant the loads depend on the spatial waves across the ship, and on the position of the ship in these waves. We may need to include such spatial effects in the limited wave runs. We hope to achieve this by constructing “most-likely” side wave cycles around each of the selected waves, and then stepping the ship through this triplet to find the resulting ship loads. We address this issue further in Section 4.5.3.

4.5.2 Selection of Waves from Stochastic Theory

A sinusoidal wave can be defined by two parameters, a wave height H and a wave period T . We verify theoretical distributions of H and T with simulated random waves. For waves in an irregular time histories (see, for example, Fig. 4.4a), we select H 's and T 's from all the wave cycles; a wave cycle is defined as the wave surface between two successive mean-upcrossings of the wave surface. H is the elevation difference between the highest and the lowest points in a wave cycle and T is the time duration between the mean-upcrossings of a wave cycle. Note that this definition of wave cycle, and corresponding H and T , is introduced here simply to permit critical comparison of separate parts of the NTF model prediction – e.g., $f(H, T)$ and $D|H, T$. These precise definitions do not effect the actual calculation of the nonlinear damage D_{NL} , nor of its estimate D_{NTF} from the NTF model.

Wave Heights from Theory

The wave heights of the selected waves are sampled from the Forristall [12] distribution which is an empirical distribution fitted to observed ocean wave heights. For the Gaussian seastate we are considering (represented by a JONSWAP spectrum with $H_s = 5$ m, $T_p = 10$ sec., and $\gamma = 3.3$), Figure 4.7 shows a comparison of 20 hours of simulated wave heights to the Forristall distribution and the Rayleigh distribution of wave heights. The cumulative distribution function (CDF) of the wave heights H is given as

$$F_H(h) = P[H < h] = 1 - \exp \left[-\frac{(h/\sigma_\eta)^\alpha}{\beta} \right] \quad (4.12)$$

where σ_η is the standard deviation of the wave elevation process $\eta(t)$, and $\alpha = 2$, $\beta = 8$ for the Rayleigh distribution and $\alpha = 2.126$, $\beta = 8.42$ for the Forristall distribution (from empirical fits). Note that the Rayleigh distribution is a theoretical distribution for a narrowband Gaussian $\eta(t)$, and to the degree $\eta(t)$ is not narrowband, the Rayleigh distribution will tend to overestimate wave height fractiles with respect to simulated Gaussian behavior. In Fig. 4.7, the Rayleigh distribution indeed overpredicts wave heights, while the Forristall distribution offers a closer fit to the simulated wave heights. Similar comparisons of the Forristall model with simulated second-order waves were also found in the wave studies conducted in Chapter 2. We will choose the Forristall model to generate the wave heights for the NTF model.

Theoretical Wave Periods given Wave Heights

Given the wave height H , we predict statistics of the wave period T for the sinusoid from the Longuet-Higgins conditional distribution [34–36, 69] of wave periods given wave heights. This distribution, based on envelopes of narrowband processes, specifies a truncated normal distribution of wave frequencies $\Omega = 2\pi/T$ given the wave amplitude $a = H/2$ as

$$P[\Omega > \omega|a] = \frac{\Phi\left[\frac{a(\bar{\omega}-\omega)}{\sigma_\eta\bar{\omega}\Delta}\right]}{\Phi\left[\frac{a}{\sigma_\eta\Delta}\right]} \quad (4.13)$$

where $P[\Omega > \omega|a]$ is the probability that Ω exceeds a specified ω value given a and $\Phi()$ is the standard normal CDF. $\bar{\omega} = \lambda_1/\lambda_0$ is a mean wave frequency in terms of the wave spectral moments $\lambda_i = \int \omega^i S_\eta(\omega) d\omega$. $\sigma_\eta = \sqrt{\lambda_0}$, and $\Delta = \sqrt{\lambda_0\lambda_2/\lambda_1^2 - 1}$ is a unitless spectral bandwidth measure. For example, $\Delta = 0.42$ for a Pierson-Moskowitz spectrum, and decreases from this value for a JONSWAP spectrum with $\gamma > 1$. Similar models for the conditional distribution have been proposed by Canavie

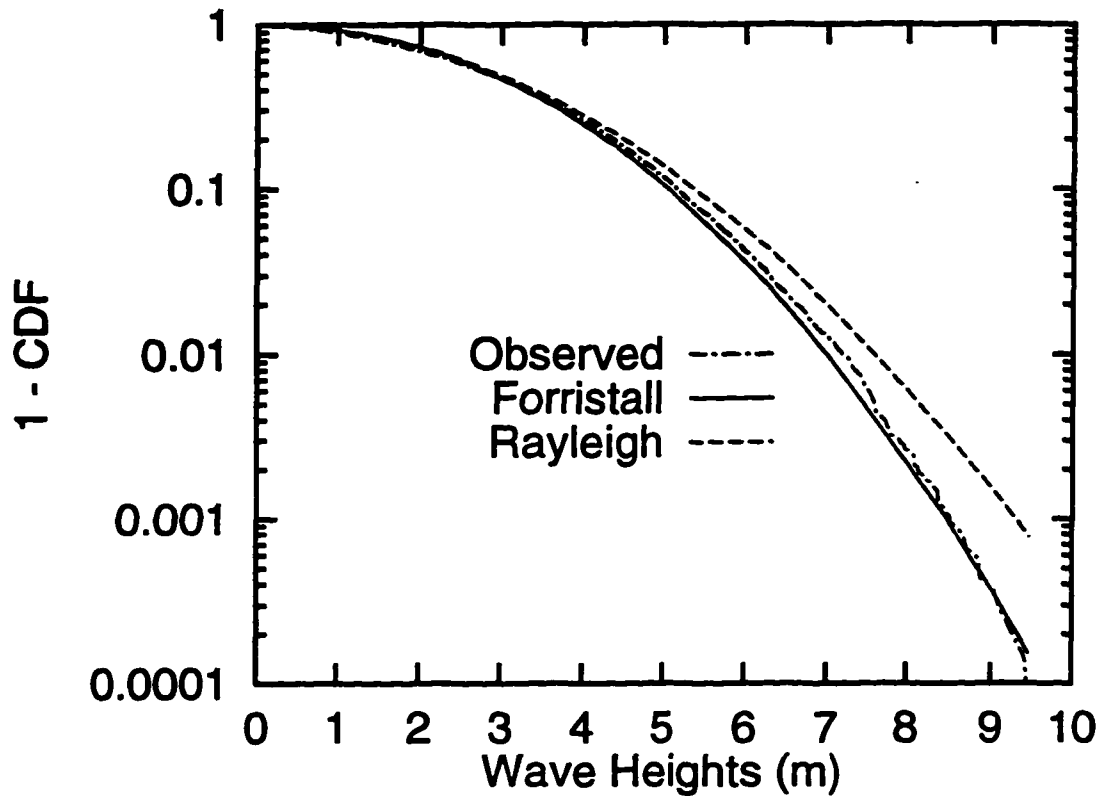


Figure 4.7: Comparison of simulated wave heights to Forristall and to Rayleigh distributions

et al. [7] and Lindgren and Rychlik [32]; however, these require at least the fourth spectral moment, which is not generally available for wave spectra and so we propose not to use these models for the fatigue analysis studies. In this study, we take $\bar{T} = 0.92T_p$ (e.g., [39]) and so will refer to it as a “modified” Longuet-Higgins distribution. For the example seastate, we find $T_c = 2\pi/\bar{\omega} = 8.35$ sec, while $\bar{T} = 0.92T_p = 9.2$ sec.

To select wave periods in the NTF model, we can relate the frequency fractile ω_p for a given a in the Longuet-Higgins model to the requested probability p . This is

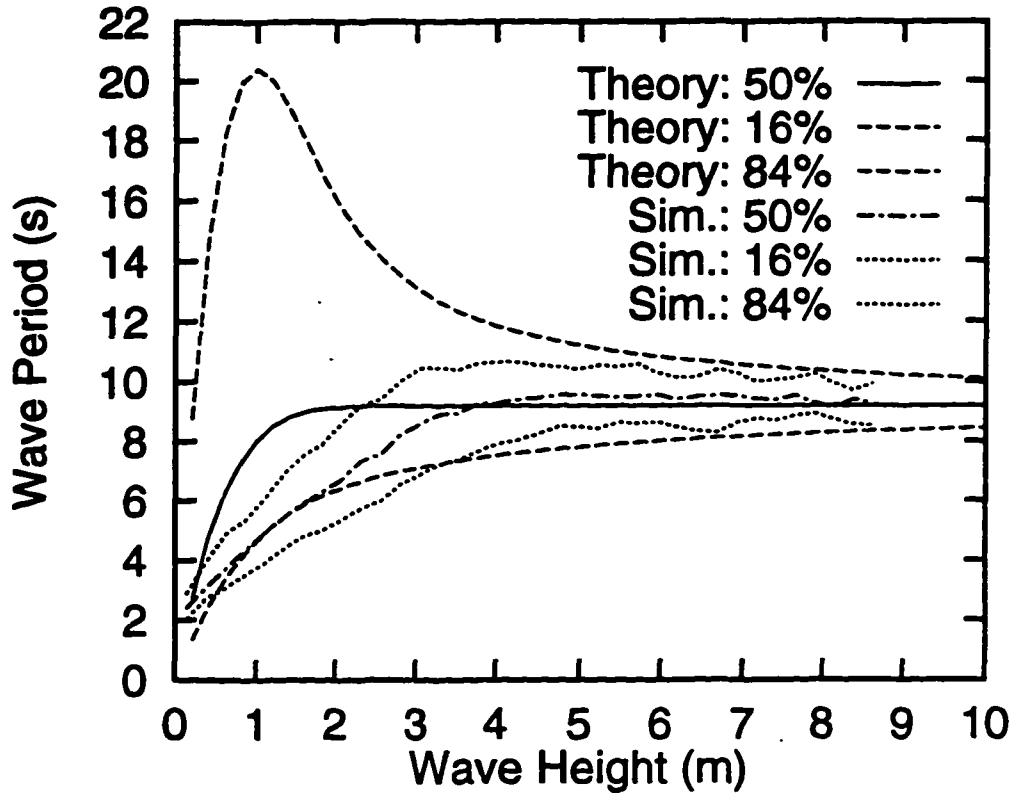


Figure 4.8: Simulated wave period vs. modified Longuet-Higgins wave period

done by setting Eqn. 4.13 equal to $1 - p$

$$\frac{\omega_p}{\bar{\omega}} = \frac{\bar{T}}{T_p} = 1 - \frac{\sigma_\eta \Delta}{a} \Phi^{-1} \left[(1 - p) \Phi \left(\frac{a}{\sigma_\eta \Delta} \right) \right] \quad (4.14)$$

We compare 20 hours of simulated wave period in this example seastate to the wave periods from this modified Longuet-Higgins model. Figure 4.8 shows a comparison of the 16-, 50- (median), and 84- percentile values of wave periods from simulation to those predicted from Eqn. 4.14. For wave heights greater than 3 meters the modified Longuet-Higgins model offers a reasonable approximation to simulated

wave periods at the median values and also at the 16 and 84 percentile values of the conditional distribution. For small wave heights, the theoretical wave periods are larger than the simulated periods; however, there is negligible contribution to fatigue damage from these small-height waves, and so, from a fatigue damage standpoint, the modified Longuet-Higgins model appears to offer a satisfactory approximation to the conditional distribution of wave periods given a wave height.

Finally, given a count of the waves to be selected, the choice of wave heights and wave periods given wave heights could, for example, be based on quadrature points. Say, 30 waves are to be selected, as will be used in this study later on. We may mesh the H - T space, so that we have 10 different H values and 3 different T values per H value adding up to 30 waves. We could first select 10 standard normal variables u at Gauss quadrature points and then transform these to H values according to the fractile p of u

$$H = \beta[-\log(1 - p)]^{1/\alpha} \quad (4.15)$$

Given an H value, we can use Eqn. 4.14 to similarly obtain three T values at 16, 50 and 84 fractiles, for example. The joint occurrence probabilities of the H - T pairs can then be easily found from weights associated with H quadrature points ($=P[U = u_i]$) and from the conditional fractiles of $T|H$.

4.5.3 Selection of Side Wave Parameters

Since a Gaussian sea has no horizontal asymmetry (reversing a Gaussian history does not change the history statistics), we assume the wave periods and the wave heights of the side waves to be the same. This results in a symmetric wave triplet. Let H_0 and T_0 denote the wave height and wave period of the side waves, respectively, and H and T denote the height and period of the middle wave, respectively (see

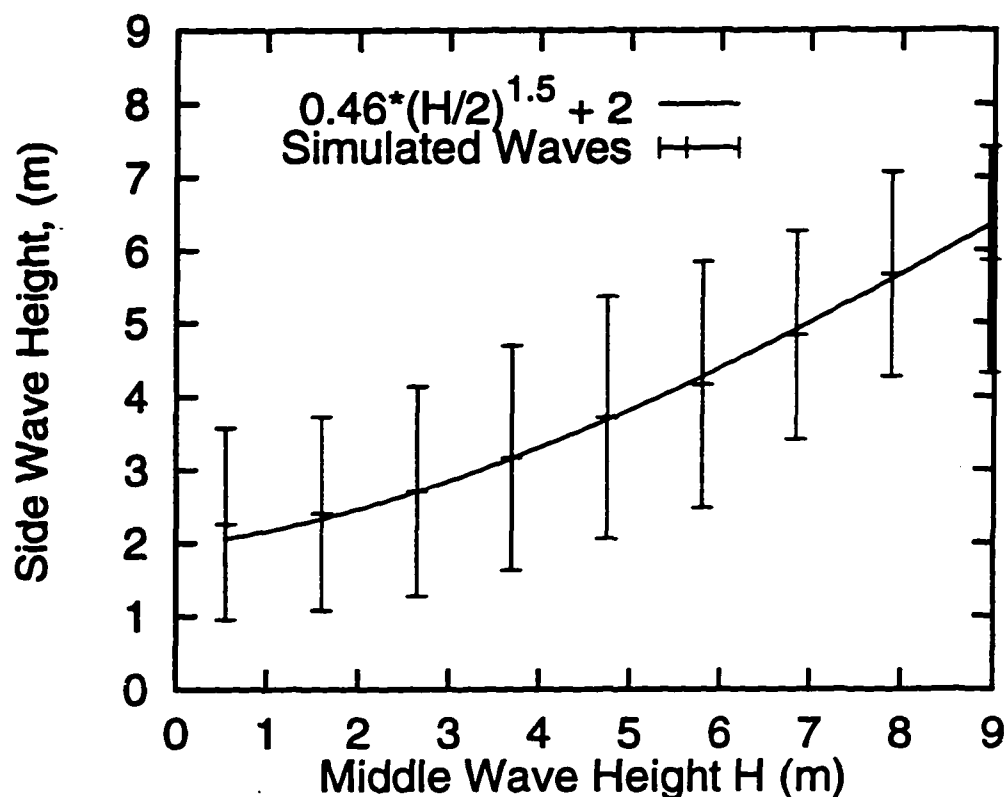


Figure 4.9: Relation of side wave height to middle wave height

Fig. 4.10). For the 20 hours of simulated Gaussian waves, we empirically relate $E[H_0|H] = 0.46(H/2)^{1.5} + 2$ as shown in Fig. 4.9. This figure shows the mean, and $\text{mean} \pm 1$ standard deviation of H_0 given various H values in the wave history. Note however that this empirical result is seastate-specific. Parametric study across a grid of $H_s - T_p$ seastates could afford more general results. Alternatively, one may seek analytical results through probability theory. For example, linear regression suggests that

$$E[H_0|H] = m_H + \rho_{H,H_0}(H - m_H) \quad (4.16)$$

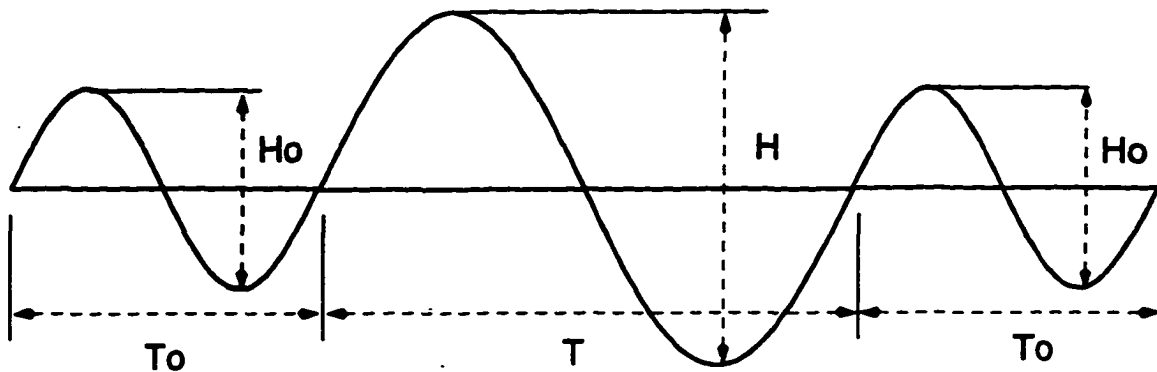


Figure 4.10: Construction of Wave Triplet for NTF Load Prediction

Values of the mean wave height, m_H , and the correlation ρ_{H,H_0} between successive heights, can be estimated by random vibration theory.

For the Gaussian wave history, we find that T_0 has negligible correlation with T in this seastate, so we let T_0 given H_0 be the median period from the modified Longuet-Higgins model, without conditioning the choice of T_0 on T . Finally, we construct a wave triplet with three sinusoids in succession (see Fig. 4.10), where H_0 , T_0 are the side wave parameters and H , T are the middle wave parameters.

4.6 Predicted NTF Fatigue Damage vs. Data

In this section, we will predict fatigue damage from the NTF model and compare it to exact damage found from 20 hours of simulated stresses. Recall that the simulated stresses are obtained from the nonlinear ship response analysis of 20 hours of Gaussian waves. This analysis is done in a seastate with $H_s = 5\text{m}$ and $T_p = 10\text{sec}$. For the NTF model, we will start out by predicting damage from 30 single sinusoidal waves, and investigate the necessity of imposing side waves on each of these 30 waves. We

will then study the accuracy of predicted damage from a reduced set of waves, for example, 15 waves instead of 30 waves.

For the NTF prediction, we select 30 waves (see Fig. 4.11) as the wave set to estimate the mid-ship bending moments. 10 equi-spaced wave heights are chosen for waves, with the maximum H value arbitrarily assumed at 10^{-6} exceedance probability (H with return period of approximately 1 in 1000 hours) according to the Forristall distribution [12]. This return period for H has been arbitrarily chosen to include large rare wave heights as well. We find the weights associated with these 10 H values from the Forristall distribution. Given the H values, the middle wave periods T are chosen to be at 16, 50 (median) and 84 percentile values according to the modified Longuet-Higgins distribution and are found from Eqn. 4.14 using $p=0.16$, 0.5 and 0.84, respectively. In general, we could increase the number of waves in the set to gain greater accuracy in the predicted results; however, as demonstrated in the following sections these 30 waves seem to represent the simulated bending moment statistics adequately. For each wave height, the three selected wave periods were chosen to have equal probability weights of 1/3 each. Finally, the marginal weights of H can be multiplied with the conditional weights of $T|H$ to find the joint weights p_j of the 30 H and T pairs.

Let $N_p = 30$ denote the number of waves used to mesh the H-T space. Thus, the H-T space can be divided into N_p cells centered around each of the selected H-T pairs. Let p_j ($j = 1 \dots N_p$) denote the probability of "falling" in the j th cell. The p_j values can also be understood as the joint weights associated with the N_p H-T pairs. The NTF predicted fatigue damage D_P from the analysis using $N_p = 30$ waves, then, is

$$D_P = T_d \nu E[S^b] = \sum_{j=1}^{N_p} n_j S_j^b \quad ; \quad n_j = N_w p_j \quad (4.17)$$

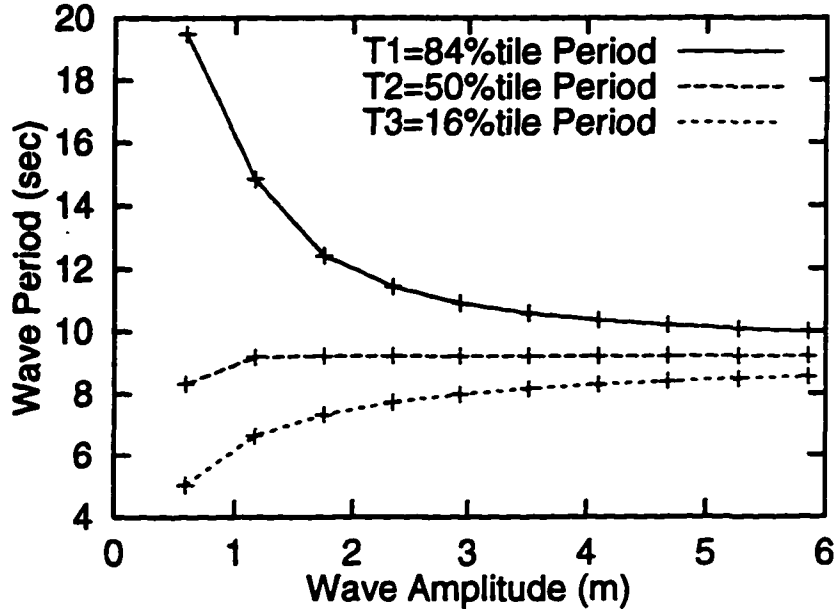


Figure 4.11: Wave heights and periods for the 30 waves used in the NTF model

where S_j is the predicted ship load, n_j is the predicted number of wave cycles for the j th H - T pair, and N_w is the total number of predicted wave cycles in duration T_d . Since the ship is moving into the waves the number of wave cycles encountered by the ship and the resulting number of stress cycles depends on the speed of the ship [11]. The number of wave cycles $N_w = \nu_{enc} T_d$, where ν_{enc} is the wave cycle rate encountered by the ship moving into the waves at speed u and is found from the theoretical (from wave spectrum) wave cycle rate ν as:

$$\omega_{enc} = \omega + \omega^2 u/g ; \quad \omega = 2\pi\nu \quad (4.18)$$

where $\nu_{enc} = \omega_{enc}/2\pi$ and g is the gravitational constant. For our example, $\nu = 0.128\text{Hz}$ for the example JONSWAP spectrum used and $u = 5.144\text{m/s}$, thus $\nu_{enc} =$

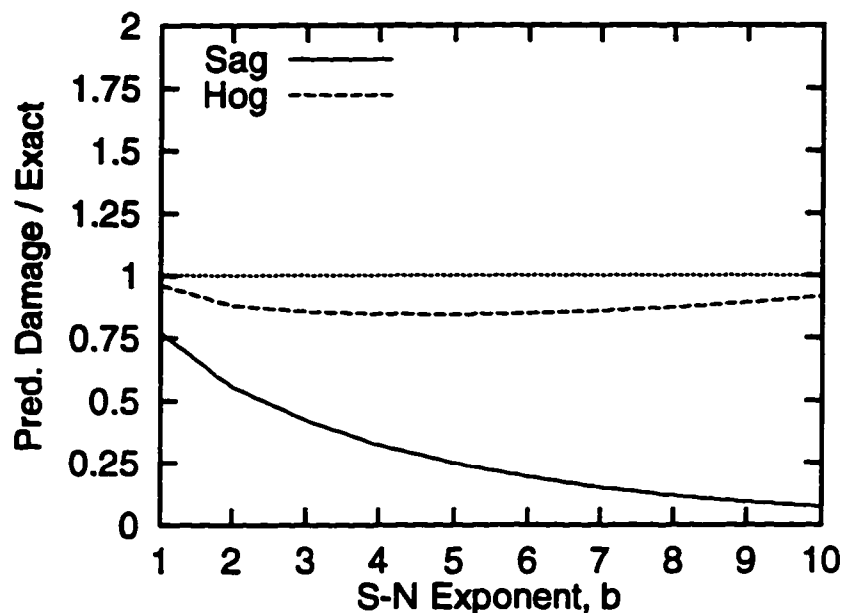


Figure 4.12: Damage prediction from response to selected sinusoidal waves. The single-wave cycle responses are used in this prediction.

0.182Hz.

We will first consider whether we need side waves to “better” predict fatigue damage. We will investigate this by first predicting damage from sinusoidal waves without constructing side waves. For each of the 30 waves shown in Fig. 4.10, we construct a regular sinusoidal wave for each $H-T$ value and step the ship through this one wave cycle to get a corresponding ship load (or stress) cycle. From this one load cycle, we pick the sag bending moment as the largest positive bending moment in the cycle. Similarly, the hog moment is the largest negative bending moment in the cycle. From the 30 sag or hog moments we can then use Eqn. 4.17 to find the predicted damage. Fig. 4.12 compares predicted damage for the selected set of 30 waves **without** side waves.

The sag damage seems to be underpredicted by about 25% at $b = 1$, 70% at $b = 4$, and by about 90% at $b = 10$. Note, however, that this prediction is better than the linear sag damage shown in Fig. 4.5. Recall the linear model underpredicted damage by about 90% for $b = 4$ and by almost 2 orders of magnitude at $b = 10$. The predicted hog damage from the sinusoidal waves seems to be in good agreement over the range of b values shown. If, instead of the single-cycle bending moments, we look at the “steady-state” predicted bending moment for each of these sinusoidal waves, we find some improvement in the predicted sag damage (see Fig. 4.13). By the steady-state moment, we mean the peak response of the ship after several cycles of the same wave so that the any transient effects will have stabilized. In this case, the model underpredicts sag damage by about 10% at $b = 1$ and by about 30% at $b = 4$. Note that for large b values the steady-state damage is now overpredicted (for example, by about 50% at $b = 10$). The hog damage is still in good agreement with simulated damage.

If we predict damage based on the 30 waves, now **with** side waves (see Fig. 4.10), we find the predicted sag damage to be in good agreement with the simulated sag damage (see Fig. 4.14). This prediction seems to be very close to the exact damage, when compared with linear predicted damage in Fig. 4.5. The hog damage, however, seems to be overpredicted for small b 's by about 30% and underpredicted for large b 's by about 20%.

Finally, if we choose to use only 15 waves instead of 30, the resulting sag and hog fatigue damage agreement (see Fig. 4.15) with simulated data reduces for large b 's. In this case, we choose 5 different wave heights based now on a transformation of Gauss-Laguerre quadrature points and for every wave height we choose 3 wave periods based on Gauss-Hermite quadrature points [69]. The resulting choices of the

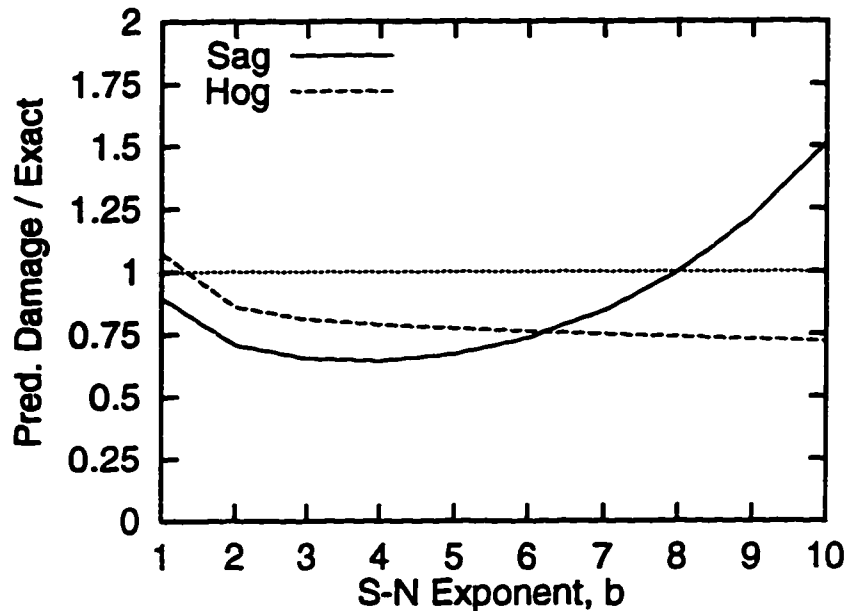


Figure 4.13: Damage prediction from response to selected sinusoidal waves. The steady-state responses to each of the regular sinusoidal waves are used in the prediction.

wave parameters are shown in Fig. 4.16. In quadrature point selection, the main idea is to transform N standard normal or exponential random variables that have been selected to give $2N - 1$ moments exactly. Standard library routines can be used to find these quadrature points which can then be transformed using Eqns. 4.14 or 4.15 at corresponding fractiles of the random variables.

To summarize, we considered four different prediction models above: (1) single-cycle regular wave model, (2) steady-state response due to regular wave, (3) single-triplet response due to 30 regular waves with side waves, and (4) single-triplet response due to 15 regular waves with side waves. We find that each of these four models predict at least the sag damage better than a linear model. The steady-state response offers

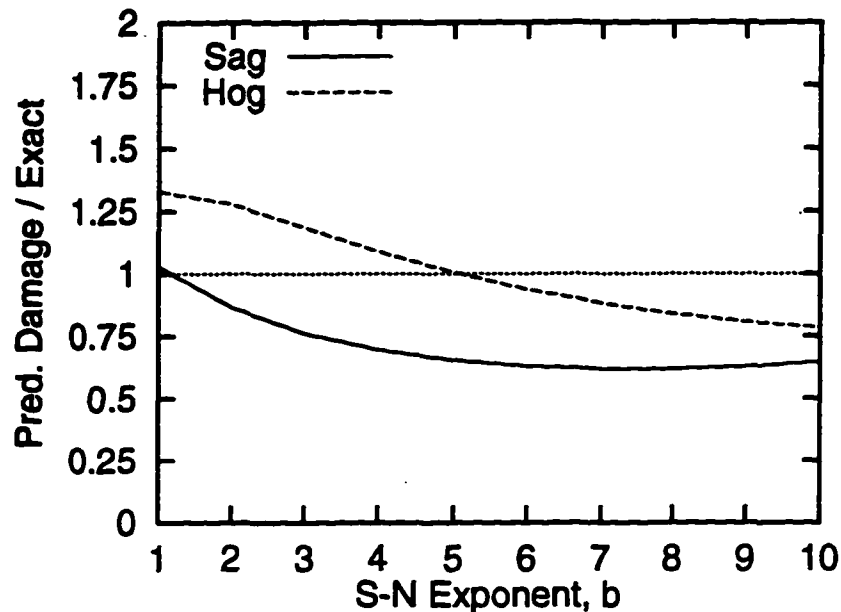


Figure 4.14: Damage prediction from response to selected waves with side waves. 30 wave triplets have been used in the fatigue prediction.

an improvement over the single-cycle regular wave model. The predictions improves further on including side waves and stepping the ship through single-triplet for each selected H - T pair. Finally, the agreement with simulated damage degrades slightly when reducing the number of waves from 15 to 30. Note that estimation of stresses and the resulting fatigue damage in each of the four models took only about 10 to 15 minutes of computer time on a HP 9000 workstation, while generation of 20 hours of simulated stresses from the random waves took about 6 days on the same computer.

In the subsequent studies, we will consider model 3 (single-triplet prediction with 30 H , T pairs) to be the base case model and attempt to further improve the agreement with simulated exact damage.

We should recognize, however, that the level of agreement seen in any of the

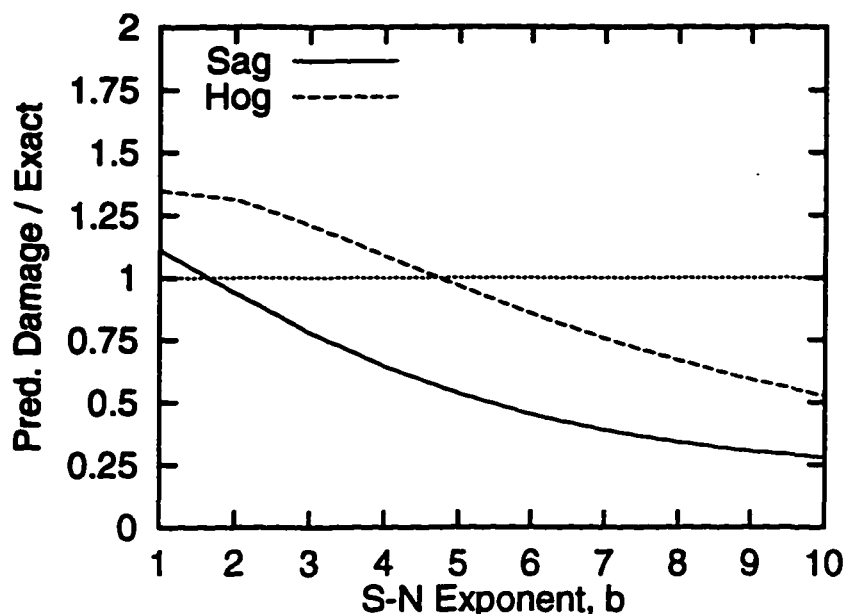


Figure 4.15: Damage prediction from response to selected waves with side waves. 15 wave triplets have been used in the fatigue prediction.

prediction models may be due to offsetting errors. For example, the model could be predicting too large bending moments from the limited wave runs, however, the absence of any scatter effects in the model could be causing a reduction in the resulting predicted damage from the too-large bending moments. By an absence of scatter effects, we mean using only a single stress value to represent several stresses, generally random in nature, in each H - T cell (see Sec. 4.6.2).

In order to diagnose these effects, we should first compare the predicted bending moments directly to the simulated bending moments. Any mismatch at the bending moment level should be corrected for, and then the scatter effects should be included to find fatigue damage. Another effect to be accounted for is the difference in the periods of the input wave cycle and resulting ship load cycle. We will look at the

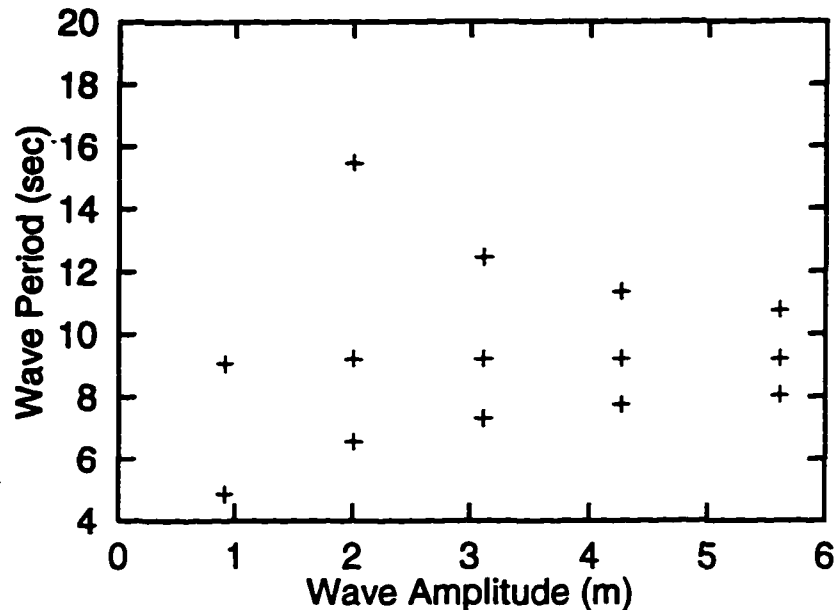


Figure 4.16: Wave parameters of the 15 waves used for predicting ship response. The wave heights and wave periods have been obtained using quadrature points. (Note the largest wave period for the smallest wave height has not been shown in this plot, to facilitate direct comparison of these parameters to the ones in Fig. 4.11)

following effects in sequence to diagnose their impact on fatigue prediction:

- **Inclusion of cycle duration correction** (Sec. 4.6.1): Typically, in an irregular history of a given duration the number of wave cycles and the number of ship load cycles are different because the time domain analysis is not a static analysis. Prediction of damage per load cycle from damage per wave cycle thus may require a modification factor accounting for the duration difference that may exist between a load cycle and a wave cycle.
- **Inclusion of scatter effects in limited wave prediction** (Sec. 4.6.2): In the NTF model, the idea is to consider only a limited, discretized set of wave

height-period pairs, $(H, T)_i$, and calculate the stress $S_i = S(H, T)_i$ associated with each. The mean value $E[S^b]$ – which is proportional to the mean damage – is then estimated from the NTF model as

$$E[S^b]_{NTF} = \sum_i p_i S(H, T)_i^b \quad (4.19)$$

Here p_i is the probability of falling into the i -th $(H - T)$ cell, centered at $(H, T)_i$. Assuming this probability p_i is correct, the “true” value of $E[S^b]$ under the nonlinear simulations is

$$E[S^b] = \sum_i p_i E[S^b | H, T] \quad (4.20)$$

Thus, the critical assumption of the NTF model is quasi-static behavior, so that a wave with height H and period T always produces the same stress $S = S(H, T)$, irrespective of the past wave/stress history. In this case, because S is deterministic given H and T , $E[S^b | H, T] = S(H, T)_i^b$ and the NTF result becomes exact. Deviations from quasi-static behavior will produce a scatter among values of S given the same H and T , and hence $E[S^b | H, T]$ will generally exceed $S(H, T)_i^b$ (at least for $b > 1$). This effect will generally be a function of both the ship and the seastate; it will be studied here for the particular ship and seastate under consideration.

- **Inclusion of bias correction** (Sec. 4.6.3): Although we attempt to get unbiased load predictions from limited wave runs, we may have a bias in our model predictions, i.e., on average the predicted stress from a wave triplet may be too large or too small compared to a mean simulated stress corresponding to such

waves from irregular waves. Any such biased estimates could be due to the inherent limitation of load prediction from short wave segments [56]. We may seek to correct for any such bias before we predict fatigue damage.

4.6.1 Modeling Duration Correction Effects

The mean damage rate based on ship load cycles is $\nu_l \overline{D_l} \propto \nu_l E[S^b]$, in which D_l is the mean damage per load cycle and ν_l is the load cycle rate. The mean damage rate in the NTF model is based on the wave cycles, since we estimate a single stress (sag, hog, or range) for a selected wave height and period. The mean damage rate from the NTF model then is $\nu_w \overline{D_w} \propto \nu_w E[S^b]$, in which D_w is the mean damage per wave cycle and ν_w is wave cycle rate. Since the actual damage per unit time occurring on the ship is the same, whether based on load cycles or on wave cycles, we should have $\nu_l \overline{D_l} = \nu_w \overline{D_w}$. In the NTF model, we base damage estimates on the theoretical wave cycles encountered, so $E[S^b]$, which yields damage per load cycle, should be corrected appropriately to account for the duration difference between a load cycle and a wave cycle. Thus, we could say

$$D_w = \frac{\nu_l}{\nu_w} D_l; \quad \text{or} \quad D_w = \frac{T_{\text{wave}}}{T_{\text{load}}} D_l \quad (4.21)$$

in which T_{wave} and T_{load} are the periods of a wave and the corresponding ship load cycle, respectively. Thus, the total damage based on wave cycles (from Eqn.s 4.17 and 4.21) is

$$D_P = \sum_{j=1}^{N_p} n_j S_j^b \frac{T_{\text{wave},j}}{T_{\text{load},j}}; \quad n_j = \text{no. of wave cycles in cell } j \quad (4.22)$$

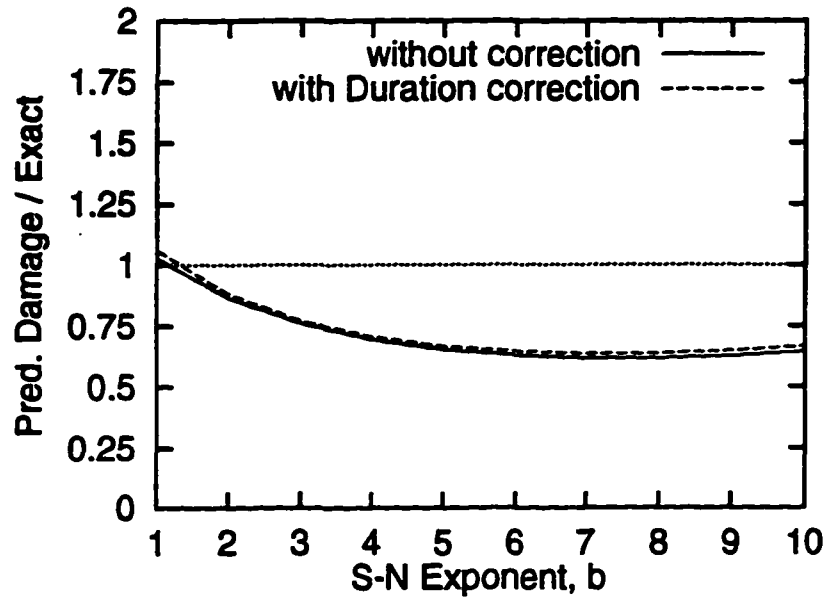
where $T_{\text{wave},j}/T_{\text{load},j}$ is the duration correction for the j th wave and predicted load cycles.

In this study, we find when converting the damage per wave cycle to damage per load cycle, the impact of this correction on the damage estimate seems insignificant as Fig. 4.17 demonstrates. Notice how the inclusion of the duration correction makes practically no difference in the prediction in either the sag or the hog damage. An explanation for this may be that the damage-contributing loads have the load cycle periods very close to the underlying wave cycle periods, the analysis being quasi-static. We therefore propose not to include this correction in the subsequent results.

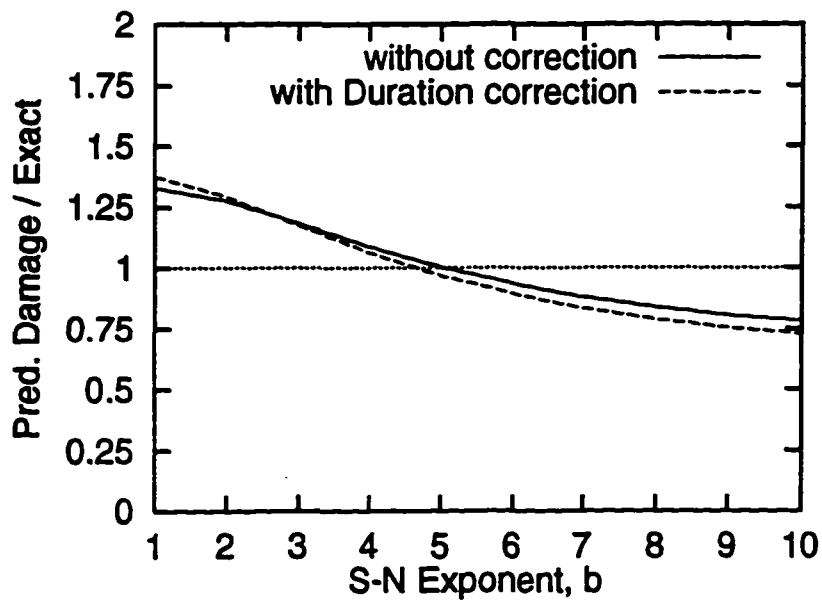
4.6.2 Modeling Scatter Effects in Ship Loads

For the waves shown in Fig. 4.11, each “+” denotes a wave pair and is considered to represent the mid-wave values of the wave parameters for the cell around it. We, then, represent the entire H-T domain by 30 cells (in this example), each of which is represented by the mid-cell H-T pair. We empirically model the scatter effects from the simulated load history by binning the 20 hours load history in this H-T space and modeling the resulting load scatter in each cell. In each load cycle, we identify the loads as, (1) sag: the maximum (positive) load in the cycle, (2) hog: the minimum (negative) load in the cycle, and (3) range (=sag+hog). The 2-dimensional binning of each of the ship loads is then based on the H-T of the wave cycle causing this load cycle.

The mean μ and standard deviation σ of the binned loads in every cell results in a coefficient of variation $\text{COV} = \sigma/\mu$ of the ship loads. A straight line fit to this simulated COV vs. wave heights is referred to, in this study, as the empirical COV



(a) Sag Fatigue Damage



(b) Hog Fatigue Damage

Figure 4.17: Demonstration of impact of duration correction on predicted fatigue damage for sag and hog bending moments

(see Figures 4.18 and 4.19). Here T_1, T_2, T_3 refer to the 84, 50 and 16 percentile conditional periods given the wave heights (see Fig. 4.11 for actual values of these periods). In general, the COV values in the cells may depend on the bin size. In this study, however, we find that making the 2D bins 4 times smaller or make it 2 times as coarse, still results in about the same COV values, suggesting that COV dependence on bin size seems to be insensitive to a broad range of bin sizes.

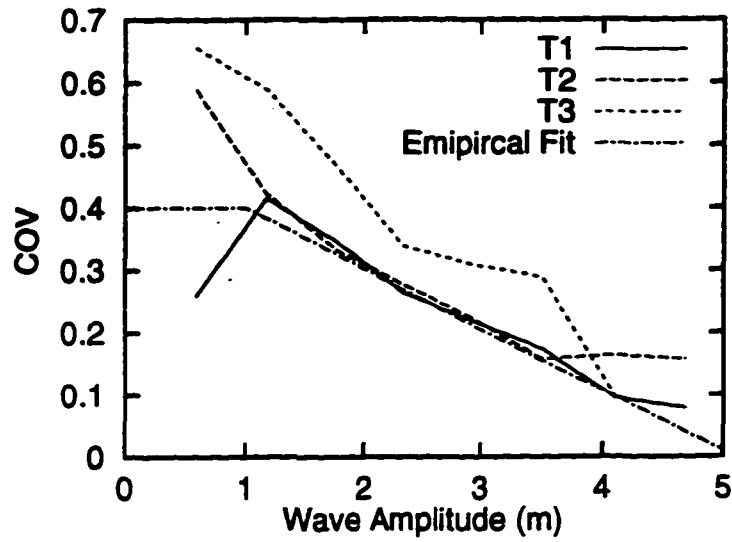
In order to understand the impact of scatter effects on fatigue damage prediction, we bin the simulated bending moments according to the chosen 30 pairs of wave parameters, and then compare the exact simulated damage to that estimated only from the mean simulated loads \bar{S} in the bins as done in the prediction models. The simulated damage without including scatter effects gives the total damage as

$$D_t = \sum_{j=1}^{N_p} n_j (\bar{S})_j^b \quad ; \quad n_j = \text{number of load cycles in cell } j \quad (4.23)$$

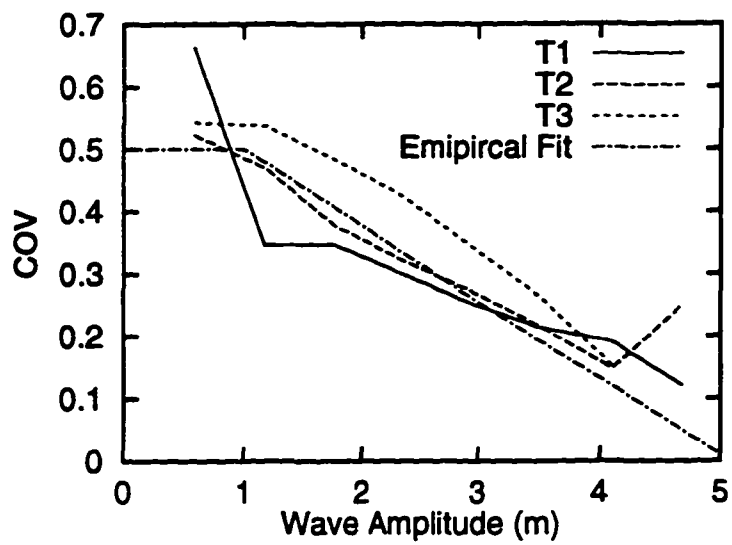
Figure 4.20 shows a ratio of total damage from this model (Eqn. 4.23) to the exact damage (Eqn. 4.9).

As seen, Eqn. 4.23 (damage without scatter effects) will underpredict the fatigue damage by as much as 25% for steel materials ($b = 4$) and by about 60% for composite materials ($b = 10$). Because of nonlinear effects, the hog loads are typically smaller than the sag loads (see Fig. 4.4), and so if scatter effects are ignored, the hog damage is affected more than sag; also the range (= sag + hog) dominated by sag contribution is influenced by the scatter effects in a manner similar to the sag load. As a simple example, the extent to which scatter effects matter can be seen when estimating $E[S^2]$ from \bar{S} :

$$E[S^2] = \text{Var}[S] + \bar{S}^2 = \bar{S}^2 (1 + \text{COV}^2) \quad (4.24)$$



(a) Sag Load



(b) Hog Load

Figure 4.18: Coefficient of Variation (COV) of simulated ship loads (sag and hog) for H-T cells in Fig. 4.11

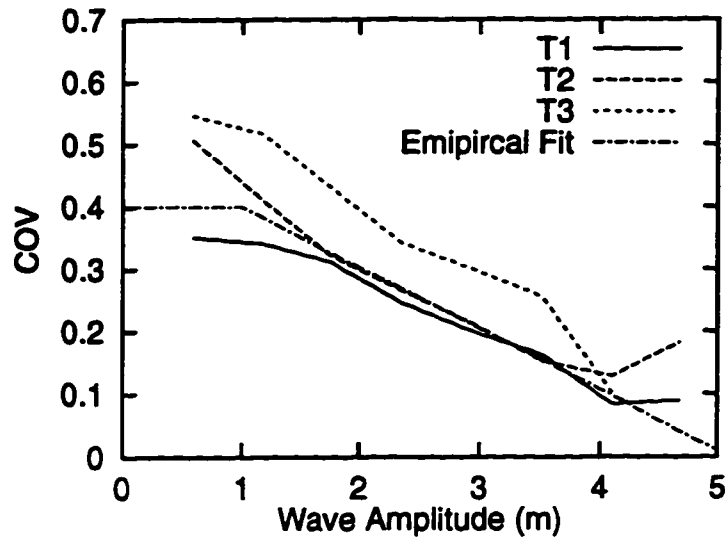


Figure 4.19: Coefficient of Variation (COV) of simulated ship loads (range) for H-T cells in Fig. 4.11

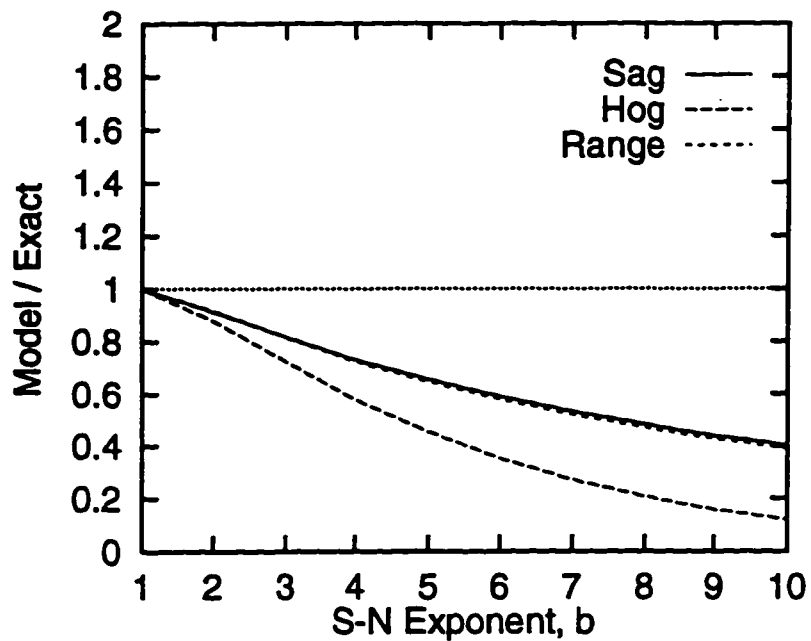
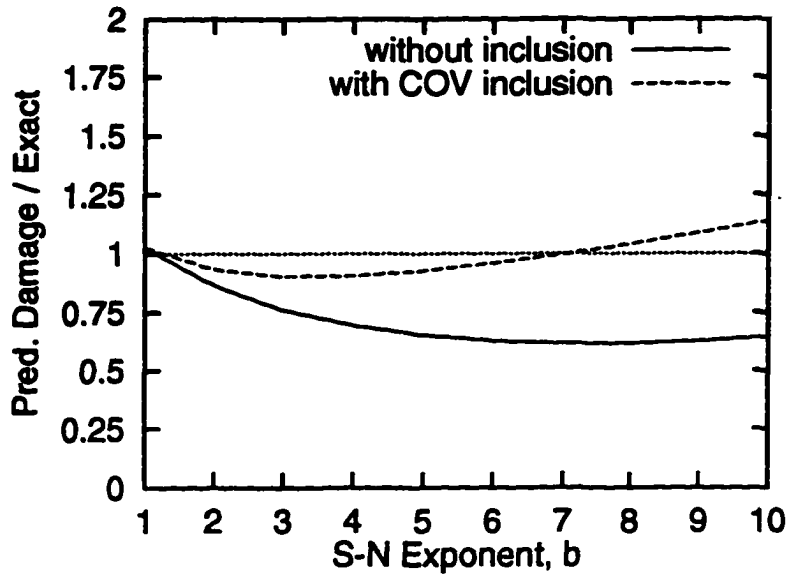


Figure 4.20: Demonstration of need for scatter estimate of response in H-T cells

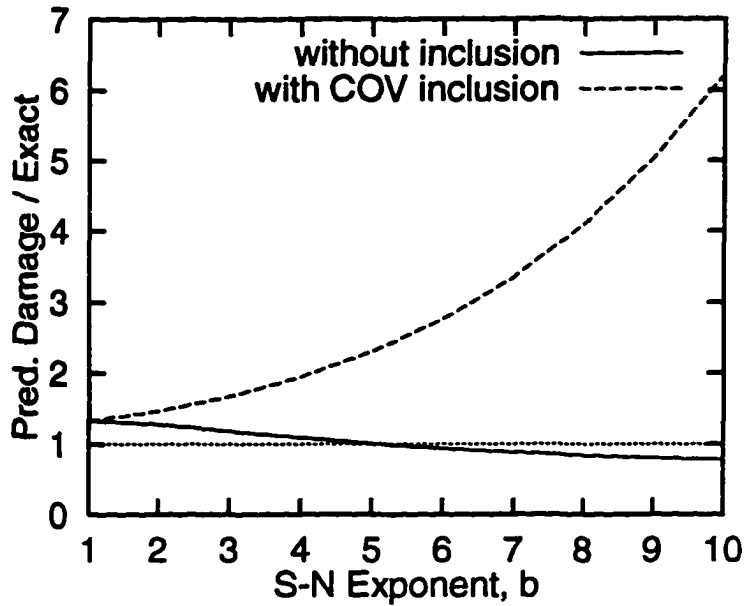
where $\text{Var}[S]$ denotes the variance of S . A factor $1 + \text{COV}^2$ larger than 1 is needed to inflate \bar{S}^2 to find $E[S^2]$ exactly; similarly, still larger factors will be required to estimate $E[S^b]$ from \bar{S}^b for $b > 2$. As demonstrated in the following sections, we strive to predict exact $E[S^b]$ from a Weibull model calibrated only to the first two moments of S .

In order to include scatter effects in the predicted damage, we use the NTF predicted bending moment in a cell and the empirical COV in that cell to calibrate a Weibull model for the load in that cell. For a Weibull load (S) model with shape parameter α and scale parameter β , the exceedance probability is $P[S > s] = \exp[-(s/\beta)^\alpha]$, where α and β are tuned to the NTF predicted bending moment and the COV in each cell. Fatigue damage, proportional to $E[S^b]$, is then found from this fitted Weibull model as $E[S^b] = \beta^b \Gamma(1 + b/\alpha)$. A weighted sum of this $E[S^b]$ across all the cells results in the total predicted fatigue damage.

Fig. 4.21 shows the predicted damage from the 30 wave triplets, including the empirical COV estimate, compared to exact damage for sag and hog bending moments. Inclusion of scatter effects for sag damage prediction, further improves the damage prediction. Now the predicted sag damage is within 10% error for all b 's shown in the plot. Again, compare this with the linear damage estimate in Fig. 4.5 that considerably underpredicts the sag damage. The hog damage, on the other hand, seems to be on the conservative side at all b values, on including the scatter effects. Note, however, that at $b = 1$ the hog damage is overpredicted by about 35%, implying that this may be a case where triplet-wave hog moment prediction is biased towards too large hog moments. We will investigate this in the next section, where we will compare the predicted moments to the mean simulated moment in each cell.



(a) Sag Fatigue Damage



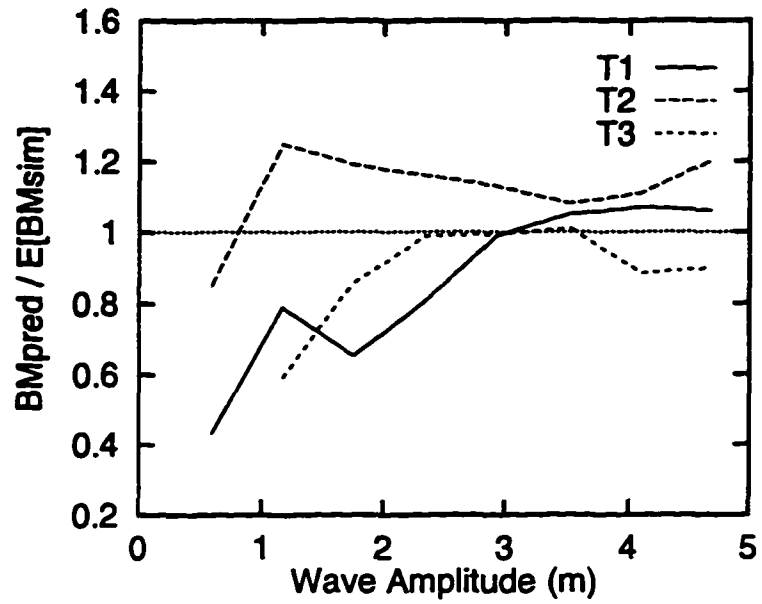
(b) Hog Fatigue Damage

Figure 4.21: Demonstration of impact of inclusion of scatter effects in the predicted fatigue damage for sag and hog bending moments

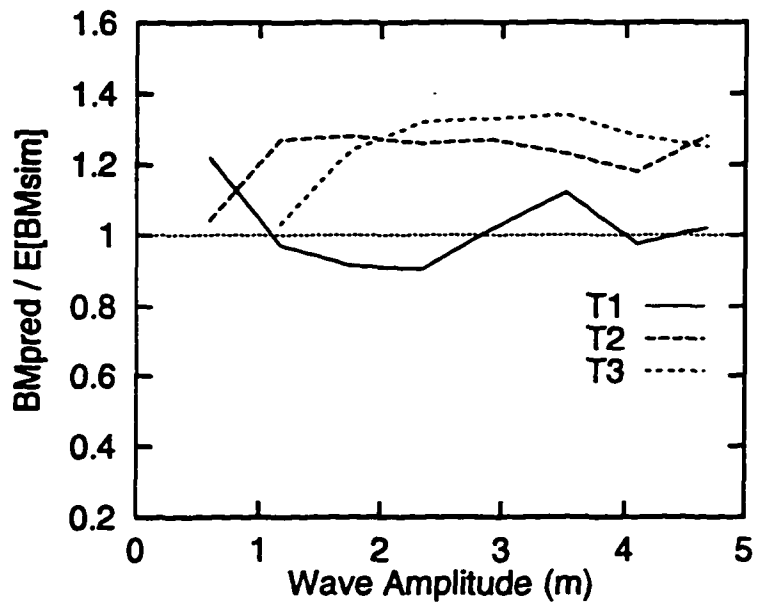
4.6.3 Inclusion of Bias Correction in the Prediction Model

To compare predicted bending moments to the simulated bending moments, we bin the 20 hours of nonlinear bending moments according to the 30 H, T pairs (shown in Fig. 4.11). Figures 4.22 and 4.23 show a comparison of the mean simulated bending moments to the predicted bending moments in each H, T cell as a function of $a = H/2$. In this figure, T1, T2, and T3 refer to the 16-, 50- and 84- percentile period values at the given H value (see Fig. 4.11 for actual values of the three periods given H). The predicted sag bending moment compares closely to the simulated sag moment, on average. This observation is in agreement with the close comparison we find for sag damage prediction at $b = 1$ in Fig. 4.21a. The hog bending moment is systematically overpredicted by approximately 20% and, consequently, the range bending moment is overpredicted by about 10%. These overpredictions may be due to an intrinsic limitation of the model in predicting hog moments from wave triplets. In any case, these overprediction factors can be treated as bias corrections to the predicted bending moments when estimating fatigue damage. As a result the predicted hog bending moments should be reduced by a factor of about 0.85 ($\approx 1/1.20$) and the range bending moment by a factor = 0.92 ($\approx 1/1.0$). The bias correction factors may also be found from Fig. 4.17b, where the model overpredicts the hog damage by approximately a factor of 1.35. Consequently the range (=sag+hog) moment will be overpredicted by a factor of about 1.175 [= (1+1.35)/2]. No bias correction will be applied to the sag bending moment damage prediction. We will now investigate the impact of these bias-corrections on fatigue damage.

Fig. 4.24 compares the predicted hog damage, with and without any bias correction, to exact damage. Note that all the hog damage predictions here include the scatter effects. As a result, the bias-corrected prediction is now from Weibull stress



(a) Sag Load



(b) Hog Load

Figure 4.22: Ratios of predicted to mean simulated (sag and hog) bending moments in H-T cells

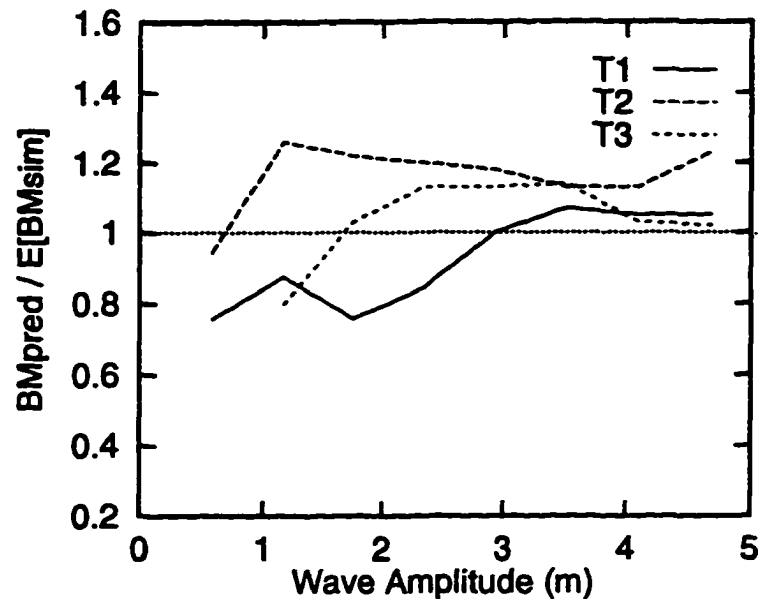


Figure 4.23: Ratios of predicted to mean simulated (range) bending moments in H-T cells

models in each cell, where α and β have been tuned to the bias-corrected hog bending moment and to the empirical COV from Figs. 4.18 and 4.19. Note how good the agreement in the predicted and exact damage is, when including the bias factor of 0.85. When a reduction factor of 0.75 is used, the first moment $E[S]$, of course, matches the exact value, however, damage for $b > 1$ seems consistently underpredicted. Further investigation on an optimum choice of the bias factor has not been done in this study. Realize, however, that in order to calibrate any bias-correction factor, a limited nonlinear analysis will have to be performed on irregular waves, as similarly required in obtaining the COV corrections.

Finally, we present a comparison of the NTF predicted damage together with the linear damage results compared to the nonlinear exact damage on the same plot. This is to directly study the difference in results. Note that no new results are

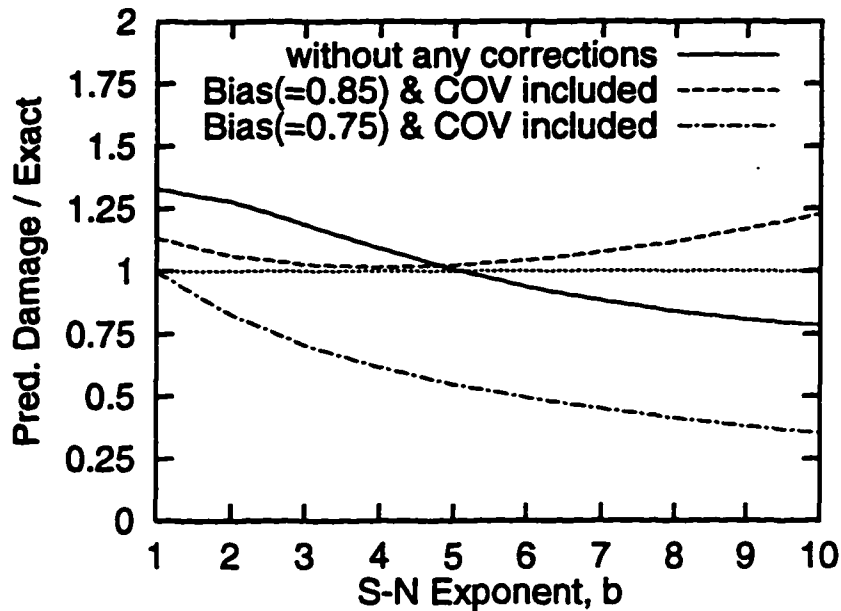


Figure 4.24: Effects of including bias-correction in hog damage prediction

being shown here, though. The NTF prediction includes bias-corrections for hog (factor=0.85) and range (factor=0.92) bending moments and includes the scatter effects for all three: sag, hog and range bending moments. Figures 4.25 and 4.26 show a comparison of total fatigue damage in 20 hours in this example seastate from the NTF model and from linear theory compared to simulated total nonlinear fatigue damage for a range of S-N exponents. Recall the significance of this example seastate is that according to linear theory it contributes most to the long-term fatigue damage (see Fig. 4.6) for an S-N exponent of 4. As seen in Fig. 4.25a, linear theory considerably underpredicts fatigue damage for sag bending moments, while the NTF model offers excellent prediction over the entire range of S-N exponents. For hog fatigue damage, the NTF prediction is much closer to simulation than is linear theory. For range bending moments, considered in damage prediction using Miner's rule, we

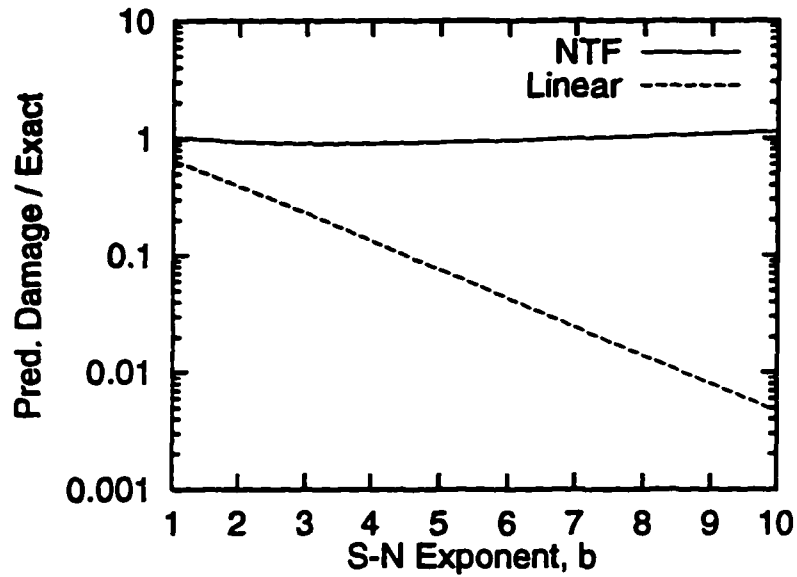
see that linear theory underpredicts damage while the NTF prediction is very close to simulation.

In summary, linear theory considerably underpredicts sag and range loads and damages, while the NTF model offers excellent agreement with the nonlinear loads and damages.

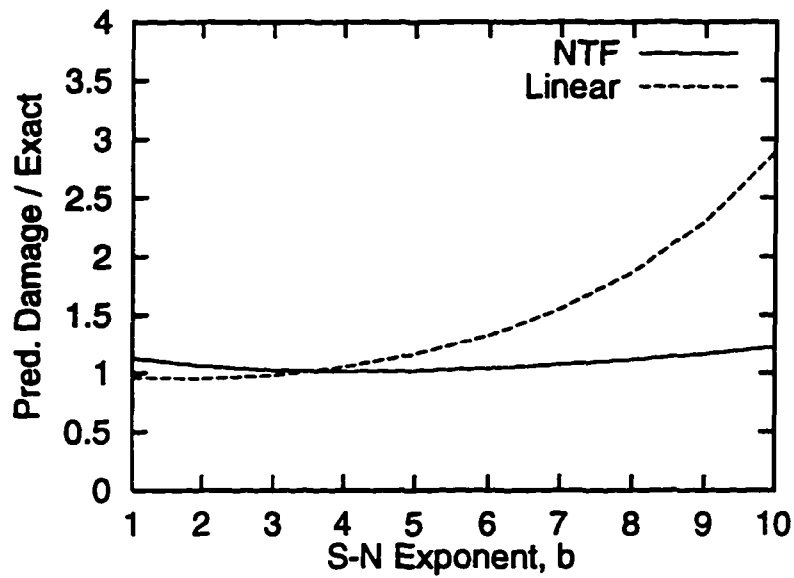
Note that the 20 hours of nonlinear irregular wave simulation used in this study took about 160 hours (≈ 6.5 days) of total computer time, while the NTF model without the COV or bias correction took only about 10 minutes of computer time. While the complete nonlinear analysis is only a 2-D analysis, a 3-D analysis of the nonlinear responses is predicted to take about 10 to 20 times longer than the 2-D analysis. In conclusion, the NTF model appears to offer an economical alternative to complete nonlinear time domain analysis for estimating fatigue damage.

4.7 Conclusions

In this study, we propose a “Nonlinear Transfer Function” model for estimating fatigue damage from a limited set of sinusoidal waves and their associated probabilities from stochastic process theory. A simple version of the NTF model, where for each selected wave height and wave period we construct side waves and apply the wave triplet on to the ship. The resulting set of stress (sag, hog, and range) for selected set of waves, along the theoretical probabilities of seeing the waves can be used to find predicted fatigue damage estimates. This damage estimate agrees well with that estimated from a complete random wave analysis, which is general is an expensive calculation. A linear analysis, on the other hand, appears to severely underpredict the sag-induced damage, while the hog damage seems to compare with the nonlinear



(a) Sag Fatigue Damage



(b) Hog Fatigue Damage

Figure 4.25: Linear, NTF, and Nonlinear Bending Moment Fatigue Damage for Range of S-N Exponents

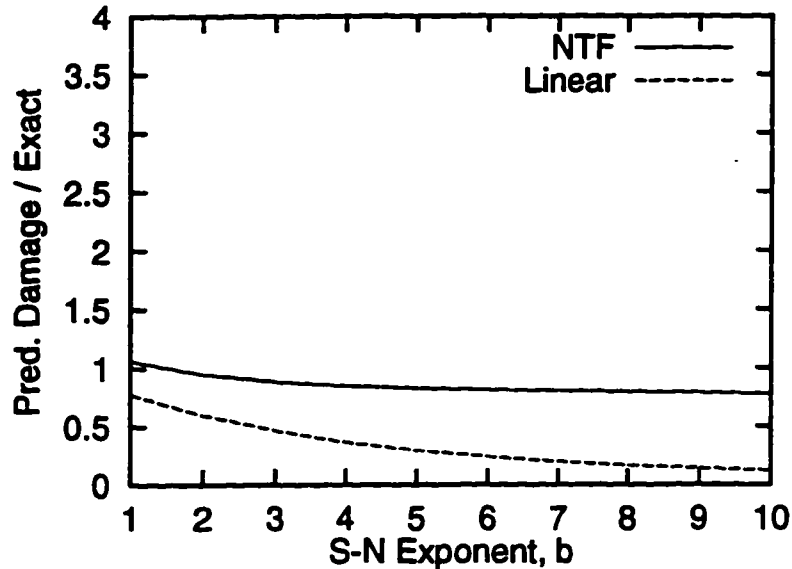


Figure 4.26: Linear, NTF, and Nonlinear Bending Moment (Ranges) Fatigue Damage for Range of S-N Exponents

time domain analysis in random waves. Note the NTF predicted damage took on the order of minutes of computer time, while the random wave analysis studied here took about 8 hours of computer to simulate 1 hour of stress time histories.

The agreement in the NTF prediction can be improved further by accounting scatter effects in the observed stresses. The hog damage estimation appeared to require a bias correction in addition. We propose use of short duration simulations in random waves in order to estimate the scatter effects and to estimate the bias factors for hog and range stresses. This still alleviates the need for long simulations to find exact fatigue damage estimates. For this flared ship in ship-length tuned seastate considered, we find the current state-of-the-art spectral analysis methods to yield considerably unconservative sag fatigue damage, and overpredict hog fatigue damage, and find that the NTF model offers a cheaper alternative and yields a more

precise estimate of fatigue damage when compared to that from nonlinear time domain analysis in random waves.

Further studies should be done to investigate generalities of this model: across different ship models, across different seastates. We speculate that the NTF model (single-triplet predictions) should be able to successfully predict damage in other seastates as well, since the seastate chosen here was supposed to severely test the model.

Chapter 5

Ship Fatigue Reliability

5.1 Introduction

This chapter describes a fatigue reliability analysis for the ship structure considered in Chapter 4. A general methodology for fatigue analysis is presented and numerical results are shown for a specific application to ship structures. The methodology presented here is largely adapted from [28].

5.2 General Fatigue Formulation

The assumption is that a complete reliability formulation generally includes uncertainty in three distinct aspects:

1. The loading environment, characterized here by random variables;
2. The gross level of structural response, given the load environment; and
3. The local failure criterion, given both the load and the gross stress response.

The general fatigue formulation requires three functional inputs: $f_{X_1}(x_1)$, $f_{S|X_1}(s|x_1)$ and $N_f(s)$ to characterize the load, response and fatigue damage, respectively. Here $f_{X_1}(x_1)$ is probability density of the environment variable X_1 , $f_{S|X_1}(s|x_1)$ is conditional probability density of the gross stress S given X_1 and $N_f(s)$ is the number of constant stress cycles with amplitude s after which the component fails. The mean damage rate \bar{D} is found by integrating over all load and response levels x_1 and s :

$$\bar{D} = \int_{x_1=0}^{\infty} \int_{s=0}^{\infty} \frac{f_{S|X_1}(s|x_1)f_{X_1}(x_1)}{N_f(s)} ds dx_1 \quad (5.1)$$

If failure is defined when damage reaches a threshold Δ , we have the time to fail

$$T_f = \Delta / (f_0 \bar{D}) \quad (5.2)$$

where f_0 is the stress cycle rate. If Miner's rule is correct we would assign $\Delta = 1$. More generally, variability in Δ would reflect the uncertainty in Miner's rule, i.e., the effect of predicting variable-amplitude fatigue behavior from constant-amplitude tests.

For the reliability analysis, the failure criterion is taken to be the difference between the computed fatigue life T_f in Eqn. 5.2 and a specified target lifetime, T_t .

$$G(X) = T_f - T_t \quad (5.3)$$

$G(X)$ is known as the failure state function that depends on all the associated random variables X . $G(X)$ is positive when the component is safe and negative when it has failed. First-order reliability methods (FORM) [36] can be used to find the failure probability, $P_f = \text{Prob.}[G(X) < 0]$.

We examine each of these in turn below for an offshore structure.

5.2.1 Load Environment

We assume that the long-term environment can be characterized by one environment variable X_1 . This could be H_s , the significant wave height describing the short-term climate conditions. A distribution of X_1 should be chosen to describe the long-term variation of the climate along the ship route (e.g., [10]). In this study, we choose the wave heights H , instead, as the environment variable X_1 , and describe it by a long-term Weibull distribution. Note that H is a local wave height that is the distance from the minimum elevation to the maximum elevation in wave cycle. Here, a wave cycle is the wave surface between two mean upcrossings.

In a short-term seastate with given H_s (typically lasting 1 to 6 hours), we assume H to be Forristall distributed (see Chapter 2). Note that in the ship fatigue analysis studies (Chapter 4), we had found that the Forristall model well predicted the simulated wave heights. This short-term distribution is given as

$$\text{Prob.}[H > h] = \exp \left[-\frac{(h/\sigma_\eta)^{2.126}}{8.42} \right] \quad (5.4)$$

in which $\sigma_\eta = H_s/4$. The long-term distribution $f_{LT}(h_{LT})$ of the wave heights can be found from the short-term Forristall distribution $f_{ST}(h|H_s)$ given H_s as

$$f_{LT}(h_{LT}) = \int_{h_s=0}^{\infty} f_{ST}(h|H_s) f_{H_s}(h_s) dh_s \quad (5.5)$$

in which $f_{H_s}(h_s)$ is the long-term distribution of H_s . To demonstrate the methodology in this study, we arbitrarily assume H_s to have a Weibull distribution with mean $E[H_s] = 3$ meters and variance $\text{Var}[H_s] = 3.6 \text{ m}^2$ [36]. $f_{LT}(h_{LT})$ in Eqn. 5.5 above,

is approximated to be a two-parameter distribution type. The two parameters are calibrated to the first two moments $E[H_{LT}]$ and $E[H_{LT}^2]$ of the long-term wave heights. These moments can readily be found from the conditional distribution as

$$E[H_{LT}] = E_{H_s}[E[H|H_s]]; \quad E[H_{LT}^2] = E_{H_s}[E[H^2|H_s]] \quad (5.6)$$

where $E_{H_s}[\]$ indicates taking expectation of random variable H_s . From these calculations we find the mean and the coefficient of variation (COV) of the long-term wave heights to be:

$$E[H_{LT}] = 1.81\text{meters} \quad \text{COV}[H_{LT}] = 0.857$$

5.2.2 Gross Response

The stress response at the location of interest is, in general, random in nature and dependent on the underlying environment X_1 . The stress may be described by a conditional distribution $f_{S|X_1}(s|x_1)$, which is assumed to be a two-parameter distribution type in this study. The two parameters are found from the conditional mean and standard deviation of the stress S given the environment variable X_1 denoted $S|X_1$.

For this study, we select the same ship as considered in Chapter 4 and use the nonlinear time domain analysis program NV1418 [13] to find the stresses in random wave conditions. We again select the seastate described by $H_s = 5\text{m}$ and $T_p = 10\text{s}$ to analyze the ship response. Recall that this was the most damaging seastate according to a linear analysis and expect to be so even according to a nonlinear analysis. The mean relation of $S|H$ found from this seastate should, generally, be applicable for

all wave heights H regardless of the seastate. The wave period dependence of the stresses (ignored in this study) may, however, effect the scatter of stresses about the mean regression line; and this scatter is likely to be seastate- or T_p -dependent.

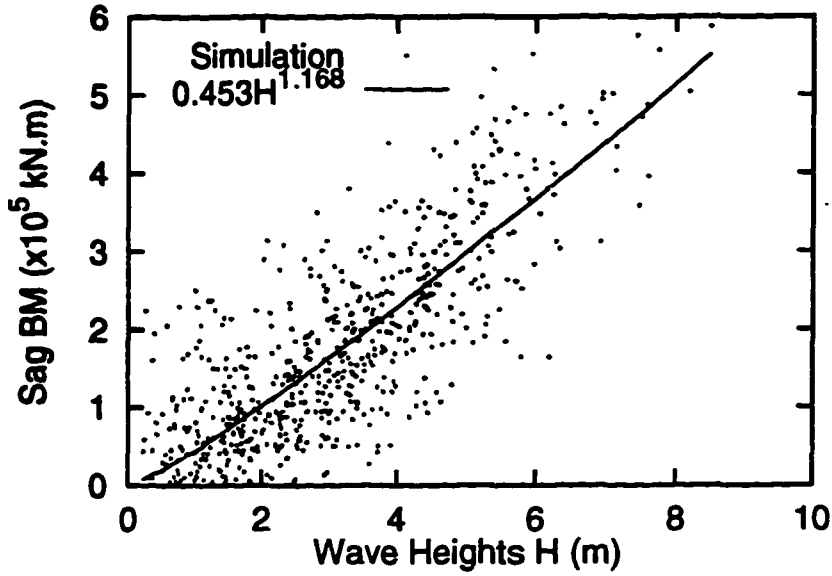
For each wave height in this one hour seastate we find the corresponding bending moments (sag, hog, and range) in the response history. A regression analysis of the form $E[S|H] = aH^p$ was performed, to fit the mean bending moment (or stress S) given H . We used a nonlinear least-squares regression method called Levenberg-Marquardt method [48] as implemented in Gnuplot [68] to estimate the mean values of the parameters a , p , their standard errors σ_a , σ_p and correlation ρ_{ap} for this data set. The standard errors reflect the uncertainty in the estimated parameters due to limited data. The regression assumed a constant conditional standard deviation $\sigma_{S|H}$, although this scatter should generally increase with increasing wave heights. In this illustration, we assume that the bending moment can be converted to stresses by simply dividing by an appropriate section modulus.

Note that the regression is based on only one seastate, the most damaging seastate. The mean regression line is assumed to be valid across all the seastates. The variability of stresses $\sigma_{S|H}$ about this mean trend, in general, may vary across different seastates. In this example, however, we will assume no uncertainty in the estimated $\sigma_{S|H}$.

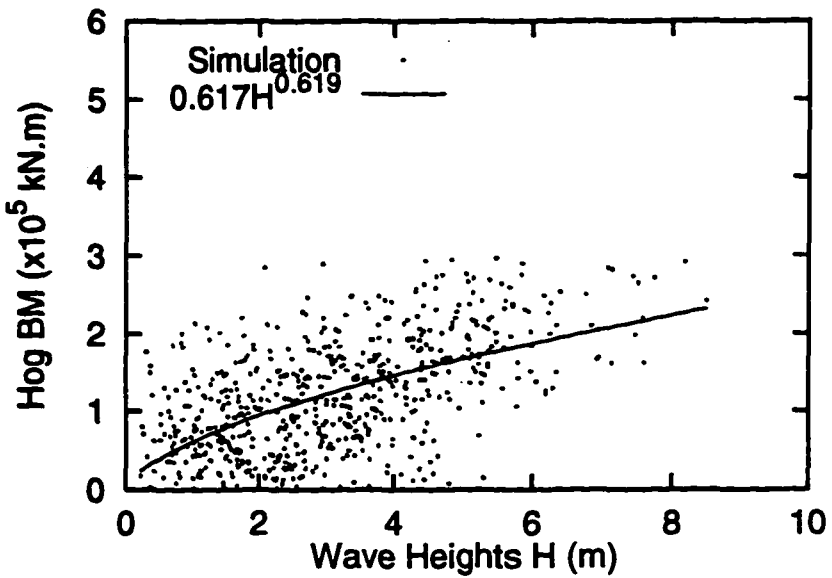
As mentioned earlier, from one hour simulation of bending moments in irregular seas ($H_s = 5\text{m}$ and $T_p = 10\text{s}$), we relate the wave heights to the corresponding sag, hog, and range bending moments (BM) assuming the following functional form:

$$E[\text{BM}|H] = aH^p \quad (5.7)$$

Figs. 5.1 and 5.2 show the resulting regression fits to the simulated bending moments. Table 5.1 gives the numerical values of the estimated parameters.



(a) Sag bending moment



(b) Hog bending moment

Figure 5.1: Nonlinear least squares regression analysis to fit sag, and hog bending moments to wave heights from 1 hour simulation of bending moments in seastate with $H_s = 5\text{m}$, and $T_p = 10\text{sec}$.

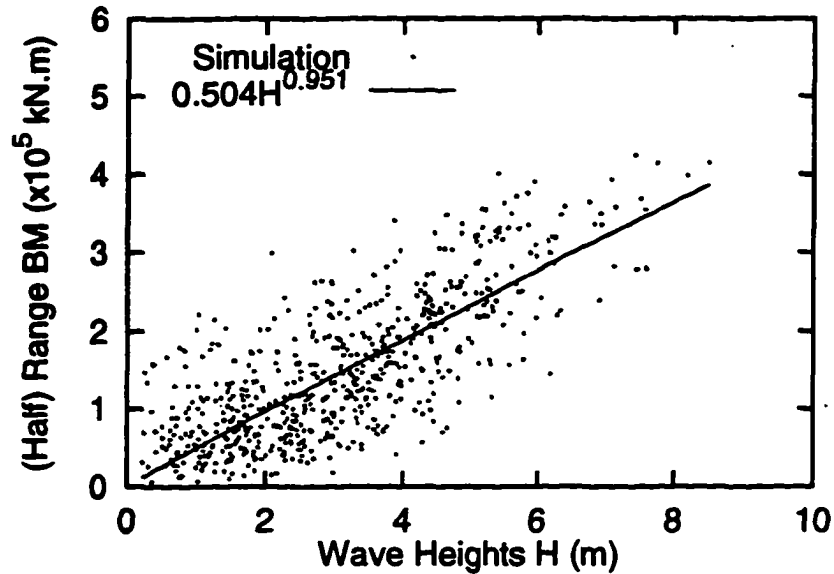


Figure 5.2: Nonlinear least squares regression analysis to fit half-range bending moments to wave heights from 1 hour simulation of bending moments in seastate with $H_s = 5\text{m}$, and $T_p = 10\text{sec}$.

In converting the bending moments to stresses we will use a constant section modulus ($= 35 \text{ m}^3$, here). In the subsequent reliability analysis, we will additionally multiply the stresses by 10^{-3} to convert to units of MPa (or N/mm^2) so as to consistently use the S - N data also given in MPa.

5.2.3 Failure Measure

We assume that fatigue test data are available at constant stress amplitudes to estimate the S - N curves. These curves present the number of stress cycles to fail for a given constant stress amplitude load on the fatigue specimen. We use Miner's rule to assign damage $1/N_f(s)$ due to a single stress amplitude s . The fatigue damage is then characterized by \bar{D} , the mean damage rate. Any variation about the mean rate

Table 5.1: Estimated mean and standard deviation of the regression parameters for bending moments (kN.m) given wave heights. The bending moments have been divided by 10^5 .

Moment	a	σ_a	p	σ_p	ρ_{ap}	$\sigma_{S H}$
Sag	0.453	0.0284	1.168	0.0404	-0.972	0.746
Hog	0.617	0.0354	0.619	0.0410	-0.945	0.593
Half-Range	0.504	0.0276	0.951	0.0366	-0.965	0.592

will average out when accumulating damage across the high-cycle fatigue applications of interest here. As a result the fatigue damage is characterized by only the mean damage rate \bar{D} , and hence by only the S-N curve.

As described in Chapter 4, typically the S-N curve is specified as

$$N = CS^{-b} \quad (5.8)$$

where C , b are the intercept and the slope of the fitted curve to $\log S$ to $\log N$ data. In general, both C and b are random in nature and C typically shows a large uncertainty – COV of the order of 50 to 60%. The regression relation gives the mean number of stress loading cycles N with amplitude S that a fatigue specimen can tolerate before failing [14]. Typical values of b for steel material may be 3–6, and may be as high as 7–10 for composite materials. Values of S-N parameters for offshore structure materials and their uncertainties can be found in various literature, including API [2] and SSC reports [43] among others.

5.3 Results

5.3.1 Numerical Values for Random Variables in Fatigue Analysis

Recall that the sag stresses cause fatigue cracks at the ship bottom and the hog stresses cause fatigue cracks in the ship deck. Other approaches use the stresses due to the range bending moments to analyze the fatigue cracks at either of these locations. Of interest is the fatigue reliability of an element (here, at the ship bottom or the ship deck) in a specified lifetime. We will show that using the sag, hog or range stresses generally leads to different estimates of reliability or the probability of failure.

The input random variables in the example fatigue analysis and their values are given in Table 5.2. The random variables listed here are common to the three stress cases (sag, hog, and range) we consider here. The COV values in Table 5.2 have been arbitrarily chosen and should generally reflect the uncertainty in the parameters either due to limited data or due to lack of knowledge. The parameters relating stresses to wave heights are given in Table 5.1. To calibrate the median time to fail \tilde{T}_f to a desired lifetime, we introduce an additional factor δ in Eqn. 5.2 so that we have

$$T_f = \delta \frac{C\Delta}{f_0(SCF)^b} \quad (5.9)$$

In this equation, we set all the random variables to their median values and calibrate δ so that we get $\tilde{T}_f = 200$. Table 5.3 gives the values for δ for each of the three cases.

Using the above random variables, we performed a FORM analysis to find the failure probabilities for a range of specified target lifetimes. In order to find the failure

Table 5.2: Numerical values of means and COVs of random variables and their distribution types used in fatigue formulation. These are common to all three stresses: sag, hog and range.

Variable	Mean	COV	Dist. Type	Description
$E[X_1]$	1.81 (m)	0.05	Normal	Mean of Long-term H
$COV[X_1]$	0.857	0.1	Normal	COV of long-term H
f_0	0.1 (Hz)	0.2	Normal	Stress cycle rate
SCF	2.5	0.1	Normal	Stress concentration factor
C	2.4×10^{15}	0.5	Weibull	S-N factor
b	4	0	-	S-N exponent
Δ	1	0.1	Normal	Damage threshold

Table 5.3: Calibrated factor δ for the three cases: sag, hog and range. Note that δ is a deterministic variable.

Variable	Sag	Hog	Range
δ	1.232	0.0213	0.0826

probabilities, all the random variables X are first transformed into a uncorrelated normal U -space. The failure state function $G(X) = 0$ is evaluated in the normal U -space and gradient search methods are employed to find where it is closest to the origin, also known as the design point. Approximation of the failure probability is obtained by fitting a tangent plane (first-order reliability method, FORM) and a parabola (second-order reliability methods, SORM) to the failure state function at the design point. The direction cosines of the vector that defines the design point are the relative measures of the importance of each of the random variables.

Fig. 5.3 compares these failure probabilities for the three different cases. The P_f estimates are somewhat different for the three stress cases. For a given target lifetime, the sag stress gives the largest P_f followed by range stress, and then the hog stress. Even though the median time to fail is the same in all the three cases, we see

such a difference because of the different conditional trends of the stresses given the wave heights that imply different magnification of the wave parameter uncertainty. Since the sag trend shows the largest nonlinearity, the wave parameter uncertainty is amplified the most among the three and this results in the largest P_f for given service lifetime. For example, at around the typical design life of 20 years, the sag case gives $P_f = 0.014$, the range case gives $P_f = 0.011$, while the hog case gives $P_f = 0.0086$. Recall that hog stresses may cause cracks in the ship deck, while the sag stresses cause cracks in the ship bottom. The P_f comparison then implies that the element at the ship deck is about 1.6 times as likely to fail compared to the ship bottom element, even though both have $\check{T}_f = 200$ years.

5.3.2 Importance Factors of Physical Random Variables

Table 5.4 gives the values of the random variables at the design points and their uncertainty contributions (squares of the direction cosines) for each of sag, hog and range cases.

The values of the random variables at the design point can be used to design the structural element and the FORM analysis would predict the design to yield the reliability level as indicated in Fig. 5.3 for a service life of 20 years. This table also indicates the relative importance or uncertainty contributions of the different random variables. In all the three cases, we see that the S-N factor C carries the most importance, followed by the SCF and the environment variables. The environmental variables seem to be relatively more important in the sag case than in the hog case. This again is due to the nonlinearity in the stress to wave height relation where the sag stress amplifies the uncertainty contribution of the environment variables more than the hog stress. In the range case, the environment importance seems to be between

Table 5.4: Values of associated random variables at “failure” point and their uncertainty contributions (for Service life of 20 years)

Sag Case		
Var.	Value	Uncert. Contrib.
$E[X_1]$	1.846	0.032
$COV[X_1]$	0.9296	0.148
a	0.4491	0.004
p	1.175	0.004
f_0	0.1064	0.021
SCF	2.660	0.085
C	5.363E+14	0.700
Δ	1.210	0.006

Hog Case		
Var.	Value	Uncert. Contrib.
$E[X_1]$	1.830	0.009
$COV[X_1]$	0.8790	0.012
a	0.6166	0.000
p	0.6214	0.004
f_0	0.1067	0.020
SCF	2.668	0.079
C	3.458E+14	0.871
Δ	0.02093	0.006

Half-Range Case		
Var.	Value	Uncert. Contrib.
$E[X_1]$	1.840	0.021
$COV[X_1]$	0.9087	0.069
a	0.5015	0.002
p	0.9555	0.002
f_0	0.1066	0.021
SCF	2.665	0.082
C	4.216E+14	0.798
Δ	0.08115	0.006

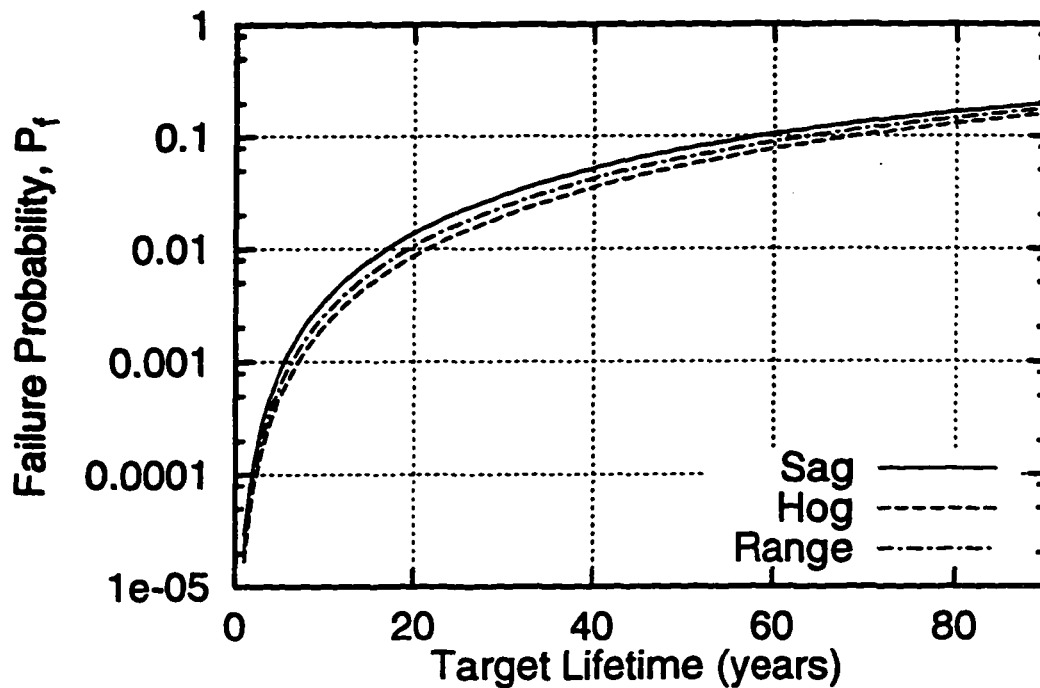


Figure 5.3: Failure probabilities for a range of target lifetimes for the three stresses: sag, hog and range

the sag and hog cases.

In the next section, we illustrate how techniques based on FORM – in particular, the inverse FORM method – can be used in design of fatigue-sensitive components. For purposes of illustration, we focus on a two variable case which assumes only the values of SCF and of C to be uncertain. The general approach can be extended to a larger number of variables, however.

5.4 Selection of Material Properties in Design to Achieve Desired Reliability

In the previous section, we saw that the stress concentration factor SCF and the S-N factor C seemed be of most importance compared to the other associated random variables in the fatigue analysis (especially true in the hog stress case). Here we demonstrate a methodology to select the SCF and C values for an element design, assuming these two variables carry all of the importance. This selection is to be based on the objective of achieving a certain given reliability β in the fatigue design.

5.4.1 Forward FORM

We first restate the forward FORM problem, where the analysis proceeds as shown in the previous section for sag, hog and range stresses. Here, the distributions of SCF and C are specified and we find the resulting reliability level from FORM analysis. Eqn. 5.2 can be rewritten as

$$T_f = \frac{C\Delta}{f_0 \text{SCF}^b E[S^b]} \quad (5.10)$$

in which we assumed \bar{D} is given as $E[S^b]/C$ scaled by the SCF. In this example, we will model the only uncertain parameters, SCF and C, as independent lognormal variables:

$$\text{SCF} = \check{K} \varepsilon_{\text{SCF}} ; \quad C = \check{C} \varepsilon_C \quad (5.11)$$

in which \check{K} and \check{C} are the median values of the random variables SCF and C, respectively. ε_{SCF} and ε_C are unit median lognormal variables with coefficients of variation V_{SCF} and V_C , respectively. The remaining parameters in Eqn. 5.10 are assumed to be

deterministic. We can rewrite T_f as

$$T_f = \check{T}_f \frac{\epsilon_C}{\epsilon_{SCF}^b} \quad (5.12)$$

in which \check{T}_f now indicates the median time to fail. Recall this was taken to be 200 years in the fatigue analysis example. Note that the assumption of only two variables that are independent and lognormally distributed is not critical here.

The $G(X)$ function 5.3 can be conveniently rewritten as

$$G(X) = \log\left(\frac{T_f}{T_t}\right) = \log\left(\frac{\check{T}_f \epsilon_C}{T_t \epsilon_{SCF}^b}\right) = \log\left(\frac{\gamma \epsilon_C}{\epsilon_{SCF}^b}\right) \quad (5.13)$$

where $\gamma = \check{T}_f/T_t$ is a ratio of a design lifetime to a specified service lifetime. Larger γ values indicate smaller service lifetimes compared to the design lifetime.

For the forward FORM problem, we choose $\gamma = 10$ implying the design life is 10 times the service life and assume $V_{SCF} = 0.1$, $V_C = 0.5$ (as in the earlier example). The S-N exponent $b = 6$, say. We find the failure probability to be $P_f = 1.27 \times 10^{-3}$ or reliability $\beta = 3.02$ and the design point is $\epsilon_C^* = 0.41$, $\epsilon_{SCF}^* = 1.267$. This says that we need to choose about 41% of the median C value (S-N curve) and should increase the median SCF by about 27% to get a β of 3.02. If we wish to use another material (another b value), we will need to rerun the forward FORM analysis to find the resulting reliability. This reliability will be different than 3.02, in general. Now, in a design scenario, where we wish to achieve a specified β value and then find the design point ϵ_C^* and ϵ_{SCF}^* when using different materials, it is easier to solve the inverse FORM problem.

5.4.2 Inverse FORM

The idea of an inverse FORM analysis is to select the design parameters to achieve a certain given reliability β . This idea has been demonstrated earlier to provide environmental contours for structural response analysis [74] of offshore structures against ultimate collapse limit states. This idea also finds application in earthquake engineering [4] where magnitude-distance contours are provided for performing probabilistic seismic hazard analysis of structures.

The first issue in the inverse FORM analysis is to find the locus of all points in the normal U -space each of which would yield the same probability of failure for a failure state function passing through the point as a tangent line. This locus of points for the two-variable case happens to be a circle of radius β around the origin. This is shown in Fig. 5.4, where the dashed line indicates $G(X) = 0$. The circle in U -space (U_1, U_2) can be transformed to the physical space (ε_C and ε_{SCF}) by first transforming U_1 marginally and then conditionally transforming U_2 using the given distribution functions of the physical variables. The transformed circle is what we call as a “material” contour.

Note that the material contour only depends on the distributions of ε_C and ε_{SCF} . This contour can be estimated regardless of the S–N exponent b and regardless of the design life to service life ratio γ . Given this contour, one can now design against a worst-case scenario. In this case, we search along the contour for the largest possible γ (minimum fatigue life) for a desired b value. Usually the physics of the problem gives a good insight into where this design point might be on the contour, in which case the search can be localized to a smaller region.

For the example problem in this study, Fig. 5.5 shows the resulting material contour for SCF and C for a $P_f = 1.27 \times 10^{-3}$ ($\beta = 3.02$). Recall this was the

reliability achieved in the forward FORM problem and so will also serve as a check of the inverse FORM problem. When we search this contour with a selected $b = 6$ (see Fig. 5.6), we find that design point turns out to be exactly at $\varepsilon_C^* = 0.41$ and $\varepsilon_{SCF}^* = 1.267$ and $\gamma = 10$ (reported as γ in the figure). Recall that these are exactly the same as the forward FORM values, confirming the inverse FORM formulation. Fig. 5.6 also shows how the design point will vary when selecting different material exponents b . For example, if b is chosen to be 3, then the design requires a smaller $\varepsilon_C^* \approx 0.3$ and smaller $\varepsilon_{SCF}^* \approx 1.17$ (i.e., more conservative C and less conservative SCF) to achieve the same $\beta = 3.02$. Recall that a smaller b value implies that the fatigue life is less sensitive to the load (SCF) versus the S-N curve variability. Note also that for $b = 3$ the element can survive for a longer duration (smaller γ) compared to $b = 6$. On the other hand, for $b = 9$ we find larger ε_C and ε_{SCF} (i.e. less conservative C and more conservative SCF) are needed compared to $b = 6$ in order to achieve $\beta = 3.02$. The fatigue life now reduces to about 1/20th of the median life when increasing b to 9.

5.5 Conclusions

In this short study on fatigue reliability applied to ship structures, we demonstrate a method to find the probability of failure or the reliability of a structural element by considering uncertainties at various levels: the environment, load given the environment, and the material strength of the element. Given estimates of the associated random variables, first- and second-order reliability methods can be used to efficiently predict the reliability of the system and to locate the design point.

Conversely, inverse FORM techniques can be used to find the design values of the

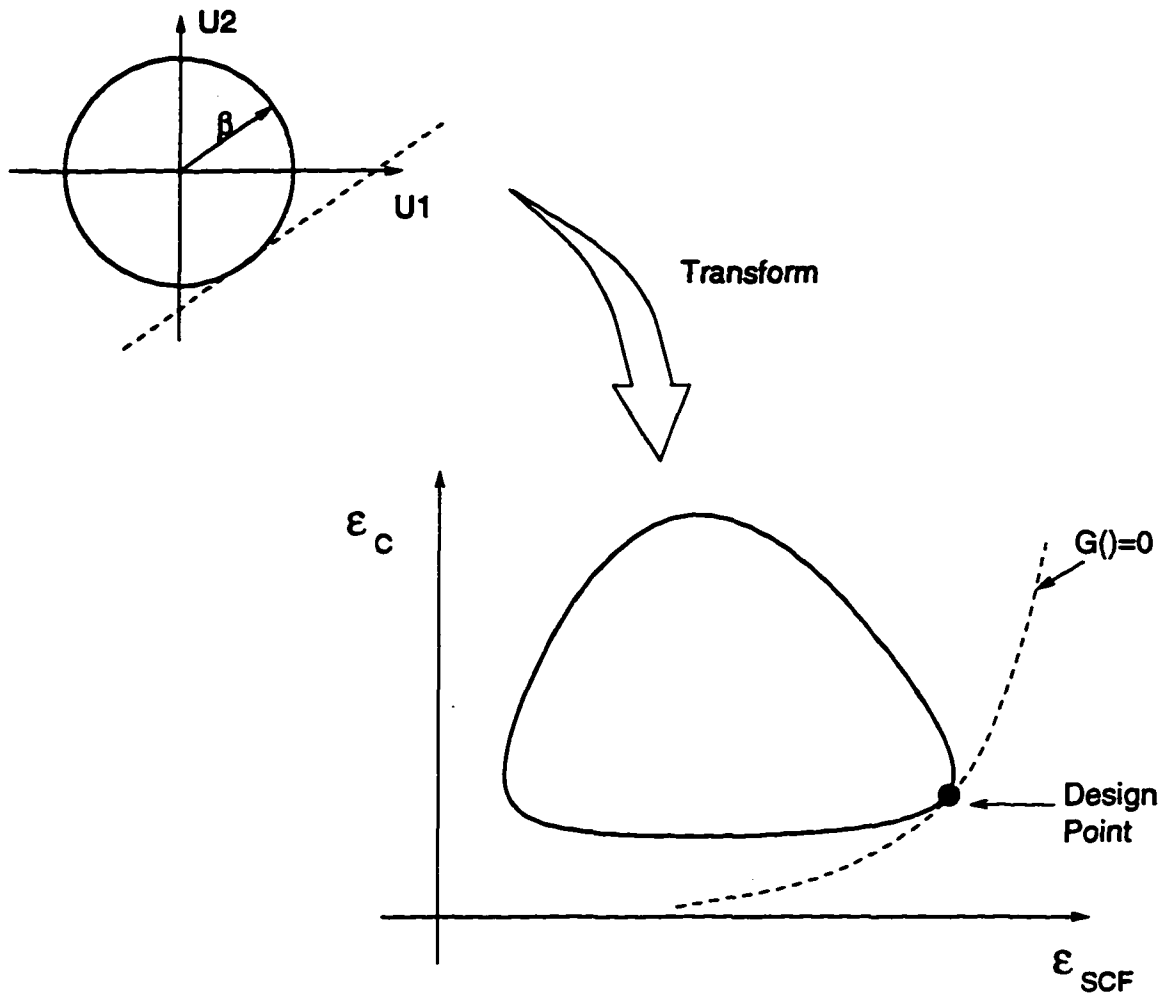


Figure 5.4: Transformation of standard normal variables (U_1 and U_2) to physical variables ϵ_C and ϵ_{SCF} to find material contour

random variables so that a pre-selected reliability level may be achieved in the design. This was successfully demonstrated for the two variable (SCF and C) example, and can, in general, be extended to more number of variables.

The above fatigue reliability analyses can be extended to include the NTF scheme to predict fatigue damage using the long-term distribution of the wave height H and

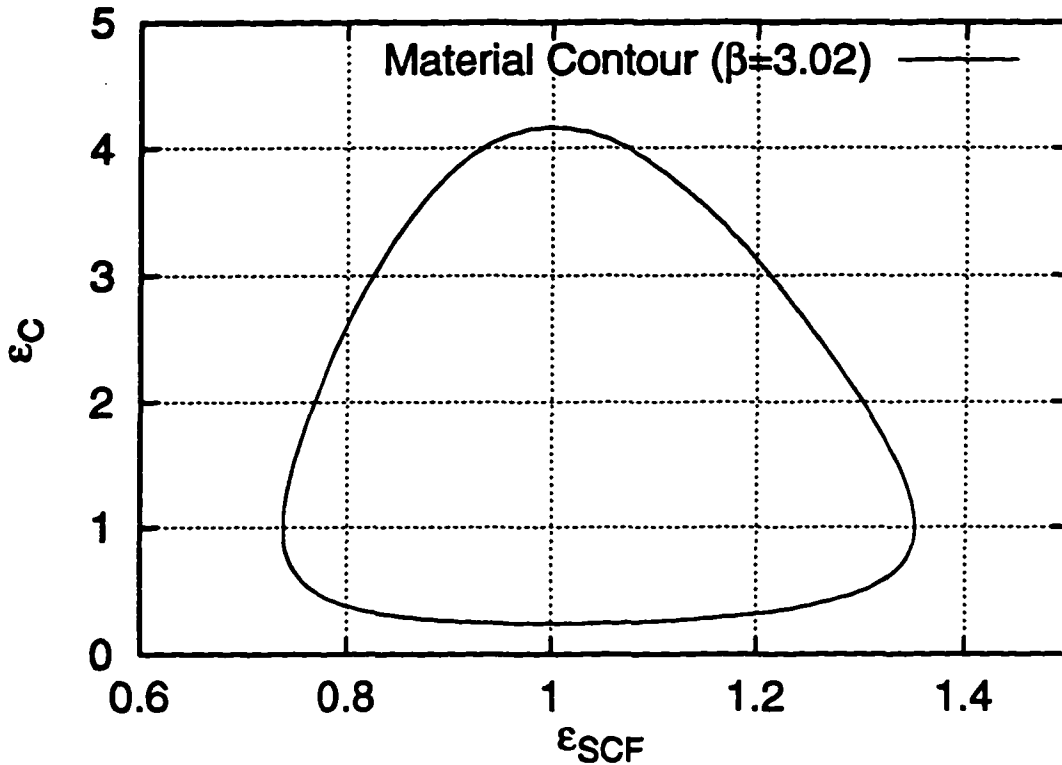


Figure 5.5: Material contour: Locus of points of ϵ_C and ϵ_{SCF} for which FORM method gives a reliability $\beta = 3.02$

periods T . Such a scheme can be easily implemented in the FORM analysis.

Alternatively, we could assume the ship load (mid-ship bending moment) to be the result of a second-order nonlinear system, and given the wave input seek to identify the first- and second-order transfer functions that define the system. Once these transfer functions are estimated, we can readily find the moment-influence coefficients (see Chapter 2: Eqn. 2.6 and 2.7) for the given seastate parameters (H_s, T_p). Using these moments, we can calibrate a distribution of the stresses and then find the resulting fatigue damage in this seastate. The long-term damage can be found by

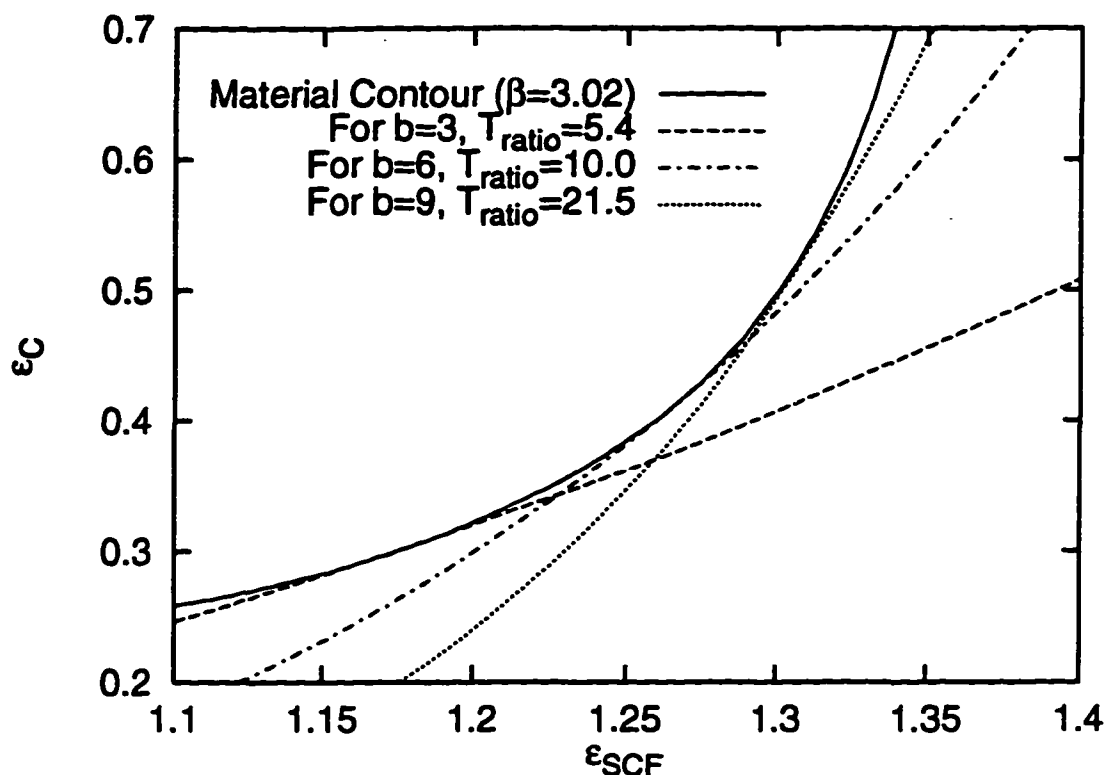


Figure 5.6: Design choices of ϵ_C and ϵ_{SCF} for different S-N exponents b that result in desired reliability $\beta = 3.02$

summing such damage estimates across a set of selected seastate parameters [57, 61]. These parameters may be selected, for example, at the quadrature points of the joint distribution of the parameters to efficiently calculate the long-term damage.

Chapter 6

Summary and Recommendations

In this chapter, we summarize the important conclusions in this dissertation and propose directions for future work.

6.1 Nonlinear Random Ocean Waves

Summary

We applied second-order random wave models to investigate the nonlinearities in measured waves (for both wave tank data and ocean field measurements). We found that the second-order model predictions compared well with wave tank results and the agreement was even better in the case of field measurements. We proposed convenient analytic formulations for skewness and kurtosis of waves as a function of the parameters (H_s, T_p, d) characterizing the climate conditions and the water depth at the site of interest. We also proposed simple analytic crest height distributions based on these predicted moments and found these predicted distributions to compare closely

with the measured results. We developed a computer program to simulate second-order nonlinear waves. Given a measured time history, this program can also identify the underlying first-order wave component which when run through the second-order predictor produces a resultant time history that agrees with the measured history at every time point.

Future Work

In order to test the limitations of this model, we suggest comparison of predictions from this second-order model across more severe climate conditions. We found that while the field results were well-predicted, the wave tank crest heights seemed to be underpredicted by the second-order wave model. A more detailed investigation of the wave tank data may help explain these results. Recall that the wave tank data comprised of 2 hour measurements and a hypothesis is that these measurements are long enough to be nonstationary. A way to confirm this hypothesis may be to investigate shorter segments of the 2 hour histories and compare model predictions to measured statistics from these smaller segments. As pointed earlier, scaling down of the waves in the tank may also be a source of error, particularly so when generating waves in severe storms.

For the wave tank data, we found that the prediction of the marginal PDF of the wave elevations was in closer agreement with the measured results than the wave crest predictions. This may suggest that the discrepancy in the wave elevation does not explain the larger discrepancy in the wave crests. A discrepancy, if any, in the comparisons of the upcrossing rates or the velocities of the second-order simulated histories to the measured results may help explain the larger discrepancy in the crest heights.

We found that the cubic Hermite model (using observed moments) slightly underpredicts the crest heights in the two to three σ_η range even though it quite accurately predicts the elevations for the wave tank data. Note that the Rayleigh crests are transformed in this Hermite prediction and consequently assumes an underlying narrow-band process. We could, instead, simulate corresponding Gaussian waves from the measured spectrum in an attempt to reflect the measured bandwidth; and transform the Gaussian elevations at every time point using the cubic Hermite model with moments of the measured history. A comparison of the crest distribution of this transformed history with the observed crest results will indicate the impact of bandwidth effects on the crest height distribution. Note here that we are attempting to preserve both the observed moments and the observed bandwidths.

Finally, estimation of extreme crest heights for a desired return period (for airgap design) could be based on inverse FORM ideas.

6.2 Spar Floating Platform

Summary

We applied second-order nonlinear wave loads on a rigid-body model of the spar to predict global horizontal displacements of the spar floating platform. We compared these to measured displacements in wave tank tests due to random waves reflecting 100-year storms in Gulf of Mexico and North Sea sites. The potential difficulties in predicting the responses included: (1) the apparent transient response seen in the hourly measurements, and (2) the few measured cycles of the slow-drift displacement components. We surveyed four prediction models: (1) nonlinear diffraction forces only, (2) diffraction forces plus wave drift damping effect, (3) model 2 plus additional

viscous forces due to undisturbed waves, and (4) model 2 plus viscous forces from disturbed waves. The diffraction force model seemed to underpredict the observed mean offset, so that the inclusion of viscous effects led to an improved prediction of the mean offset. The four models generally give good agreement with observed results and even seem to predict the apparent mode-swapping. Model 4 appears to better predict the occurrence of these mode-swapping times as well.

Future Work

The first proposal is to perform additional investigations in an effort to further improve the agreement between the predicted and measured results. We could, for example, investigate half-hour measurements instead of the hourly measurement in an attempt to identify effects of nonstationarity on predicted response. Another interesting study would be to quantify the mode-swapping effects seen in the measured histories using a moving window. We could study a ratio of the rms surge to pitch response across these windows and develop a strategy for identify the occurrence of mode-swapping ranges in the time history. We could similar scheme to the predicted history as well and the compare it to measured results.

In the model formulations, we suggest investigating other schemes to calibrate the damping ratios in the four prediction models. For example, we could tune the damping estimates to match the rms of the measured response, instead of the spectral bandwidth as used in this study. The model accuracy can then be gauged by comparing the predicted and measured spectral bandwidths. The methods studied in this dissertation can be extended to other responses, for example, the heave response of the spar in random waves to design the airgap of the spar.

Given successful comparison of predicted results to measurement, the model can

be applied, for example, to perform a fatigue or ultimate strength analysis of the spar. We could use these to develop load and resistance design factors for the limit states considered.

6.3 Nonlinear Ship Loads

Summary

In this study, we compared fatigue damages from a linear to a nonlinear analysis of a monohull ship with flared cross-sections at the ends. Although a linear analysis permits a quick estimate of mean fatigue damage, we find that it underpredicts the corresponding damage from a nonlinear analysis. This was shown for the most damaging seastate according to a linear analysis. The nonlinear analysis used here is based on a 2-D strip theory where we integrate water pressures to the instantaneous wetted surface on the ship. The fatigue damage is due to the tensile stresses caused by the gross mid-ship bending moments. We applied an NTF (“Nonlinear Transfer Function”) model to efficiently predict fatigue damage. This damage is much closer to the damage estimate from a nonlinear analysis than is the damage from a linear analysis. In the example seastate demonstrated in the thesis, the 20 hours of simulated stresses from the nonlinear analysis about 6 days of computer time on a HP 900 workstation, while the NTF model took on the order of minutes to predict fatigue damage. We further improved these NTF predicted damage by introducing empirical corrections. For sag-induced damage, these corrections were to account for the random nature of stress due to a wave with a given a wave height and wave period. For hog-induced damage, we additionally included a bias correction. It is suggested that as part of the NTF model, these empirical corrections be obtained from limited

random wave runs of the nonlinear analysis.

Future Work

The NTF predictions were compared to the nonlinear analysis results in a single seastate. We suggest additional comparisons be performed in other seastates as well; and finally compare the long-term predicted damage from the NTF model to simulated long-term damage from the nonlinear analysis. The nonlinear analysis could be performed across a set of climate conditions (H_s, T_p) with probabilities chosen to reflect the long-term distribution of these parameters. The simulated damage in each of these seastates could be weighted and summed to result in a long-term damage from the nonlinear analysis. The NTF model, on the other hand, may be used to predict fatigue from a selected set of wave heights and wave periods whose occurrence probabilities reflect the long-term distribution of the wave parameters. The nonlinear stresses from these selected waves can then be used to predict the long-term NTF fatigue damage. An agreement in these two long-term damage estimate will further test the NTF model capabilities. We could similarly predict and compare long-term fatigue damage from a linear analysis as well to demonstrate performance of linear analysis in predicting long-term fatigue damage.

As part of the future work, we also recommend that the NTF model studies be generalized to other seastates, other loads on the ship, other ship models, and to other ship analysis programs. Finally, impact of nonlinearities in the waves on fatigue in ship can be investigated by analyzing the ship in waves simulated from the second-order wave model, instead of using linear (Gaussian) waves.

6.4 Ship Fatigue Reliability

Summary

In this study, we demonstrated a fatigue reliability analysis of a ship structure by integrating uncertainties at three levels: (1) the environment, (2) the structural response given the environment, and (3) the resistance properties of the structural element. We estimated the failure probability P_f (probability of fatigue life being less than a specified service life) from the associated random variables using a FORM (“First-Order Reliability Method”) analysis. We showed an inverse FORM analysis scheme to select the design parameters (stress concentration factor SCF and S–N factor C) given a target failure probability.

Future Work

In modeling the response (S) given the environment (H) denoted as “ $S|H$ ”, we chose the form $E[S|H] = aH^p$, in which a and p were found from regression analysis using one hour of stress simulation in a specific seastate. This was the most damaging seastate according to a linear analysis. We suggest investigating the impact on P_f when using simulations in other seastates to estimate a and p .

Another suggestion is to extend the fatigue reliability analysis to include the NTF scheme to predict fatigue damage using the long-term distribution of the wave height H and periods T . Such a scheme can be easily implemented in the FORM analysis.

Alternatively, we could assume the ship load (mid-ship bending moment) to be the result of a second-order nonlinear system, and given the wave input seek to identify the first- and second-order transfer functions that define the system. Once these transfer functions are estimated, we can readily find the moment-influence coefficients (see

Chapter 2: Eqn. 2.6 and 2.7) for the given seastate parameters (H_s , T_p). Using these moments, we can calibrate a distribution of the stresses and then find the resulting fatigue damage in this seastate. The long-term damage can be found by summing such damage estimates across a set of selected seastate parameters [57, 61]. These parameters may be selected, for example, at the quadrature points of the joint distribution of the parameters to efficiently calculate the long-term damage.

Bibliography

- [1] ABS. Guide for dynamic based design and evaluation of bulk carrier structures. Technical report, American Bureau of Shipping, New York, NY, USA, 1995.
- [2] American Petroleum Institute. *Recommended Practice for Planning, Designing and Constructing Fixed Offshore Platforms - Load and Resistance Factor Design 2A-LRFD (RP 2A-LRFD)*, first edition edition, 1993.
- [3] K. Anastasiou, R. G. Tickell, and J. R. Chaplin. The nonlinear properties of random wave kinematics. In *Proceedings of the 3rd International Conference on behavior of offshore structures*. MIT, Massachusetts, 1982.
- [4] P. Bazzurro, S.R. Winterstein, T.C. Ude, and C.A. Cornell. Magnitude-distance contours for probabilistic seismic hazard analysis. In *7th ASCE Probabilistic Engineering Mechanics Conference*, Worcester, Massachusetts, 1996.
- [5] R. F. Beck and A. Magee. *Developments in Marine Technology: 7: Dynamics of Marine Vehicles and Structures in Waves*, chapter Time-Domain Analysis for Predicting Ship Motions. Elsevier Science Publishers B. V., Amsterdam, 1991.
- [6] T. Børresen. NV1418- time domain solution of large-amplitude ship motions in head seas: Users manual. Technical Report 81-0575, Det Norske Veritas, Oslo, Norway, 1981.

- [7] A. Canavie, M. Arhan, and R. Ezraty. A statistical relationship between individual heights and periods of storm waves. In *Proceedings BOSS'76*, volume 2, Trondheim, Norway, 1976.
- [8] DNVC. Fatigue assessment of ship structures. Technical Report 93-0432, Det Norske Veritas Classification AS, Høvik, Norway, 1994.
- [9] Vanmarcke E. Properties of spectral moments with applications to random vibration. *Journal of Engineering Mechanics*, 98, 1972.
- [10] Bitner-Gregersen E.M., E.H. Cramer, and R. Loseth. Uncertainties of load characteristics and fatigue damage of ship structures. In *Offshore Marine and Arctic Engineering OMAE, Safety and Reliability*, volume II, 1993.
- [11] O. M. Faltinsen. *Sea Loads on Ships and Offshore Structures*. Cambridge University Press, 1990.
- [12] G. Z. Forristall. On the statistical distribution of wave heights in a storm. *Journal of Geophysical Research*, 83(C5):2353–2358, 1978.
- [13] F. Frimm. Implementation of irregular waves into program NV1418. Technical report, Veritas Marine Services (U.S.A), Inc., 1991.
- [14] H. O. Fuchs and R. I. Stephens. *Metal Fatigue in Engineering*. John Wiley & Sons, 1980.
- [15] P.F. Hansen and Winterstein S.R. Fatigue damage in the side shells of ships. *Marine Structures*, 8:631–655, 1995.

- [16] R. E. Haring, A. R. Oseborne, and Spencer L.-P. Extreme wave parameters based on continental shelf storm wave records. In *Proceedings of the 15th Coastal Engineering Conference*, pages 151–170, 1976.
- [17] K. Hasselmann. On the non-linear energy transfer in a gravity-wave spectrum. *Journal of Fluid Mechanics*, (12):481–500, 1962.
- [18] S. Haver and K. A. Nyhus. A wave climate description for long term response calculations. In *Proceedings of the 5th OMAE Symposium*, number IV, pages 27–34. American Society of Mechanical Engineers, 1986.
- [19] S.-L. J. Hu and D. Zhao. Non-Gaussian properties of second-order random waves. *Journal of Engineering Mechanics*, 199(2):344–364, 1993.
- [20] N. E. Huang, S. R. Long, C-C. Tung, Y. Yuan, and L. F. Bliven. A non-Gaussian statistical model for surface elevation of nonlinear random wave fields. *Journal of Geophysical Research*, 88(C12):7597–7606, 1983.
- [21] R. T. Hudspeth and M.-C. Chen. Digital simulation of nonlinear random waves. *Journal of the Waterway, Port, Coastal and Ocean Division*, 105(WW1):67–85, 1979.
- [22] H.O. Jahns and J.D. Wheeler. Long-term wave probabilities based on hindcasting of severe storms. *Journal of Petroleum Technology*, pages 473–486, April 1973.
- [23] A. K. Jha and S. R. Winterstein. Simulation and identification of second-order random waves. Technical Report RMS-22, Reliability of Marine Structures Program, Stanford University, Dept. of Civil Engineering, 1996.

- [24] A.K. Jha. QTF surface spline interpolation: A pre-processor to TFPOP. Technical report, Reliability of Marine Structures, 1996. In TFPOP report RMS-18.
- [25] M.H. Kim and D.K.P. Yue. The complete second-order diffraction solution for an axisymmetric body. Part 1: Monochromatic incident waves. *Journal of Fluid Mechanics*, 200:235–264, 1989.
- [26] M.P. Kim and D.K.P. Yue. Sum- and difference-frequency wave loads on a body in unidirectional gaussian seas. *Journal of Ship Research*, 35(2):127–140, 1991.
- [27] D. C. Kring. *Time Domain Ship Motions by a 3-Dimensional Rankine Panel Method*. PhD thesis, Massachusetts Institute of Technology, May 1994.
- [28] C.H. Lange and Winterstein S.R. Fatigue reliability: Formulation and analysis. Technical Report RMS-13, Reliability of Marine Structures, Civil Engineering Department, Stanford University, 1994.
- [29] R. S. Langley. A statistical analysis of non-linear random waves. *Ocean Engineering (Pergamon)*, 14(5):389–407, 1987.
- [30] W.-M. Lin, M. J. Meinhold, N. Salvesen, and D. K. P. Yue. Large-amplitude motions and wave loads for ship design. *20th Symposium on Naval Hydrodynamics*, August 1994.
- [31] W. M. Lin and D. K. P. Yue. Numerical solutions for large-amplitude ship motions in the time domain. In *18th Symposium on Naval Hydrodynamics*. University of Michigan, Ann Arbor, MI, USA, 1990.
- [32] G. Lindgren and I. Rychlik. Wave characteristic distributions for gaussian waves. *Ocean Engineering*, 9:411–432, 1982.

- [33] M. S. Longuet-Higgins. The effect of non-linearities on statistical distributions in the theory of sea waves. *Journal of Fluid Mechanics*, 17(3):459–480, 1963.
- [34] M. S. Longuet-Higgins. On the joint distribution of the period and amplitude of sea waves. *Journal of Geophysical Research*, 80:2688–2694, 1975.
- [35] M. S. Longuet-Higgins. On the joint distribution of wave periods and amplitudes in a random wave field. In *Proceedings of the Royal Society of London*, number A389, pages 241–258, April 1983.
- [36] H. O. Madsen, S. Krenk, and N. C. Lind. *Methods of Structural Safety*. Prentice-Hall, Inc., New Jersey, 1986.
- [37] MARINTEK. TLP hydrodynamic model tests. Technical Report 511138.01, MARINTEK Trondheim, Norway, 1989.
- [38] MARINTEK. TLP hydrodynamic model tests. Technical Report 511217.01, MARINTEK Trondheim, Norway, 1990.
- [39] T. Marthinsen and S. R. Winterstein. On the skewness of random surface waves. In *Proceedings of the 2nd International Offshore and Polar Engineering Conference, San Francisco*, pages 472–478. ISOPE, 1992.
- [40] Massachusetts Institute of Technology, Department of Ocean Engineering, Cambridge. *SWIM: Users Manual*.
- [41] B. B. Mekha, D. C. Weggel, C. P. Johnson, and J. M. Roesset. Effects of second order diffraction forces on the global response of spars. In *ISOPE*, 1996. To appear.

- [42] B.B. Mekha, C.P. Johnson, and J.M. Roesset. Nonlinear response of a spar in deep water: Different hydrodynamic and structural models. In *5th International Offshore and Polar Engineering Conference (ISOPE)*, volume III, pages 462–469, The Hague, The Netherlands, 1995.
- [43] W. H. Munse, T. W. Wilbur, M. L. Tellalian, K. Nicoll, and K. Wilson. Fatigue characterization of fabricated ship details for design. Technical Report SR-1257, Ship Structure Committee, U.S. Coast Guard, Washington, D.C., August 1982.
- [44] D. E. Nakos and P. D. Sclavounos. Ship motions by a three-dimensional rankine panel method. In *Proceedings of the 18th Symposium on Naval Hydrodynamics*, Ann Arbor, Michigan, 1990.
- [45] J.N. Newman. Second order, slowly varying forces on vessels in irregular waves. In Bishop R.D. and Price W.G., editors, *Proc. Int. Symp. Dynamics of Marine Vehicles and Structures in waves*, pages 182–186. Mechanical Engineering Publications, 1974.
- [46] OTRC. Spar model test: Joint industry project - final report, volume I. Technical report, Offshore Technology Research Center, 1995.
- [47] A. Papoulis. *Probability, random variables and stochastic processes*. McGraw-Hill, Inc., 1991.
- [48] W.H. and Teukolsky S.A. Press, Vetterling W.T., and Flannery B.P. *Numerical recipes in FORTRAN: The art of scientific computing*. Cambridge University Press, second edition edition, 1992.
- [49] Z. Ran, M.-H. Kim, J.M. Niedzwecki, and R.P. Johnson. Responses of a spar platform in random waves and current. In *5th International Offshore and Polar*

- Engineering Conference (ISOPE)*, volume III, pages 363–371, The Hague, The Netherlands, 1995.
- [50] M. Schetzen. *The Volterra and Wiener Theories of Nonlinear Systems*. John Wiley & Sons, New York, 1980.
- [51] J. N. Sharma and R. G. Dean. *Development and evaluation of a procedure for simulating a random directional second order sea surface and associated wave forces*. PhD thesis, University of Delaware, July 1979.
- [52] C. Sundararajan, editor. *Probabilistic Structural Mechanics Handbook: Theory and Industrial Applications*. Chapman & Hall, New York, 1995.
- [53] SWIM 2.0. *SWIM: Slow Wave-Induced Motions– User’s Manual*. Dept. of Ocean Engineering, M.I.T., 1995.
- [54] M. A. Tayfun. Narrow-band nonlinear sea waves. *Journal of Geophysical Research*, 85(C3):1548–1552, 1980.
- [55] L. J. Tick. A non-linear random model of gravity waves I. *Journal of Mathematics and Mechanics*, 8(5):643–651, 1959.
- [56] R. Torgaus. *Extreme response of nonlinear ocean structures: Identification of minimal stochastic wave input for time-domain simulation*. PhD thesis, Stanford University, 1996.
- [57] T. C. Ude. Second-order load and response models for floating structures: Probabilistics analysis and system identification. Technical Report RMS–16, Reliability of Marine Structures, Dept. of Civil Engr., Stanford University, 1994.

- [58] T. C. Ude, S. Kumar, and S. R. Winterstein. Stochastic response analysis of floating structures under wind, current, and second-order wave loads. Technical Report RMS-18, Reliability of Marine Structures, Civil Engineering Department, Stanford University, 1996.
- [59] T. C. Ude and S. R. Winterstein. Calibration of models for slow drift motions using statistical moments of observed data. In *6th International Offshore and Polar Engineering Conference ISOPE*, 1996.
- [60] T.C. Ude, A.K. Jha, and Winterstein S.R. QTSTAT: Statistics of second-order systems. MAXMIN: Extremes of non-gaussian processes. Technical Report TN-1, Reliability of Marine Structures, 1993.
- [61] T.C. Ude and S.R. Winterstein. Predicting fatigue damage matrices for floating structures across multiple seastates: The DamMat routine. Technical report, Civil Engr. Dept., Stanford University, 1996.
- [62] J.K. Vandiver and A.B. Dunwoody. A mathematical basis for the random decrement vibration signature analysis technique. *ASME Journal of Mechanical Design*, 1981. Paper No. 81-DET-13.
- [63] T. Vinje and S. Haver. On the non-Gaussian structure of ocean waves. In *Proceedings of the 7th International Conference on the Behaviour of Offshore Structures (BOSS)*, volume 2, pages 453-480, 1994.
- [64] WAMIT 4.0. *WAMIT: A Radiation-Diffraction Panel Program for Wave-Body Interactions-User's Manual*. Dept. of Ocean Engineering, M.I.T., 1995.
- [65] WAVESHIP, 6.1. *Wave Loads on Slender Vessels - Users Manual*. Det Norske Veritas - SESAM, Høvik, Norway, 1993.

- [66] D.C. Weggel and J.M. Roesset. Second-order dynamic response of a large spar platform: Numerical predictions versus experimental results. In *15th International Conference on Offshore Mechanics and Arctic Engineering (OMAE)*, Florence, Italy, 1996. ASME.
- [67] J.D. Wheeler. Method for calculating forces produced by irregular waves. *Journal of Petroleum Technology*, pages 359–367, March 1970.
- [68] T. Williams and C. Kelley. *GNU PLOT: Public-domain interactive plotting program*. Internet URL http://www.cs.dartmouth.edu/gnuplot_info.html.
- [69] S. R. Winterstein. Nonlinear effects of ship bending in random seas. Technical Report 91-2032, Det Norske Veritas, Oslo, Norway, 1991.
- [70] S. R. Winterstein, E. M. Bitner-Gregersen, and K. O. Ronold. Statistical and physical models of nonlinear random waves. In *OMAE - Volume II, Safety and Reliability*, pages 23–31. ASME, 1991.
- [71] S. R. Winterstein and A. K. Jha. Random models of second-order waves and local wave statistics. In *Proceedings of the 10th Engineering Mechanics Speciality Conference*, pages 1171–1174. ASCE, 1995.
- [72] S. R. Winterstein, T. C. Ude, and G. Kleiven. Springing and slow-drift responses: Predicted extremes and fatigue vs. simulation. In *Proceedings of the 7th International Conference on the Behaviour of Offshore Structures (BOSS)*, volume 3, pages 1–15, 1994.
- [73] S. R. Winterstein, T. C. Ude, and T. Marthinsen. Volterra models of ocean structures: Extreme and fatigue reliability. *Journal of Engineering Mechanics, ASCE*, 120(6):1369–1385, 1994.

- [74] S.R. Winterstein, T.C. Ude, P. Bazzurro, and C.A. Cornell. Ocean environment contours for structural response analysis and experiment design. In *7th ASCE Probabilistic Engineering Mechanics Conference*, Worcester, Massachusetts, 1996.

Appendix A

Appendix: Methodology of First-order Wave Identification

The idea here is to identify the implied first-order history $\eta_1(t)$ (of an observed history $\eta_{\text{obs}}(t)$) which, when run through the second-order predictor, yields an incident wave that agrees with $\eta_{\text{obs}}(t)$. The reader is referred to [23] for details on the algorithm.

In the first-order wave process $\eta_1(t)$, see Eqn. 2.2, written as a Fourier sum of N frequencies,

$$\eta_1(t) = \sum_{k=1}^{N/2} A_k \cos(\omega_k t + \theta_k) = \sum_{k=1}^N X_k e^{i\omega_k t} \quad (\text{A.1})$$

we need to identify only the lower half X_k components, since the upper half values are complex conjugates of the lower half. Let us denote $X_k = U_k + iV_k$, where U_k, V_k are the real and imaginary parts of the complex Fourier component X_k , respectively.

The predicted second-order wave process (see Eqn. 2.4) as evaluated from the QTFs is

$$\Delta\eta_2(t) = 2\text{Re} \sum_{m=1}^{N/2} \sum_{n=1}^{N/2} X_m X_n H_{mn}^+ e^{i(\omega_m + \omega_n)t} + X_m X_n^* H_{mn}^- e^{i(\omega_m - \omega_n)t} \quad (\text{A.2})$$

This may be rewritten in the form of a Fourier sum as

$$\Delta\eta_2(t) = \sum_{k=1}^N Y_k e^{i\omega_k t} \quad (\text{A.3})$$

where $Y_k = Y_k^+ + Y_k^-$ are the combined sum and difference frequency components. Here again, Y_k possesses conjugate symmetry so that only the lower half contains unique information. Y_k^+ can be shown to be

$$\begin{aligned} Y_k^+ &= \sum_{m+n,k} X_m X_n H_{mn}^+ \\ &= \sum_{m+n,k} [(U_m U_n - V_m V_n) + i(V_m U_n + U_m V_n)] H_{mn}^+ \end{aligned} \quad (\text{A.4})$$

where the summation symbol indicates a double summation

$$\sum_{m+n,k} = \sum_{m=1}^{N/2} \sum_{n=1}^{N/2} \quad \text{such that } \omega_m + \omega_n = \omega_k \quad (\text{A.5})$$

and

$$\begin{aligned} Y_k^- &= \sum_{m-n,k} X_m X_n^* H_{mn}^- \\ &= \sum_{m-n,k} [(U_m U_n + V_m V_n) + i(V_m U_n - U_m V_n)] H_{mn}^- \end{aligned} \quad (\text{A.6})$$

where

$$\sum_{m-n,k} = \sum_{m=1}^{N/2} \sum_{n=1}^{N/2} \quad \text{such that } |\omega_m - \omega_n| = \omega_k \quad (\text{A.7})$$

The combined predicted wave process is

$$\eta_{\text{pred}}(t) = \eta_1(t) + \Delta\eta_2(t) \quad (\text{A.8})$$

The identification scheme strives to simultaneously match $\eta_{\text{pred}}(t)$ to the observed wave history $\eta_{\text{obs}}(t)$ at every value of t . Alternatively, we can perform the identification in the frequency domain and strive to simultaneously match the predicted Fourier components to the observed Fourier components at all frequencies.

$\eta_{\text{obs}}(t)$ can be represented in the frequency domain as

$$\eta_{\text{obs}}(t) = \sum_{k=1}^N Z_k e^{i\omega_k t} \quad (\text{A.9})$$

where Z_k 's also possess conjugate symmetry. If the first-order components are identified exactly, from Eqn.s A.1, A.3 and A.9 we will have

$$Z_k = X_k + Y_k \quad ; \quad \text{for all } k = 1 \dots N/2 \quad (\text{A.10})$$

Note that the upper half values can be obtained from conjugate symmetry of the lower half values. In the Newton-Raphson identification scheme we will try to simultaneously minimize $X_k + Y_k - Z_k$; for $k = 1 \dots N/2$ to achieve convergence. Now, this scheme requires a Jacobian of $X_k + Y_k - Z_k$ with respect to the unknowns X_k —such a complex differentiation will lead to numerical discontinuities so we will minimize an equivalent real function $\sqrt{\sum_1^N f_k^2 / N}$ instead, where for $k = 1 \dots N/2$

$$\begin{aligned} f_k &= \text{Re}(X_k + Y_k - Z_k) \\ f_{k+N/2} &= \text{Im}(X_k + Y_k - Z_k) \end{aligned} \quad (\text{A.11})$$

The identification of the lower half X_k values requires a simultaneous solution of the nonlinear equations in A.11 such that $f_k \rightarrow 0$ for all $k = 1 \dots N$, or alternately

$\sqrt{\sum_1^N f_k^2/N} \rightarrow 0$. We will formulate the Newton-Raphson scheme in vector form as

$$\mathbf{f} = \left[\frac{\text{Re}\mathbf{X}}{\text{Im}\mathbf{X}} \right] + \left[\frac{\text{Re}\mathbf{Y}}{\text{Im}\mathbf{Y}} \right] - \left[\frac{\text{Re}\mathbf{Z}}{\text{Im}\mathbf{Z}} \right] \quad (\text{A.12})$$

where bold face letters denote vectors, and vectors $\mathbf{X}, \mathbf{Y}, \mathbf{Z}$ contain the complex Fourier components $X_k, Y_k, Z_k, k = 1 \dots N/2$, respectively. Here, $\left[\frac{\text{Re}\mathbf{X}}{\text{Im}\mathbf{X}} \right]$ is a vector containing the real part of \mathbf{X} in the upper half and the imaginary part of \mathbf{X} in the lower half.

Let us denote

$$\begin{aligned} \mathbf{A} &= \left[\frac{\text{Re}\mathbf{X}}{\text{Im}\mathbf{X}} \right] = \left[\begin{array}{c} \mathbf{U} \\ \mathbf{V} \end{array} \right] \\ \mathbf{B} &= \left[\frac{\text{Re}\mathbf{Y}}{\text{Im}\mathbf{Y}} \right] \\ \mathbf{C} &= \left[\frac{\text{Re}\mathbf{Z}}{\text{Im}\mathbf{Z}} \right] \end{aligned} \quad (\text{A.13})$$

Note that the vector \mathbf{A} , of length N , is constructed such that lower half values are the real parts of $X_k; k = 1 \dots N/2$ and the upper half is the imaginary part of $X_k; k = 1 \dots N/2$. Similarly, \mathbf{B} and \mathbf{C} , each of length N , contain real and imaginary parts of the lower half of the second-order correction and the observed Fourier components, respectively. The elements of \mathbf{A} and \mathbf{B} are denoted by a_l and b_k , respectively, where $l, k = 1 \dots N$. The objective function in vector notation now is

$$\mathbf{f}(\mathbf{A}) = \mathbf{A} + \mathbf{B} - \mathbf{C} \quad (\text{A.14})$$

A first-order Taylor approximation of $\mathbf{f}(\mathbf{A})$ about a given $\mathbf{A}^{(0)}$ is

$$\mathbf{f}(\mathbf{A}) = \mathbf{f}(\mathbf{A}^{(0)}) + [\mathbf{J}](\mathbf{A} - \mathbf{A}^{(0)}) \quad (\text{A.15})$$

where $[J]$ is a $N \times N$ Jacobian matrix denoting the derivatives of the elements f_k in vector $\mathbf{f}(\mathbf{A})$ with respect to each of the unknowns a_l in \mathbf{A} where $k, l = 1 \dots N$. The Newton-Raphson scheme at iteration $p + 1$ is then formulated as

$$\mathbf{A}^{(p+1)} = \mathbf{A}^{(p)} + \mathbf{h} \quad (\text{A.16})$$

where \mathbf{h} , a vector of length N , is found from a Cholesky decomposition followed by a back-substitution scheme from

$$[J]\mathbf{h} = -\mathbf{f}(\mathbf{A}^{(p)}) \quad (\text{A.17})$$

It can be easily shown from Eqn. A.14 that the entries $J_{k,l}$ of the matrix $[J]$ are

$$J_{k,l} = \frac{\partial f_k}{\partial a_l} = \delta_{kl} + \frac{\partial b_k}{\partial a_l} \quad (\text{A.18})$$

where $\partial b_k / \partial a_l$ indicates the partial derivative of b_k with respect to a_l , and

$$\delta_{kl} = \begin{cases} 1 & \text{if } k = l \\ 0 & \text{otherwise} \end{cases} \quad (\text{A.19})$$

To find $\partial b_k / \partial a_l$, recall from notation in A.13

$$\begin{aligned} b_k &= \text{Re}Y_k & \text{and} & & b_{k+N/2} &= \text{Im}Y_k & \text{for } k &= 1 \dots N/2 \\ a_l &= \text{Im}X_l = U_l & \text{and} & & a_{l+N/2} &= \text{Im}X_l = V_l & \text{for } l &= 1 \dots N/2 \end{aligned}$$

so that from Eqn.s A.4 and A.6 we have

$$\begin{aligned}
\frac{\partial \text{Re}Y_k}{\partial U_l} &= \sum_{m+n,k} (U_n \delta_{ml} + U_m \delta_{nl}) H_{mn}^+ + \sum_{m-n,k} (U_n \delta_{ml} + U_m \delta_{nl}) H_{mn}^- \\
\frac{\partial \text{Re}Y_k}{\partial V_l} &= \sum_{m+n,k} -(V_n \delta_{ml} + V_m \delta_{nl}) H_{mn}^+ + \sum_{m-n,k} (V_n \delta_{ml} + V_m \delta_{nl}) H_{mn}^- \quad (\text{A.20}) \\
\frac{\partial \text{Im}Y_k}{\partial U_l} &= \sum_{m+n,k} (V_m \delta_{nl} + V_n \delta_{ml}) H_{mn}^+ + \sum_{m-n,k} (V_m \delta_{nl} - V_n \delta_{ml}) H_{mn}^- \\
\frac{\partial \text{Im}Y_k}{\partial V_l} &= \sum_{m+n,k} (U_n \delta_{ml} + U_m \delta_{nl}) H_{mn}^+ + \sum_{m-n,k} (U_n \delta_{ml} - U_m \delta_{nl}) H_{mn}^-
\end{aligned}$$

Schematically,

$$[J] = [I] + \left[\begin{array}{c|c} \frac{\partial \text{Re}Y_k}{\partial U_l} & \frac{\partial \text{Re}Y_k}{\partial V_l} \\ \hline \frac{\partial \text{Im}Y_k}{\partial U_l} & \frac{\partial \text{Im}Y_k}{\partial V_l} \end{array} \right] \quad (\text{A.21})$$

where $[I]$ is the identity matrix.

Appendix B

FITQTF: QTF Surface Spline Interpolation—A Pre-processor to TFPOP

B.1 Introduction

A need to have better interpolation schemes for QTFs in second-order analysis using TFPOP [58] motivated the development of this tool. The analysis required to obtain QTF values is usually an expensive process, as a result the values are estimated only for a sparse number of frequency pairs. TFPOP provides options for a few interpolation schemes (see [58]), that are based on weighted linear interpolation of QTF values within a specified radius. This tool supplements the available interpolation schemes in TFPOP and provides for a flexible means of interpolating a sparse QTF data set into a fine mesh for direct input to TFPOP. The salient features of this tool are:

- The input QTF data is in WAMIT [64] format, this is also the format in which TFPOP reads in the QTFs. The output interpolated QTF is also in a format that TFPOP can read directly.
- The input QTF can be a sparse data set on a regular or irregular grid of frequency (period) pairs. The data set need not be any order. Due to symmetry conditions, the input QTF should only be provided on either the upper or the lower triangle about the principal diagonal ($\omega_i = \omega_j$) of the frequency axis.
- The interpolation is based on a flexible scheme of surface-fitting. FITQTF allows for surface-spline fits of various orders in both frequency directions.
- The interpolation can be based on the axes being any one of frequency (Hz), wave period (seconds), wavelength (meters), or wave number (per meter).

B.2 Interpolation Options

The input QTF is interpolated by fitting spline surfaces of different orders, k_x and k_y (specified by the user), in the two directions x and y . FITQTF can fit splines of orders ranging from 1 through 5 in each direction. Different orders of splines can be chosen in the two directions. The data can also be rotated by 45 degrees in the frequency plane and then interpolated. This rotated interpolation offers a benefit of fitting along the principal diagonal, for example, without using any information from the off-diagonal terms. The user can also specify the x and y coordinate axes used in interpolation to be one of: frequency (Hz), wave period (seconds), wavelength (meters), or wave number (per meter).

Table B.1: Description of error messages from FITQTF

	Description
ier	Unless the routine detects an error, ier contains a non-positive value on exit
ier=0	Normal return. the spline returned has a residual sum of squares fp such that $\text{abs}(fp-s)/s \leq \text{tol}$ with tol a relative tolerance set to 0.001 by the program
ier=-1	Normal return. the spline returned is an interpolating spline (fp=0)
ier=-2	Normal return. the spline returned is the weighted least- squares polynomial of degrees kx and ky. in this extreme case fp gives the upper bound for the smoothing factor s

FITQTF requires as input a parameter s that governs the level of smoothing desired in fitting the surface data. A very large value of s will result in a least-squares fit to the surface, while, in theory, a value $s = 0$ will result in an interpolating spline. However, such an interpolating spline may not always be possible owing to possible theoretical (refer to the subroutine comments regarding more details on s and corresponding error messages). Public domain subroutines (surfit and bispev) are used to fit a surface to the QTF data and the resulting spline coefficients are used for interpolation. For a specified s value, the program tries to fit a surface and then estimates the sum of the residuals squared, and prints these out on standard error. Error flags are also printed to convey the success in fitting the data. The details of the interpretation of the error messages are in the comments of the subroutine surfit, and Table B.1 presents a list of "acceptable" error message values ier:

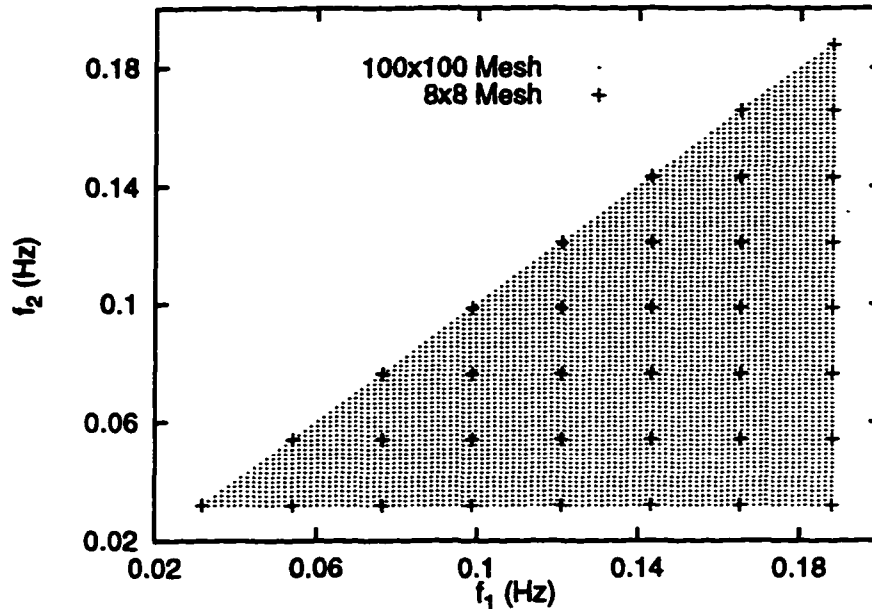


Figure B.1: Frequency grid points of the sparse and the finely meshed QTF values from SWIM

B.3 Verification Studies of FITQTF Interpolation

Some verification studies were done on the accuracy of interpolation from FITQTF for surge response analysis of the OTRC spar. For the spar modeled as a 1-DOF model in the surge direction, a diffraction analysis was performed on a fine mesh of difference frequency QTFs to generate the mean and standard deviation of the surge response. We also perform the same diffraction analysis, but now using various interpolated QTF schemes starting from a sparse QTF data set. The sparse QTF data set contains about 10 times fewer values than the fine mesh QTF as shown in Fig. B.1. Both the QTF data sets were generated using SWIM [53].

The diffraction analysis involved finding the mean, μ , and standard deviation, σ , of the surge response from direct statistics, and from an hourly prediction of the

response in a seastate characterized by $H_s = 14.1\text{m}$, $T_p = 13.8\text{s}$, $\gamma = 2.2$. Three models of the spar were analyzed, assuming the natural periods to be 330 sec, 100 sec, and 71 sec. Each of the three models were analyzed assuming two damping values of 2.4% and 5% in the surge direction. Thus, we have a total of six cases that were analyzed for μ and σ . "Exact" moments for these models were generated from the 100x100 finely meshed QTF. The moments were also generated using various interpolated QTFs starting from the 8x8 QTF and compared to the exact moments.

The different interpolation schemes adopted in this comparison study are:

- **realimag**: Using the TFPOP built-in interpolation on real and imaginary QTF values within a specified radius of 0.032 Hz.
- **11,0**: Using FITQTF to interpolate to a fine mesh by fitting linear splines in both directions without any rotation of the axes
- **11,45**: Using FITQTF to interpolate to a fine mesh by fitting linear splines in both directions after rotating the axes by 45 degrees
- **33,0**: Using FITQTF to interpolate to a fine mesh by fitting cubic splines in both directions without any rotation of the axes
- **33,45**: Using FITQTF to interpolate to a fine mesh by fitting cubic splines in both directions after rotating axes by 45 degrees

Figures B.2 and B.3 show μ and σ from direct statistics for the various interpolated QTFs versus the exact moments from the 100x100 QTF. Each vertical strip on these plots corresponds to a natural frequency, and along each vertical strip there are two sets of points corresponding to the two damping ratios used for each natural frequency. All the structures are analyzed assuming the same QTF, and are analyzed in the same

seastate so the mean surge does not depend on the natural period, as a result the mean ratio for an interpolation model does not change with natural period. Also, the damping ratio does not affect the mean, so we two sets of mean for the two damping ratios lie on top of each other for a given natural frequency. It is seen from this plot that FITQTF substantially reduces the error in estimating the mean. The *realimag* interpolation yields about 8% smaller mean than the exact answer, and the FITQTF interpolations closer predictions.

Similarly, we see in Fig. B.3 that a bi-linear interpolation without any rotation is in error by a maximum of 20%, while the rest of the interpolation schemes give a significantly better fit to the exact answer across the three natural periods, and across the two damping ratios. The closest fit among the interpolation schemes shown, seems to be provided by the bi-cubic interpolation in both μ and σ .

Another set of comparison of the interpolated QTF moments to the exact moments are shown in Figs B.4 and B.5 for 1-hour prediction in the same seastate. Here again, we find similar observations as in the direct statistics comparison. The closest fit to the exact answer seems to be offered by the bi-cubic splines.

In conclusion, we find that FITQTF seems to offer a flexible, convenient and reliable means of interpolating the QTFs.

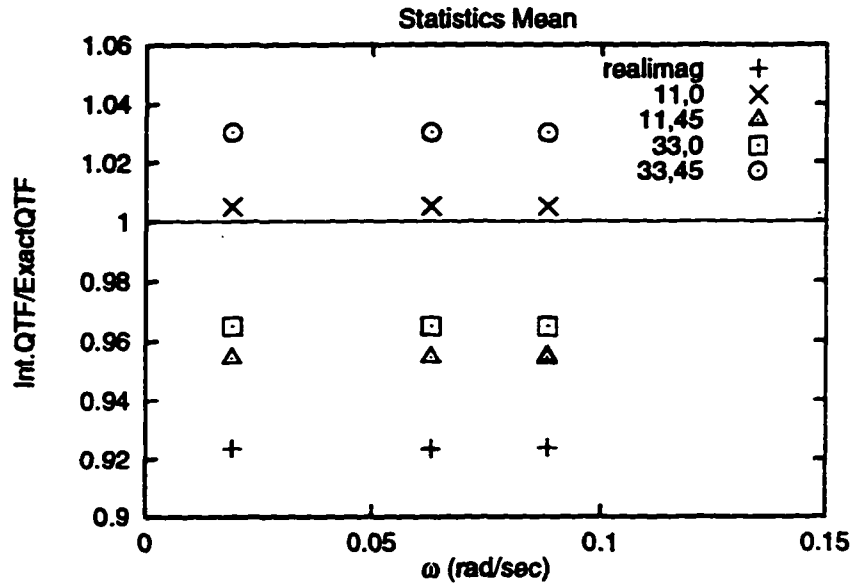


Figure B.2: Direct statistics mean for interpolated QTFs from sparse QTF vs. exact mean from finely meshed QTF (from diffraction analysis)

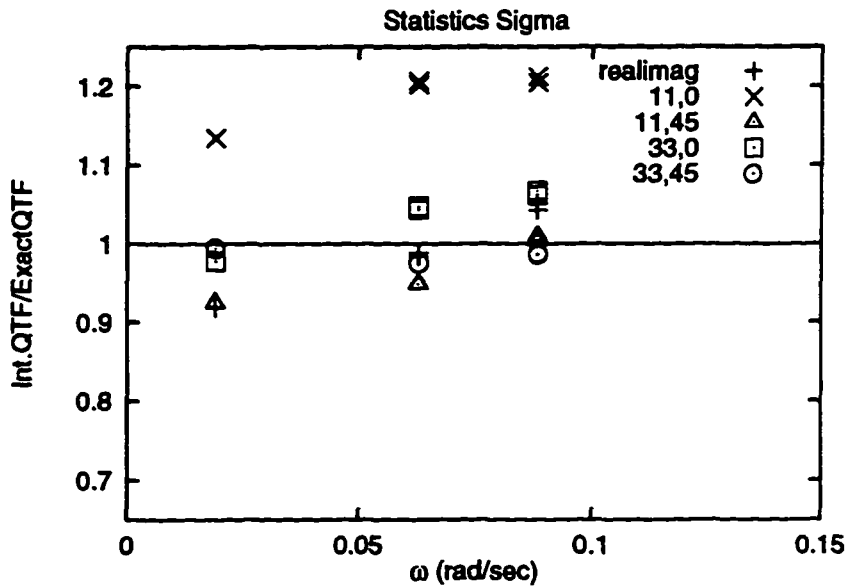


Figure B.3: Direct statistics standard deviation for interpolated QTFs from sparse QTF vs. exact mean from finely meshed QTF

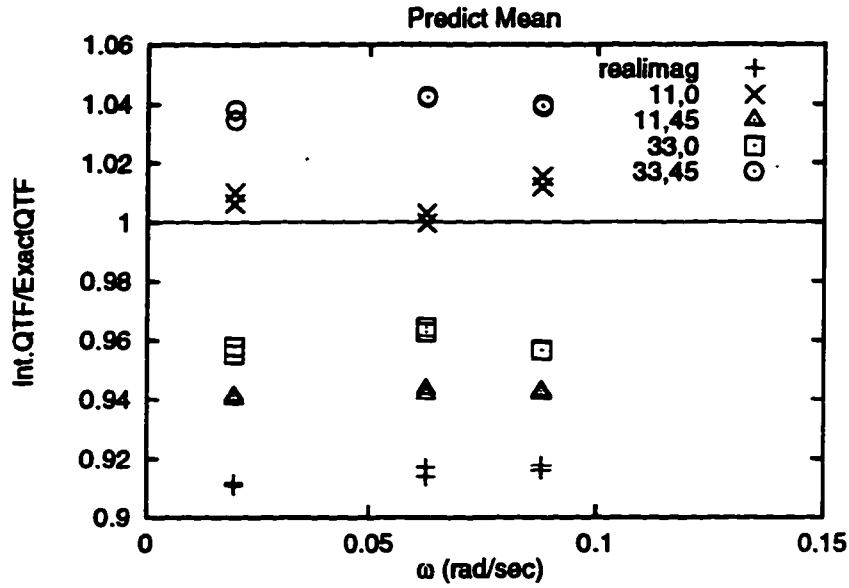


Figure B.4: 1-hour predicted mean for interpolated QTFs from sparse QTF vs. exact mean from finely meshed QTF

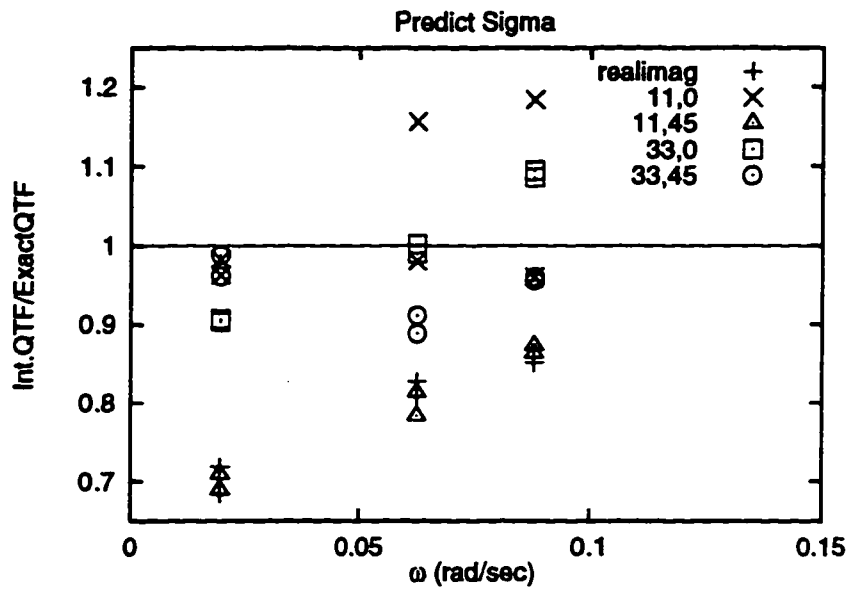


Figure B.5: 1-hour predicted standard deviation for interpolated QTFs from sparse QTF vs. exact mean from finely meshed QTF